2-1-1988

Reflection Mode Diffraction Tomography

Barry A. Roberts
Purdue University

A. C. Kak
Purdue University

Roberts, Barry A. and Kak, A. C., "Reflection Mode Diffraction Tomography" (1988). *Department of Electrical and Computer Engineering Technical Reports.* Paper 593.
https://docs.lib.purdue.edu/ecetr/593

Reflection Mode Diffraction Tomography

Barry A. Roberts
A. C. Kak

TR-EE 88-8
February 1988

School of Electrical Engineering
Purdue University
West Lafayette, Indiana 47907

REFLECTION MODE DIFFRACTION TOMOGRAPHY

Barry A. Roberts
A. C. Kak

School of Electrical Engineering
Purdue University
West Lafayette, Indiana 47907

TR-EE 88-8
February 1988

TABLE OF CONTENTS

APPENDICES

LIST OF FIGURES

Figure Page

Appendix
Figure

ABSTRACT

In the field of ultrasound diffraction tomography, a cross section of a weakly scattering object is reconstructed from measurements of the sound scattered from the insonified object. This research studies tomographic imaging algorithms that deal only with the sound that is backscattered from the object. The use of the backscattered sound provides higher resolution reconstructions due to the higher spatial frequency information about the object that is obtained from the backscatter. Unfortunately the cost of the high frequency information contained in the backscatter is the loss of low frequency information. Different approaches to compensate for this loss are discussed. An additional benefit of reflection mode tomography is that it has the advantage of requiring only 180° access to the object whereas transmission mode requires 360°.

The charter of this research is to explore the effectiveness of current reflection mode diffraction tomography algorithms and to theoretically develop, as well as experimentally verify, new algorithms. Different scanning geometries with different methods of insonification are explored. Many different approaches to the analysis of the problem are taken.

INTRODUCTION

The field of computed tomography involves the non-destructive reconstruction of a slice of an object from measurements made external to the object. There are a variety of ways in which the object is irradiated and in which the measurements are made. In this proposal only ultrasound is considered as the source of energy to use in irradiating the object. Ultrasound has the advantage of being harmless to living tissue but is disadvantaged in that traveling sound waves are diffracted and refracted when they encounter dense or otherwise strongly scattering objects. For this reason the type of tomography considered here is named diffraction tomography. This name might deceive the reader into thinking that cross-sections of strongly scattering objects can be reconstructed. Unfortunately, reconstructions can only be accurately obtained when the object under examination is a weakly scattering object. As object complexity increases, reconstruction quality degrades.

Many different approaches to reflection mode diffraction tomography (RMDT) have been proposed in the literature. The first approach that should be mentioned is the paper presented by Johnson et al. [John77] which discusses a ray tracing approach to synthetic aperture, reflectivity imaging. The approach does correct for refraction and attenuation but does not take into consideration diffraction effects and is aimed at tissue parameterization.

Secondly, the work of Norton and Linzer [Nor79a] analyzes backprojection methods for reconstructing cross-sectional images of ultrasonic reflectivity. The data necessary for reconstruction is obtained from single frequency CW backscattered wave measurements. Reconstructions of ultrasonic reflectivity from experimental data have been carried out with promising results by K. Dines [Dines].

Norton and Linzer [Nor81] have also presented 3-dimensional inversion equations that are based upon the use of broad-band, pulsed, point sources and receivers. The resulting equations that are based upon the Born approximation are in the form of a filtered backprojection operation and are derived for 3 different scanning geometries.

A third source of reflection mode imaging work comes from Azimi and Kak [ManiTR] which considers the reflection mode version of a synthetic aperture reconstruction algorithm proposed in [Nah84]. The approach is based on the Fourier diffraction theorem and seems to efficiently collect data due to the fact that only two rotational views of the object are required. This benefit is offset by the complexity of the transducer arrays and the time consuming manner in which the scattered field measurements are made.

All of the techniques mentioned in the previous paragraphs suffer from a lack of low frequency information inherent in reflection mode imaging and/or the lack of consideration of diffraction effects.

In this proposal the basic concepts underlying reflection mode diffraction tomography will be described and the promise of higher resolution reconstructions, generated from backscatter, will be examined. An intuitive argument that supports this claim, follows in the next paragraph.

The backscattered waves that can be received in a pulse-echo system, can be attributed to the relatively large density (or refractive index) changes within the object being scanned. Hence the information about the object that is contained within the backscattered waves, provide us with only the high frequency changes within the object. The forward scattered wave contains information about the average density (or refractive index) within the object. Hence low frequency information is inherently obtained by transmission tomography. The above intuition will be mathematically supported in chapter one.

Chapter one serves to provide the reader with the basics of RMDT: the approximations and methods of reconstructions that are used. In the following chapter a different type of reflection mode imaging, named ultrasonic reflectivity tomography (URT), is analyzed in both the time and frequency spaces. Chapter three describes a newly conceived algorithm which uses a simple scanning aparatus and delves into experimental issues related to implementing the algorithm. Chapter four builds upon three by describing methods of extrapolating the low frequency information in the backscattered wave measurements that other reflection mode algorithms simply do without. Simulated results of the new algorithm are provided with and without the use of the spectral extrapolation necessary to regain the low frequency information.

Finally, chapter five will examine synthetic aperture diffraction tomography as applied to backscattered fields.

A moment must be spent before the thesis begins, to point out crucial notation that will be used throughout the document. Firstly, all bold characters are vectors. When a character that is known to be a vector quantity is not bold it represents the magnitude of the vector, $r = |\mathbf{r}|$. A phasor representation of wavefronts will be used. This means that the function $u(\mathbf{r},t)$ will be represented by $\mathrm{Re}\,\{U(\mathbf{r})\,e^{j\omega t}\}$ where $U(\mathbf{r})$ is a complex function of position that is equal to $U(\mathbf{r})\,e^{-j\phi(\mathbf{r})}$. In short

CHAPTER 1

DIFFRACTION TOMOGRAPHY

The mathematical background presented in the next section can be passed over by the reader having sufficient background in tomography. In subsequent sections, equations used in this preliminary chapter will be referenced when needed.

1.1 Mathematical Foundation

The fundamental equation on which diffraction tomography algorithms are based is the scalar wave equation

$$\nabla^2 u(\mathbf{r},t) - \frac{1}{c^2(\mathbf{r})}\frac{\partial^2 u(\mathbf{r},t)}{\partial t^2} = 0 \tag{1}$$

where $c(\mathbf{r})$ is the speed of sound and $u(\mathbf{r},t)$ is the spatially and temporally varying pressure wave of the wave. Note that for our purposes, c will only vary within the object that is being imaged and will remain constant in the surrounding medium. If the source of the wave is simple-harmonic such that $u(\mathbf{r},t) = U_\omega(\mathbf{r})\, e^{-j\omega t}$, the wave equation reduces to the following Helmholtz equation,

$$\nabla^2 U_\omega(\mathbf{r}) + \frac{\omega^2}{c^2(\mathbf{r})} U_\omega(\mathbf{r}) = 0 \ . \tag{2}$$

To change the equation into a more manageable form it is convenient to normalize $c(\mathbf{r})$ by the constant c_o which is the sound speed in the surrounding medium.

$$\nabla^2 U_\omega(\mathbf{r}) + k_o^2 U_\omega(\mathbf{r}) = -\omega^2 \left[\frac{1}{c^2(\mathbf{r})} - \frac{1}{c_o^2} \right] U_\omega(\mathbf{r}) \ . \tag{3}$$

The constant k_o is the wave number of the surrounding medium which is equivalent to ω/c_o. The form of Eq. (3) is that of an inhomogeneous wave equation in which the forcing function is

$$F(\mathbf{r})\,U_\omega(\mathbf{r}) = k_o^2\left[\,1 - n^2(\mathbf{r})\right]\,U_\omega(\mathbf{r})\ .$$

The ratio $c_o/c(\mathbf{r}) = n(\mathbf{r})$ is referred to as the refractive index. Hence the wave equation of interest appears as follows

$$\nabla^2 U_\omega(\mathbf{r}) + k_o^2 U_\omega(\mathbf{r}) = -F(\mathbf{r})\,U_\omega(\mathbf{r})\ . \tag{4}$$

Note that the function $F(\mathbf{r})\,U_\omega(\mathbf{r})$ should more appropriately be called the scattering potential since it accounts for the scattering of the sound as it propagates through the object being insonified. The scattering potential describes the inhomogeneity of the object which causes the scattering.

The model of the scattering potential that was just discussed could not take into consideration the scattering effects of the object's compressibility, κ, or density, ρ, which together determine the speed of propagation ($c = 1/\sqrt{\kappa\rho}$). A more accurate wave equation that includes the effects of κ and ρ is [Morse, pg.408-410]

$$\nabla^2 U_\omega + k_o^2 U_\omega = -k_o^2 U_\omega \gamma_\kappa(\mathbf{r}) + \nabla\cdot\left[\,\gamma_\rho(\mathbf{r})\nabla U_\omega\right]\ . \tag{5}$$

The scattering potential in Eq. (5) is effectively that of a viscous compressible fluid. It has been assumed in Eq. (5) that the functions representing the variation in κ and ρ,

$$\gamma_\kappa(\mathbf{r}) = \frac{\kappa-\kappa_o}{\kappa_o} \quad \text{and}$$

$$\gamma_\rho(\mathbf{r}) = \frac{\rho-\rho_o}{\rho}\ ,$$

do not vary with time.

On the assumption that the scattering effects of compressibility are very much smaller than those of the density, $\gamma_\kappa \ll \gamma_\rho$, the equation

$$\nabla^2 U_\omega + k_o^2 U_\omega = \nabla\cdot\left[\,\gamma_\rho(\mathbf{r})\nabla U_\omega\right] \tag{6}$$

can be used as the basis of an inverse scattering algorithm that reconstructs the parameter ρ. It is possible to avoid the above assumption by making use of the fact that the angular dependence of the scattering caused by κ and ρ differs. This dependence will be mathematically described in section 1.3 .

There are two practical methods used to express the solution to the inhomogeneous wave equation in Eq. (4): the separation of variables method and the integral solution method. The first of the methods can be used when the dependence of the pressure wave on each of the coordinates, can be separated. In other words it must be possible that the pressure wave $u(\mathbf{r},t)$ can be expressed as the product of the wave's dependence upon each of the variables used to describe the coordinate system (i.e. $R(r)O(\theta)Z(z)$ in cylindrical coordinates). This approach typically provides the solution in the form of an infinite series which is mathematically correct but might converge too slowly to be useful.

The second of the methods is more general in part due to its independence from the coordinate system being used. Because of its generality, discussion will henceforth be limited to the integral solution method.

The solution of the time harmonic wave equation in Eq. (4) can easily be expressed as follows [Morse, pg.319-321]

$$U_\omega(\mathbf{r}) = \int_S \left[G_\omega(\mathbf{r}\,|\,\mathbf{r}_o) \frac{\partial U_\omega(\mathbf{r}_o)}{\partial n_o} - U_\omega(\mathbf{r}_o) \frac{\partial G_\omega(\mathbf{r}\,|\,\mathbf{r}_o)}{\partial n_o} \right] dS_o$$

$$+ \int_V F(\mathbf{r}_o)\, U_\omega(\mathbf{r}_o)\, G_\omega(\mathbf{r}\,|\,\mathbf{r}_o)\, dv_{\mathbf{r}_o}\ , \tag{7}$$

where $U_\omega(\mathbf{r})$ is the spatial variation of the pressure wave within and on the surface bounding the medium, and dS_o is the elementary unit of surface area on the boundary of the region of interest. The first term on the right hand side of Eq. (7) is the integral over the surface enclosing the region of interest, S, which accounts for reflections from, and sources on, the boundary. In our case we are dealing with an infinite medium for which the boundary integral will reduce to $U_i(\cdot)$ which is the time-harmonic incident wave whose source is on the boundary. This is a good approximation because in this work the received backscatter is time gated such that the transducer does not sense any part of the scattered waves from the sides of our imaging tank. Hence the pressure wave can be expressed as

$$U_\omega(\mathbf{r}) = U_i(\mathbf{r}) + \int_V F(\mathbf{r}_o)\, U_\omega(\mathbf{r}_o)\, G_\omega(\mathbf{r}\,|\,\mathbf{r}_o)\, dv_{\mathbf{r}_o} = U_i(\mathbf{r}) + U_s(\mathbf{r}) \tag{8}$$

where $G_\omega(\mathbf{r}\,|\,\mathbf{r}_o)$ is the solution of the wave equation in Eq. (A1) indicating that the function represents the spatial variation of the pressure wave due to a unit harmonic point source at $\mathbf{r}_o$. Essentially, the second term on the right hand side of Eq. (8), represents the summation of waves scattered from point sources that are weighted by $F(\mathbf{r}_o)\, U_\omega(\mathbf{r}_o)\, dv_{\mathbf{r}_o}$. This weighting term is typically called the scattering amplitude.

It is interesting to note the form of the above solution if the source of the pressure wave is non-harmonic. In this case it is necessary to consider $U_\omega(\mathbf{r})$ as a function of ω, instead of simply being parameterized by ω.

$$U(\mathbf{r},\omega) = \int_{-\infty}^{\infty} u(\mathbf{r},t)\, e^{j\omega t}\, dt$$

The resulting scattered wave can be expressed as follows:

$$u_s(\mathbf{r},t) = \int_V F(\mathbf{r}_o) \int_{-\infty}^{\infty} u(\mathbf{r}_o,t_o)\, g(\mathbf{r},t\,|\,\mathbf{r}_o,t_o)\, dt_o\, dv_{\mathbf{r}_o} \tag{9}$$

The above equation is a convolution of the forcing function, f(•), and the time domain Green's function, g(•) in Eq. (A8), in space and time. This free space result will lead to the following expression for the scattered wave,

$$u_s(\mathbf{r},t) = \int_V \frac{F(\mathbf{r}_o)}{4\pi\,|\mathbf{r}-\mathbf{r}_o|}\, u\left[\mathbf{r}_o,\, t-\frac{|\mathbf{r}-\mathbf{r}_o|}{c}\right] dv_{\mathbf{r}_o} \ . \tag{10}$$

1.1.1 The Born Approximation

The solution to the inhomogeneous wave equation in Eq. (4), is

$$U_\omega(\mathbf{r}) = U_i(\mathbf{r}) + \iiint_V F(\mathbf{r}_o)\, U_\omega(\mathbf{r}_o)\, G_\omega(\mathbf{r}\,|\,\mathbf{r}_o)\, dv_{\mathbf{r}_o} \tag{11}$$

which appears to be a Fredholm equation of the second kind. The solution to such an equation can be obtained at great cost by iterative-perturbation methods [MorFes]. To simplify the expression for $U_\omega(\cdot)$ into a more manageable form, we will make use of the Born approximation which assumes that the object is weakly scattering, $|U_s| \ll |U_i|$. Making the assumption that the total wave is equal to the incident wave plus the scattered wave and using the Born approximation, Eq. (11) becomes

$$U_\omega(\mathbf{r}) = U_i(\mathbf{r}) + \iiint_V F(\mathbf{r}_o)\, U_i(\mathbf{r}_o)\, G_\omega(\mathbf{r}\,|\,\mathbf{r}_o)\, dv_{\mathbf{r}_o} \ . \tag{12}$$

The equation above represents only a first order approximation to the total wave, U_ω. The integral term in Eq. (12) represents the scattered wave,

$$U_s(\mathbf{r}) = \iiint_V F(\mathbf{r}_o)\, U_i(\mathbf{r}_o)\, G_\omega(\mathbf{r}\,|\,\mathbf{r}_o)\, dv_{\mathbf{r}_o} \ . \tag{13}$$

It is this relationship between the scattered wave and the scattering potential, henceforth referred to as "the object," which is the crux of diffraction tomography. Of course, higher order approximations to $U_s(\cdot)$ can be made, but the fact remains that Eq. (13) is the basis of most algorithms. Unfortunately the same approximation used to obtain the scattered wave equation also represents the most severe limitation to reconstruction accuracy.

To reduce Eq. (13) to a more desirable form, the Green's function can be replaced by its angular spectrum expansion which is Eq. (A5) in the 3 dimensional case or Eq. (A6) in the 2D case. If we stick to the 3D problem, the scattered wave becomes

$$U_s(\mathbf{r}) = \frac{j}{8\pi^2} \iiint_V dv_{\mathbf{r}_o}\, F(\mathbf{r}_o)\, U_i(\mathbf{r}_o) \int_{-\infty}^{\infty}\!\!\int dK_x\, dK_y\, e^{j\left[K_x(x-x_o)+K_y(y-y_o)\right]}$$

$$\cdot \frac{e^{j\gamma\,|z-z_o|}}{\gamma}\ , \gamma = \sqrt{k_o^2-K_x^2-K_y^2}\ . \tag{14}$$

1.1.2 The Fourier Diffraction Theorem

Since we are only interested in the reflection mode problem, let's consider a scanning geometry in which the z component of the observation point **r** always has a value less than the value of z_0. Figure (1) illustrates the geometry in which $|z-z_0| = z_0-z$. Note that the value of **r** will be allowed to vary only over the plane $z = l_0$. If the incident wave is a time harmonic plane wave, $U_i(\mathbf{r}) = U_0 e^{jk_o\hat{\mathbf{a}}_z\cdot\mathbf{r}}$, the integration with respect to $\mathbf{r}_o = (x_0,y_0,z_0)$ in Eq. (14) can be carried out, resulting in

$$U_{s,\hat{a}_z}(\mathbf{r}) = \frac{jU_o}{8\pi^2} \int_{-\infty}^{\infty}\!\!\int dK_x\, dK_y \iiint_V dv_{\mathbf{r}_o}\, F(\mathbf{r}_o)\, \frac{e^{jk_oz_o}}{\gamma} e^{-j[K_xx_o+K_yy_o-\gamma z_o]}\, e^{j[K_xx+K_yy-\gamma l_0]}$$

$$= \frac{jU_o}{8\pi^2} \int_{-\infty}^{\infty}\!\!\int dK_x\, dK_y\, \tilde{F}(K_x,K_y,-\gamma-k_o)\, e^{j[K_xx+K_yy-\gamma l_0]}\, \frac{1}{\gamma}\ , \tag{15}$$

where $\tilde{F}(\cdot)$ is equal to the Fourier transform of $F(\cdot)$ and $\hat{a}_z$ is the unit vector in the positive z direction. *Note that the Fourier transformation operation can only be carried out if we limit ourselves to consider only nonevanescent waves for which $k_o^2>K_x^2+K_y^2$.* Refer to Appendix C for a discussion on evanescent waves and the implications of their exclusion.

The final step needed to obtain the desired spatial frequency domain relationship between the scattered wave and the object, is the Fourier transformation of $U_s(\cdot)$ over the measurement plane, $z = l_0$. This transformation yields,

$$\tilde{U}_{s,\hat{a}_z}(\alpha,\beta;l_0) = \frac{jU_o}{2}\, \frac{e^{-j\sqrt{k_o^2-\alpha^2-\beta^2}\,l_0}}{\sqrt{k_o^2-\alpha^2-\beta^2}}\, \tilde{F}(\alpha,\beta,-\sqrt{k_o^2-\alpha^2-\beta^2}-k_o)\ . \tag{16}$$

Note that the above equation was obtained with the following two basic relationships:

$$\int_{-\infty}^{\infty} e^{-j(\alpha-K)x}\, dx = 2\pi\delta(\alpha-K) \quad \text{and} \quad \int_{-\infty}^{\infty} F(K)\,\delta(\alpha-K)\, dK = F(\alpha)\ .$$

Equation (16) is called the Fourier diffraction theorem (FDT) in three dimensions. It relates the Fourier transform of the scattered wave on the surface of a plane to the transform of the object over surfaces known as Ewald spheres.

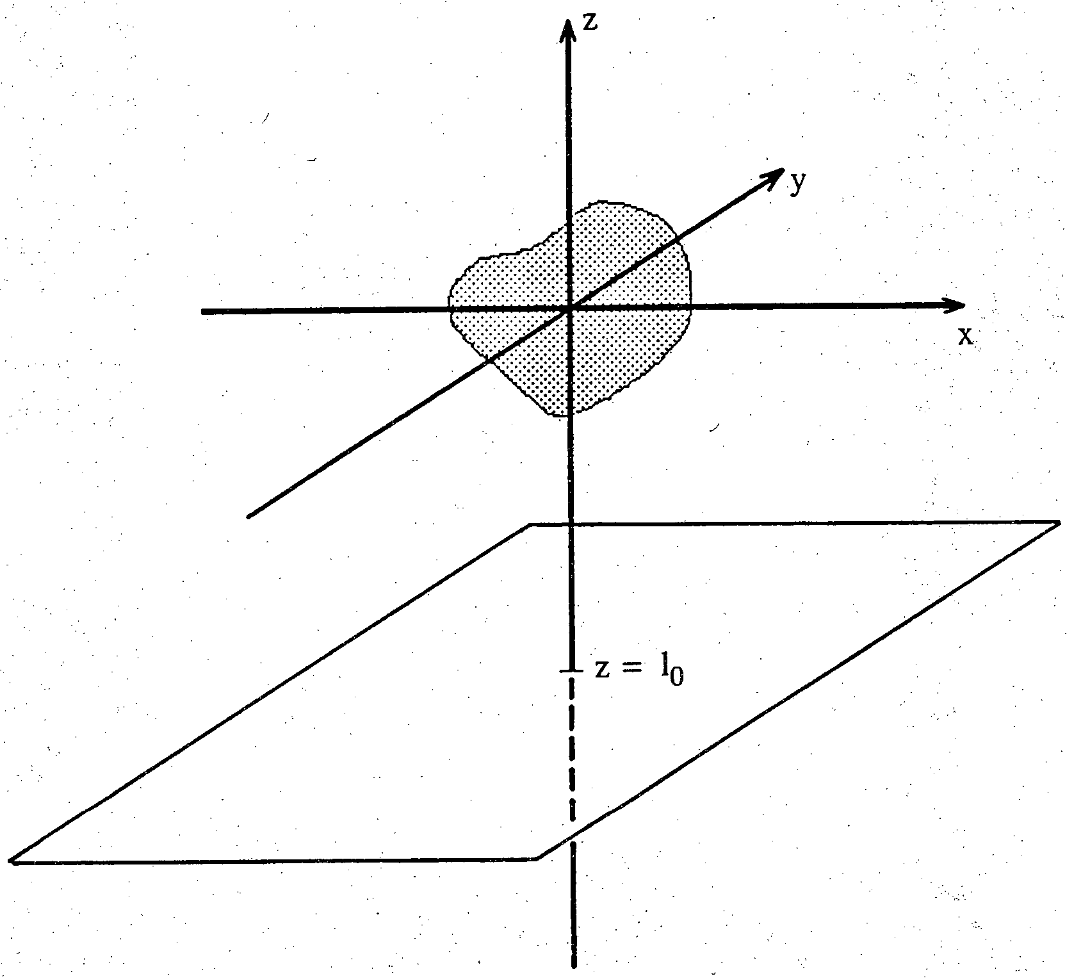

Figure (1) A simple illustration of the location of the transducer plane in a 3D experiment. The transducer plane is $z = l_0$.

The fact that an object's spatial frequency components are known on a spherical surface is a result of the argument of the function F(**W**) where $\mathbf{W} = (\zeta,\eta,\gamma)$. Equating the components of **W** with the x, y and z spatial frequency components used in Eq. (16), results in

$$\zeta = \alpha \ , \ \eta = \beta \ , \ \gamma = -\sqrt{k_o^2-\alpha^2-\beta^2} - k_o \ .$$

If the dependence of the components of **W** on α and β is eliminated we have

$$(\gamma+k_o)^2+\zeta^2+\eta^2 = k_o^2$$

which is the equation for a sphere centered at the spatial frequency $(0,0,-k_o)$ with a radius of k_o. This describes the Ewald sphere corresponding to plane wave insonification of the object in the positive z direction. One thing that must be pointed out is the extent of the sphere that can actually be recovered from the measured scattered wave. Remember that our discussion is limited to nonevanescent waves thereby bounding the value of γ, $-2k_o<\gamma<-k_o$. Hence the recoverable portion of the sphere will always be the hemisphere furthest from the origin. The coverage of the opposite hemisphere is attributed to the backscattered evanescent waves which attenuate in the direction of the receiving plane and are too weak to be received at a distance of a few wavelengths. Note that the sphere is divided into hemispheres by the plane perpendicular to the vector in the direction of the center of the sphere and containing the center of the sphere. Hence we have mathematically shown that a backscattered wave measurement only provides high frequency information about the object being insonified.

In the above paragraph, discussion was limited to a particular geometry but now let's generalize the discussion and examine plane wave insonification from any direction. Let's use the plane wave $e^{j(k_o\hat{s}_o\cdot r-\omega t)}$, which propagates in the direction $\hat{s}_o$. The expression for the FDT remains the same, although the axes used have been rotated about the origin such that the new z axis has the unit vector $\hat{s}_o$. Following the discussion related to Eq. (15), one can see that the Ewald sphere will end up being centered at $-k_o\hat{s}_o$ in the spatial frequency domain.

To obtain the FDT for the case of forward scattered waves instead of backscattered waves, simply replace $|z-z_o|$ with $z-z_o$ since the observation plane is $z=l_0$ where l_0 is always greater than z_o. In this case coverage in the object's frequency domain will always lie on the hemisphere closest to the origin thereby containing zero frequency information about the object.

A similar FDT in two dimensions can easily be obtained by dropping the z dependence of the object and using the angular spectrum expansion for the 2D Green's function, Eq. (A6), in Eq. (13). Figure (2) illustrates the simple scanning configuration in which the line of transducers is located at $y=l_0$ and $\hat{s}_o=\hat{a}_y$. Figure (3) illustrates

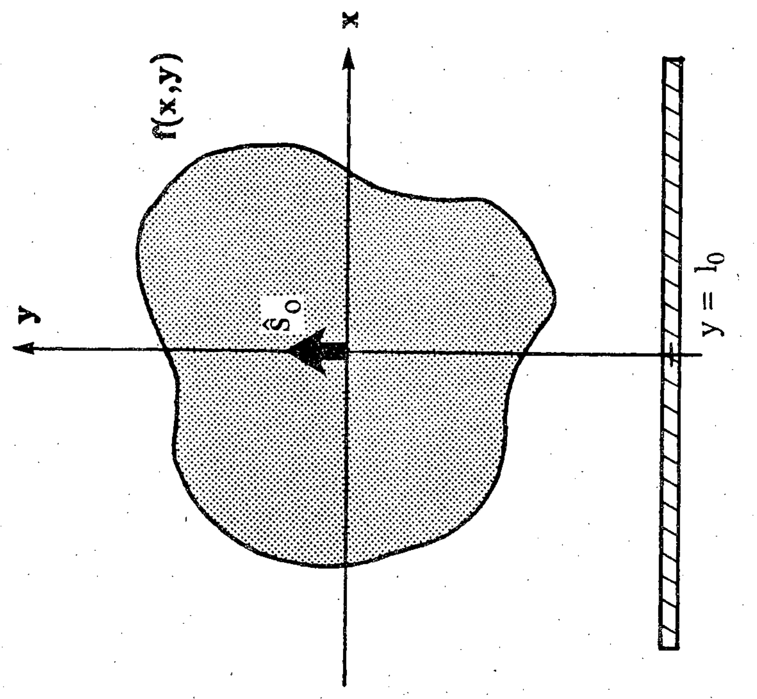

Figure (2) The scanning geometry used in obtaining backscattered field measurements for use in the algorithms. The single plane wave transducer lies on the line $y = l_0$.

the FDT in 2 dimensions (I can't draw 2D representations of 3D relationships very well). Note that in transmission mode, the object coverage obtained is indicated in figure (3) by the dashed line portion of the "Ewald circle."

1.2 Methods of Reconstruction

The two most popular approaches to carrying out the reconstruction of the interior of an object from scattered wave measurements, are called filtered backpropagation [Dev82] and frequency domain filling [Pan83]. In the following two sub-sections both approaches will be briefly described in reflection mode.

1.2.1 Frequency Domain Filling

One reconstruction approach is that in which the object's spatial frequency domain is filled in with the scaled and phase shifted Fourier transform of the backscattered wave. For the 2D case of an incident monochromatic plane wave having a direction of propagation indicated by $\hat{s}_o$ ($\hat{s}_o \cdot \hat{a}_x = \cos\phi$), the following 2D Fourier diffraction theorem follows from Eq. (16)

$$\tilde{F}(\alpha, -\sqrt{k_o^2-\alpha^2}-k_o) = -j2\sqrt{k_o^2-\alpha^2}\, e^{j\sqrt{k_o^2-\alpha^2}\, l_0}\, \tilde{U}_{s,\hat{s}_o}(\alpha; y = l_0) \qquad (17)$$

where $\alpha = v\cos\phi - u\sin\phi$. Note that the function $\tilde{F}(\cdot)$ is the 2D Fourier transform of the function $F(\cdot)$ and $\tilde{U}_{s,\hat{s}_o}(\cdot)$ is the Fourier transform of the scattered wave received on the line $y = l_0$. The function $F(\cdot)$ represents the object being imaged and is part of the forcing function in the following wave equation

$$\nabla^2 U_\omega(\mathbf{r}) + k_o^2 U_\omega(\mathbf{r}) = -F(\mathbf{r})U_\omega(\mathbf{r}) \ .$$

To reinforce the reader's understanding of the FDT, it is necessary to refer to figure (3) and point out where the functions in Eq. (17) originate. The function $\tilde{U}_{s,\hat{s}_o}(\alpha; l_0)$ is the Fourier transform of the backscatered wave along the receive line which is at a distance of l_0 from the origin. This transform, after scaling and phase shifting, provides values of the spatial transform of the object function, $\tilde{F}(u,v)$, on the reflection portion of the arc in the (u,v) plane. A bandlimited region of $\tilde{F}(u,v)$ is obtained by making scattered wave measurements at various positions around the object at integral values of ϕ in the range of $[0,2\pi]$. The resulting coverage of $\tilde{F}(u,v)$ lies between the 2 circles of radius $\sqrt{2}\, k_o$ and k_o rad/m. This coverage, as illustrated in figure (4) is missing a large portion of $\tilde{F}(u,v)$.

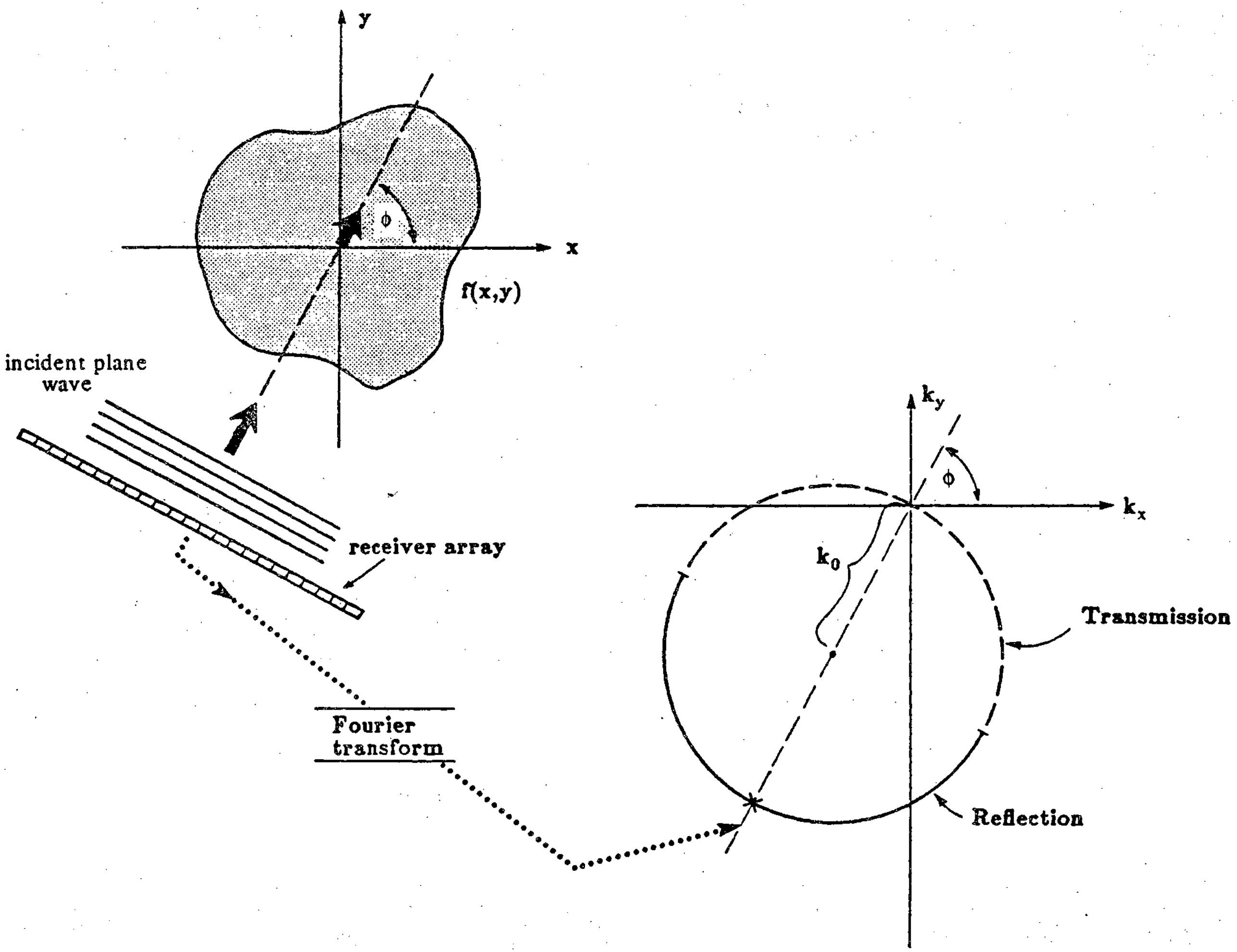

Figure (3) The Fourier diffraction theorem is illustrated in reflection mode. In transmission mode the forward scattered field is linearly related to the 2D Fourier domain data lying on the dashed portion of the Ewald circle.

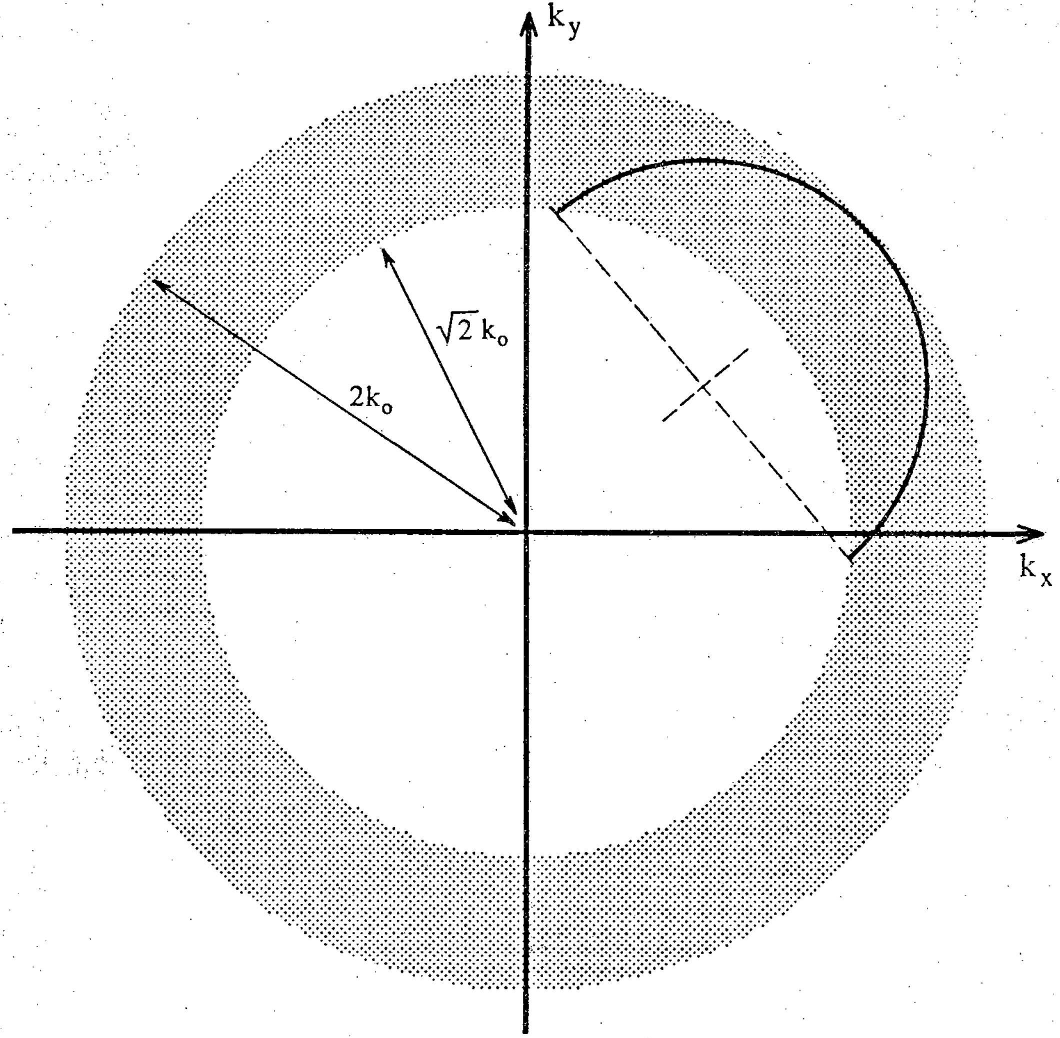

Figure (4) The object's spatial frequency domain coverage obtainable from only backscattered field measurements.

To obtain values of $\tilde{F}(u,v)$ from $\tilde{U}_{s,\hat{s}_o}(\alpha;l_0)$ we need equations relating u,v,α and ϕ. In pursuit of these equations we refer to figure (5) and recognize the relationships,

$$2(\pi-\phi+\theta)+\chi+\frac{\pi}{2}=\pi \quad \text{and} \quad \frac{w}{2}=k_o\sin\left[\frac{\chi}{2}+\frac{\pi}{4}\right],$$

from which the desired equations result,

$$\phi=\frac{3\pi}{4}+\frac{\chi}{2}+\arctan\left[\frac{v}{u}\right] \quad \text{and} \quad \alpha=k_o\cos\chi$$

where

$$\chi=2\left[\arcsin\left[\frac{\sqrt{u^2+v^2}}{2k_o}\right]\right]-\frac{\pi}{2}$$

For a computer implementation of this approach to cross-section reconstruction, $\tilde{F}(u,v)$ must first be estimated at every point on a rectangular sampling grid such that a subsequent inverse fast Fourier transform can be carried out to obtain our approximation to f(x,y). For a particular u and v the values of ϕ and α may not correspond actual samples of $\tilde{U}_{s,\hat{s}_o}(\cdot)$ since there are a finite number of receiving transducers and backscattered wave measurements are only taken at 1 degree increments at best. Therefore it is necessary to approximate the value at (u,v) by one of two ways. One may interpolate the value of (u,v) from nearby samples of $\tilde{U}_{s,\hat{s}_o}(\alpha;l_0)$ that are known, or simply accept the nearest known value of $\tilde{U}_{s,\hat{s}_o}(\alpha;l_0)$. A good comparison of the two approaches to frequency domain filling when applied to inversion of the forward scattered waves, is provided in [Pan83].

Once a sufficient number of $\tilde{F}(u,v)$ samples have been obtained, a simple Fourier inversion provides us with a band-pass estimate to f(x,y).

1.2.2 Filtered Backpropagation

In this section the backscattered wave version of the filtered-backpropagation approach (FBP) to object cross-section reconstruction will be described. An excellent reference for this approach, formulated for forward scattered waves, is presented by its inventor in [Dev82]. Note that only the 2D problem with plane wave insonification will be discussed in this section.

To start off the discussion we first examine the Fourier transform relationship,

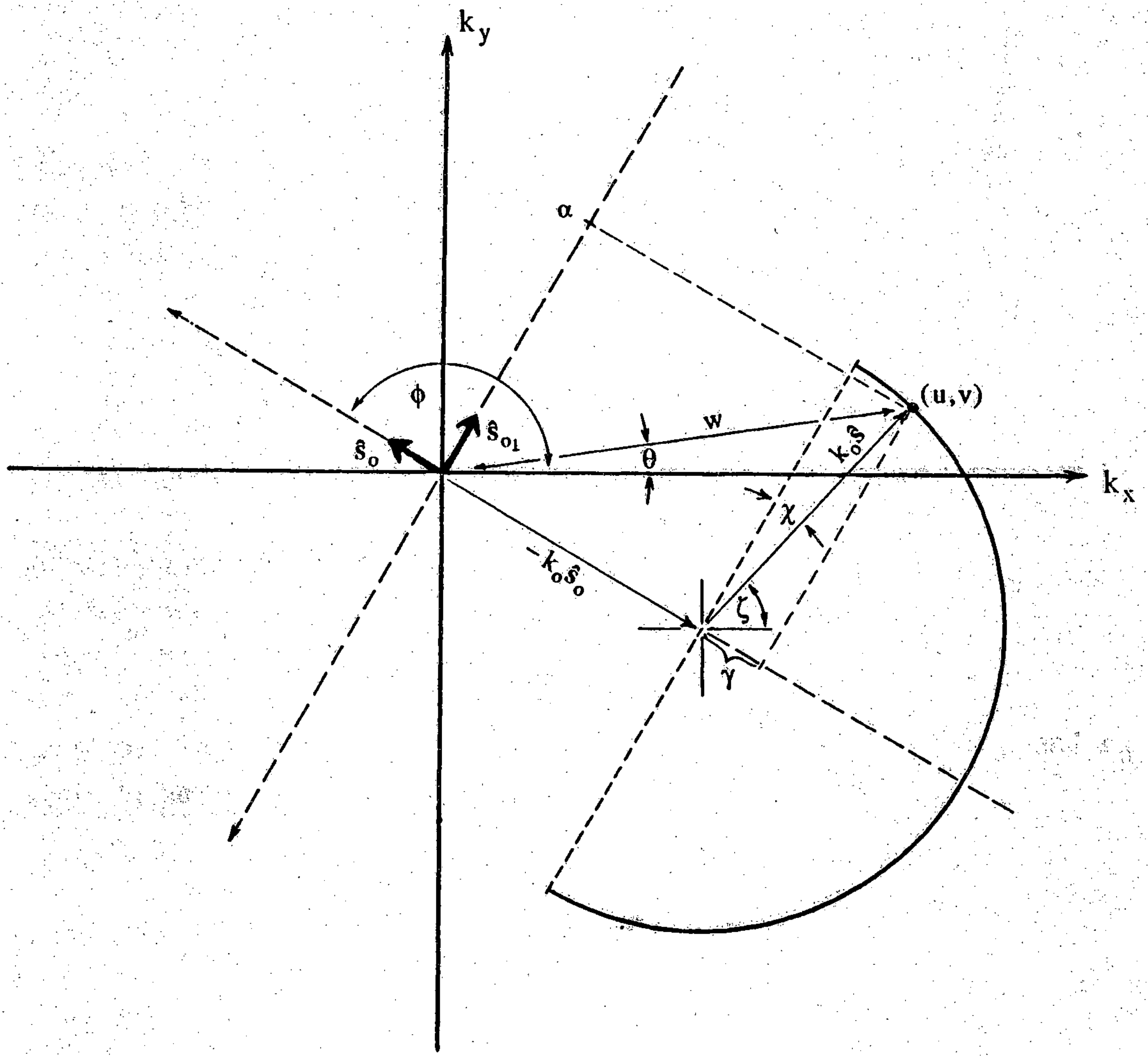

Figure (5) The Frequency domain relationship between $\tilde{U}_{S,\hat{s}_o}(\alpha, y = l_0)$ and the samples in the object's spatial frequency domain.

$$f_{BP}(x,y) = \frac{1}{4\pi^2} \iint_D F(u,v)\, e^{j(ux+vy)}\, du\, dv \tag{18}$$

in which D is the shaded area in (u,v) space as illustrated in figure (4). Using the Ewald circle geometry in figure (5), the first step in deriving the FBP algorithm is to convert the integrations with respect to u and v in Eq. (18) to integrations with respect to the variables ϕ and ζ. To do this let's first formulate the change of variables that must occur and then calculate the necessary jacobian,

$$u = k_o(\cos\zeta - \cos\phi) \qquad v = k_o(\sin\zeta - \sin\phi)$$

$$du\, dv = \begin{vmatrix} -k_o\sin\zeta & k_o\sin\phi \\ k_o\cos\zeta & -k_o\cos\phi \end{vmatrix} d\zeta\, d\phi$$

$$= k_o^2\sqrt{1-\cos^2(\zeta-\phi)}\; d\zeta\, d\phi = k_o^2\sqrt{1-(k_o^2-\alpha^2)/k_o^2}\; d\zeta\, d\phi = k_o\,|\alpha|\; d\zeta\, d\phi\ .$$

With this knowledge Eq. (18) becomes,

$$f_{BP}(x,y) = \frac{k_o}{4\pi^2}\int_{-\pi}^{\pi} d\phi \int_{\phi-\pi/2}^{\phi+\pi/2} d\zeta\ |\alpha|\ F\Big[\, k_o(\hat{s}-\hat{s}_o)\Big]\ e^{jk_o(\hat{s}-\hat{s}_o)\cdot \mathbf{r}}\ ,$$

where $\hat{s}$ and $\hat{s}_o$ are unit vectors in the directions indicated in figure (5). For convenience let's make the change the variable ζ into the more suitable angle χ where $\zeta = \phi-\chi+\pi/2$ and $d\zeta = -d\chi$. Hence,

$$f_{BP}(x,y) = \frac{-k_o}{4\pi^2}\int_{-\pi}^{\pi} d\phi \int_{0}^{\pi} d\chi\ |\alpha|\ F\Big[\, k_o(\hat{s}-\hat{s}_o)\Big]\ e^{jk_o(\hat{s}-\hat{s}_o)\cdot \mathbf{r}}\ .$$

in which another change of variable is necessary. This time let's replace χ with α where $d\alpha = -k_o\sin\chi\, d\chi = -\gamma\, d\chi$ and $\gamma = \sqrt{k_o^2-\alpha^2}$. Next we replace $F(\cdot)$ with its equivalent described in Eq. (17) which yields,

$$f_{BP}(x,y) = \frac{k_o}{4\pi^2}\int_{-\pi}^{\pi} d\phi \int_{k_o}^{-k_o} d\alpha\ \frac{|\alpha|}{\gamma}\left[\ \frac{2\gamma}{j}\, e^{j\gamma l_0}\, \tilde{U}_{s,\hat{s}_o}(\alpha; l_0)\right]\ e^{j[\alpha\hat{s}_{o\perp}-(\gamma+k_o)\hat{s}_o]\cdot\mathbf{r}}\ . \tag{19}$$

Note the use of the unit vector $\hat{s}_{o\perp}$ which is perpendicular to $\hat{s}_o$.

The implementation of Eq. (19) is better seen if the equation is rewritten as follows:

$$f_{BP}(x,y) = \frac{k_o}{4\pi^2}\int_{-\pi}^{\pi} d\phi \int_{-k_o}^{k_o} d\alpha\ 2j\, e^{j\gamma l_0}\ |\alpha|\ \tilde{U}_{s,\hat{s}_o}(\alpha; l_0)\, e^{-j(\gamma+k_o)\eta}\ e^{j\alpha\xi}$$

$$= \frac{1}{4\pi^2}\int_{-\pi}^{\pi} d\phi \int_{-\infty}^{\infty} d\alpha\ A(\alpha)\, \tilde{U}_{s,\hat{s}_o}(\alpha; l_0)\, P_\eta(\alpha)\, e^{j\alpha\xi}$$

where $\left[\ A(\alpha) = 2jk_o|\alpha| \ \ , -k_o<\alpha<k_o \right]$ is the frequency dependent weighting and $\left[\ P_\eta(\alpha) = e^{j\gamma l_o} e^{-j(\gamma+k_o)\eta} \ \ , |\alpha| \le k_o \right]$ is a phase factor proportional to the distance traveled by the incident wave. Also note that the reconstruction point (x,y) is described by ($\xi = -x\sin\phi + y\cos\phi$, $\eta = x\cos\phi + y\sin\phi$) in the rotated coordinate plane (η,ξ).

The form of the $P_\eta(\alpha)$ filter is interesting because it is dependent upon the point within the object that is being reconstructed. In actual implementation each measured backscattered wave would have to be filtered many times with $P_\eta(\cdot)$ for a range of η values that covers the region of the object's cross-section that is of interest. Of course this is quite a time consuming process but if only a small region needs to be reconstructed, the amount of additional filtering is only marginal.

It is important to keep in mind that $f_{BP}(x,y)$, as its subscript proclaims, is only a bandpass approximation to $f(x,y)$.

1.3 Separation of the Effects of Compressibility and Density

In reference [Nor83] a unique scanning geometry along with plane wave insonification is shown to allow separate reconstructions to be made of the compressibility and density within the object being imaged. The following presents a very compact mathematical explanation of how separate reconstructions of compressibility and density can be obtained.

The free space scattering amplitude of Eq. (5), with the aid the Born approximation, is expressed as

$$\phi_s(\mathbf{r}) = \int_V k_o^2 \gamma_\kappa(\mathbf{r}_o) U_i(\mathbf{r}_o) G_\omega(\mathbf{r}|\mathbf{r}_o) - \nabla_o \cdot [\gamma_\rho(\mathbf{r}_o)\, \nabla_o U_i(\mathbf{r}_o)\,]\, G_\omega(\mathbf{r}|\mathbf{r}_o)\, dv_{\mathbf{r}_o} \ ,$$

where ∇_o is the gradient operator applied to the $\mathbf{r}_o$ variable. The above expression can be simplified with the vector identity

$$\psi\nabla\cdot\mathbf{A} = \nabla\cdot(\psi\mathbf{A}) - \mathbf{A}\cdot\nabla\psi$$

which leads to

$$\phi_s(\mathbf{r}) = \int_V k_o^2\, U_i(\mathbf{r}_o)\gamma_\kappa(\mathbf{r}_o)\, G_\omega(\mathbf{r}|\mathbf{r}_o)\, dv_{\mathbf{r}_o} + \int_V \gamma_\rho(\mathbf{r}_o)\, \nabla_o U_i(\mathbf{r}_o)\cdot\nabla_o G_\omega(\mathbf{r}|\mathbf{r}_o)\, dv_{\mathbf{r}_o}$$
$$- \int_S \gamma_\rho(\mathbf{r}_o)\, \nabla_o U_i(\mathbf{r}_o)\cdot\nabla_o G_\omega(\mathbf{r}|\mathbf{r}_o)\, dv_{\mathbf{r}_o} \ . \qquad (20)$$

The last integral on the right hand side of the above equation, will equal zero since $\gamma_\rho(\cdot)$ equals zero on the surface *S* that lies outside of the object and bounds the region.

Next, let us once again look at the scattering amplitude,

$$\phi_s(\mathbf{r}) = \int_V k_o^2\, U_i(\mathbf{r}_o)\gamma_\kappa(\mathbf{r}_o)\, G_\omega(\mathbf{r}\,|\,\mathbf{r}_o)\, dv_{\mathbf{r}_o} + \int_V \gamma_\rho(\mathbf{r}_o)\, \nabla_o U_i(\mathbf{r}_o)\cdot\nabla_o G_\omega(\mathbf{r}\,|\,\mathbf{r}_o)\, dv_{\mathbf{r}_o}\ , \tag{21}$$

and take the spatial transform of both sides of the equation with respect to **r**. This leads to the Fourier transform of the scattering amplitude being expressed as

$$\Phi_s(\mathbf{K}) = \int_V k_o^2\, U_i(\mathbf{r}_o)\gamma_\kappa(\mathbf{r}_o)\, \tilde{G}_\omega(\mathbf{K}\,|\,\mathbf{r}_o)\, dv_{\mathbf{r}_o} + j\int_V \gamma_\rho(\mathbf{r}_o)\, \nabla_o U_i(\mathbf{r}_o)\cdot\mathbf{K}\, \tilde{G}_\omega(\mathbf{K}\,|\,\mathbf{r}_o)\, dv_{\mathbf{r}_o}\ ,$$

into which we substitute Eq. (A3) and subsequently carry out the integration with respect to $\mathbf{r}_o$ [Morse, pg.413-414]. The result is

$$\begin{aligned}\Phi_s(\mathbf{K}) &= \int_V k_o^2\, U_i(\mathbf{r}_o)\gamma_\kappa(\mathbf{r}_o)\, \frac{e^{-j\mathbf{K}\cdot\mathbf{r}_o}}{|\mathbf{K}|^2-k_o^2}\, dv_{\mathbf{r}_o} \\ &\qquad + j\int_V \gamma_\rho(\mathbf{r}_o)\, \nabla_o U_i(\mathbf{r}_o)\cdot\mathbf{K}\, \frac{e^{-j\mathbf{K}_s\cdot\mathbf{r}_o}}{|\mathbf{K}|^2-k_o^2}\, dv_{\mathbf{r}_o}\ , \\ &= \frac{k_o^2 \int \tilde{U}_i(\Lambda)\Gamma_\kappa(\mathbf{K}-\Lambda)\, dv_\Lambda - (\mathbf{k}_i\cdot\mathbf{K}) \int \tilde{U}_i(\Lambda)\Gamma_\rho(\mathbf{K}-\Lambda)\, dv_\Lambda}{|\mathbf{K}|^2-k_o^2}\ ,\end{aligned} \tag{22}$$

where $\tilde{U}_i(\mathbf{k}_i) = \int U_i(\mathbf{r})\, e^{-j\mathbf{k}_i\cdot\mathbf{r}}\, dv_{\mathbf{r}}\ ,\ \Gamma_\rho(\mathbf{K}) = \int \gamma_\rho(\mathbf{r})\, e^{-j\mathbf{K}\cdot\mathbf{r}}\, dv_{\mathbf{r}}\ .$

The integrals in Eq. (22) are now spatial frequency domain convolutions that result because of $\mathfrak{F}\{\nabla_o U_i(\mathbf{r}_o)\} \Longleftrightarrow j\mathbf{K}\tilde{U}_i(\mathbf{K})$.

The dot product $\mathbf{k}_i\cdot\mathbf{K}$ in Eq. (22), is equivalent to $|\mathbf{k}_i||\mathbf{K}|\cos\theta$ where θ is the angle between the vector of incidence $\mathbf{k}_i = k_o\hat{\mathbf{a}}_i$ and the vector in the direction of observation $\mathbf{K} = k_o\hat{\mathbf{a}}_r$. When this angle is equal to $\pi/2$ radians we can see that the second term on the right hand side of Eq. (22), will equal zero. Hence we can use a scanning geometry, illustrated in figure (6), consisting of two perpendicular, phase insensitive, plane wave transducers in the near field of the object, one operating in pulse-echo mode and the other serving only as a receiver. The transducer operating in pulse-echo mode will receive the scattered wave as described by both terms in Eq. (22) and the "receive only" transducer will receive only the first term on the right hand side.

For the case of plane wave insonification

$$U_i(\mathbf{r}) = e^{j(k_o\mathbf{a}_i\cdot\mathbf{r}-\omega t)}\ ,\ \tilde{U}_i(\mathbf{K}) = \delta(\mathbf{K}-\mathbf{k}_i)\ ,$$

resulting in

$$\Phi_s(\mathbf{K}) = \frac{k_o^2}{|\mathbf{K}|^2-k_o^2}\left[\, \Gamma_\kappa(\mathbf{K}-\mathbf{k}_i) - \Gamma_\rho(\mathbf{K}-\mathbf{k}_i)\, \hat{\mathbf{a}}_i\cdot\hat{\mathbf{a}}_r \right]\ .$$

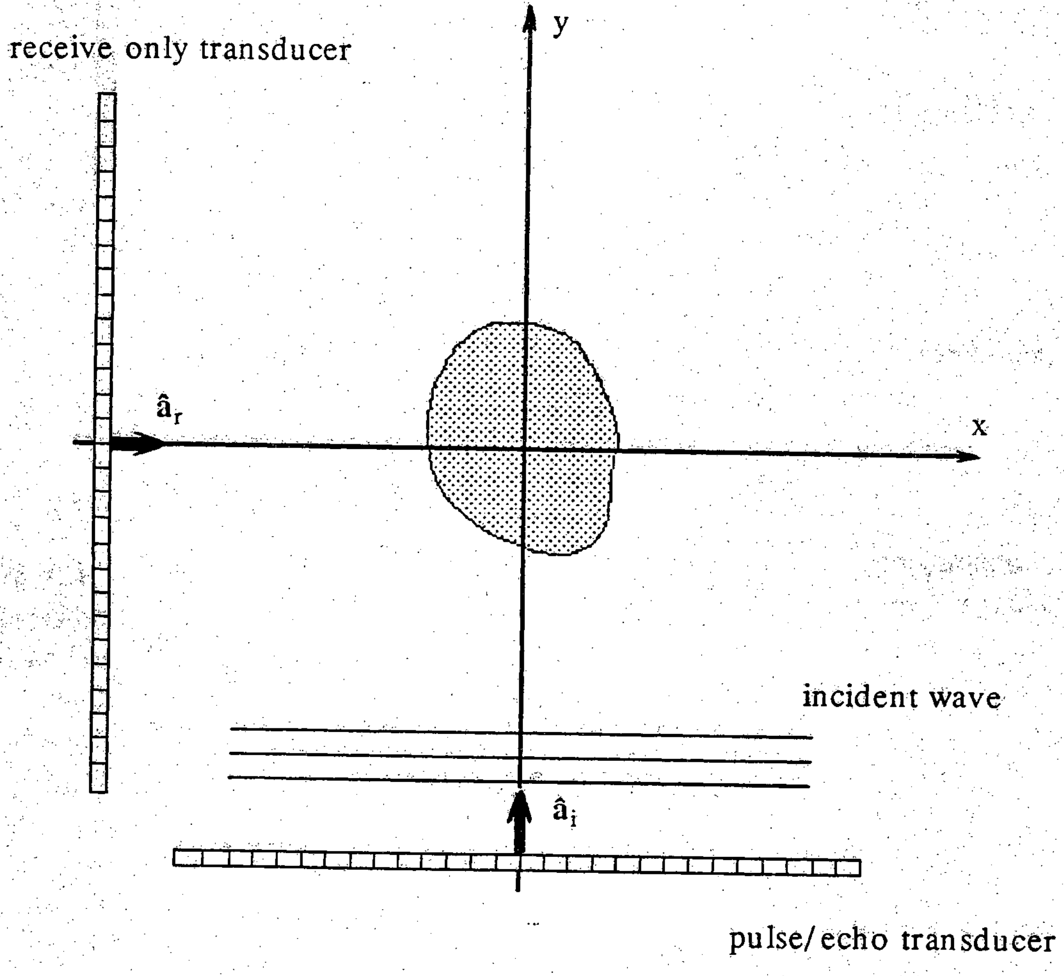

Figure (6) The scanning geometry that allows the separate reconstruction of compressibility and density. Only the pulse-echo transducer will generate the incident wave, and other transducer is passive.

This is quite a simple relationship that describes the Fourier transform of the scattered wave that each transducer will receive. Combining the measured waves would allow the elimination of either the effects of compressibility or density.

In the diffraction tomography algorithms discussed in this document, only the pulse-echo transducer is used which leads to $\hat{\mathbf{a}}_i \cdot \hat{\mathbf{a}}_r = -1, \ \hat{\mathbf{a}}_i = \hat{\mathbf{a}}_r$

1.4 Summary

This chapter has provided the basic concepts underlying the current state of diffraction tomography. A solution to the wave equation has been found with the aid of the Born approximation which has lead us to a spatial frequency domain relationship between the backscattered wave and the object causing the scattering. With this relationship in mind, a process that can simply be termed inverse scattering, can be carried out to obtain an estimate of the cross-section of the object. Two different techniques of object reconstruction have been presented in enough detail for one to implement the techniques. It is important to note that the region of the object's frequency domain obtainable with either reconstruction approach, is only an approximation.

Within this chapter no consideration of the effects of attenuation nor refraction, has been made. Also frequency dependent scattering and attenuation have being neglected.

CHAPTER 2

ULTRASONIC REFLECTIVITY TOMOGRAPHY

In this chapter a reflection mode reconstruction algorithm that was first described in [Nor79a,Nor79b,Nor81] will be analyzed. The name given to this approach is ultrasonic reflectivity tomography (URT) because the backscattered fields result from an object parameter named "reflectivity." This differs from non-diffraction transmission tomography which has been used to image an object parameter such as attenuation or speed of sound. In reference [Dines87] a reflectivity technique, having a theoretical basis similar to that in [Nor79a], has been developed and experimentally tested.

2.1 Time Domain Analysis of the Technique

In this section URT is analyzed in the time domain in two steps. The first step involves the basic formulation of the technique and describes its interaction with a point object. The use of the point object aids in defining the optimum filter to use in filtering the reflected signals. The second step is to model the reflected signals from a true object. The mathematical analysis of URT presented, follows that in [Nor79a].

2.1.1 Point Object

To start off this chapter we first analyze the basic scanning geometry, illustrated in figure (7), that consists of a point target and a point source. In actual implementation, the source would either travel on a circle of radius R centered at the location of the point target or there would be a ring of transducers encircling the object. The advantages to this imaging modality are that higher spatial frequency information about the object is obtained and that no transducer movement is required if a ring of transducers is used, thereby leading to faster data acquisition.

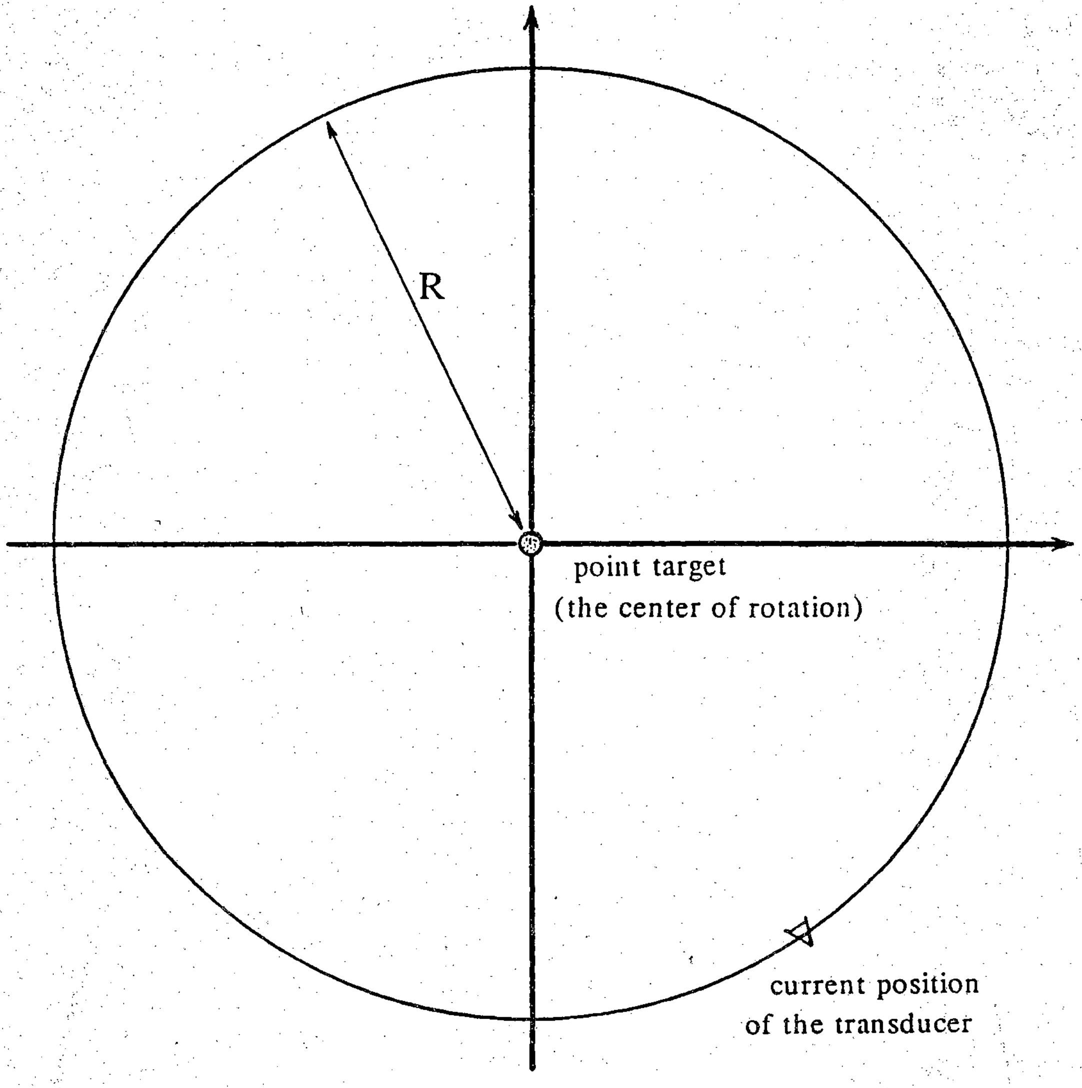

Figure (7) A basic geometry used in analyzing the echo received from a point target in URT.

If the point source emits a broad-band pulse, $p_T(\cdot)$, the received waveform should be $p_R(t) = p_T(t)*h(t)$, where h(t) represents any filtering of the transmitted signal by the transducer and/or any modification due to the mechanics of backscattering. To indicate the time it took for the pulse to travel, $p_R(\cdot)$ is convolved with the Dirac delta function $\delta(t-2R/c)$ where c is the speed of propagation within the medium. Incorporating the time shift into the expression for $p_R(\cdot)$ yields,

$$p_R(t-2R/c) = p_T(t)*h(t-2R/c)$$

To compensate for the attenuation of the pulse, h(t) could also contain a function which would scale the amplitude of the received pulse in proportion to the time of travel. The scaling would have to be done under the assumption that the absorption within the object is uniform and attenuation due to scattering is negligible. This assumption allows us to model attenuation as a constant number of dB per meter and thereby compensate for attenuation and beam divergence with a time-gain amplifier.

If a simple backprojection is carried out to reconstruct the point object, $\hat{o}(r,\theta)$, then

$$\hat{o}(r,\theta) = \int_0^{2\pi} p_R\left[\frac{2}{c}\,d(R,\phi;r,\theta) - \frac{2R}{c}\right] d\phi \tag{23}$$

which is terribly incorrect. To accurately reconstruct the point target, the function $p_R(\cdot)$ must be modified by inverse filtering as will be described. The point target, $\hat{o}(r,\theta)$, is equivalent to the delta function in polar coordinates, $\frac{\delta(r)}{\pi|r|}$. Refer to Appendix F for a discussion of this delta function.

In search of the proper function with which to filter $p_R(\cdot)$, it is necessary to expand Eq. (23) and examine the frequency domain of $p_R(\cdot)$. Substituting the expression for $d(\cdot)$ into Eq. (23) yields

$$\hat{o}(r,\theta) = \int_0^{2\pi} p_R\left[\frac{2}{c}\sqrt{R^2+r^2-2rR\cos(\theta-\phi)} - \frac{2R}{c}\right] d\phi \tag{24}$$

in which the square root can be replaced by terms in its binomial expansion that are lower than second order in (r/R)

$$\sqrt{1+(r^2-2rR\cos(\theta-\phi))/R^2} \approx 1 + \frac{r^2}{2R^2} - \frac{r}{R}\cos(\theta-\phi) - \frac{r^2}{2R^2}\cos^2(\theta-\phi)\ .$$

This approximation will prove to be a good one when (r,θ) is close to the origin. As a result Eq. (24) becomes

$$\hat{o}(r,\theta) = \int_0^{2\pi} p_R\left[\frac{r^2}{2Rc} - \frac{2r}{c}\cos(\theta-\phi) - \frac{r^2}{2Rc}\cos(2\theta-2\phi)\right] d\phi\ .$$

The next step is to replace $p_R(\cdot)$ with an expression containing it's Fourier transform,

$$p_R(t) = \int_{-\infty}^{\infty} P_R(f)\, e^{j2\pi ft}\, df \ ,$$

which results in,

$$\hat{o}(r,\theta) = \int_{0}^{2\pi}\int_{-\infty}^{\infty} P_R(f)\, e^{j2\pi fr^2/(2Rc) - j2\pi fr^2\cos(2\theta-2\phi)/(2Rc)}\, e^{-j4\pi fr\cos(\theta-\phi)/c}\, df\, d\phi \ .$$

Still this equation is unmanageable, therefore the next step is to replace the first complex exponential with a series expansion such that

$$\hat{o}(r,\theta) = \int_{0}^{2\pi}\int_{-\infty}^{\infty} P_R(f)\ e^{-j4\pi fr\cos(\theta-\phi)/c}\, df\, d\phi \tag{25}$$

$$+ \int_{0}^{2\pi}\int_{-\infty}^{\infty} P_R(f) \left[jf\alpha - \frac{f^2\alpha^2}{2} - \frac{jf^3\alpha^3}{6} - \cdots \right] e^{-j4\pi fr\cos(\theta-\phi)/c}\, df\, d\phi$$

where $\alpha = \frac{r^2}{2Rc} - \frac{r^2}{2Rc}\cos(2\theta-2\phi)$. Equation (25) breaks the reconstruction up into two parts, $\hat{o}(r,\theta) = o_o(r,\theta) + o_\varepsilon(r,\theta)$, and henceforth only the term o_o will be considered since interest lies in points near the origin and α is small close to the origin. Hence, if the substitution $\psi = \theta + \pi$ is made in $o_o(\cdot)$

$$\hat{o}(r,\psi) \approx o_o(r,\psi) = 2\pi \int_{-\infty}^{\infty} P_R(f)\, J_o(4\pi fr/c)\, df$$

since,

$$J_o(fr) = \frac{1}{2\pi}\int_{0}^{2\pi} e^{jfr\cos\theta}\, d\theta \ .$$

Recalling the goal of $\hat{o}(r,\theta) = \delta(r)/(\pi\,|r|)$, the choice of the optimum $P_R(f)$ can now be made. With the use of the relationship

$$\frac{1}{2}\int_{-\infty}^{\infty} J_o(fq)\ |f|\ df = \int_{0}^{\infty} J_o(fq)\ |f|\ df = \frac{1}{|f|}\delta(f) \ ,$$

it is obvious that $P_R(f) = |f|$ would be optimum. Unfortunately, that pulse would be unobtainable due to its infinite bandwidth. Therefore a bandlimited approximation $|f|\ \mathrm{rect}(f/2f_c)$ where f_c is the cutoff frequency, is the best that can be done. This leads to the observation that the mainlobe width of $o_o(r,\theta)$, which is the *point spread function of the system, is limited mainly by signal bandwidth.* The resolution of the reflectivity reconstruction that is obtainable with this technique is directly linked to the width of the mainlobe of $o_o(r,\theta)$, therefore the wider the bandwidth, the more accurate the reconstruction.

The paragraphs above lead us to the conclusion that the optimum filter to use in shaping $P_R(\cdot)$ is

$$H_{opt}(f) = \frac{\mathrm{rect}(f/2f_c)\ |f|}{P_T(f)} \ . \qquad (26)$$

Of course the division by $P_T(f)$ would be implemented more wisely by a Wiener filter. A much more through analysis of the filtering should be carried out so that the best possible realizable point spread function is obtained. For example, constrained deconvolution would be a more accurate method to use in removing the effects of $P_T(f)$ [Hunt72]. The current discussion serves only to point out the basic properties of URT.

2.1.2 True Object

For the purpose of mathematical convenience, the following discussion will use the geometry in figure (8) wherein the point source is the origin of our coordinate system and the object is centered at location (R,θ). For the particular geometry described above, an identical received pulse is obtained if a point target is moved along an arc of radius R that is centered at the point source. As a result, one can see that the received waveform at the instant of time 2R/c, relative to the transmission of $p_T(\cdot)$, could represent the coherent summation of the scattered fields due to all scatterers on the arc described in the previous sentence. Of course this assumes the absence of multiple scattering.

Now let us discuss a more challenging object whose properties we will describe momentarily. The A-scan, $Q_\theta(t)$, received from the point transducer can approximate a set of arc-integrals through the object wherein the radius of the arc-integration varies as a function of time. Figure (9) illustrates the paths of integration and indicates the interdependence of arc radius and the received echo at time t. At time t_1 after the pulse was transmitted, the returned A-scan corresponds to the object integrated over the arc of radius $(t_1 c/2)$ convolved with the reflection received from a point object, $p_R(t)$. From here on, such an arc will be referred to as a "constant time" arc. Mathematically,

$$Q_\theta(t) = \int_{R_{min}}^{R_{max}} p_R(t - \frac{2R}{c}) \int_{\theta-\pi/2}^{\theta+\pi/2} o(R,\phi)\, d\phi\, dR \qquad (27)$$

where $o(R,\phi)$ represents the variation in reflectivity, and θ indicates the current

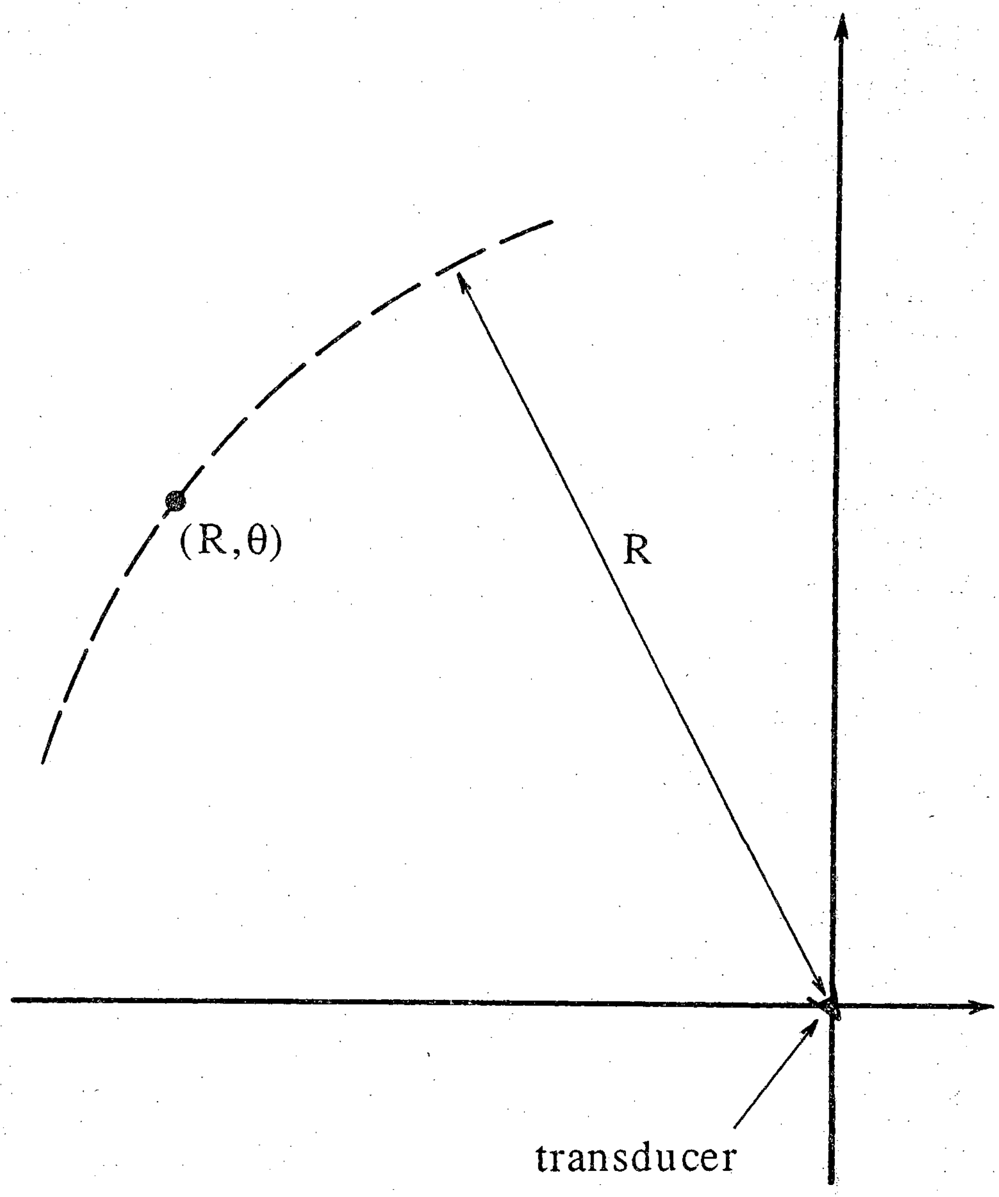

Figure (8) The scanning geometry used for convenience in the analysis of the A-scans in URT.

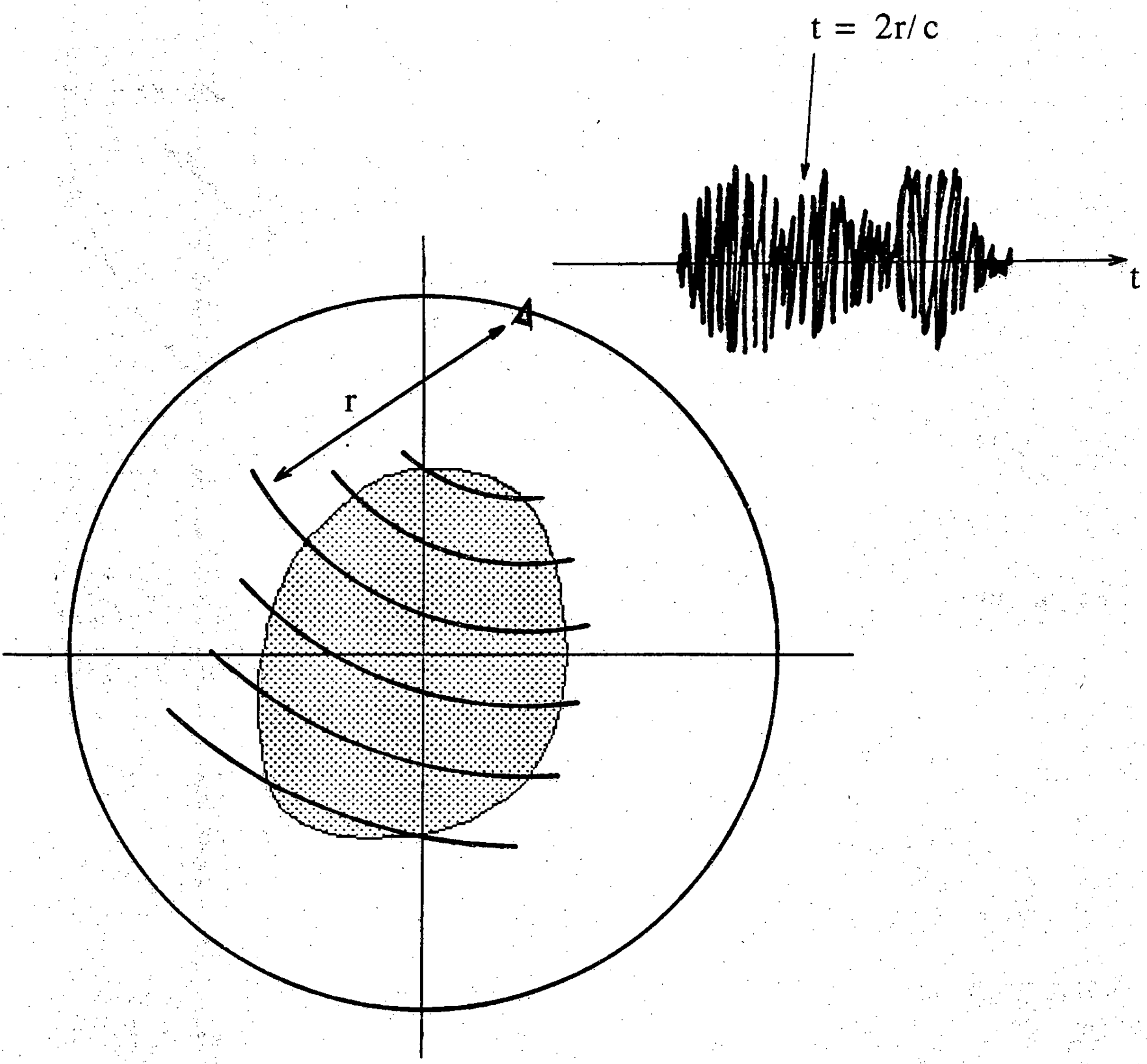

Figure (9) An illustration of the relationship between arc radius and the time of arrival within an A-scan.

position of the center of the object as illustrated in figure (10). Note that the integration in Eq. (27) assumes that the point source emits a pulse that has constant amplitude wavefront in all directions. If the transducer being used emits a wavefront whose amplitude varies with θ, an additional factor, representing the amplitude variation along the constant time arc, can be included in the integrand of Eq. (27). Measurement of the amplitude pattern can be crudely achieved with the lab equipment described in the second section of appendix D.

The family of A-scans/arc-integrals obtained by either rotating the transducer about the object or rotating the object itself, is analogous to the line-integral projection data obtained in non-diffraction tomography [KakRob]. To make this analogy possible, the object must have a number of simplifying properties. The following are but a few of the properties/assumptions that make the "A-scan" to "arc-integral" relationship possible:

a.) most importantly the object must be weakly reflecting,
b.) there must be no variations in sound velocity large enough to produce deformities in the constant-time arcs,
c.) the object under investigation must consist only of isotropic scatterers
d.) the attenuation due to scattering is negligible and
e.) a uniform absorbency exists within the object and the surrounding medium.

Note that in defense of the above assumptions, it is necessary to point out that the same assumptions are also used in B-scan imaging [Fate80].

In what follows, a reconstruction algorithm will be presented that will appear to carry out an inverse Radon transform [Dean] analogous to the reconstruction algorithm used in non-diffraction tomography. The analogy is clearly illustrated in [Nor79a].

As described above, the data represented by $Q_\theta(\cdot)$ describes a set of arc-integrals which shall be called a projection. By measuring $Q_\theta(\cdot)$ at angular intervals as the center of the object moves about the source, enough information would be obtained to reconstruct, with the use of backprojection, an approximation to the object's reflectivity. Using the geometry in figure (8), the backprojection can be described in a manner similar to that in Eq. (23),

$$\hat{o}(r,\phi) = \int_0^{2\pi} Q_\theta(2r/c)\, d\theta \; . \tag{28}$$

Unfortunately this expression is just as incorrect as was Eq. (23). The function that should be backprojected is

$$I_\theta(t) = \int_{\theta-\pi/2}^{\theta+\pi/2} o(tc/2,\phi)\, d\phi \quad \text{where} \quad Q_\theta(t) = \int_{R_{min}}^{R_{max}} p_R\left(t - \frac{2R}{c}\right) I_\theta\left(\frac{2R}{c}\right) dR \; .$$

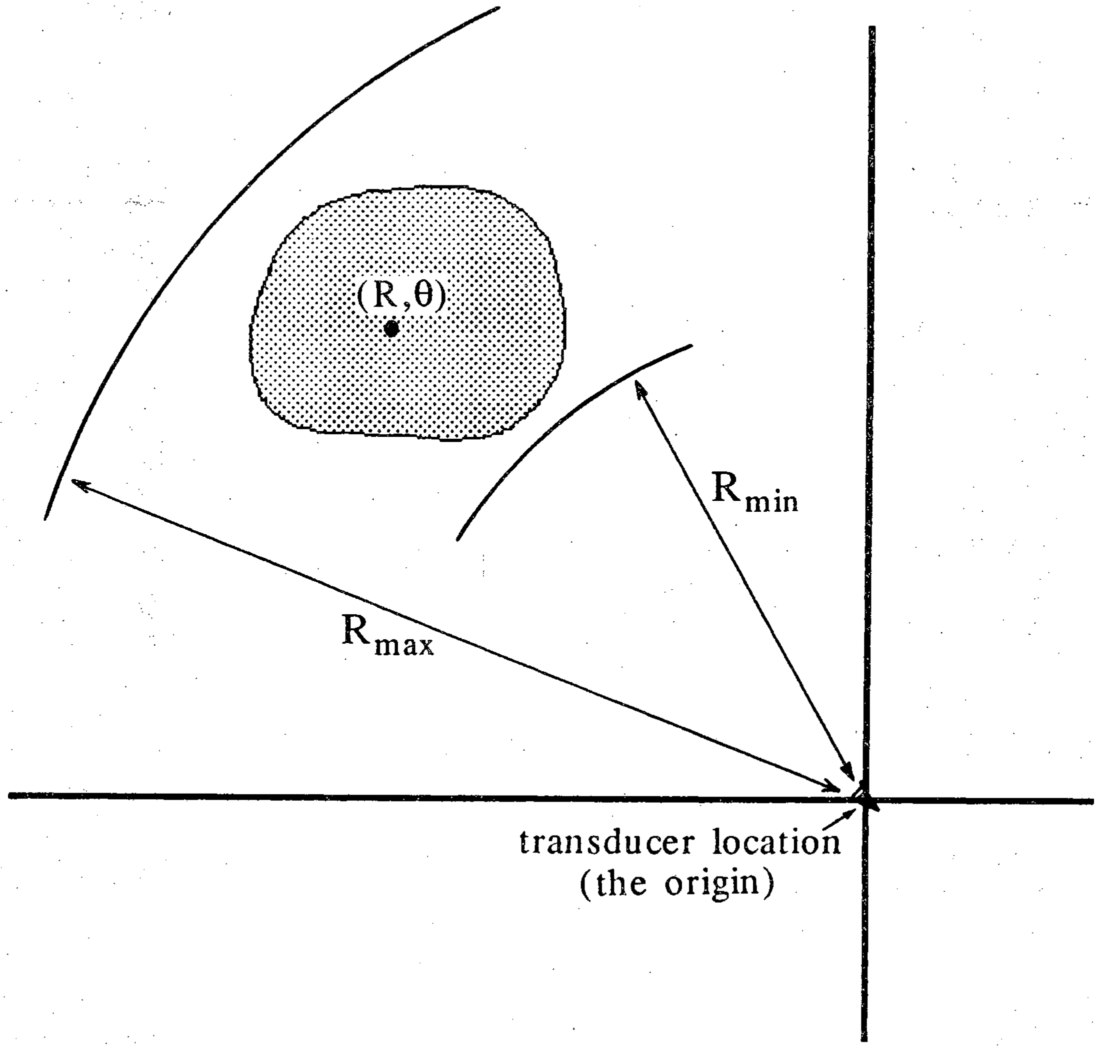

Figure (10) An illustration of the variables used in equation (27).

Therefore a filter is required to remove the effects of $p_R(t)$ before the backprojection in Eq. (28) is carried out.

$$\hat{o}(r,\phi) = \int_0^{2\pi} \left[Q_\theta(t) * h(t) \right] \Big|_{t=2r/c} \, d\theta$$

The frequency domain form of h(t) has already been expressed in Eq. (26). Hence the filtering process can be described:

$$\mathfrak{F}\left\{ Q_\theta(t) \right\} \mathfrak{F}\left\{ h(t) \right\} = |f| \, \mathrm{rect}\left[\frac{f}{2f_c} \right] \mathfrak{F}\left\{ I_\theta(t) \right\} .$$

This is equivalent to deconvolving $p_R(t)$ from $Q_\theta(\cdot)$ and then convolving the result with $\mathfrak{F}^{-1}\left\{ |f| \mathrm{rect}\left[\frac{f}{2f_c} \right] \right\}$.

It is interesting to note that both non-diffraction tomography (NDT) and URT use a $|f|$ filter [Robr85] although *in URT it is applied to the temporally varying projections* unlike in NDT where the projections vary spatially.

2.2 Fourier Domain Analysis of the Technique

This section takes the classical approach to the problem, that involves Fourier domain analysis and the wave equation.

The Born approximated solution to Eq. (5) is the summation of the scattering amplitude, as described in Eq. (21), and the incident field,

$$U_T(\mathbf{r},\omega) = U_i(\mathbf{r},\omega) + \int_V k_o^2 \, U_i(\mathbf{q})\gamma_\kappa(\mathbf{q}) \, G_\omega(\mathbf{r}\,|\,\mathbf{q}) \, dv_\mathbf{q}$$
$$+ \int_V \gamma_\rho(\mathbf{q}) \, \nabla_\mathbf{q} U_i(\mathbf{q}) \cdot \nabla_\mathbf{q} G_\omega(\mathbf{r}\,|\,\mathbf{q}) \, dv_\mathbf{q} \; , \qquad (29)$$

where $k_o = \omega/c$ and the volume V encompasses all volume where γ_ρ and γ_κ are nonzero. The incident field used in URT is a broadband pulse. Hence, mathematically the incident pulse, $u_i(\mathbf{r},t)$, that will be used is the solution to [Morse]

$$\nabla^2 u_i - \frac{1}{c_o^2} \frac{\partial^2 u_i}{\partial t^2} = -p(t) \, \delta(\mathbf{r}-\mathbf{r}_0) \; ,$$

which describes the waves generated by a broadband point source. In the temporal frequency domain the same wave equation becomes

$$\nabla^2 U_i(\mathbf{r},\omega) - k_o^2 \, U_i(\mathbf{r},\omega) = -P(\omega) \, \delta(\mathbf{r}-\mathbf{r}_o) \; ,$$

which has the solution $U_i(\mathbf{r},\omega) = P(\omega)\, G_\omega(\mathbf{r}\,|\,\mathbf{r}_o)$ where $G_\omega(\mathbf{r}\,|\,\mathbf{r}_o)$ is the free space Green's function in Eq. (A2). When the expression for U_i is inserted into Eq. (29), the resulting equation,

$$U_T(\mathbf{r},\omega) = U_i(\mathbf{r},\omega) + k_o^2 P(\omega) \int_V \gamma_\kappa(\mathbf{q})\, G_\omega(\mathbf{q}\,|\,\mathbf{r}_o)\, G_\omega(\mathbf{r}\,|\,\mathbf{q})\, dv_\mathbf{q}$$

$$+ P(\omega) \int_V \gamma_\rho(\mathbf{q})\, \nabla_\mathbf{q} G_\omega(\mathbf{q}\,|\,\mathbf{r}_o) \cdot \nabla_\mathbf{q} G_\omega(\mathbf{r}\,|\,\mathbf{q})\, dv_\mathbf{q} \ , \tag{30}$$

proves to be interesting due to the abundance of Green's functions. For the case of observing backscatter, the observation point, $\mathbf{r}$, can be the same point as the source, $\mathbf{r}_o$, which will reduce the dot product of the gradients in the above equation to $\nabla_\mathbf{q} G_\omega \cdot \nabla_\mathbf{q} G_\omega = \left[jk_o - |\mathbf{r}-\mathbf{q}|^{-1} \right]^2 G_\omega^2(\mathbf{r}\,|\,\mathbf{q})$ which is approximately equal to $-k_o^2 G_\omega^2(\mathbf{r}\,|\,\mathbf{q})$ when $|\mathbf{r}-\mathbf{q}| \gg \lambda$. Simplifying Eq. (29) with the above approximation and the condition $\mathbf{r} = \mathbf{r}_o$, yields

$$U_T(\mathbf{r},\omega) = U_i(\mathbf{r},\omega) + k_o^2 P(\omega) \int_V \gamma_\kappa(\mathbf{q})\, G_\omega^2(\mathbf{r}\,|\,\mathbf{q})\, dv_\mathbf{q}$$

$$- P(\omega) \int_V \gamma_\rho(\mathbf{q})\, k_o^2\, G_\omega^2(\mathbf{r}\,|\,\mathbf{q})\, dv_\mathbf{q} \tag{31}$$

therefore

$$U_T(\mathbf{r},\omega) = U_i(\mathbf{r},\omega) + k_o^2 P(\omega) \int_V [\gamma_\kappa(\mathbf{q}) - \gamma_\rho(\mathbf{q})\,]\, G_\omega^2(\mathbf{r}\,|\,\mathbf{q})\, dv_\mathbf{q} \ . \tag{32}$$

Now we have a more compact expression for the total field that only requires that $|\mathbf{r}-\mathbf{q}| \gg \lambda$.

What is desired is an expression for the total field in a form similar to that in Eq. (8). From now on lets only consider the scattering potential term in Eq. (32) and see what can be done to simplify the G_ω^2 term. Hence our starting point is the equation

$$\phi(\mathbf{r},\omega) = k_o^2 P(\omega) \int_V F(\mathbf{q})\, \frac{e^{j2k_o|\mathbf{r}-\mathbf{q}|}}{16\pi^2 |\mathbf{r}-\mathbf{q}|^2}\, dv_\mathbf{q}$$

where $F(\mathbf{q}) = [\gamma_\kappa(\mathbf{q}) - \gamma_\rho(\mathbf{q})\,]$. The first step is to carry out an ideal inverse filtering operation to "normalize" the scattering potential's temporal spectrum. Next, a scaling of the temporal frequency variable is necessary in which $\omega_1/2$ is substituted for ω. A subsequent step is the differentiation of both sides of the equation with respect to ω_1. All of the above steps are reflected in the equation,

$$4c^2 \frac{\partial}{\partial \omega_1} \left[\frac{\phi(\mathbf{r},\omega_1/2)}{\omega_1^2 P(\omega_1/2)} \right] = \frac{j}{4\pi c} \int_V F(\mathbf{q})\, \frac{e^{j\omega_1|\mathbf{r}-\mathbf{q}|/c}}{4\pi |\mathbf{r}-\mathbf{q}|}\, dv_\mathbf{q} \ .$$

If both sides of the equation are multiplied by $-j4\pi c$, the resulting right hand side could be referred to as a new scattering potential function, $\psi(\mathbf{r},\omega_1)$,

$$\psi(\mathbf{r},\omega_1) = -j16\pi c^3 \frac{\partial}{\partial\omega_1}\left[\frac{\phi(\mathbf{r},\omega_1/2)}{\omega_1^2 P(\omega_1/2)}\right] = \int_V F(\mathbf{q})\,\frac{e^{j\omega_1|\mathbf{r}-\mathbf{q}|/c}}{4\pi|\mathbf{r}-\mathbf{q}|}\,dv_{\mathbf{q}}\ . \qquad (33)$$

This equation *provides us with a direct relationship, first seen in chapter 1, between our reflectivity function and a modified, measured, backscattered field.*

To obtain a linear relationship between $\psi(\cdot)$ and $F(\cdot)$, the angular spectrum expansion, Eq. (A5), can be substituted for the Green's function in Eq. (33),

$$\psi(\mathbf{r},\omega_1) = \frac{j}{8\pi^2}\int_V F(\mathbf{q}) \int\!\!\int_{-\infty}^{\infty} e^{j\left[K_x(x-q_x)+K_y(y-q_y)\right]}\,\frac{e^{j\sqrt{k_1^2-K_x^2-K_y^2}\,|z-q_z|}}{\sqrt{k_1^2-K_x^2-K_y^2}}\,dK_x\,dK_y\,dv_{\mathbf{q}}\ .$$

Carrying out the volume integral with respect to $\mathbf{q}(=(q_x,q_y,q_z))$, where z will always be less than q_z, results in

$$\psi(\mathbf{r},\omega_1) = \frac{j}{8\pi^2}\int\!\!\int_{-\infty}^{\infty} \tilde{F}(K_x,K_y,-\sqrt{k_1^2-K_x^2-K_y^2})\,e^{j\left[K_x x+K_y y\right]}\,\frac{e^{-j\sqrt{k_1^2-K_x^2-K_y^2}\,z}}{\sqrt{k_1^2-K_x^2-K_y^2}}\,dK_x\,dK_y$$

in which $\tilde{F}(\cdot)$ is the Fourier transform of $F(\cdot)$. If the spatial Fourier transform of ψ is taken over a plane $z = l_0$ where $l_0 < q_z$ always, we have

$$\Psi(u,v,l_0,\omega_1) = \frac{j}{2}\int\!\!\int_{-\infty}^{\infty}\delta(K_x-u)\delta(K_y-v)\,\tilde{F}\left[K_x,K_y,-\sqrt{k_1^2-K_x^2-K_y^2}\right] \cdot\frac{e^{-j\sqrt{k_1^2-K_x^2-K_y^2}\,l_0}}{\sqrt{k_1^2-K_x^2-K_y^2}}\,dK_x\,dK_y\ .$$

The necessary final step is to carry out the trivial integrations with respect to K_x and K_y which leave

$$\Psi(u,v,l_0,\omega_1) = \frac{j}{2}\,\tilde{F}\left[u,v,-\sqrt{k_1^2-u^2-v^2}\right]\frac{e^{-j\sqrt{k_1^2-u^2-v^2}\,l_0}}{\sqrt{k_1^2-u^2-v^2}}\ . \qquad (34)$$

The above equation appears to be similar to the Fourier diffraction theorem of subsection 1.2.2 although the Ewald sphere in this case is centered at the origin of the spatial frequency space of $\psi(\cdot)$. Essentially, the 2D Fourier transform of the modified received field on the plane $z = l_0$ provides us with values of the 3D FT of the reflectivity function over a hemisphere. The hemisphere of the sphere in question is once again determined by the avoidance of evanescent waves which requires that $k_1^2 \geq K_x^2+K_y^2$ and therefore $0 > K_z > k_1$. Figure (11) attempts to illustrate the relationship indicated in Eq. (34).

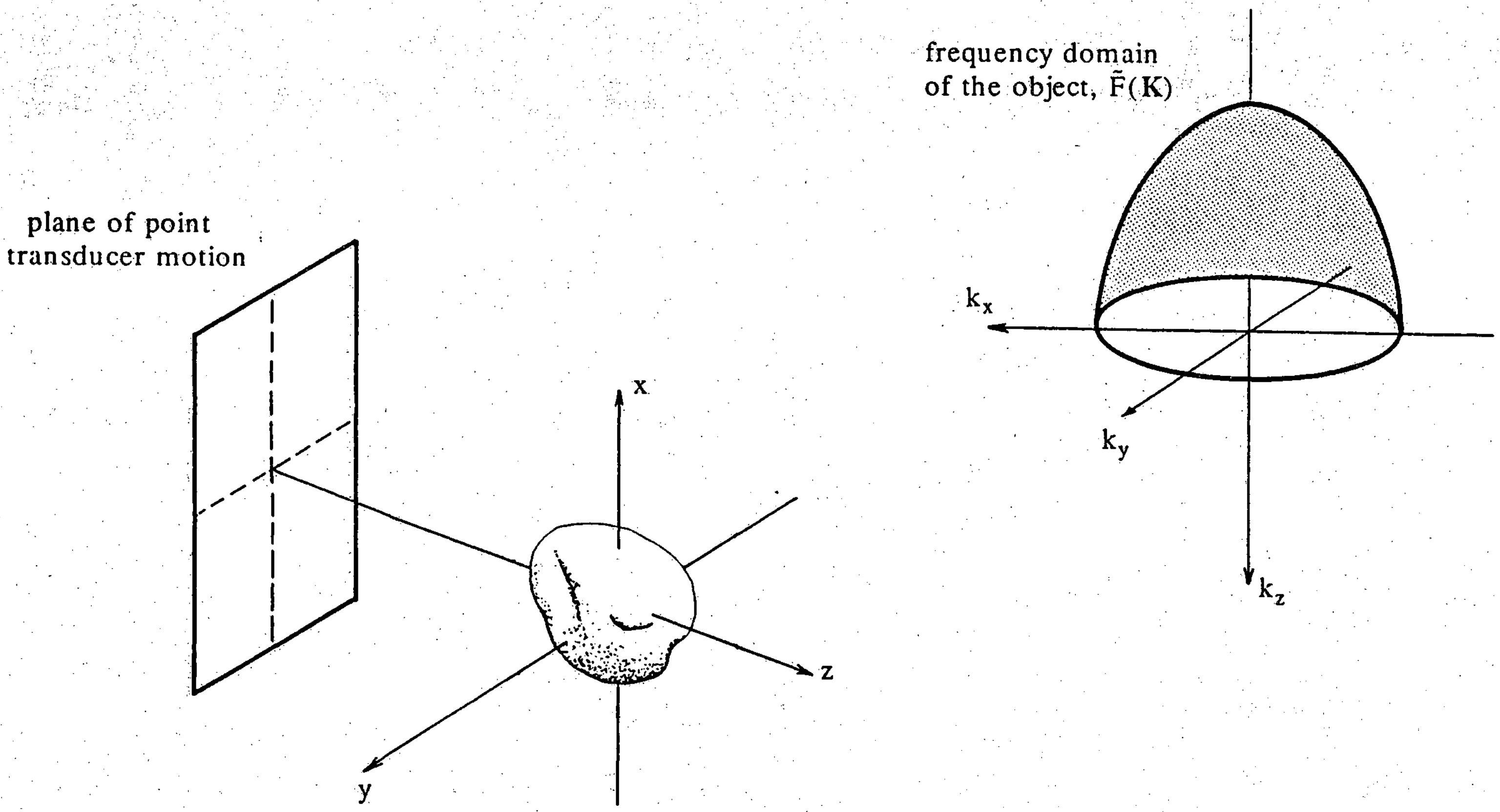

Figure (11) The coverage of the object's frequency domain that is recovered from the illustrated position of the transducer plane, is lying on one half of the surface of the sphere of radius ω/c. One monochromatic point transducer of temporal frequency ω, moved over the transducer plane, is used in obtaining this coverage.

To summarize this discussion the following enumerates the steps involved in using the Fourier domain method as discussed to reconstruction the reflectivity function:

1.) The broadband point source is moved over the receive plane, $z = l_0$, and at each sampling position, the A-scan received, $u_s(x,y,l_0,t)$, is recorded.
2.) The temporal spectrum of u_s is normalized with the spectrum of the pulse transmitted by the point source and the temporal frequency variable is scaled such that $2\omega=\omega_1$.
3.) Next the function is differentiated with respect to ω_1 which is analogous to multiplication by 2t in the temporal domain.
4.) The result is multiplied by the complex term $-j4\pi c$.
5.) The last step involves taking the 2D FT of $\psi(\mathbf{r},\omega_1)$ over the receive plane, adding a phase shift, and multiplying by a scaling factor.

The result of steps 1 through 5 operating on the received field, for a particular ω_1, is equal to the spatial transform of the object function on a semi-spherical surface centered at the origin of the frequency space with a radius of ω_1/c. All of the temporal frequencies within the bandwidth of the transducer have a similar shell, but with a different radius of course.

To fill the reflectivity function's frequency space, one must use two positions of the receiving plane or have two receiving planes on opposite sides of the object. The data obtained from the two positions/planes is enough to completely cover the 3D frequency domain within a volume bounded by the spheres of radius of ω_{min}/c and ω_{max}/c where ω_{min} and ω_{max} are, respectively, the low and high temporal frequency limits of the bandwidth of the transducer. It is then possible, albeit time consuming, to apply a spectral extrapolation technique, as will be presented in chapter 4, to the 3D frequency domain to obtain an estimate of the missing low frequency information.

2.3 Mathematical Relationship between the Time Domain and Frequency Domain Formulations of URT

In this section we would like to show that the time domain description of the backscatter provided by URT agrees with that obtained from the Born approximation solution to the wave equation. To begin let's examine Eq. (9) after replacing the total field, u(•), by the incident field,

$$u_S(\mathbf{r},t) = \int_V F(\mathbf{r}') \int_{-\infty}^{\infty} u_i(\mathbf{r}',t_o)\, g(\mathbf{r},t\,|\,\mathbf{r}',t_o)\, dt_o\, dv_{\mathbf{r}'} \; .$$

In the temporal frequency domain the incident field is expressed by $U_i(\mathbf{r},\omega) = P(\omega)\, G_\omega(\mathbf{r}\,|\,\mathbf{r}_o)$ which is expressed in the time domain as

$$u_i(\mathbf{r},t) = p(t) * \delta\left[t - \frac{|\mathbf{r}-\mathbf{r}_o|}{c} \right] \frac{1}{4\pi|\mathbf{r}-\mathbf{r}_o|} = p\left[t - \frac{|\mathbf{r}-\mathbf{r}_o|}{c} \right] \frac{1}{4\pi|\mathbf{r}-\mathbf{r}_o|} \; ,$$

since the Green's function is a weighted Dirac delta function in the time domain as stated by Eq. (A8). Hence,

$$u_S(\mathbf{r},t) = \int_V F(\mathbf{r}') \int_{-\infty}^{\infty} p\left[t_o - \frac{|\mathbf{r}'-\mathbf{r}_o|}{c} \right] \frac{1}{4\pi|\mathbf{r}'-\mathbf{r}_o|}\, g(\mathbf{r},t\,|\,\mathbf{r}',t_o)\, dt_o\, dv_{\mathbf{r}'}$$

$$= \int_V F(\mathbf{r}') \frac{p\left[t - \frac{|\mathbf{r}'-\mathbf{r}_o|}{c} - \frac{|\mathbf{r}-\mathbf{r}'|}{c} \right]}{4\pi|\mathbf{r}'-\mathbf{r}_o|\; 4\pi|\mathbf{r}-\mathbf{r}'|}\, dv_{\mathbf{r}'}$$

The above equation indicates that the backscattered wave at time t, is an attenuated and time delayed version of the original pulse resulting from all scatterers within the object whose position, $\mathbf{r}'$, satisfies the equation

$$t = \frac{|\mathbf{r}'-\mathbf{r}_o|}{c} + \frac{|\mathbf{r}-\mathbf{r}'|}{c} \; .$$

In addition, if the positions of the source and receiver happen to coincide, the time that the pulse is delayed becomes

$$t_{delay} = \frac{2|\mathbf{r}'-\mathbf{r}_o|}{c}$$

This is just what is proposed as the model for backscatter in the time domain analysis of the previous section. Essentially the "constant time" arcs and Eq. (27) have been rediscovered.

The above time domain expression for the backscattered field was obtained from the Born approximated solution to the wave equation in Eq. (4). This adds some rigor to the time domain formulation of URT. Hopefully other interesting time domain relationships can be obtained from inverse Fourier transforming traditionally frequency domain operations.

2.4 Experimental Considerations

The speed of sound within the object being imaged is typically going to be a function of position. This throws a monkey-wrench into the whole concept of constant time arcs. A cure for the degradations caused by this saddening fact can be taken from B-mode signal processing [Kim84]. The idea is this, why not create a time-of-flight (TOF) computed tomography (CT) slice of the object to obtain an estimate of the speed of sound throughout the object. With this "speed of sound map," one can directly compute the constant-time arcs at each discrete time for each position of the insonifying transducer.

In the effort to save processing time, the deconvolution of the incident pulse from the reflected pulse is sometimes approximated by envelope detection. Using the envelope detected, measured reflected signals is inherently bad [Robi84, Fate80] because information is being thrown away by the nonlinear effects of the envelope detection. In section 3.4 envelope detection is used on experimental backscatter measurements and compared to the result of inverse filtering.

A discussion on attenuation modelling and subsequent compensation for attenuation, will be postponed until Chapter 3.

2.5 Summary

This chapter has formulated two different approaches to Ultrasonic Reflectivity Tomography (URT). The technique has been analyzed in both the time domain, in which it has been implemented [Dines87], and analyzed with greater rigor in the Fourier domain. In section 3 of this chapter, the similarities between the algorithms formulated in the two domains, have been coarsely pointed out thereby leading us to the conclusion that similar reconstruction quality will be obtained regardless of the domain in which one works. Both approaches utilize broadband point sources that encircle an object, obtain A-scan data, and require normalization by the incident pulse spectrum.

CHAPTER 3

SINGLE TRANSDUCER REFLECTION MODE DIFFRACTION TOMOGRAPHY

In this chapter a reconstruction algorithm is presented which possesses a simple scanning geometry and reaps the benefits of higher resolution reconstructions provided by the knowledge of higher spatial frequency information about the object being imaged. This broad-band reflection mode algorithm inherently lacks a large amount of low frequency information but an estimate of the missing frequency content can be recovered by spectral extrapolation as discussed in the next chapter. The resolution of the algorithm will be shown to be fundamentally limited by the Born approximation as well as the bandwidth and physical size of the single plane wave transducer that is used to obtain backscattered wave measurements for the algorithm.

The second half of the chapter delves into various topics that are pertinent to the experimental implementation of the single transducer reflection mode (STRMDT) algorithm. Topics covered are wavefront modelling, the effect of attenuation, and the modelling of backscatter from transducer generated wavefronts.

3.1 Algorithm Description

In this section the new reconstruction algorithm and its benefits are described. This algorithm employs a single, phase sensitive, broadband transducer that serves as both the source and receiver of acoustical energy. The output of the transducer, $P_\phi(\omega,y=l_0)$, is effectively the integration of the sound impinging upon the surface of the transducer and is a function of the temporal frequency of insonification, ω, and the physical location of the transducer, l_0. Hence for the case of an incident plane wave of temporal frequency ω

$$P_\phi(\omega,y=l_0) = \int_{-L/2}^{L/2} U_{S,\mathbf{a}_y}(x,y=l_0;\omega)\, dx \ , \tag{35}$$

where L is the total length of the transducer and ϕ is the angle between the vector $\hat{s}_o$ and the positive x axis. As L goes to infinity, the transducer output happens to be equal to the zero frequency component of the Fourier transform of the scattered field, $P_\phi(\omega,y=l_0) = \tilde{U}_{S,\hat{a}_y}(\alpha,y=l_0;\omega)$ with $\alpha = 0$. Therefore with the use of Eq. (17), Eq. (35) can be rewritten with $\alpha = 0$ to yield

$$P_\phi(\omega,y=l_0) = \frac{j}{2k_o} e^{-jk_o l_0} \tilde{F}(0,-2k_o) \ , \ k_o = \omega/c \qquad (36)$$

which provides a direct relationship between the spatial transform of the object function, F(•), and the output of the transducer. With the Born approximation and the additional assumption that the transducer is long enough to measure nearly all of the backscattered field, Eq. (36) becomes the basis of the reconstruction algorithm.

Given the output of the transducer, Eq. (36) provides us with the value of a single point in the object's spatial frequency domain, marked by an "×" in figure (3). Note that the relationship is dependent upon temporal frequency, $\omega = k_o c_o$ where c_o is equal to the speed of sound propagation in the medium surrounding the object.

If Eq. (36) is implemented at multiple temporal frequencies for a particular value of ϕ, what is obtained is an estimate of the object along a line in the spatial frequency domain. The coverage for fixed $\phi = 0°$ is illustrated in figure (12) and results from the changing radius of the Ewald circle as temporal frequency changes. By rotating the transducer about the object, the line of coverage rotates too, thereby filling in the frequency domain of the object. Data collection is fast and simple. Figure (13) illustrates the obtainable frequency domain coverage by the area between the two dashed circles centered at the origin. Obviously, low spatial frequency content is missing.

Object reconstruction can be accomplished simply by filling the spatial frequency domain with the nearest sample of $P_\phi(\omega,l_0)$. The value at frequency (u,v) is obtained by using the value of $P_\phi(\omega,l_0)$ that is closest to the values of ω and ϕ calculated with the equations

$$\omega = \sqrt{u^2+v^2} \qquad \phi = \arctan\left[\frac{v}{u}\right] .$$

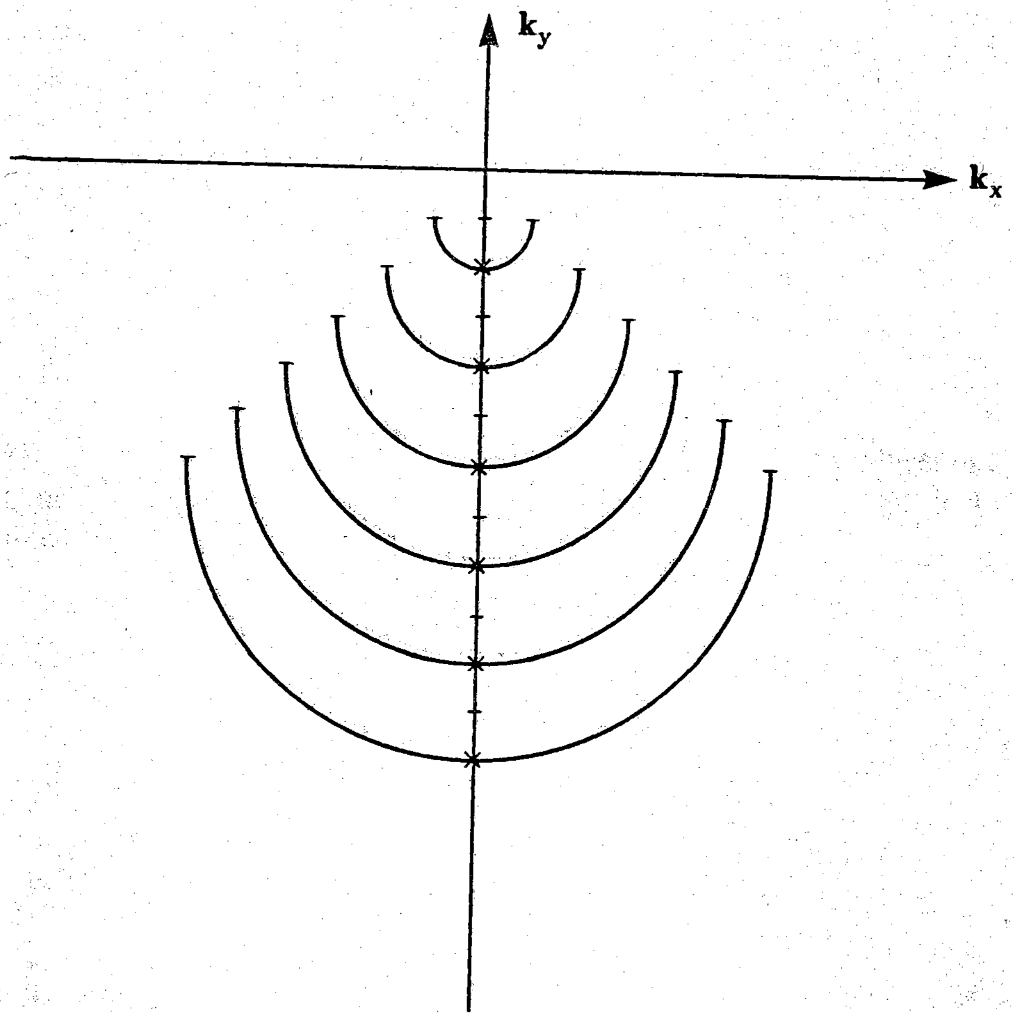

Figure (12) A monochromatic insonification by a phase insensitive transducer at six different temporal frequencies would yield the Fourier domain coverage indicated by the semicircles.

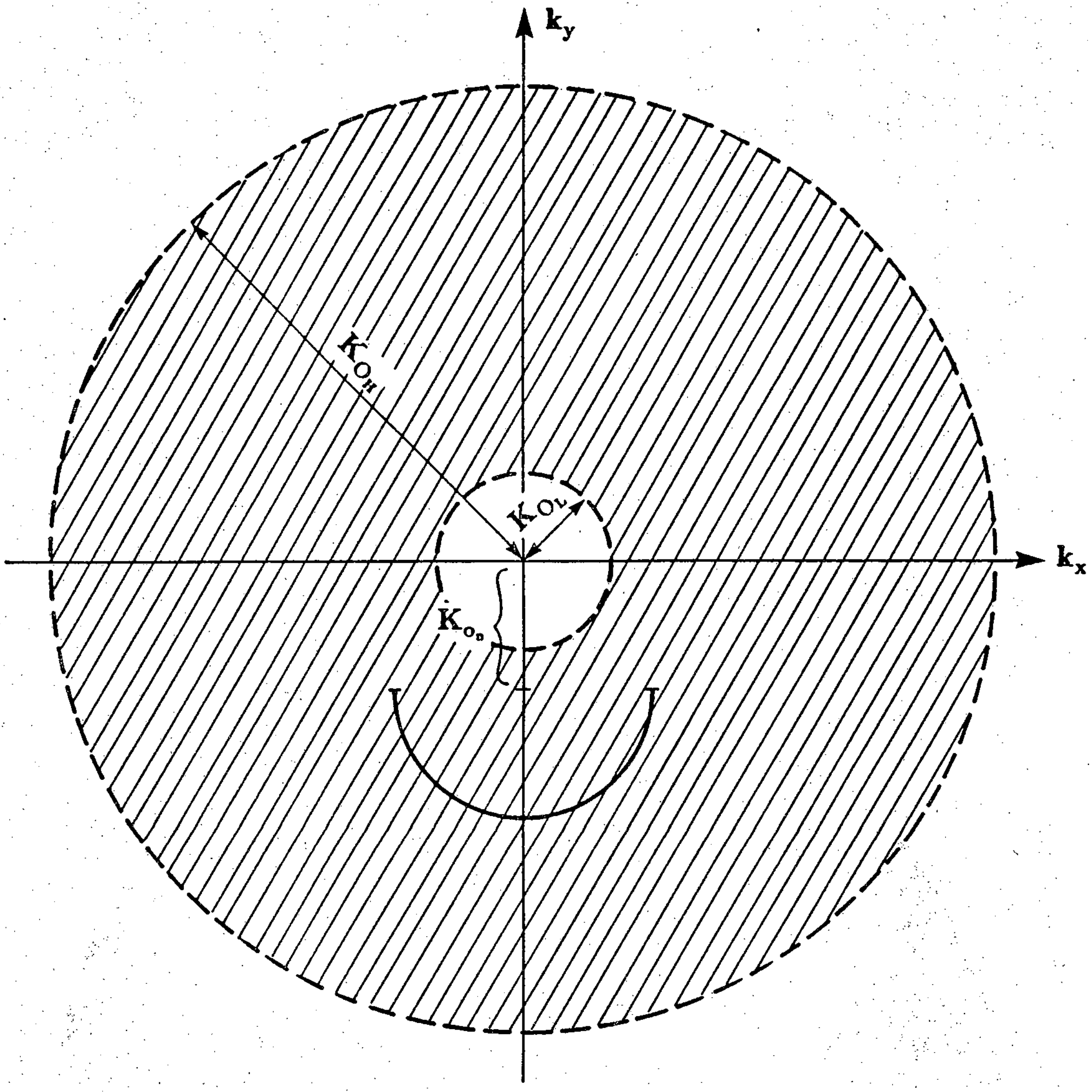

Figure (13) The portion of the scattering potential's spatial frequency space that is theoretically obtainable with the STRMDT algorithm. Note that λ, as used in this presentation, will be defined as $2\pi/k_{oc}$.

3.2 Computer Simulations

To simulate the algorithm, it is necessary to use an object for which an exact expression for the scattered field is obtainable. For this reason, the object used is a constant refractive index cylinder for which the scattered field is exactly known, [Morse pp. 464].

Generating the data necessary to fill the frequency domain consists of calculating the scattered field for each of the sampled temporal frequencies within the bandwidth of the transducer. This calculation needs to be done only for one angular position of the transducer since the object is circularly symmetric as is the spatial frequency domain of the object. Figure (14) is a plot of the real part of the slice of the frequency domain coverage obtained from a single measurement of the broad-band field scattered from a cylinder. In this case, the cylinder is of radius 2λ and has a refractive index of 1.01 . Note that the center of the plot is where the zero frequency component is located and that $2k_{0_H}$ is the highest spatial frequency obtainable. The value of λ that is referred to above is by our definition $2\pi/k_{0_C}$ where $\omega_C = ck_{0_C}$ is the center temporal frequency of the incident pulse and $8k_{0_C} = 5k_{0_H}$ for the simulated transducer. The solid line in the plot is the result obtained with simulated scattered field data and the dashed line is the true slice of the real part of the object's Fourier transform. The coverage provided seems quite good within the range of spatial frequencies for which data can be obtained. Note that the solid line simulates the data that could be obtained from a transducer that has a bandwidth of approximately 6 MHz and a center frequency of 5 MHz. This particular transducer bandwidth will be used in all subsequent simulations. A more detailed explanation of the simulated experiment is provided in appendix E.

Likewise, figure (15) presents a plot of a slice of the real part of the frequency spectrum obtained when the object is a 2λ cylinder with a refractive index of 1.1 . The reader will probably notice that the data obtained for the cylinder of higher refractive index does not match the exact frequency domain coverage. This fault is due solely to the first order Born approximation.

When many such broad-band scattered field measurements, where each measurement results in a slice of $F(u,v)$, are obtained by rotating the transducer about the object, enough data is obtained to essentially reconstitute $F(u,v)$. In this presentation, the only technique used to reconstruct $f(x,y)$ is that of direct filling of the frequency space with the aid of bilinear interpolation followed by two-dimensional Fourier inversion.

The plots in figures (16) and (17) are the real parts of the reconstructions of two cylinders both having a radius of 2λ but having refractive indices of 1.01 and 1.1 respectively. For clarity, the center slice of each reconstruction is provided in part (b)

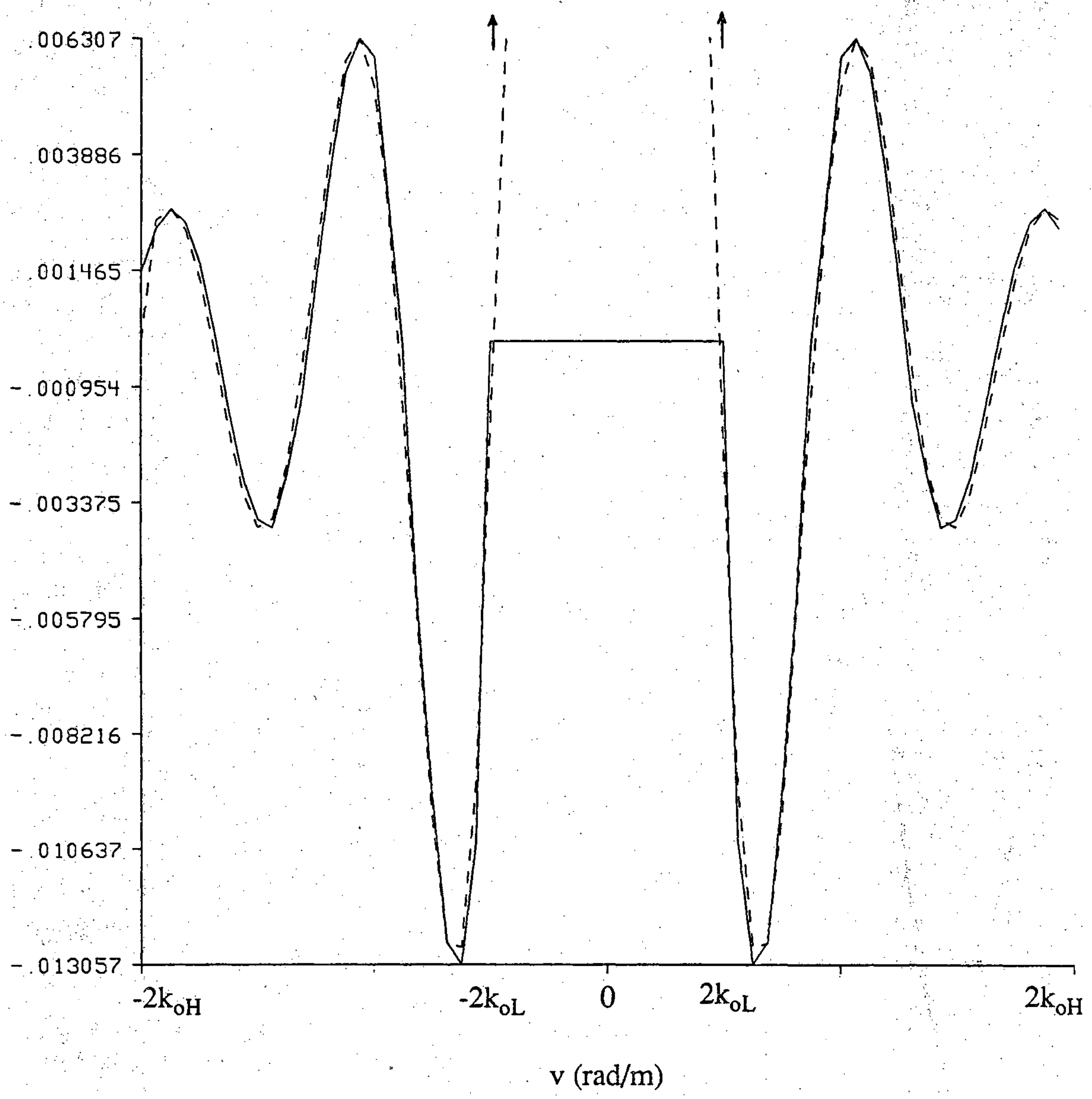

Figure (14) A comparison of the true slice of the scattering potential's frequency spectrum (dashed line) and the slice obtained from the algorithm. The object in this figure is a cylinder of constant refractive index 1.01 and a radius of 2λ (λ is defined in the caption of figure (13) and in the text).

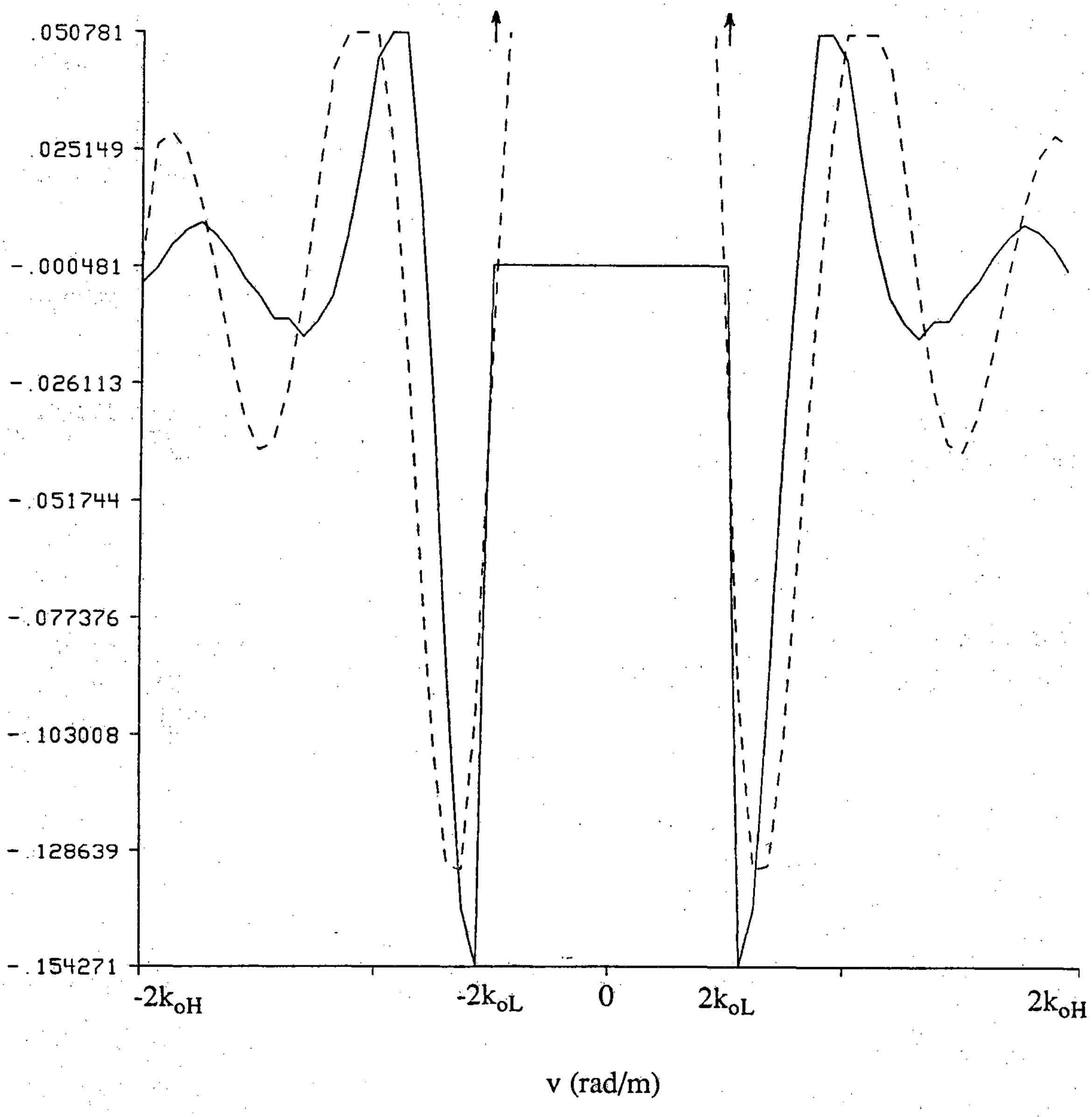

Figure (15) A comparison of the true slice of the scattering potential's frequency spectrum (dashed line) and the slice generated by the algorithm. The object in this figure is a cylinder of constant refractive index 1.1 and a radius of 2λ.

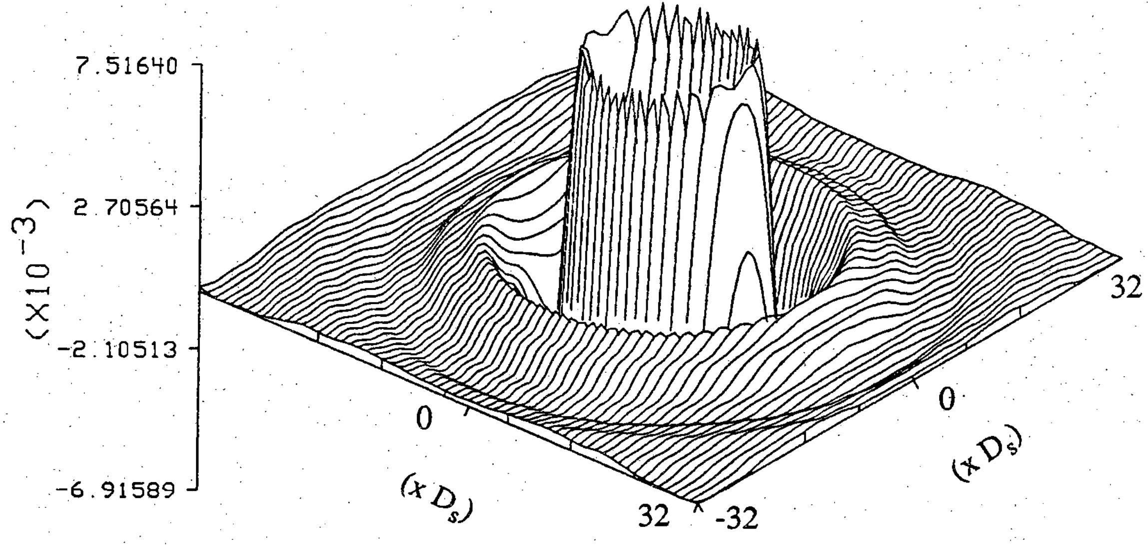

(a)

Figure (16) The real part of the cross section of a cylinder of radius 2λ having a 1.01 refractive index is plotted in (a). This reconstruction does not make use of any kind of spectral estimation. Only the frequency domain coverage obtained from the backscattered field is utilized. The solid line in (b) is the center slice of the reconstruction and the dashed line is the true center slice.

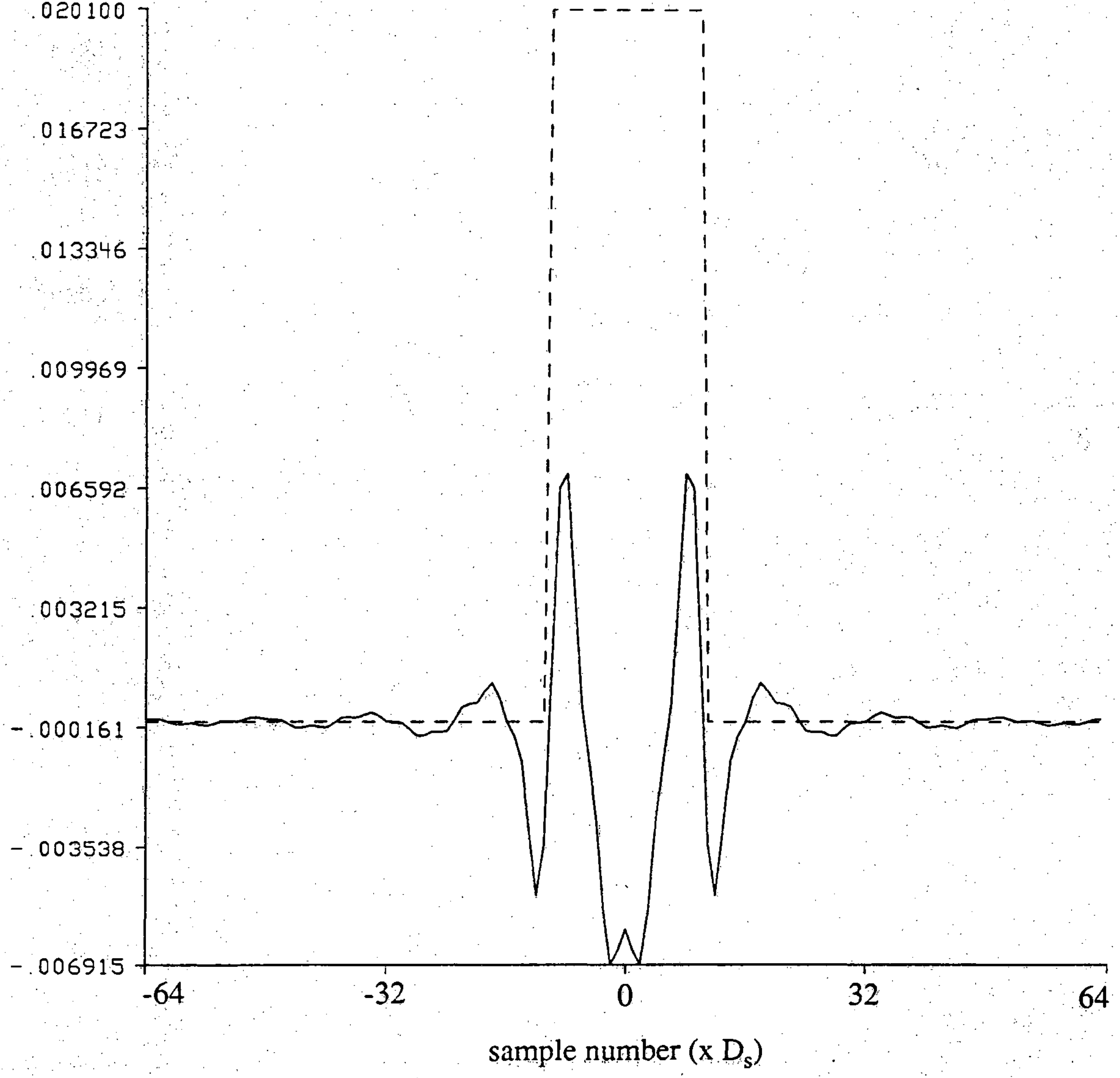

(b)

Figure (16), continued.

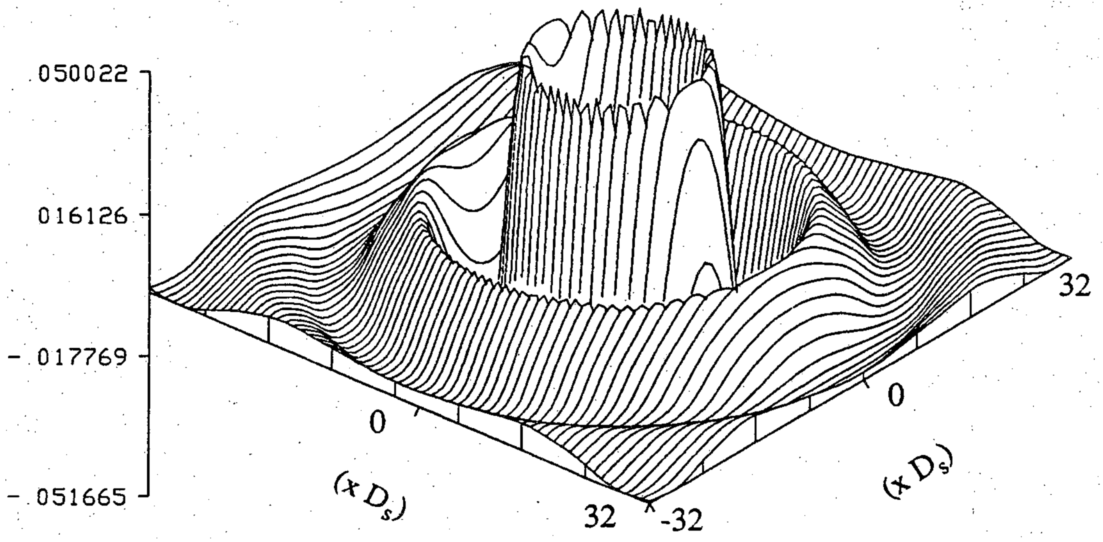

(a)

Figure (17) The real part of the cross section of a cylinder of radius 2λ having a 1.1 refractive index is plotted in (a). This reconstruction does not make use of any kind of spectral estimation. The solid line in (b) is the center slice of the reconstruction and the dashed line is the true center slice.

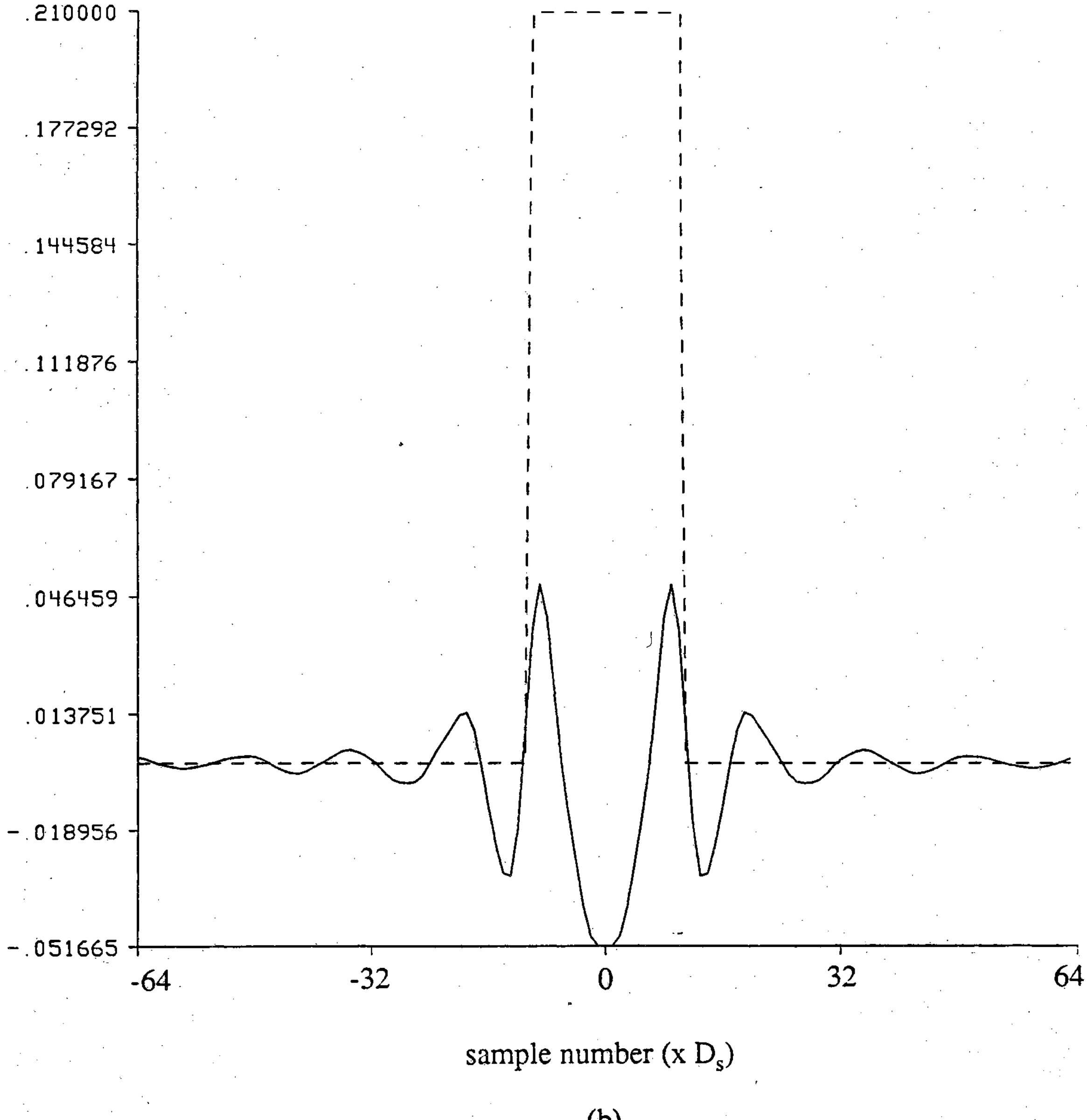

(b)

Figure (17), continued.

of each figure. Along with the center slices, the dashed lines indicate the position of the true center slice although it couldn't be plotted to its maximum extent. If the true slices had been plotted fully, the reconstructed slices would appear as nearly straight lines since they have such a small magnitude in comparison to the true slices The only observable merit of the reconstructions lies in their specification of the discontinuities in refractive index which occur at the object boundary.

It is interesting to note that the lower frequencies that are missing in the reconstructions, cause the reconstructions to somewhat resemble the derivative of the object function.

For pedagogical purposes, figure (18) is theoretically the best reconstruction of the 2λ radius, 1.01 refractive index, cylinder obtainable with the algorithm. Note that we have used the whole temporal frequency range to insonify the object. From the extremely wide bandwidth scattered fields, all the samples of $F(u,v)$ are obtained except for the zero frequency component which is estimated by polynomial interpolation. Just by chance, the amplitude of this real portion of the reconstruction is close to the accurate value of 0.0201 due to the fortunate filling of the frequency domain near zero frequency.

In the next chapter the Gerchberg-Papoulis algorithm will be employed in extrapolating the low frequency information unobtainable from the scattered field measurements made for the algorithm described in section 3.1 . In this presentation no other methods of spectral extrapolation have been implemented. Note that a study of the range of objects that can be accurately reconstructed under the Born approximation has not been done here. For the interested reader a study has been provided by Slaney et al. [Slane84] for the case of transmission mode tomography. Since both reflection and transmission modes suffer from the same assumptions and approximations, there is reason to believe that similar bounds on reconstructable objects can be assumed.

3.3 Experimental Implementation Issues

In this somewhat lengthy section various topics that are pertinent to the experimental implementation of diffraction tomography are presented. In particular, transducer wavefronts are modelled, a theoretical discussion of the effects of attenuation is presented along with a method to compensate for attenuation, and a model for backscattered waves is presented. Each topic is helpful in obtaining experimental reconstructions of an object's two dimensional cross-section.

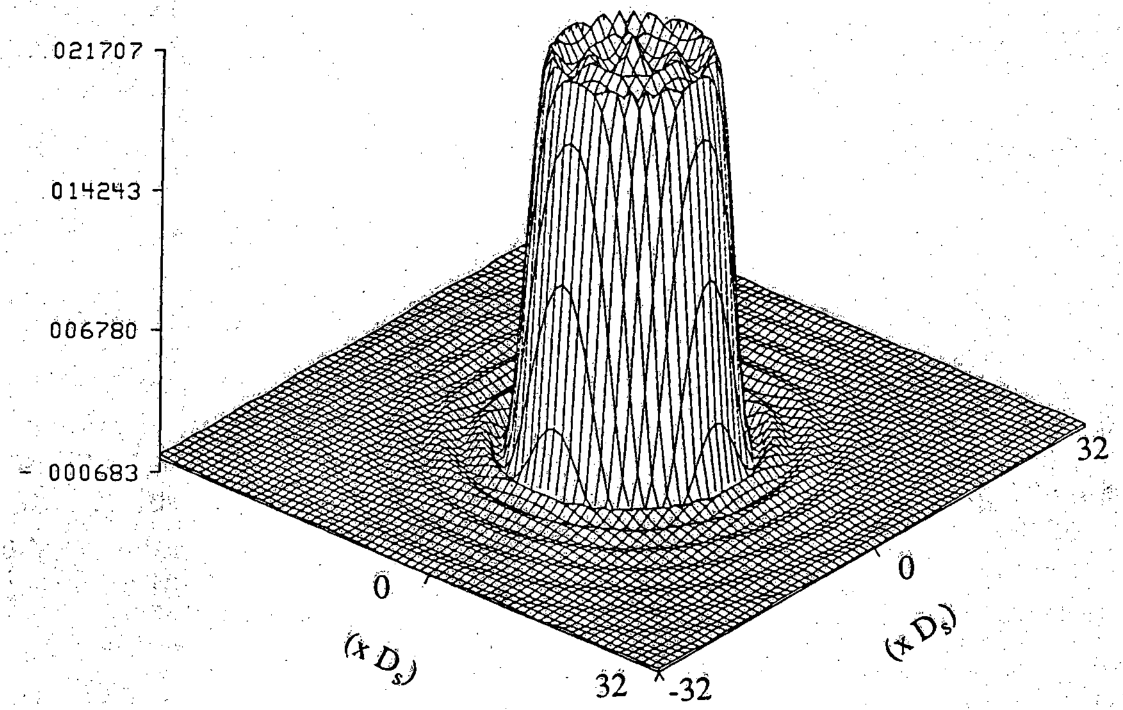

Figure (18) The real part of the reconstruction of a cylinder of radius 2λ having a refractive index of 1.01. An "infinite" bandwidth transducer has provided the frequency domain data for this reconstruction. Note that polynomial interpolation has been used to approximate the zero frequency sample of the frequency domain before Fourier inversion.

3.3.1 Transducer Modeling

The following describes a model for the wavefront radiating from an unfocused piston and a rectangular ultrasound transducer. The purpose of this investigation is to accurately, mathematically describe the wavefront emitted by a generic transducer. As a result, a description of wavefront dispersion will be generated and to that, the next section will add a model for the effects of attenuation within the media.

Below, it will be assumed that the face of the transducer lies in the $x = 0$ plane such that the wave generated travels in the +x direction.

3.3.1.1 Focussing Effects

Focussing of transducers can occur in two common ways. The first method involves shaping the transducer crystal itself and the second involves attaching a lens to the face of the transducer. In this subsection a "thin-lens" approximation will be used to describe the effect of shaping the transducer's crystal such that the resulting wavefront is focussed in the elevation plane. Figure (19) illustrates a cross section of the rectangular crystal which is positioned identically to the aperture in figure (20). The transducer's surface varies along the z axis and has a constant shape along the y axis.

The shaping of the crystal can easily be modelled as a plano-convex lens of the same refractive index as the crystal, attached to the crystal face which is located at the $x = -D$ plane. To describe the effect of this "lens," the thin-lens approximation, used in optics, is employed [Good68]. The approximation essentially states that no translation of a ray traveling through the lens will take place and that the only effect of the lens is to modify the phase of the incident wavefronts.

The phase delay is proportional to the thickness of the lens,

$$\phi(y,z) = \frac{\omega}{c_c}\, d(z) + \frac{\omega}{c_w}\, [D-d(z)] \ ,$$

where $d(z)$ is the thickness of the lens as a function of z, D is its maximum thickness, c_c is the speed of propagation in the crystal and c_w is the speed in the surrounding medium. If within the crystal there is a plane wave propagating in the positive x direction, then at the plane $x = -D$ we can say that the wavefront, $U(-D,y,z)\, e^{-j\omega t}$, has a constant amplitude which can be set equal to one. The wavefront amplitude at the plane $x = 0$ will be

$$U(0,y,z,t) = e^{j\phi(y,z)}\, U(-D,y,z)\, e^{-j\omega t} = \exp\left[j\omega \left[\frac{d(z)}{c_c} + \frac{D-d(z)}{c_w} \right] \right] e^{-j\omega t}$$

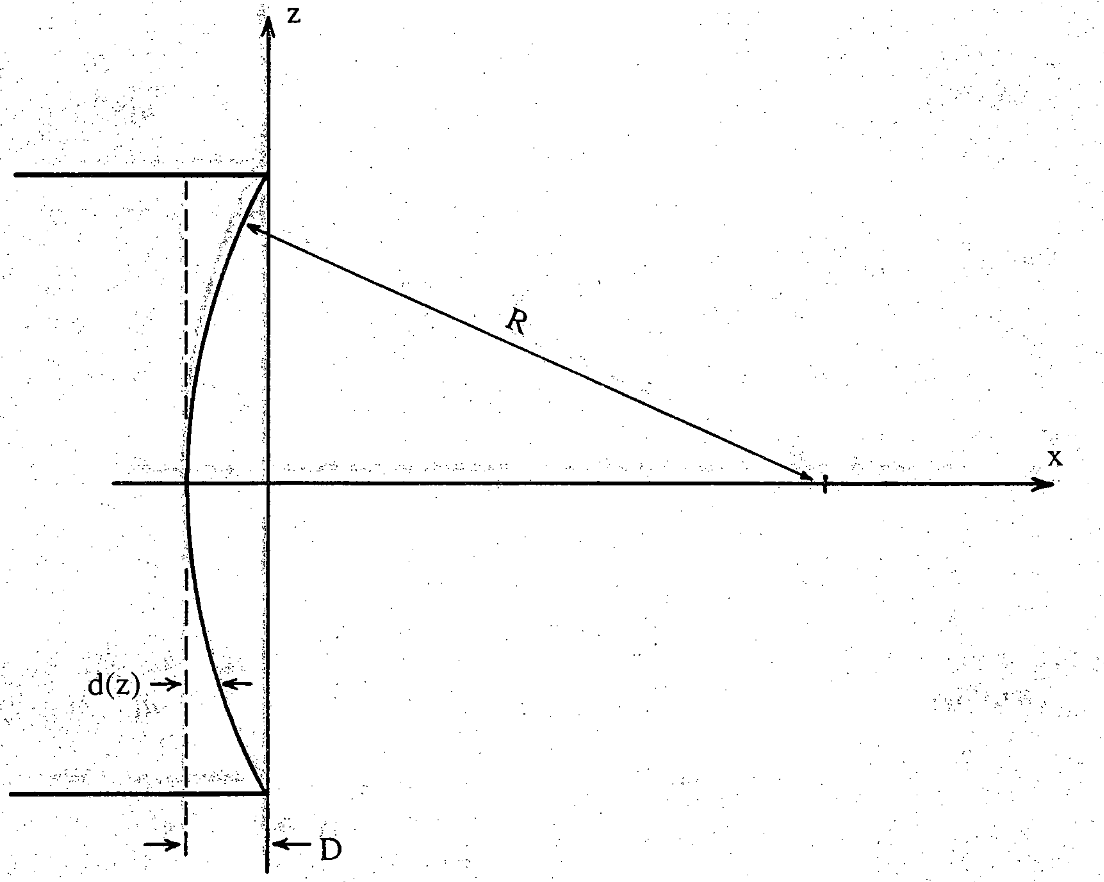

Figure (19) The cross section of a focussed transducer is provided here to aid in describing how such transducer surface variations affect the generated wavefronts.

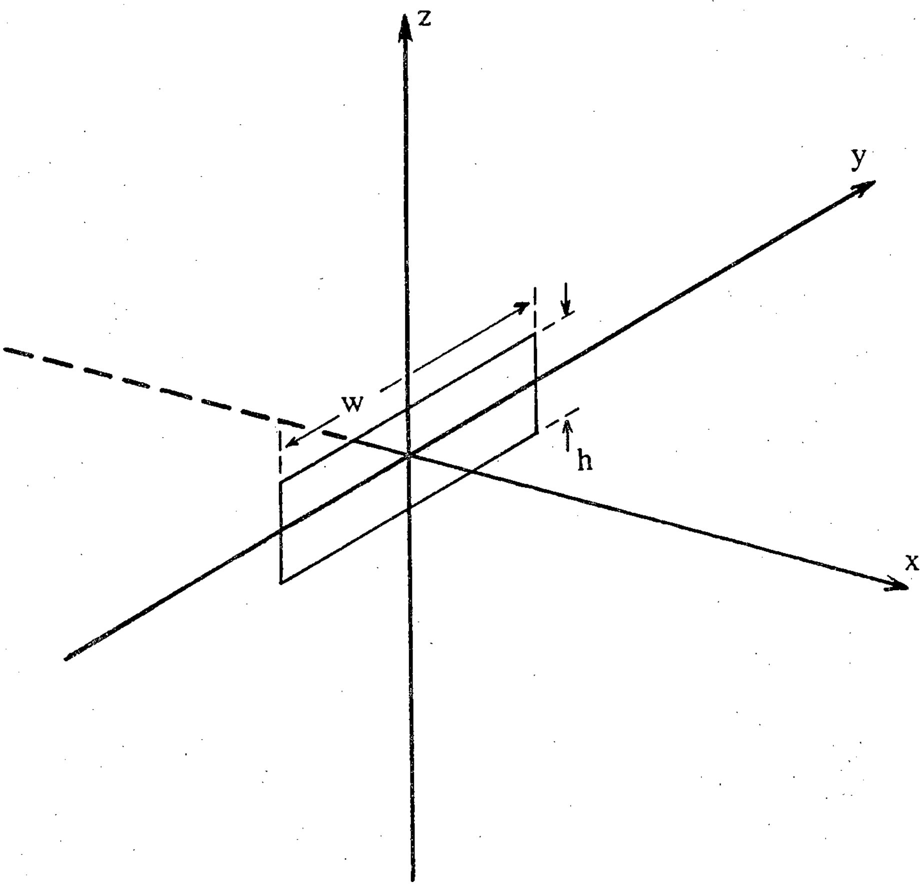

Figure (20) The coordinate frame used is shown here along with the orientation of the transducer which is being modelled as an aperture in an infinite plane.

The distance $d(z_o)$ is equal to $R-\sqrt{R^2-z_o^2}$ and $D=R-\sqrt{R^2-z_{max}^2}$. To get these distance equations in a better form, a paraxial approximation is made which proves to be acceptable since z_o is very much less than the radius of curvature, R,

$$d(z_o)=R-R\sqrt{1-z_o^2/R^2}\approx R-R\left[1-\frac{z_o^2}{2R^2}\right]=\frac{z_o^2}{2R}\ .$$

Hence

$$\begin{aligned}U(0,y,z,t)&=\exp\left[j\omega\left[\frac{z^2}{2Rc_c}-\frac{z^2}{2Rc_w}-\frac{D}{c_w}\right]\right]e^{-j\omega t}\\&=\exp\left[\frac{j\omega z^2}{2R}\left[\frac{1}{c_c}-\frac{1}{c_w}\right]-\frac{j\omega D}{c_w}\right]e^{-j\omega t}\\&=\exp\left[\frac{jz^2}{2R}k(n-1)-jkD\right]e^{-j\omega t}\end{aligned}\tag{37}$$

where $n\,(=c_w/c_c)$ is the refractive index of the crystal and $k\,(=\omega/c_w)$. It is the expression for U(0,y,z,t) in Eq. (37) which can be the complex amplitude within the aperture of figure (20).

3.3.1.2 Rayleigh-Sommerfeld Diffraction

The approach used to describe transducer wavefronts involves the diffraction formula of Rayleigh and Sommerfeld in which the transducer face is a hole in an infinite plane ($x=0$ plane). The radiated wave is generated by a time-harmonic plane wave incident on the infinite plane from the -x direction. From the second Green's identity it is well known [Good68] that the complex amplitude of a wavefront at $\mathbf{r}_o$ within a region bounded by the surface S can be expressed in terms of the wavefront measured on the surface S,

$$U(\mathbf{r}_o)=\frac{1}{4\pi}\iint_S\left[\frac{\partial U}{\partial n}G(\mathbf{r}\,|\,\mathbf{r}_o)-\frac{\partial G}{\partial n}U(\mathbf{r})\right]da_r\ .\tag{38}$$

In the case of interest, the surface of integration consists of the infinite plane $x=0^+$ and the hemispherical shell of infinite radius extending in the positive x and bounded by the $x=0^+$ plane. The surface *A* corresponds to the hole in the $x=0^+$ plane which corresponds to the transducer face. With the use of Kirchhoff's boundary conditions [Good68] and the free space Green's function

$$G(\mathbf{r} \,|\, \mathbf{r}_o) = \frac{\exp(jk\,|\mathbf{r}-\mathbf{r}_o|)}{|\mathbf{r}-\mathbf{r}_o|} \;, \tag{39}$$

the surface of integration in Eq. (38) can be replaced by the surface *A*. Hence

$$U(\mathbf{r}_o) = \frac{1}{4\pi} \iint_A \left[\frac{\partial U}{\partial n} G - \frac{\partial G}{\partial n} U \right] dy\,dz \quad , x = 0 \;. \tag{40}$$

To eliminate the requirement of knowing U(·) and ∂U / ∂n on the surface *A*, the following choice for the Green's function

$$G_o(\mathbf{r}) = \frac{\exp(jk\,|\mathbf{r}-\mathbf{r}_o|)}{|\mathbf{r}-\mathbf{r}_o|} - \frac{\exp(jk\,|\mathbf{r}-\tilde{\mathbf{r}}_o|)}{|\mathbf{r}-\tilde{\mathbf{r}}_o|} \;, \quad \mathbf{r}_o = (c,y,z), \;\; \tilde{\mathbf{r}}_o = (-c,y,z), \;\; c > 0$$

will always evaluate to zero on the surface *A*. Hence

$$U(\mathbf{r}_o) = \frac{-1}{4\pi} \iint_A \frac{\partial G_o}{\partial n} U(\mathbf{r})\, dy\,dz \quad , \mathbf{r} = (0,y,z) \;. \tag{41}$$

With the geometry used in this analysis

$$\frac{\partial G_o}{\partial n} = \nabla G_o \cdot \hat{\mathbf{a}}_x$$

where $\hat{\mathbf{a}}_x$ is the unit vector in the positive x direction. The normal derivative of $G_o(\cdot)$ becomes

$$\frac{\partial G_o}{\partial n} = 2\, \frac{\exp(jk\,|\mathbf{r}-\mathbf{r}_o|)}{|\mathbf{r}-\mathbf{r}_o|} \left[jk - |\mathbf{r}-\mathbf{r}_o|^{-1} \right] \cos(\psi)$$

where ψ is the angle between the vectors $(\mathbf{r}-\mathbf{r}_o)$ and $\hat{\mathbf{a}}_x$. Note that since $|\mathbf{r}-\mathbf{r}_o| = |\mathbf{r}-\tilde{\mathbf{r}}_o|$, only $\mathbf{r}_o$ will be used henceforth in this analysis. If we only consider points, $\mathbf{r}_o$, that lie many wavelengths away from the x = 0 plane, the above expression can be simplified since $|\mathbf{r}-\mathbf{r}_o| \gg \lambda$. With the use of this approximation, the substitution of the expression for the normal derivative of $G_o(\cdot)$ into Eq. (41) yields the equation

$$\begin{aligned} U(\mathbf{r}_o) &= \frac{-1}{4\pi}\, j2k \iint_A U(\mathbf{r})\, \frac{\exp(jk\,|\mathbf{r}-\mathbf{r}_o|)}{|\mathbf{r}-\mathbf{r}_o|} \cos(\psi)\, dy\,dz \;. \\ &= \frac{1}{j\lambda} \iint_A U(\mathbf{r})\, \frac{\exp(jk\,|\mathbf{r}-\mathbf{r}_o|)}{|\mathbf{r}-\mathbf{r}_o|} \cos(\psi)\, dy\,dz \;. \end{aligned} \tag{42}$$

The cos(·) factor in the equation accounts for the nonisotropic pattern of the wavefront and is called the obliquity factor.

Equation (42) is a description of a transducer generated wavefront at position $\mathbf{r}_o$ when the insonifying wave within the aperture of the transducer is known. This result holds for general aperture illuminations. For example if the wave incident on the back side of the aperture ($x = 0^-$) is a plane wave

$$U(\mathbf{r}) = A\, e^{jk(x-x_s)}\ ,\ x_s < 0 \tag{43}$$

the amplitude of the wave observed at $\mathbf{r}_0$ can be expressed by

$$\begin{aligned} U(\mathbf{r}_0) &= \frac{1}{j\lambda}\iint_A A\, e^{-jkx_s}\, \frac{\exp(jk\,|\mathbf{r}-\mathbf{r}_0|)}{|\mathbf{r}-\mathbf{r}_0|}\cos(\psi)\, dy\, dz \\ &= \frac{Ae^{-jkx_s}}{j\lambda}\iint_A \cos(\psi)\, \frac{\exp(jk\,|\mathbf{r}-\mathbf{r}_0|)}{|\mathbf{r}-\mathbf{r}_0|}\, dy\, dz\ . \end{aligned} \tag{44}$$

What has been discussed up to this point is a method of describing the position varying complex amplitude of a wavefront attributed to a single temporal frequency, ω, of insonification. In other words Eq. (42) describes the spatially varying complex amplitude of a wavefront, $u(\mathbf{r}_0,t)$, whose time dependence is harmonic and can be described by $e^{-j\omega t}$, $u(\mathbf{r}_0,t) = U(\mathbf{r}_0)\, e^{-j\omega t}$.

What is desired is a description of a wavefront that is generated by a transducer that outputs a pulse with a finite temporal bandwidth. Hence it is important to note the dependence of $U(\mathbf{r}_0)$ upon ω which now justifies the addition of ω as an argument of $U(\mathbf{r}_0)$. Replacing k by ω/c and λ by $2\pi c/\omega$ in Eq. (42) clarifies this dependence,

$$U(\mathbf{r}_0,\omega) = \frac{\omega}{j2\pi c}\iint_A U(\mathbf{r},\omega)\, \frac{\exp(j\omega\,|\mathbf{r}-\mathbf{r}_0|/c)}{|\mathbf{r}-\mathbf{r}_0|}\cos(\psi)\, dy\, dz\quad , x = 0\ . \tag{45}$$

In the time domain, $U(\mathbf{r}_0,\omega)$ can be expressed as

$$u(\mathbf{r}_0,t) = \int_{-\infty}^{\infty} U(\mathbf{r}_0,\omega)\, e^{-j\omega t}\, d\omega\ ,$$

into which the expression for $U(\cdot)$ can be substituted to yield

$$u(\mathbf{r}_0,t) = \int_{-\infty}^{\infty}\iint_A \frac{\omega}{j2\pi c}\, U(\mathbf{r},\omega)\, \frac{\exp(j\omega\,|\mathbf{r}-\mathbf{r}_0|/c)}{|\mathbf{r}-\mathbf{r}_0|}\cos(\psi)\, e^{-j\omega t}\, dy\, dz\, d\omega\ .$$

Making use of the relationship

$$\frac{\partial}{\partial t}u(\mathbf{r},t) = -j\omega \int_{-\infty}^{\infty} U(\mathbf{r},\omega)\, e^{-j\omega t}\, d\omega\ ,$$

simplifies the expression for $u(\cdot)$ to the form

$$u(\mathbf{r}_0,t) = \iint_A \frac{\cos(\psi)}{2\pi c\,|\mathbf{r}-\mathbf{r}_0|}\, \frac{\partial}{\partial t}u\left[\mathbf{r}, t - \frac{|\mathbf{r}-\mathbf{r}_0|}{c}\right] dy\, dz\quad , x = 0\ . \tag{46}$$

This equation is most interesting since it describes the position-time variation of the wavefront. The wavefront depends upon the scaled time derivative of the time delayed pulse generated within the aperture. The amount of time delay corresponds to the time to travel from the aperture to $\mathbf{r}_o$ and the amount of scaling is inversely proportional to distance from the aperture.

3.3.1.3 Fresnel Approximation

To simplify Eq. (42) a couple of approximations referred to as Fresnel approximations can be used that provide an accurate result for distances that are many wavelengths from the aperture. The distance $|\mathbf{r}-\mathbf{r}_o| = \sqrt{x_o^2+(y-y_o)^2+(z-z_o)^2}$ can be replaced by x_o in the denominator of Eq. (42). Although in the numerator $|\mathbf{r}-\mathbf{r}_o|$ must be approximated with the use of the binomial expansion since the error of an approximation is amplified by the very large wave number, k. Using the first two terms of the binomial expansion allows the approximation

$$|\mathbf{r}-\mathbf{r}_o| \approx x_o\left[1+\frac{1}{2}\left[\frac{(y-y_o)}{x_o}\right]^2+\frac{1}{2}\left[\frac{(z-z_o)}{x_o}\right]^2\right] \quad . \tag{47}$$

One further approximation is to let $\cos(\psi) = 1$ which assumes that the angle of observation is very small and/or x_o is very large. Alternatively, the obliquity term can be replaced with the expression $\cos(\psi) = x_o \,/\, |\mathbf{r}-\mathbf{r}_o|$.

Utilizing the above approximations Eq. (42) can be expressed as follows

$$U(\mathbf{r}_o,\omega) = \frac{e^{jkx_o}}{j\lambda x_o}\iint_A U(\mathbf{r},\omega)\,\exp\left\{\frac{jk}{2x_o}\left[(y-y_o)^2+(z-z_o)^2\right]\right\} dy\,dz \quad . \tag{48}$$

Essentially the following approximation has been made

$$\frac{1}{j\lambda}\,\frac{\exp(jk|\mathbf{r}-\mathbf{r}_o|)}{|\mathbf{r}-\mathbf{r}_o|}\cos(\psi) \approx \frac{e^{jkx_o}}{j\lambda x_o}\exp\left\{\frac{jk}{2x_o}\left[(y-y_o)^2+(z-z_o)^2\right]\right\} \quad .$$

This approximation has the capability of introducing error into the phase and magnitude of the expression for the wavefront amplitude. To ensure accuracy, a condition may be placed upon x_o such that the maximum phase change caused by the next higher term in the expansion for $|\mathbf{r}-\mathbf{r}_o|$ is limited to one radian. The condition is [Good68]

$$x_o^3 \gg \frac{\pi}{4\lambda}\left[(y-y_o)^2+(z-z_o)^2\right]^2_{\max_{y,z}}$$

This provides a means by which the goodness of the wavefront expression can be roughly determined.

The final step in this subsection is to expand the squared terms in Eq. (48) which yields

$$U(\mathbf{r}_o,\omega) = \frac{e^{jkx_o}}{j\lambda x_o} \exp\left[\frac{jk}{2x_o}\left[y_o^2+z_o^2\right]\right] \iint_A U(\mathbf{r},\omega) \exp\left[\frac{jk}{2x_o}\left[y^2+z^2\right]\right]$$
$$\cdot \exp\left[\frac{-jk}{x_o}\left[y_o y+z_o z\right]\right] dy\,dz \quad . \qquad (49)$$

It is interesting to note the two quadratic phase functions. If it were not for the quadratic phase term inside the integrand, the integrand would essentially Fourier transform $U(\mathbf{r},\omega)$ over the $x = 0$ plane and evaluate it at particular frequencies.

3.3.1.4 Fraunhofer Approximation

In this subsection one further approximation is made which limits the region of validity even further although simplifying wavefront amplitude calculations. The quadratic phase function within the integrand of Eq. (49),

$$\zeta(y,z) = \exp\left[\frac{jk}{2x_o}\left[y^2+z^2\right]\right] \quad ,$$

can be approximated by unity if

$$x_o \gg \frac{k\left[y^2+z^2\right]_{\max_{y,z}}}{2} \quad .$$

The resulting expression for the wavefront at $\mathbf{r}_o$ takes the form

$$U(\mathbf{r}_o,\omega) = \frac{e^{jkx_o}}{j\lambda x_o} e^{jk(y_o^2+z_o^2)/(2x_o)} \iint_A U(0,y,z,\omega) \exp\left[\frac{-j2\pi}{\lambda x_o}\left[y_o y + z_o z\right]\right] dy\,dz \qquad (50)$$

which is equal to the Fourier transform of the wave within the aperture, $U(\cdot)$, evaluated at the frequencies $(y_o/(\lambda x_o), z_o/(\lambda x_o))$.

Now as an example, let the aperture be a rectangular region, $A = \mathrm{rect}(y/s_y)\,\mathrm{rect}(z/s_z)$ as illustrated in figure (20), and let the wavefront within the aperture be a plane wave as in Eq. (43). As the result, the observed wavefront amplitude becomes

$$U(\mathbf{r}_o,\omega) = \frac{e^{jkx_o}}{j\lambda x_o} \exp\left[\frac{jk}{2x_o}\left[y_o^2 + z_o^2\right]\right] \int_{-\infty}^{\infty}\!\!\int \mathrm{rect}\left[\frac{y}{s_y}\right] \mathrm{rect}\left[\frac{z}{s_z}\right] e^{-j\omega t}$$
$$\cdot\, e^{-jkx_s} \exp\left[\frac{-j2\pi}{\lambda x_o}\left[y_o y + z_o z\right]\right] dy\, dz$$

This is the case of utmost importance to the algorithm presented in section 3.1 which is unique to this research. Carrying out the integration yields

$$U(\mathbf{r}_o,\omega) = \frac{e^{jk(x_o-x_s)}}{j\lambda x_o} \exp\left[\frac{jk}{2x_o}\left[y_o^2 + z_o^2\right]\right] s_y\, s_z\, \mathrm{sinc}\left[\frac{y_o s_y}{\lambda x_o}\right] \mathrm{sinc}\left[\frac{z_o s_z}{\lambda x_o}\right] e^{-j\omega t} \qquad (51)$$

To be even more specific, a rectangular transducer that is available in the lab has the dimensions specified in appendix E and a center frequency of 5 MHz,

$$\frac{w}{2} = s_y = 127.5\,\lambda_C \qquad \frac{h}{2} = s_z = 21.25\,\lambda_C \qquad x_o = 334.661\,\lambda_C\ ,$$

in which the value of x_o is chosen to be the focal length of the transducer. The plot in figure (21) is the magnitude of the wavefront generated by a transducer of this size although the wave is monochromatic with a temporal frequency of 5 MHz.

To illustrate the dependence upon ω, we replace λ by 2πc/ω and k by ω/c in Eq. (50),

$$U(\mathbf{r}_o,\omega) = \frac{\omega e^{j\omega x_o/c}}{j2\pi c x_o}\, e^{\frac{j\omega}{2cx_o}\left[y_o^2+z_o^2\right]} \iint_A U(0,y,z,\omega) \exp\left[\frac{-j\omega}{cx_o}\left[y_o y + z_o z\right]\right] dy\, dz \qquad (52)$$

What is desired is a description of a pulse generated by a transducer that has a finite temporal bandwidth. Assuming linearity it is feasible to sum the amplitudes of the wavefronts at each temporal frequency within the bandpass of a transducer and incorporate a weighting factor to model the shape of the bandpass. Therefore

$$u_{BP}(\mathbf{r}_o,t) = \frac{1}{2\pi}\int_{-\infty}^{\infty} B(\omega)\, U(\mathbf{r}_o,\omega)\, e^{j\omega t}\, d\omega$$

where B(·) is the shape of the temporal bandpass. Substituting Eq. (52) for $U(\mathbf{r}_o,\omega)$ results in

$$u_{BP}(\mathbf{r}_o,t) = \int_{-\infty}^{\infty} \frac{\omega e^{j\omega x_o/c}}{j2\pi c x_o} \exp\left[\frac{j\omega}{2cx_o}\left[y_o^2 + z_o^2\right]\right] B(\omega)$$
$$\cdot \iint_A U(0,y,z)\, e^{-j\omega t} \exp\left[\frac{-j\omega}{cx_o}\left[y_o y + z_o z\right]\right] dy\, dz\, d\omega\ , \qquad (53)$$

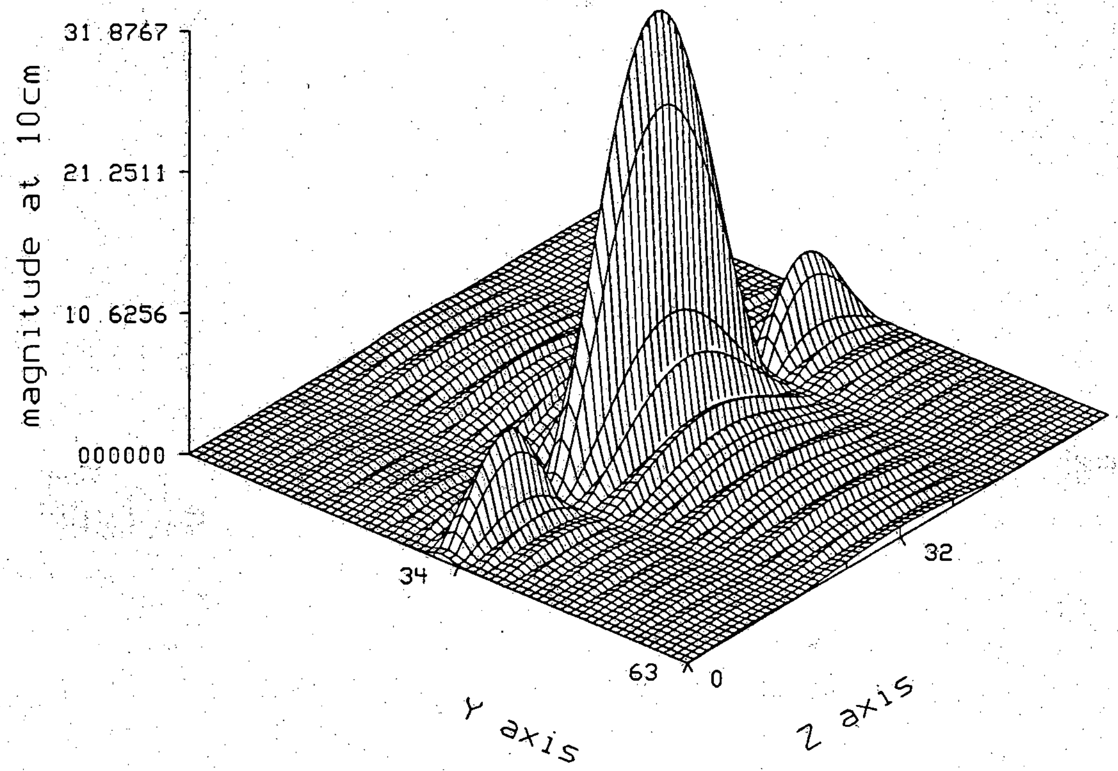

Figure (21) The Fourier domain magnitude of the generated wavefront at a distance of 10 cm when the wave in the aperture is a 5 MHz monochromatic wave.

in which a Fourier transform relationship again arises. If the aperture *A* is a rectangular region and the wave in the aperture is a plane wave, the steps leading to Eq. (51) can again be taken to result in

$$u_{BP}(\mathbf{r}_o,t) = \int_{-\infty}^{\infty} \frac{\omega e^{j\omega x_o/c}}{j2\pi c x_o} \exp\left[\frac{j\omega}{2cx_o}\left[y_o^2 + z_o^2\right]\right] B(\omega)\, e^{-j\omega t}$$

$$\cdot\, s_y\, s_z\, \mathrm{sinc}\left[\frac{y_o \omega s_y}{2\pi c x_o}\right] \mathrm{sinc}\left[\frac{z_o \omega s_z}{2\pi c x_o}\right] d\omega \ .$$

This result describes the wavefront of a broadband plane wave transducer having the bandpass specified by B(·). The integration with respect to ω seems horrendous although to simulate this result the expression for $U(\mathbf{r}_o,\omega)$ in Eq. (51) can be calculated at discrete temporal frequencies and the result of each calculation can be summed,

$$u_{BP}(\mathbf{r}_o,t) \approx \sum_{m=-n/2}^{n/2} \frac{m\Omega e^{jm\Omega x_o/c}}{j2\pi c x_o} \exp\left[\frac{jm\Omega}{2cx_o}\left[y_o^2 + z_o^2\right]\right] B(m\Omega)\, s_y\, s_z\, e^{-jm\Omega t}$$

$$\cdot\, \mathrm{sinc}\left[\frac{m\Omega y_o s_y}{2\pi c x_o}\right] \mathrm{sinc}\left[\frac{m\Omega z_o s_z}{2\pi c x_o}\right] ,\ \Omega = (\omega_h - \omega_l)/n \ . \tag{54}$$

If the wave in the aperture is focussed as described in Eq. (37), the expression for the broadband pulse in Eq. (53), becomes

$$u_{BP}(\mathbf{r}_o,t) = \int_{-\infty}^{\infty} \frac{\omega e^{j\omega x_o/c}}{j2\pi c x_o} \exp\left[\frac{j\omega}{2cx_o}\left[y_o^2 + z_o^2\right]\right] B(\omega)$$

$$\cdot \iint_A \exp\left[\frac{jz^2}{2R} k(n-1) - jkD\right] e^{-j\omega t} \exp\left[\frac{-j\omega}{cx_o}\left[y_o y + z_o z\right]\right] dy\, dz\, d\omega \ , \tag{55}$$

Unfortunately the integration involved is much too complex to be carried out or even computer calculated due to the dependence of the phase term, $\exp\left[\frac{jz^2}{2R} k(n-1) - jkD\right]$, upon z^2 and $\omega = kc$. Hence the transducer surface will be approximated by a flat surface.

3.3.1.5 The Angular Spectrum

In this subsection a short description of the angular spectrum approach to describing the effects of an aperture on incident waves, is presented. The result of this subsection is an approximate expression for the angular spectrum of a plane wavefront after being disturbed by an aperture. The main benefit of this section will occur in a following subsection on the subject of attenuation. The angular spectrum propagation will provide insight on the affect that attenuation has upon the RMSTDT algorithm of chapter three.

As before, the wave incident upon the back side of the plane containing the aperture, will be a plane wave as described in Eq. (43). The angular spectrum of the incident wave on the $x_s = x$ plane is

$$A_i(u,v) = \int\int_{-\infty}^{\infty} e^{-j(uy+vz)}\,dydz = 2\pi\delta(u,v)$$

where the spatial frequencies used have units of radians/m . When the wave reaches the diffracting plane ($x = 0$) the angular spectrum of U_i is multiplied by the phase term of the form $e^{jk_t|x_s|}$ representing the change resulting from the wave propagation to the aperture plane. Using Kirchhoff's boundary conditions at the aperture we can express the wave in the aperture as

$$U_a(0,y,z) = U_i(0,y,z)\,p(y,z)$$

where $p(\cdot)$ describes the shape of the aperture itself. It is important to realize that Kirchhoff's boundary conditions are not exactly true [Good68]. The operation in the spatial frequency domain that is analogous to the above multiplication is

$$A_a(u,v) = A_i(u,v)\,e^{j\sqrt{k^2-u^2-v^2}\,|x_s|} * P(u,v) = 2\pi\,e^{jk|x_s|}P(u,v)$$

To obtain an expression for the wave at $\mathbf{r}_o = (x_o,0,0)$, $(x_o>0)$, one must simply propagate the angular spectrum of the wave in the aperture, out to position $\mathbf{r}_o$ and then inverse transform,

$$\begin{aligned} A_o(u,v) &= \exp\left[j\sqrt{k^2-u^2-v^2}\,x_o\right] A_a(u,v) \\ &= 2\pi\,e^{jk|x_s|}\exp\left[j\sqrt{k^2-u^2-v^2}\,x_o\right] P(u,v) \ . \end{aligned}$$

For the typical non-focussed piston type of transducer, the aperture will be a circle with a radius of $m\lambda$. In this case

$$P(u,v) = 2\pi m\lambda\,\frac{J_1(m\lambda\sqrt{u^2+v^2})}{\sqrt{u^2+v^2}}$$

which is the Fourier-Bessel transform of $\mathrm{circ}\left[\sqrt{y^2+z^2}/m\right]$.

If it is assumed that x_s is a multiple of λ, the expression for A_o could be simplified since the phase term $e^{jk|x_s|}$ would equal one,

$$A_o(u,v) = \exp\left[j\sqrt{k^2-u^2-v^2}\,x_o\right] P(u,v) \ .$$

Essentially what has been outlined here is that the process of propagation and aperture disturbance can be modelled as a product of the 2-D Fourier transform of the aperture function and a phase factor which is dependent upon spatial frequency.

3.3.2 Attenuation

The attenuation experienced by an ultrasound waveform is contributed to by beam divergence, scattering, wave mode conversion, and absorption [Wells75]. In this section only divergence and absorption are discussed. The other effects are considered negligible within the scalar diffraction theory used in this work.

The first subsection hopes to build, through an understanding of fundamental theory, an accurate model for the effects of attenuation. The subsection draws upon Maxwell's equations to add rigor to the discussion and extends the discussion to ultrasound waves and analyzes the effects of attenuation upon the Fourier diffraction theorem. The second subsection narrows the scope of the discussion to consider the affects felt by the single transducer, reflection mode, diffraction tomography (STRMDT) algorithm that is presented at the beginning of the chapter.

3.3.2.1 Theory

The purpose of the following is to draw upon the electromagnetic discussion of attenuation presented in [Born] to describe the effects of attenuation on ultrasound waves. The following refers to the material constants ε, μ, and σ as well as some of Maxwell's equations. The discussion will not go into detail but serves to give the reader a feel for the theoretical basis upon which the rest of our discussion of attenuation will lie.

In an conducting medium such as a metal, the electric charge density ρ can be set to zero since ρ falls off very rapidly within the medium. Therefore $\nabla \cdot \mathbf{E} = 0$ which leads to the wave equation

$$\nabla^2 \mathbf{E} = \frac{\mu\varepsilon}{c^2}\ddot{\mathbf{E}} + \frac{4\pi\mu\sigma}{c^2}\dot{\mathbf{E}}$$

in which the term involving $\dot{\mathbf{E}}$ causes the wave to be damped/attenuated as it propagates within the medium. With the use of Maxwell's equations and assuming time-harmonic electric and magnetic fields of the form $\mathbf{E} = \mathbf{E}_o e^{-j\omega t}$, the helmholtz equation for $\mathbf{E}$ can be rewritten as

$$\nabla^2 \mathbf{E} + k_{co}^2 \mathbf{E} = 0$$

where $k_{co} = \frac{\omega^2\mu}{c^2}\left[\varepsilon + j\frac{4\pi\sigma}{\omega}\right]$ is a complex wave number. It is also interesting to note that we now have a complex refractive index n_{co} which is equivalent to $c_o/c_{co} = c_o\, k_{co}/\omega$. It is a refractive index map of the object that can be stated as the goal of tomography.

The simplest solution to the new helmholtz equation is a plane, time-harmonic wave

$$\mathbf{E} = \mathbf{E}_o\, e^{j(k_{co}\mathbf{r}\cdot\hat{\mathbf{a}}_s - \omega t)}$$

in which $\hat{\mathbf{a}}_s$ is a unit vector in the direction of propagation. Expanding this solution yields

$$\mathbf{E} = \mathbf{E}_o \exp\left[j\frac{\omega n}{c}\mathbf{r}\cdot\hat{\mathbf{a}}_s - \frac{\omega\kappa n}{c}\mathbf{r}\cdot\hat{\mathbf{a}}_s - \omega t\right]$$

where $k_{co} = \omega n_{co}/c = \omega n(1 + j\kappa)/c$ in which κ is called the attenuation index.

Leaving the complex exponential domain and returning to real expressions, leaves the result

$$\mathbf{E} = \mathbf{E}_o\, e^{-\omega\kappa n\,\mathbf{r}\cdot\hat{\mathbf{a}}_s/c} \cos\left[\omega\left[\frac{n}{c}\mathbf{r}\cdot\hat{\mathbf{a}}_s - t\right]\right]$$

in which there is a plane wave being attenuated by an exponential term.

The above discussion may be extended to ultrasound waves by adopting the complex wave number as a way of characterizing attenuation. This approach does run into problems because, as will be shown, the Fourier diffraction theorem (FDT) depends upon the wave number being real.

The first step in this investigation is to let the wave number in Eq. (14) be complex, $k_{co} = k_o + j\alpha_o$,

$$U_s(\mathbf{r}) = \frac{jU_o}{8\pi^2}\iiint_V dv_{\mathbf{r}_o}\, F(\mathbf{r}_o)\, U_i(\mathbf{r}_o) \int_{-\infty}^{\infty}\!\!\int dK_x\, dK_y\, e^{j\left[K_x(x-x_o)+K_y(y-y_o)\right]}$$

$$\cdot\frac{e^{j\gamma|z-z_o|}}{\gamma}\;,\;\gamma = \sqrt{k_{co}^2 - K_x^2 - K_y^2}\;. \tag{56}$$

As in subsection 1.1.2, the incident wave will be a time harmonic plane wave although in this case the wave number is complex,

$$U_s(\mathbf{r}) = \frac{jU_o}{8\pi^2}\iiint_V dv_{\mathbf{r}_o}\, F(\mathbf{r}_o)\, e^{jk_{co}\hat{\mathbf{a}}_z\cdot\mathbf{r}_o} \int_{-\infty}^{\infty}\!\!\int dK_x\, dK_y\, e^{-j[K_x x_o + K_y y_o - \gamma z_o]}\, e^{j[K_x x + K_y y - \gamma l_0]}\,\frac{1}{\gamma} \tag{57}$$

where the receiving plane is again $z = l_0$. When deriving the Fourier diffraction theorem, the next step is to carry out the integration with respect to $\mathbf{r}_o$ which results in Fourier transforming F(·) as expressed in Eq. (15). Taking a closer look at the integral

$$\iiint_V dv_{\mathbf{r}_o}\, F(\mathbf{r}_o)\, e^{jk_{co}z_o}\, e^{-j[K_x x_o+K_y y_o-\gamma z_o]} = \iiint_V dv_{\mathbf{r}_o}\, F(\mathbf{r}_o)\, e^{-j[K_x x_o+K_y y_o]}\, e^{j(k_{co}+\gamma)z_o}$$

indicates that the Fourier transform operation is no longer possible due to the complex spatial frequency variable $(k_{co}+\gamma)$ whereas transformation with respect to x_o and y_o is possible. The above integration with respect to z_o is termed a Fourier-Laplace integral [Roseau],

$$Q(c+jv) = \int_{-\infty}^{\infty} q(t)\, e^{-ct}\, e^{-jvt}\, dt$$

in which the integrand is equal to $q(t)\, e^{-ct}$ for $t \geq 0$ and equal to zero when $t < 0$. The Fourier-Laplace integral does not have a solution for nonconstant c therefore leaving us without a convenient relationship between the object and backscattered fields.

The affect that attenuation has upon STRMDT and the approach taken to compensate for the attenuation, is presented in the next subsection.

3.3.2.2 The Affect of Attenuation on STRMDT

To establish the detrimental affect of attenuation on STRMDT, we go back to Eq. (57) and take it one step further by Fourier transforming both sides of the equation,

$$\begin{aligned}\tilde{U}_s(\Lambda) &= \int_{-\infty}^{\infty}\!\!\int dx\, dy\, e^{-j(\alpha x+\beta y)}\, \frac{jU_o}{8\pi^2} \iiint_V dv_{\mathbf{r}_o}\, F(\mathbf{r}_o) \int_{-\infty}^{\infty}\!\!\int dK_x\, dK_y\, \frac{e^{jk_{co}z_o}}{\gamma}\, e^{-j[K_x x_o+K_y y_o-\gamma z_o]} \\ &\qquad \cdot\, e^{j[K_x x+K_y y-\gamma l_0]} \\ &= \frac{jU_o}{2} \int_{-\infty}^{\infty}\!\!\int dK_x\, dK_y \iiint_V dv_{\mathbf{r}_o}\, F(\mathbf{r}_o)\, e^{jk_{co}z_o}\, e^{-j[K_x x_o+K_y y_o-\gamma z_o]}\, \frac{e^{-j\gamma l_0}}{\gamma}\, \delta(\alpha-K_x)\, \delta(\beta-K_y) \\ &= \frac{jU_o}{2} \iiint_V dv_{\mathbf{r}_o}\, F(\mathbf{r}_o)\, e^{jk_{co}z_o}\, e^{-j[\alpha x_o+\beta y_o-\gamma z_o]}\, \frac{e^{-j\gamma l_0}}{\gamma} \quad , \ \gamma = \sqrt{k_{co}^2-\alpha^2-\beta^2}\ ,\end{aligned}$$

but under STRMDT $\alpha = \beta = 0$; hence

$$\tilde{U}_s(0,0,k_{co}) = \frac{jU_o e^{-jk_{co}l_0}}{2k_{co}} \iiint_V F(\mathbf{r}_o)\, e^{j2k_{co}z_o}\, dv_{\mathbf{r}_o}\ .$$

Here again the convenient Fourier transform relationship between $\tilde{U}_s(\cdot)$ and $\tilde{F}(\cdot)$ is unobtainable so what can be done? A possible technique for getting around the mathematical stumbling block is to assume that $k_o \gg \alpha_o$ and therefore $k_{co} \approx k_o$ which allows the use of the FDT.

Since the above approach led to no conclusions other than to ignore attenuation, we next discuss the severity of attenuation's affect on STRMDT and suggest a stopgap measure to compensate for its affect.

It is the hypothesis of the following, that STRMDT algorithm is affected less by attenuation than other approaches to tomography. A discussion similar to what is presented below appears in [ManiTR].

From subsection 3.3.5 we have the relationship

$$A_o(u,v) = \exp\left[jx_o\sqrt{k_{co}^2-u^2-v^2} \right] P(u,v) \;=\; e^{jw_c x_o} P(u,v)$$

where $k_{co} = k_o + j\alpha_o$ is the complex wave number which accounts for attenuation. The function $A_o(\cdot)$ is simply the spatial Fourier transform of the scattered wave on the plane $x = x_o$ for fixed ω and $P(\cdot)$ is the spatial Fourier transform of the aperture.

$$U(r)\,\big|_{\omega=\omega_o} = \mathcal{F}_{2D}^{-1}\left\{ A_o(u,v) \right\} \tag{58}$$

Expanding upon w_c and using the relationship $w^2 = k_o^2-u^2-v^2$, yields

$$\begin{aligned} A_o(u,v) &= \exp\left[jx_o\sqrt{k_o^2-\alpha_o^2-u^2-v^2+j2k_o\alpha_o} \right] P(u,v) \\ &= \exp\left[jx_o\sqrt{w^2-\alpha_o^2+j2k_o\alpha_o} \right] P(u,v) \ . \end{aligned}$$

Essentially, the vector, $\mathbf{t} = (w,u,v)$ indicates the direction of propagation of a plane wave. When w equals zero a plane wave is propagating in the y–z plane parallel to the $x = x_o$ plane and when w equals k_o a plane wave is propagating perpendicular to the $x = x_o$ plane.

A plot of the loss attributed to the real exponential term versus w and α_o is presented in figure (22). The plot computes the loss in dB over the range of valid w, as dictated by the exclusion of evanescent waves, and over a one to five dB/cm range of α_o. We can see from the plot that as w becomes smaller the attenuation increases. This implies, for a fixed temporal frequency, ω, that the high spatial frequencies of the scattered wave on the $x = x_o$ plane are experiencing more attenuation than the lower frequencies.

In the two dimensional case $A_o(v) = \mathcal{F}_{1D}\{U(y)\}$ is the spatial Fourier transform of a backscattered wave along the line $x = x_o$,

$$A_o(v) = \exp\left[jx_o\sqrt{k_o^2-v^2-\alpha_o^2+j2k_o\alpha_o} \right] P(v) = W(v)\,P(v) \ .$$

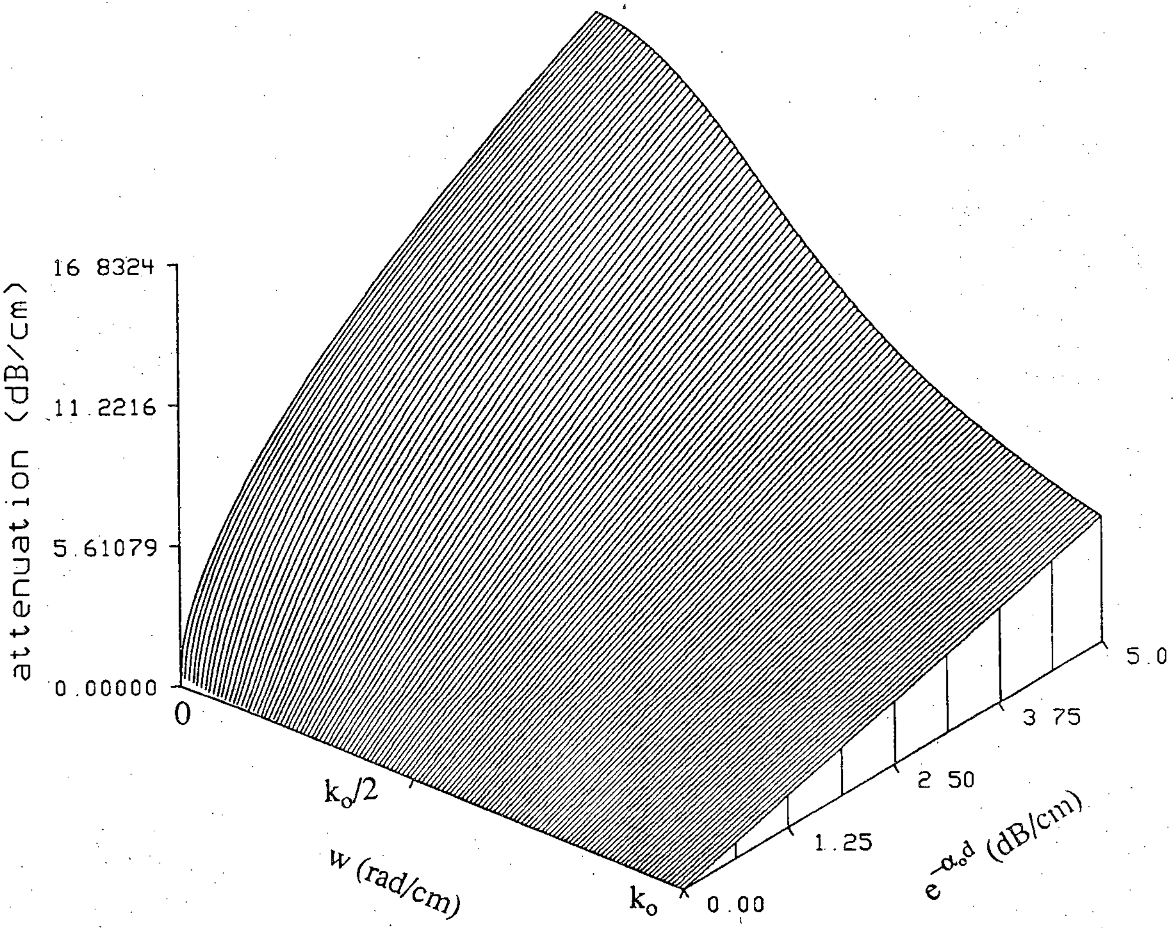

Figure (22) This plot illustrates how attenuation varies with wavenumber, w, and attenuation constant, α_o.

Drawing upon the discussion in subsection 3.3.2.1 we may substitute the backscattered wave, U_s, in place of U in Eq. (58) and take another look at the Fourier diffraction theorem. Recalling the 2-D FDT relationship illustrated in figure (3), the influence of the weighting function W(v) is indicated in figure (23). Since STRMDT requires only the $v = 0$ value of $A_o(\cdot)$, it is affected the least by object and medium attenuation,

$$A_o(0) = e^{jx_o k_{co}} P(0) = e^{-x_o \alpha_o} e^{jx_o k_o} P(0) \ .$$

Therefore a feasible method of compensating for attenuation is to measure the attenuation of the medium and the average attenuation of the objects being imaged and simply amplify accordingly.

Our last investigation in attenuation modelling comes from a paper by Kak and Dines [Kak78] in which a useful linear phase model for the effects of object attenuation is presented and experimentally verified. Unfortunately the model is incorrect in ignoring the effect that attenuation has upon the phase of a signal [Kuc84]. In defense of the paper, one must note that only the magnitudes of the reflected signals are required to reach the goal of the paper which is to determine the attenuation coefficient, α.

In [Kak78] the amplitude of a plane wave after traveling through a medium of thickness d, is described as

$$U(d,t) = I_o(f)\, e^{-\alpha(f)d}\, e^{-j\beta(f)d}\, e^{j2\pi ft}$$

where $I_o(f)$ is the amplitude of the original wave as a function of frequency, $\alpha(f)$ is the attenuation coefficient of the medium, and $\beta(f)$ is the phase shift of the medium. Within this paper, $\beta(f)$ is assumed to be a linear function of frequency equal to $2\pi f/c$ and $\alpha(f)$ is assumed to be equivalent to $\alpha_o |f|$. The assumption about $\alpha(f)$ is a good one which has been experimentally verified in many places, [Dunn62,Moun72]. It is the assumption about $\beta(f)$ which falls under suspicion. For the interested reader, Kuc [Kuc84] explores the $\beta(f)$ assumption and proposes a "minimum phase filter" to accurately describe the effect that attenuation has upon signal phase. The minimum phase filter is derived from the fact that a real, causal sequence can be described solely in terms of the real part of its Fourier transform [OppScf]. Hence knowledge of $\alpha(f)$ leads to an expression for $\beta(f)$. Unfortunately time and space is not available to explore this type of filter. Instead the original linear phase assumption will be used.

Now, returning to the model and making the assumptions mentioned above, yields

$$U(d,t) = I_o(f)\, e^{-\alpha_o |f| d}\, e^{-j2\pi fd/c}\, e^{j2\pi ft} \ .$$

If the amount of attenuation caused by the exponential term, $e^{-\alpha_o |f| d}$, were not a

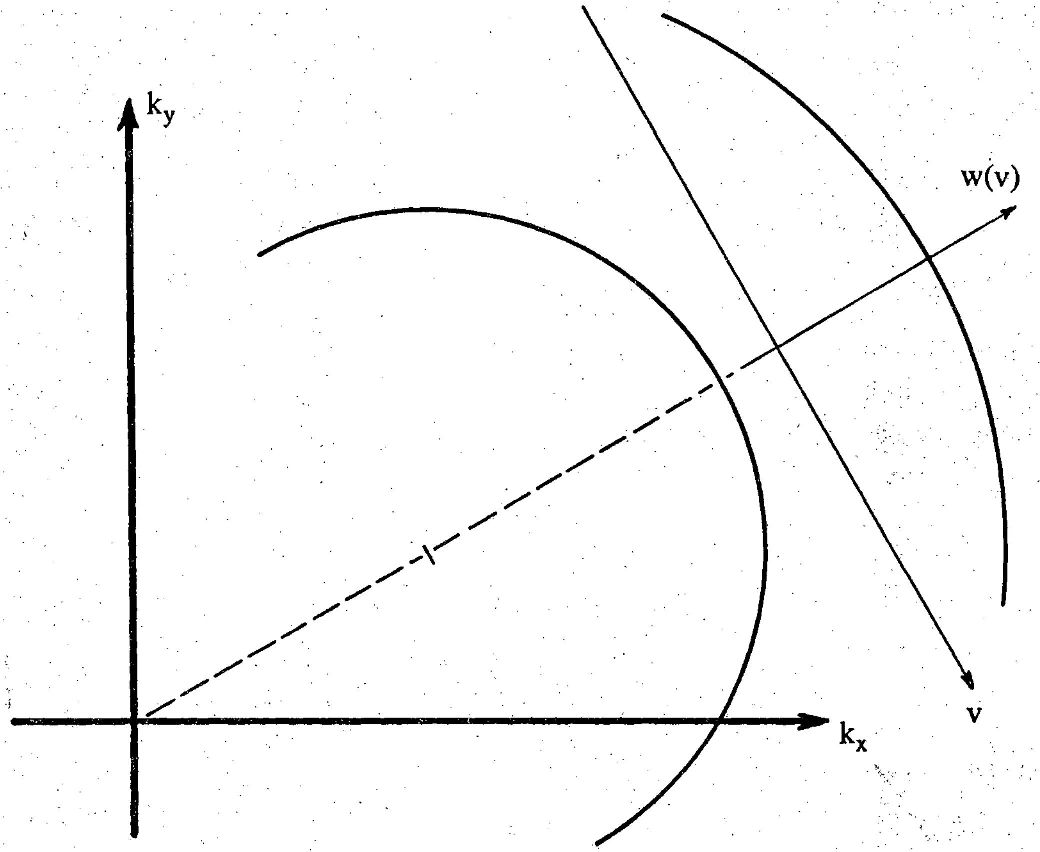

Figure (23) The variable affect of attenuation upon the different spatial frequencies within the backscatter measured along the receiving line, is illustrated by the curve labeled w(v) which is laying beyond the FDT arc.

function of temporal frequency, f, the amplification would be of a fixed amount over the time span of the backscattered wave. The time domain equation for the wave takes the form,

$$u(t) = i_o \left[t - \frac{d}{c} \right] e^{-\alpha_o f_c d} ,$$

when the wave is narrowband and $|f|$ is approximated by the center frequency, f_c. The narrowband approximation removes the frequency dependence although it presents a problem because the insonifying wavefronts generated for STRMDT must be broadband. The unfortunate lack of a better method of removing frequency dependence forces the use of the narrowband method in the implementation of STRMDT.

If the average value of α_o for the type of objects being imaged is known or measurable, then a time varying amplifier can be used to compensate for object attenuation. The dependence of d, the distance traveled within the object, upon time, t, within the backscattered signal is described as

$$d = c(t - t_o) ,$$

where t_o is the initial time of the echo arrival. It becomes obvious that an amplifier with time variation described by $a(t) = e^{\alpha_o f_c c(t - t_o)} u(t - t_o)$ would approximately compensate for object attenuation. Figure (24) helps clarify what is meant by t_o and illustrates the time variation of the amplifier.

Of course the second factor causing energy loss is beam divergence which is represented in the incident wave expression in Eq. (46) by the term $1/|\mathbf{r}-\mathbf{r}_o|$. The position $\mathbf{r}_o$ is the point of observation and $\mathbf{r}$ is a position within the $x = 0$ plane which represents the aperture of the transducer. A similar dependence upon distance is exhibited in the time domain expression for the scattered wave, $u_s(\cdot)$, in Eq. (10). At first glance one might compensate for this inverse dependence upon distance with a time-gain amplifier since $|\mathbf{r}-\mathbf{r}_o|$ is equivalent to $c\,t/2$ where c is the speed of propagation. But one must note that the incident wavefront, $u_i(\cdot)$, is a plane wave which is only affected by beam divergence at its edges. Since the object space, as indicated in figure (25), used in the STRMDT approach, lies within the lateral center of insonifying wavefronts, beam divergence is not considered. It is the scattered wave, $u_s(\cdot)$, which suffers from beam divergence because the wave resembles a wave generated by a point source or, more accurately stated, by a collection of point sources. Such a diverging wave looses energy proportionally to r^{-2}. Hence only the divergence of the scattered wave will be accounted for by a time-gain amplifier.

Drawing upon the approximation made for $|\mathbf{r}-\mathbf{r}_o|^{-1}$ in section 3.3.1.3, the dependence upon distance can be replaced by x_o^{-1}. As is evident from figure (25), for

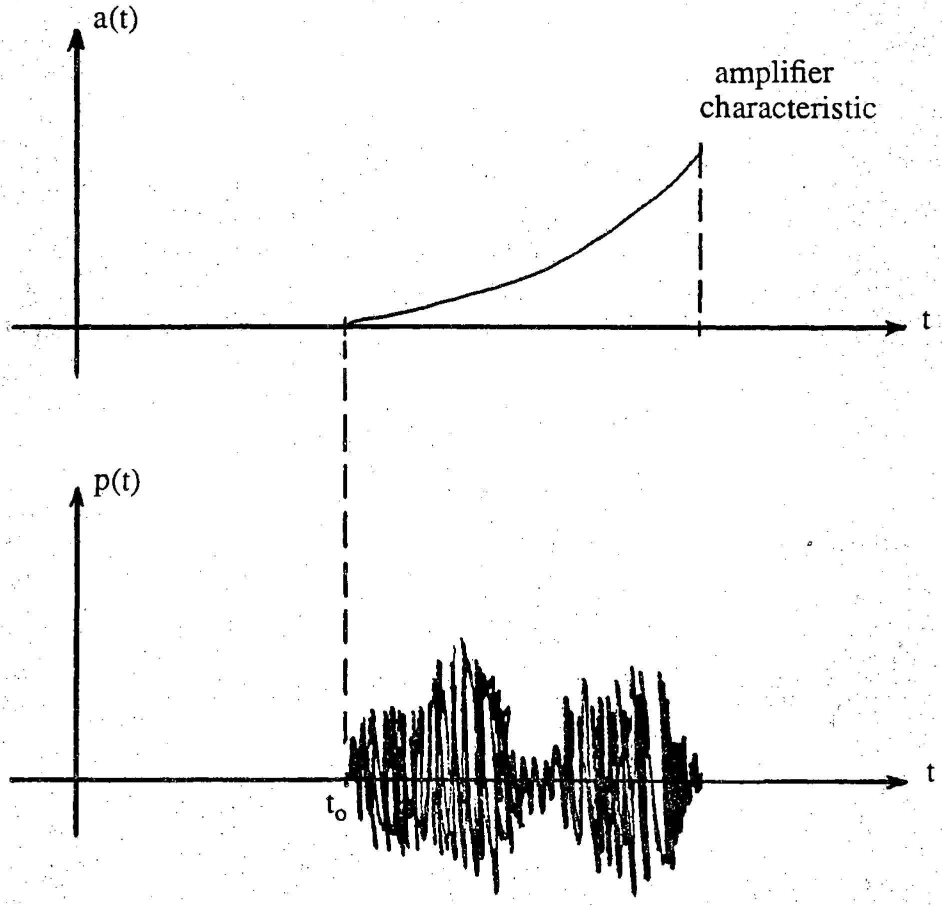

Figure (24) The amplifier which compensates for object attenuation must be time delayed until time t_o which is the time it takes for a wavefront to travel out to the surface of the object and back again. The amplifier's variation with time, a(t), is illustrated above the simulated backscatter.

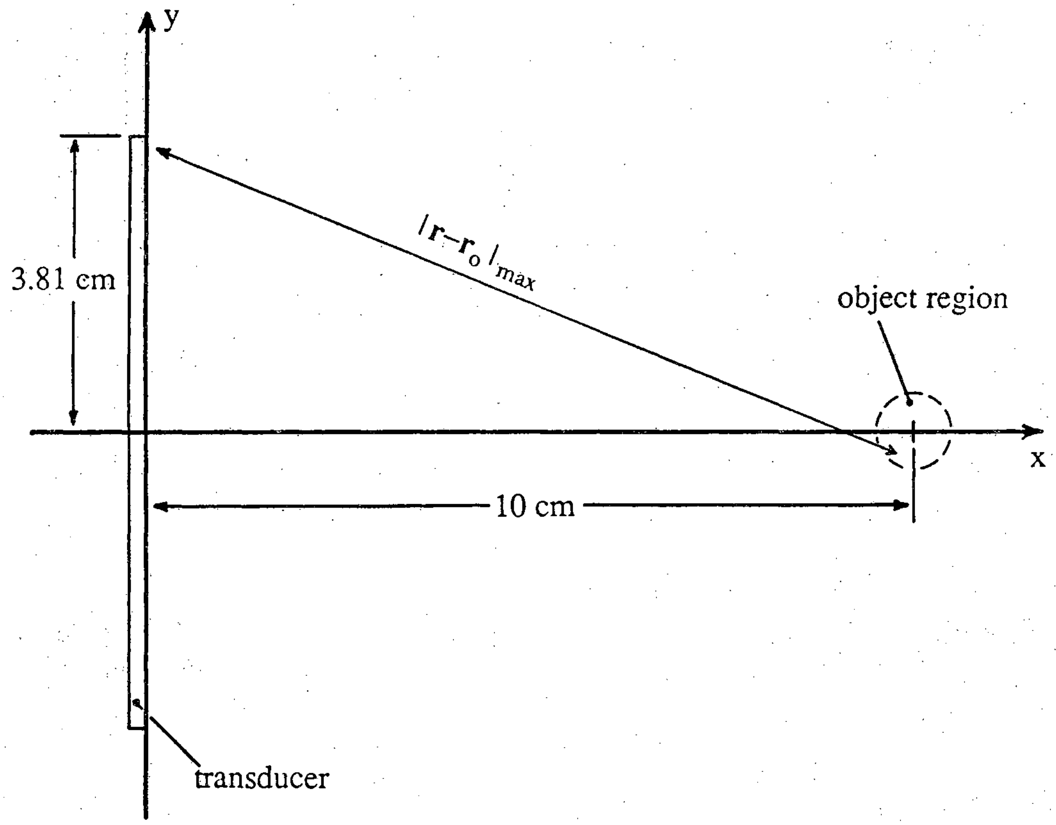

Figure (25) The scanning geometry used for experimental implementation of the STRMDT algorithm.

the particular scanning geometry that is used to experimentally obtain scattered wave measurements, replacing $|\mathbf{r}-\mathbf{r}_0|$ by x_0 results in a seven percent maximum error in distance. Therefore the amplifier that compensates for beam divergence has the time dependence described by $b(t) = c\,t/2$. This is due to the fact that at time t' in the backscattered wave, the maximum distance traveled by the wave is equivalent to $2x_0'$ where x_0' is the maximum perpendicular distance from the transducer that a wavefront could have reached. A more accurate version of $b(\cdot)$ is the following which takes into consideration the change of c within the object,

$$b(t) = \begin{cases} c\,t/2 & , t<t_0 \\ c_{ave}\,t/2 & , t>t_0 \end{cases}$$

where c_{ave} is the average propagation speed within the object. This might be an appropriate amplifier if the receiving transducer were small in relation to the scattering object, but in our case of interest the transducer is much larger than the object and can sense a large percentage of the backscattered energy. Hence it isn't clear what effect that beam divergence will have on the energy levels received by the "long" transducer. Therefore the experimental work presented in section 3.4 will only compensate for object attenuation and rely upon the line spread function discussed in subsection 3.3.3.1 to account for beam divergence.

At this point two amplifiers have been derived to compensate for the types of attenuation that are most bothersome to ultrasound tomgraphy:

$$a(t) = e^{\alpha_0 f_c c(t-t_0)}\,u(t-t_0)$$

$$\text{and} \qquad b(t) = c\,t/2 \quad .$$

The first of these amplifiers is incorporated into the experimental data collection process in a later section.

3.3.3 A Model for Backscatter

Three major steps are necessary to arrive at an accurate description of the output of a plane wave transducer of the kind used in the single transducer RMDT algorithm described in section 3.1:

- Describe the pulse emanating from a transducer as a function of position **r**.
- Use this "incident wave" expression in the time domain Born approximated expression for the scattered wave.

- Integrate the scattered wave over the face of the transducer to obtain an expression for the actual output signal of the transducer.

The first step is accomplished by Eq. (46),

$$u_i(\mathbf{r}_o,t) = \iint_A \frac{\cos(\theta)}{2\pi c\,|\mathbf{r}'-\mathbf{r}_o|}\,\frac{\partial}{\partial t}u_a\left[\mathbf{r}',\,t-\frac{|\mathbf{r}'-\mathbf{r}_o|}{c}\right]dy'\,dz' \quad,\ \mathbf{r}'=(0,y',z')\ . \tag{59}$$

where $u_a(\cdot)$ is the wave within the transducer "aperture" as could be described from Eq. (37) for a focussed transducer. The second step is provided by Eq. (10)

$$u_s(\mathbf{r},t) = \iiint_V \frac{F(\mathbf{r}_o)}{4\pi\,|\mathbf{r}-\mathbf{r}_o|}\,u_i\left[\mathbf{r}_o,\,t-\frac{|\mathbf{r}-\mathbf{r}_o|}{c}\right]dv_o\ .$$

Note that the above equation describes the scattered field at a particular position **r** and time t, as the integral over a circular arc of radius $|\mathbf{r}-\mathbf{r}_o| = tc$. Note also that the equation ignores multiple scattering.

Lastly, step number three is the integration

$$p_{out}(t) = \int_{-s_y}^{s_y}\int_{-s_z}^{s_z} u_s(\mathbf{r},t)\,dz\,dy \quad,\ \mathbf{r}=(0,y,z)\ ,$$

which yields the expression for the output signal. It is obvious that the curvature of the transducer face is being ignored in this integration for the purpose of simplifying the calculation.

Combining all three steps results in the equation

$$p_{out}(t) = \int_{-s_y}^{s_y}\int_{-s_z}^{s_z}\iiint_V \frac{F(\mathbf{r}_o)}{4\pi\,|\mathbf{r}-\mathbf{r}_o|}\iint_A \frac{\cos(\theta)}{2\pi c\,|\mathbf{r}'-\mathbf{r}_o|} \tag{60}$$

$$\cdot\,\frac{\partial u_a}{\partial t}\left[\mathbf{r}',\,t-\frac{|\mathbf{r}-\mathbf{r}_o|}{c}-\frac{|\mathbf{r}'-\mathbf{r}_o|}{c}\right]dy'\,dz'\,dv_{\mathbf{r}_o}\,dy\,dz\ .$$

The above result of this subsection is used subsequently to generate a description of the line spread function corresponding to the backscattering process.

3.3.3.1 The Line Spread Function

It is important to have an accurate description of the "impulse function" of the imaging process which for this discussion is called the line spread function, the term used in image processing. The use of the line spread function (lsf) instead of the point spread function (psf) is justified by pointing out that the interaction of the ultrasound wave with the object is confined to a slice of the object. Confining the ultrasound and object interaction, is accomplished by using a transducer that is focussed in the plane in which lies the object slice whose reconstruction is desired. In short, focussing is in the elevation plane.

In this subsection a theoretical description of the lsf is derived from the background provided in the previous subsections. Given the theoretical lsf, an implementable form is derived for use in inverse filtering the experimentally obtained backscatter from real objects.

The point spread function of a linear imaging system is defined to be the A-scan of a point object. To generate an expression for the psf of a pulse-echo system, steps similar to those outlined in section 3.3.3 can be followed. This time the object function $F(\mathbf{r}_o)$ will be an impulse function which results in the psf

$$\begin{aligned} g(\mathbf{r},t;\mathbf{p}) &= \int_V \frac{\delta(\mathbf{r}_o-\mathbf{p})}{4\pi|\mathbf{r}-\mathbf{r}_o|}\, u_i\left[\mathbf{r}_o, t-\frac{|\mathbf{r}-\mathbf{r}_o|}{c}\right] dv_o \\ &= \frac{1}{4\pi|\mathbf{r}-\mathbf{p}|}\, u_i\left[\mathbf{p}, t-\frac{|\mathbf{r}-\mathbf{p}|}{c}\right] . \end{aligned}$$

where **p** is the vector indicating the position of the point target. We see that the psf is a function of relative distance between the observation point **r** and the object point **p**. Therefore, unfortunately, this psf does not possess the shift-invariant property which would allow a convenient deconvolution of the psf.

If a focussed transducer is used, the object-wavefront interaction is limited to a narrow strip of the object thereby justifying the use of a system lsf instead of the psf,

$$g_l(x,y,t;\mathbf{p}) = \int_{-\infty}^{\infty} g(x,y,z,t;\mathbf{p})\, dz ,$$

although the problem of shift-variance remains. To avoid the shift-variance problem it is necessary to examine the scanning geometry dictated by the STRMDT algorithm. If the vector **p** is restricted to lie within the object region that is illustrated in figure (25), shift-invariance can be reasonably approximated within that object region. Considering the dimension of the object region, this approximation for the lsf is in error in magnitude only slightly.

Now since the shift-invariance of $g_l(\cdot)$ is established, the next step is to consider the output of the transducer, $h_{sl}(\cdot)$,

$$h_{sl}(t) = \iint_A g_l(x,y,t)\, da$$

$$= \iint_A \frac{1}{|\mathbf{r}-\mathbf{p}|} u_i\left[\mathbf{p}, t - \frac{|\mathbf{r}-\mathbf{p}|}{c}\right] da \ , \ \mathbf{r} = (0,y,0) \ , \ \mathbf{p} = (x_p,0,0) \ , \qquad (61)$$

in which **p** is a constant at the center of the object region. The subscript 's' attached to the function $h_{sl}(\cdot)$ indicates that this lsf accounts for the scattering effects but does not account for the electro-mechanical effects of the transducer itself. As in [Fate80] the total line response of the data collection system, $h_l(\cdot)$ can be broken into the two parts just mentioned,

$$h_l(t) = h_{sl}(t) * h_{em}(t) \ . \qquad (62)$$

If it were necessary to obtain an expression for the electro-mechanical impulse function, one would have first look at Eq. (62) in the frequency space,

$$H_l(\omega) = H_{sl}(\omega)\, H_{em}(\omega) \ ,$$

from which we obtain

$$h_{em}(t) = \mathcal{F}^{-1}\left\{ \frac{H_l(\omega)}{H_{sl}(\omega)} \right\} \ .$$

Hence all that is needed are the Fourier transforms of $h_{sl}(\cdot)$ and $h_l(\cdot)$. The total line response can be measured experimentally and $h_{sl}(\cdot)$ can be theoretically calculated.

The line spread function, $h_l(\cdot)$, which is equivalent to the backscatter received from a line at the center of the object region, is illustrated, as obtained from experimental measurements, in figure (26). Along with the time domain plot, the magnitude of the Fourier transform of $h_l(\cdot)$ is provided in figure (27).

To calculate the function $h_{sl}(\cdot)$ it is necessary to return to Eq. (61) and come up with an accurate expression for $u_i(\cdot)$ and $u_a(\cdot)$ within the object region. To aid in coming up with an efficient expression for $u_i(\cdot)$, Eq. (59) is used to calculate $u_i(\cdot)$ for the four different sizes of transducer illustrated in figure (28). For the largest transducer the incident wave, plotted in figure (29), is constant over the width of the object region due to the integration over the large surface area of the transducer itself. The wavefronts generated by the other transducers, plotted in figures (30,31,32), are not nearly as uniform. Since the transducer used in the lab is by our definition much longer than the width of the object region, as would be the case in figure (29), $u_i(\cdot)$ can be safely approximated within the object region as

$$u_i(x,t) \approx \frac{\partial}{\partial t} u_a\left[t - \frac{x}{c}\right]$$

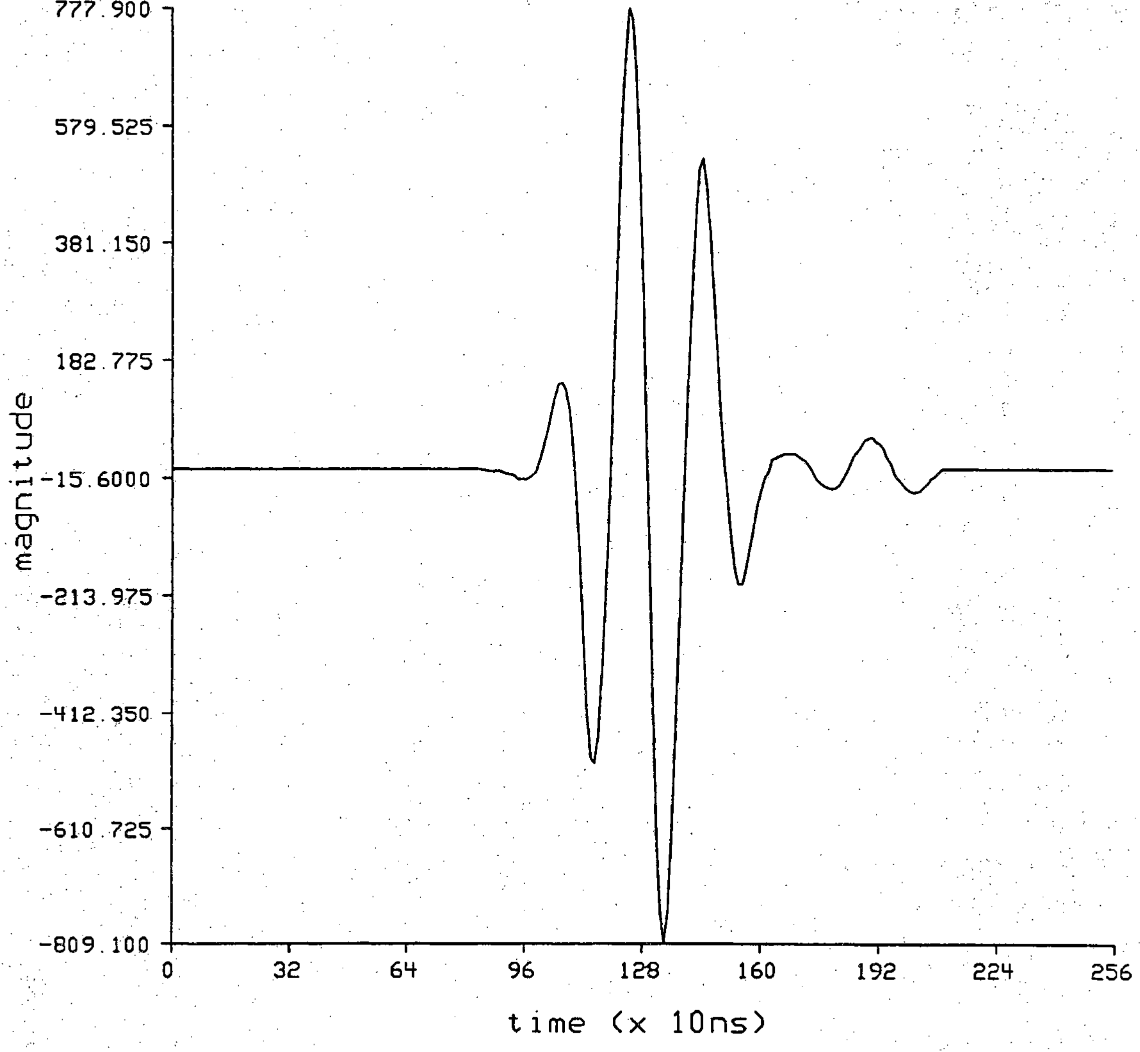

Figure (26) The transducer output resulting from backscatter from a line target placed at the center of the object region. This signal is essentially the line spread function of the experimental imaging system.

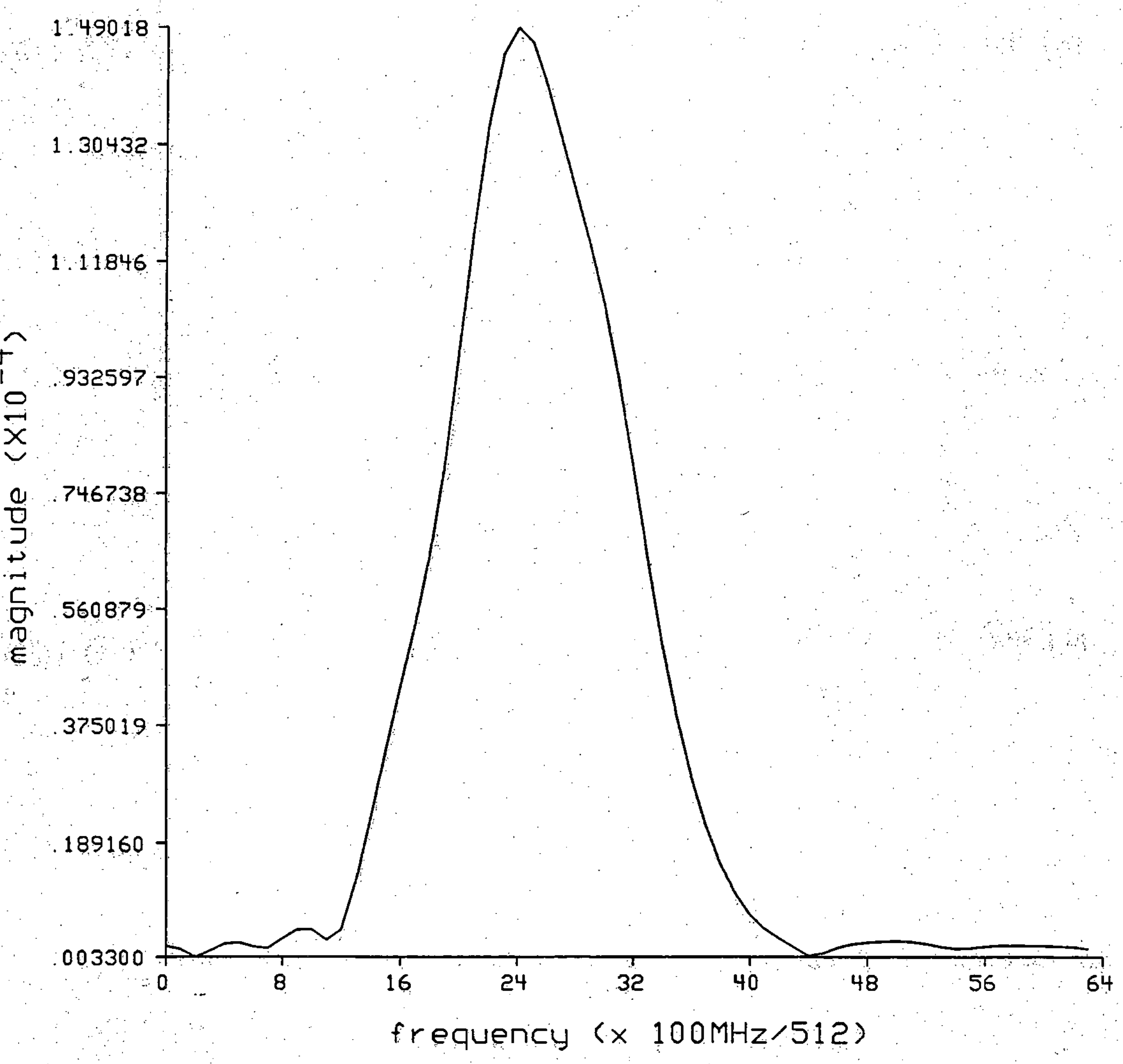

Figure (27) The magnitude of the Fourier transform of the line spread function in figure (26).

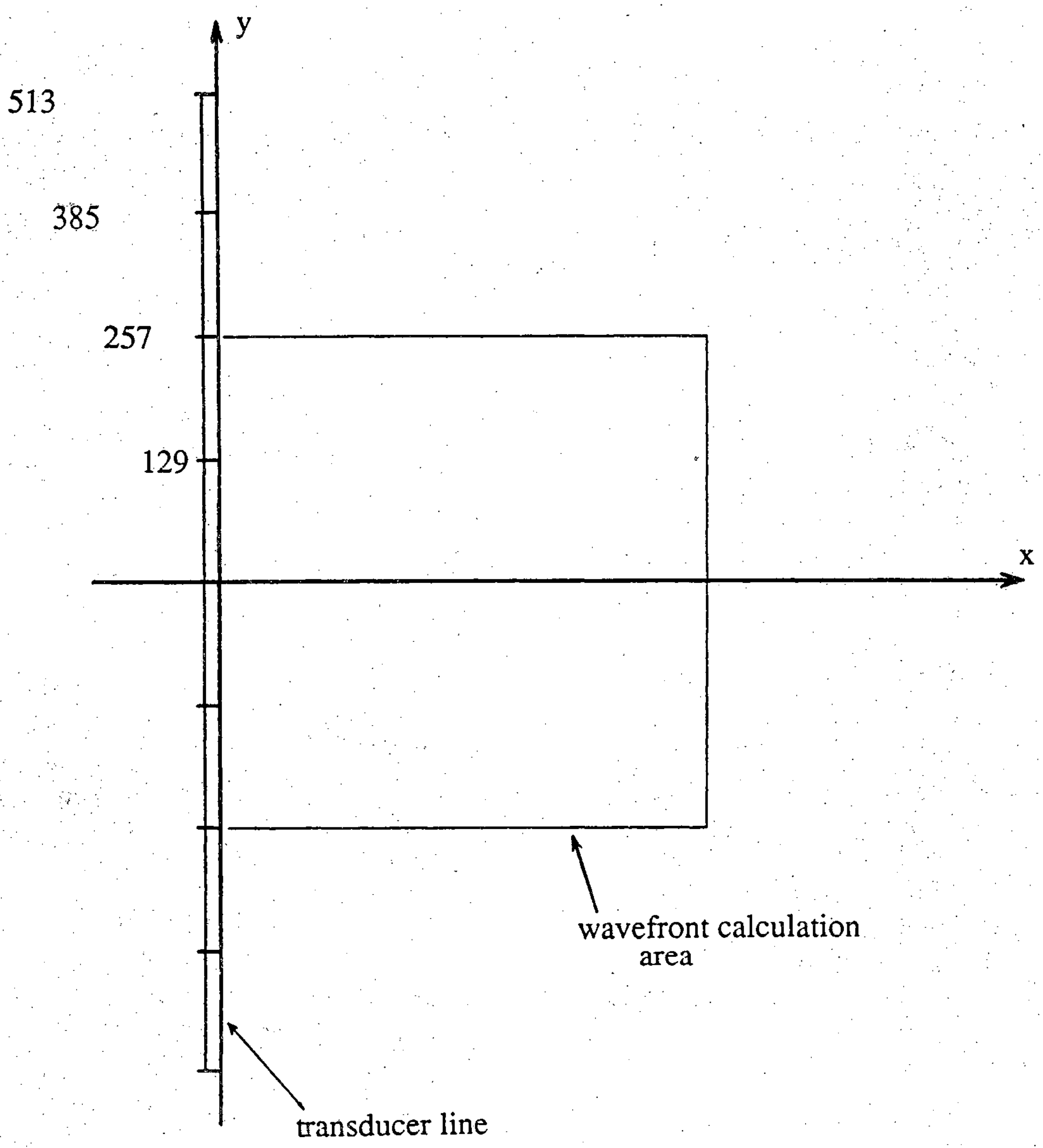

Figure (28) To obtain an intuitive feel for the form of the incident wave within the object region, Eq. (59) is used to calculate the wavefronts generated by four different sizes of transducers. The conditions of the simulations and the relative sizes of the transducers are illustrated here.

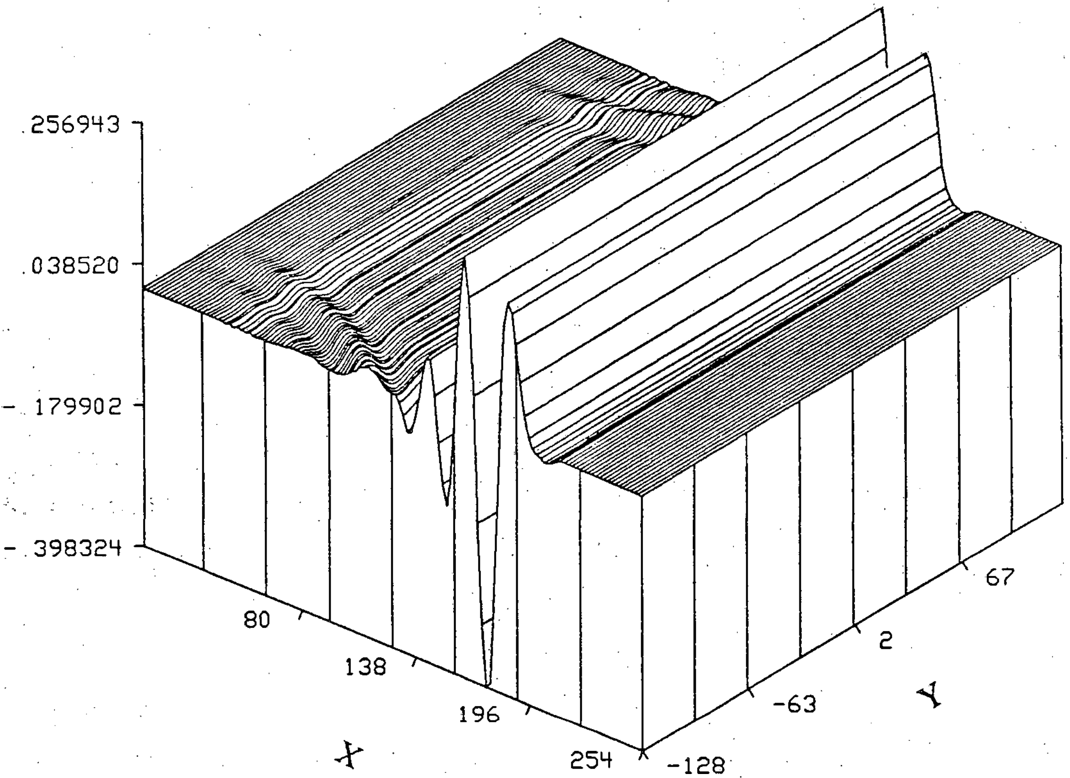

Figure (29) The wavefront generated by a simulated transducer of 513 samples. Note that within the calculated region, the wavefront is constant with respect to y.

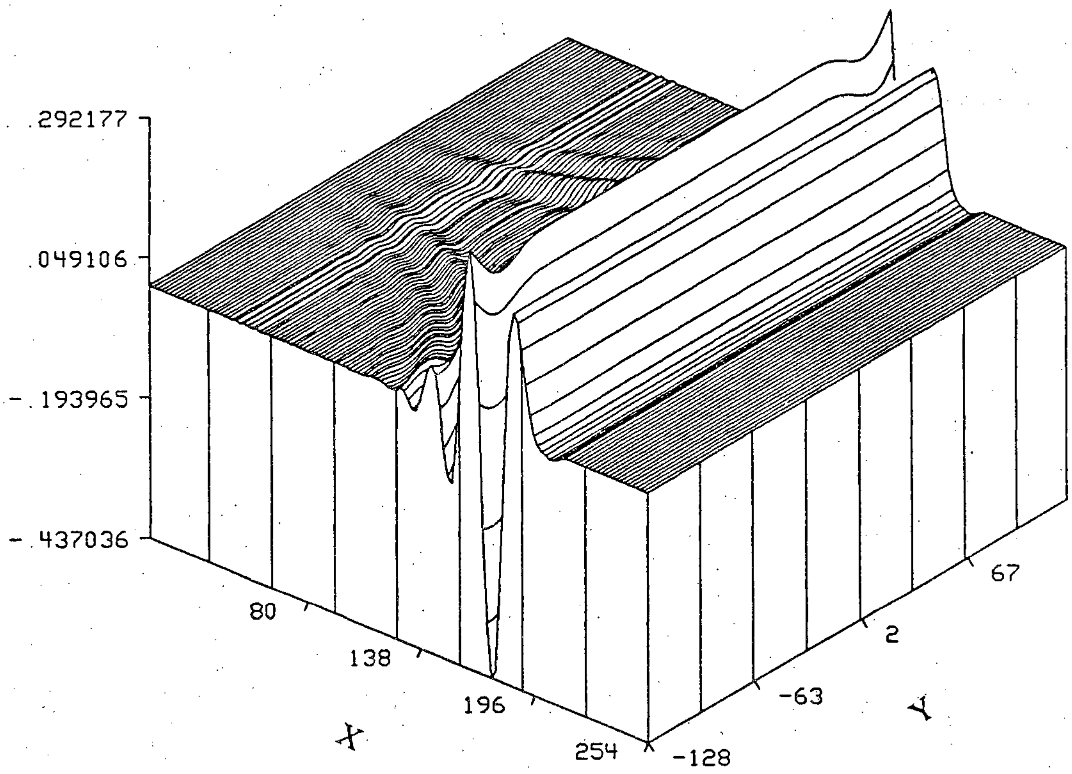

Figure (30) The wavefront generated by a simulated transducer of 385 samples.

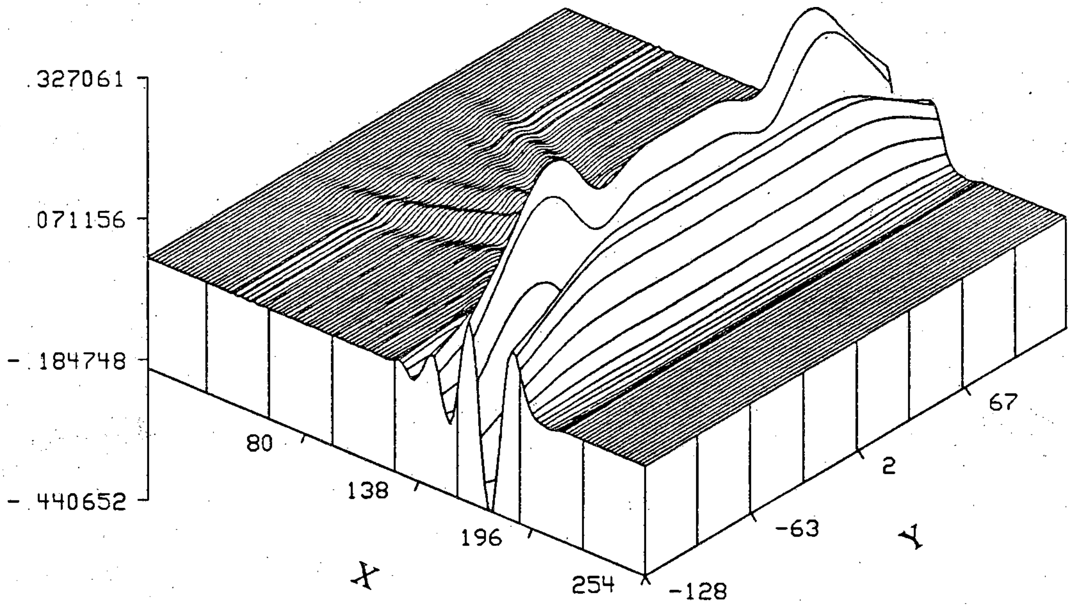

Figure (31) The wavefront generated by a simulated transducer of 257 samples.

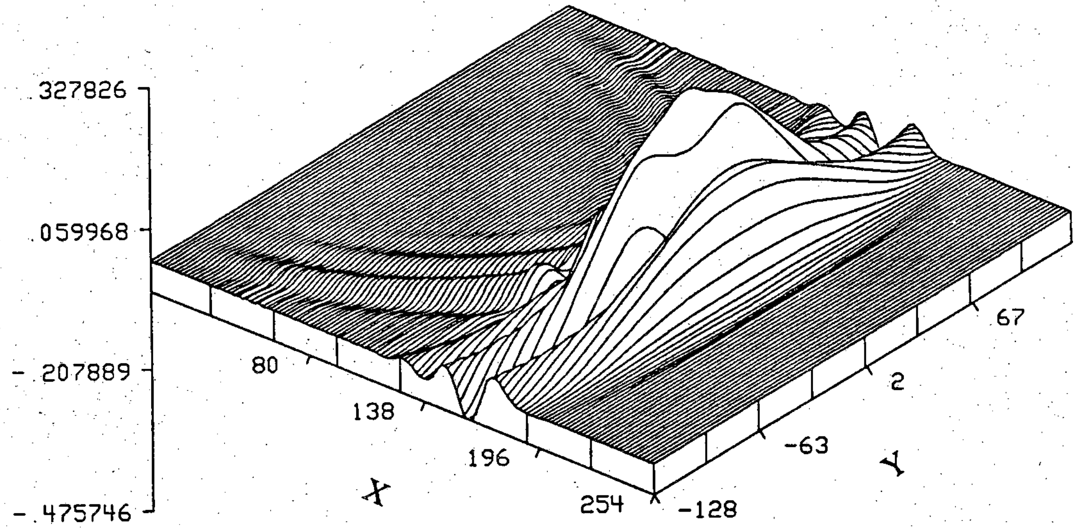

Figure (32) The wavefront generated by a simulated transducer of 129 samples.

where the wave within the aperture, $u_a(\cdot)$ is no longer a function of position but rather only a function of time. Next, the function $u_a(\cdot)$ is determined with the aid of the measured backscatter from a planar surface as plotted in figure (33). This is done under the assumption that the backscatter will have the same general bandwidth as $u_a(\cdot)$ and that it is possible to model the wave as

$$\frac{\partial}{\partial t} u_a(t) = \int_{-\infty}^{\infty} \omega\, B(\omega)\, e^{-j\omega t}\, d\omega \ .$$

where the function $B(\cdot)$ is the magnitude of the Fourier transform of the planar surface backscatter as illustrated in figure (34).

The above was an interesting diversion into how one would calculate $h_{sl}(\cdot)$ and into the type of incident waves that the object region experiences, but now we must get back to the issues at hand. What this subsection provides is an experimentally measured line spread function to use when inverse filtering the A-scans of real objects as described in the next section. Well there you have it, in the next section we will describe how the experimental imaging system makes use of the lsf in obtaining $u_s(t)$ measurements.

3.4 Experimentation

A feasible technique for constructing a tomogram is illustrated in figure (35):

☐ record the A-mode signal with the use of a large broadband transducer
☐ amplify the signal to compensate for object attenuation and beam divergence
☐ deconvolve the line spread function from the signal
☐ Fourier transform and extrapolate the spectrum of the resulting signal
☐ Place the slice in its proper position in Fourier space

After applying the necessary amplification as outlined in subsection 3.3.2.2, we can return to Eq. (36) and obtain the function of ω, $P_\phi(\omega, y=l_0)$, by dividing the spectrum of $p_{out}(t)$ by the spectrum of $h_l(t)$ and staying in the Fourier domain. The division of spectra is a crude attempt at deconvolution which can be improved upon by resorting to a more robust approach such as Wiener filtering or constrained deconvolution. Once $P_\phi(\omega, y=l_0)$ is known it is a simple matter to obtain an estimate of the object function's Fourier space along a line,

$$\tilde{F}(0, -2\omega/c) = \frac{2\omega}{jc}\, e^{jk_o l_0}\, P_\phi(\omega, y=l_0)$$

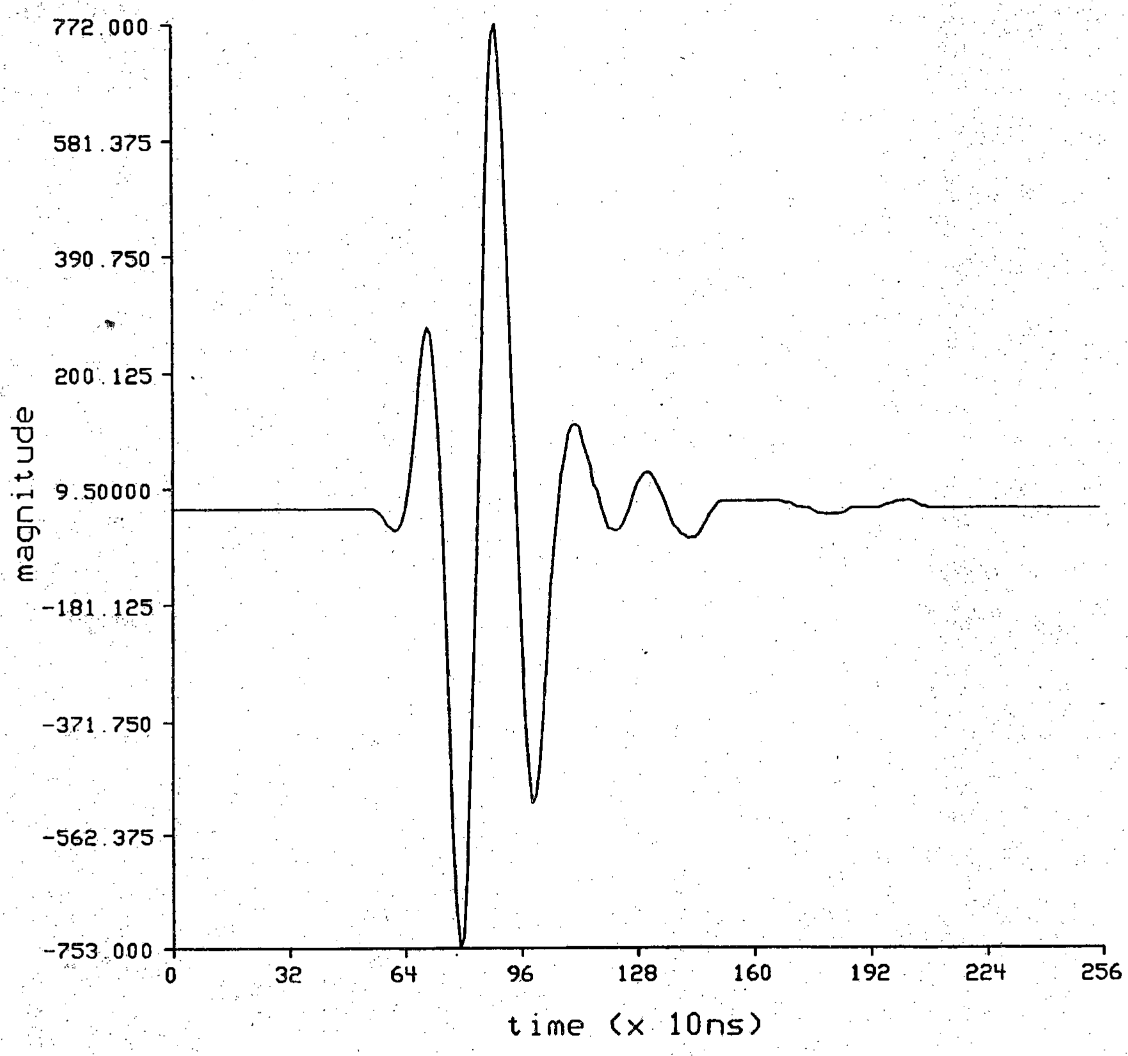

Figure (33) The transducer output resulting from backscatter from a planar surface located at the center of the object region.

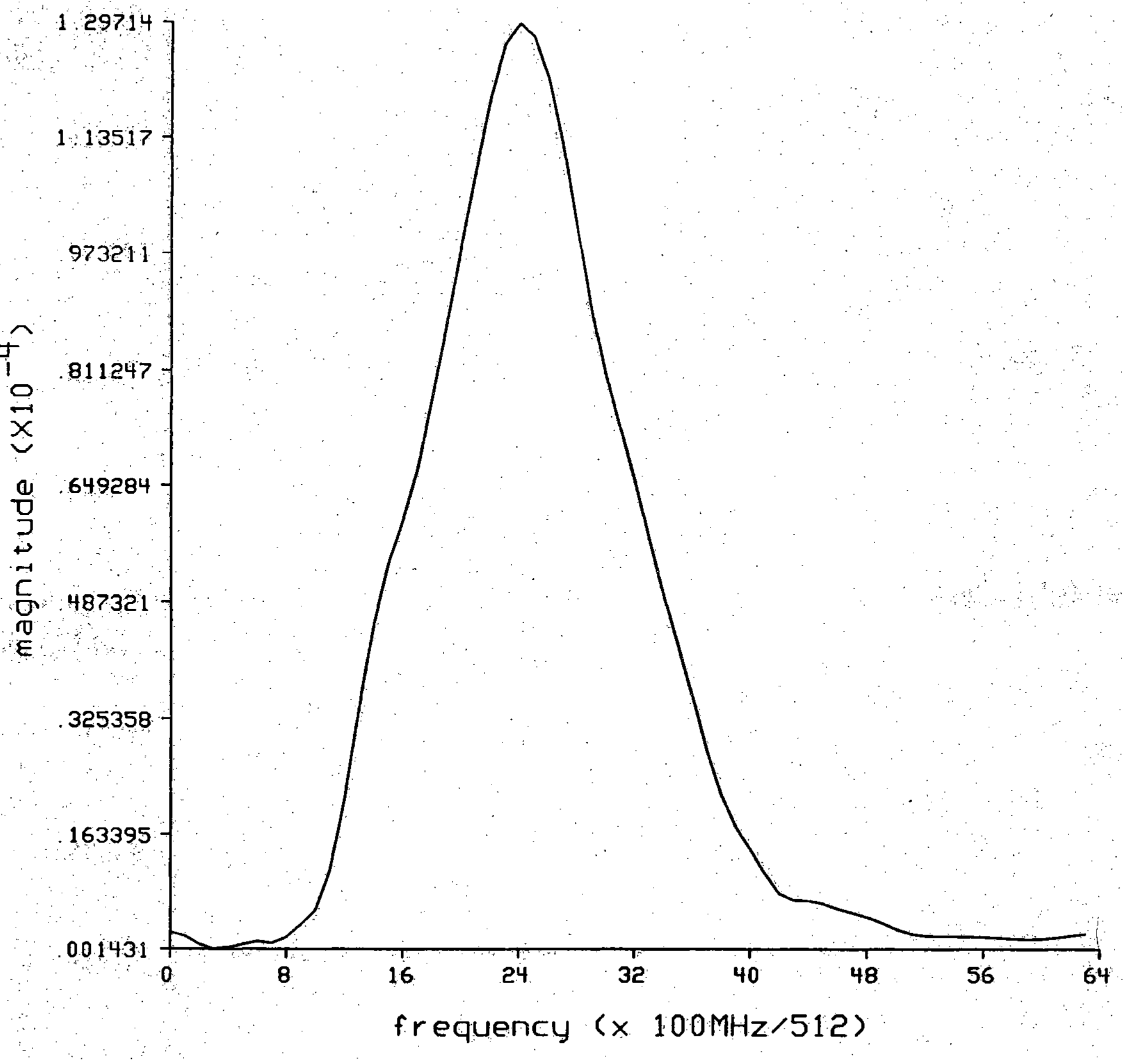

Figure (34) The magnitude of the Fourier transform of the planar backscatter in figure (33).

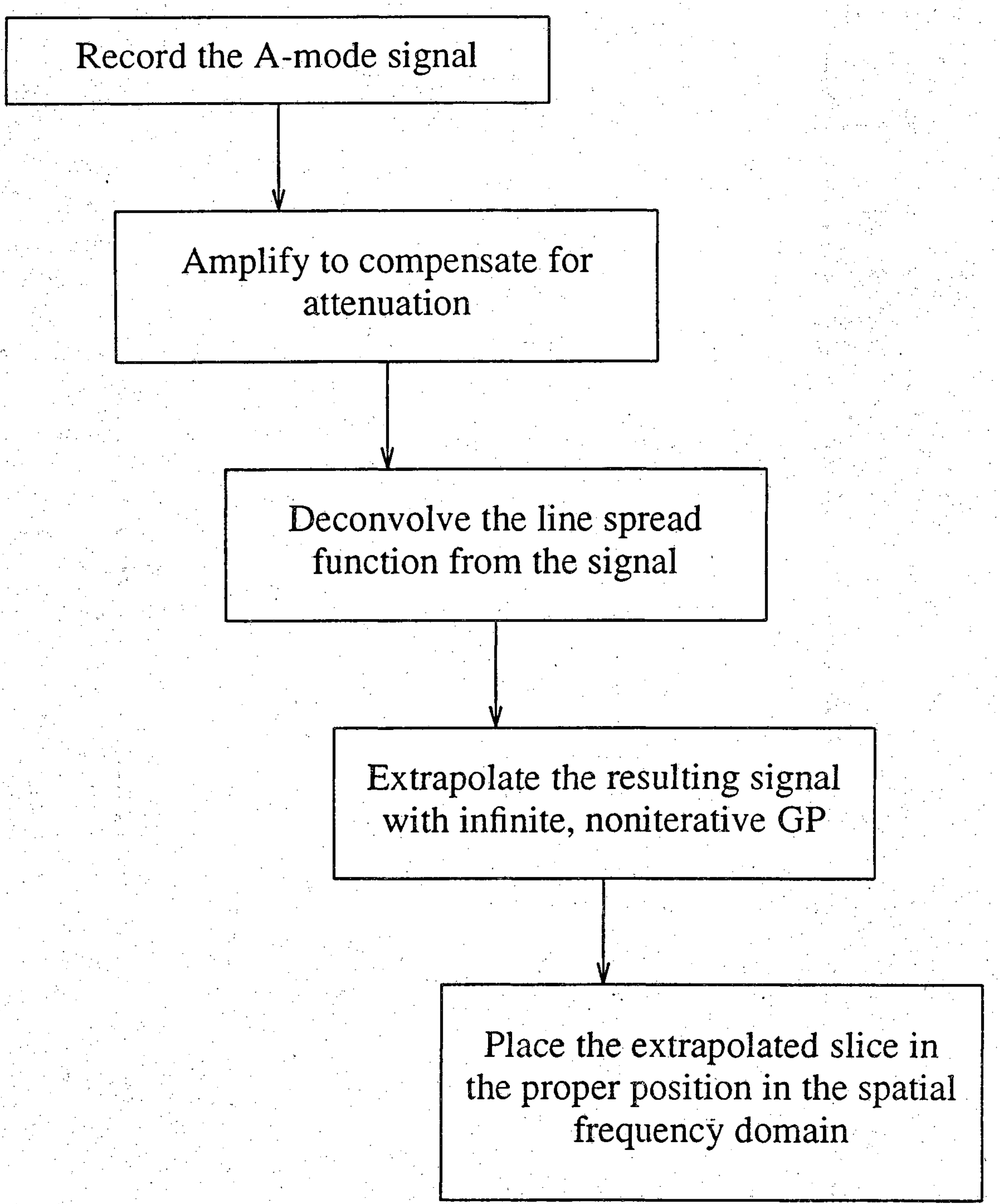

Figure (35) The approach taken to experimentally implement the STRMDT algorithm is illustrated by the block diagram.

Before showing experimental results it is necessary to say a few words about the immediate goals and the type of experimental measurements that were made. The specifications of the transducer used to make the measurements are included in appendix E, the lsf is presented in the previous section, and the configuration of the insonifying aparatus is presented in figure (25). If the object region is confined to be of radius $2\lambda_C$ so that reconstruction quality will be acceptable, than the region would only have a diameter of 1.2mm at best. The statement concerning reconstruction quality comes from the discussion in the summary of chapter 4 and the array of reconstructions that is presented there. From that discussion and the associated plots, it becomes obvious that reconstruction quality becomes questionable for objects of radius larger than $2\lambda_C$. It is this restriction along with the fact that the insonifying transducer must be much longer than the greatest dimension of imaged objects, that leaves us with very little choice as to the size of the object region.

The purpose of this section is to illustrate a process for obtaining data, manipulating it, and using it to obtain cross-sectional reconstructions of objects. In the hope of fulfilling this purpose, an plexiglas rod of diameter 0.3175cm ($= 10.65\lambda_C$) is used as an object. It is difficult to obtain "core samples" of tissue mimicking material that would be small enough to fit within the object region, hence the choice of the above mentioned object.

The echo from the rod is plotted in figure (36). To deconvolve the line spread function a combination of Wiener filtering and simple Fourier domain division can be carried out. The combined filter, $H_f(\omega)$, takes the form

$$H_f(\omega) = \begin{cases} \dfrac{1}{|H_l(\omega)|} , & \omega_{pl} < \omega < \omega_{ph} \\[2ex] \dfrac{H_l^*(\omega)}{|H_l(\omega)|^2 + |N(\omega)/P(\omega)|^2} , & \omega \text{ elsewhere} \end{cases} ,$$

where the function $N(\omega)$ is the noise spectrum and $P(\omega)$ is the echo spectrum. In addition to the filtering, a gaussian shaped window centered at the center frequency of the transducer is applied since the spectra of both the line response and the echo are narrowband. The result of applying this filtering to the rod echo is shown in figure (37). Ideally the result would appear to be two impulse functions.

The time conscious experimenter might resort to envelope detection to approximate the deconvolution of line response from the echo. To numerically calculate the envelope of the rod echo it is first necessary to Fourier transform the signal and zero out all of its negative frequency content. Then inverse transform, take

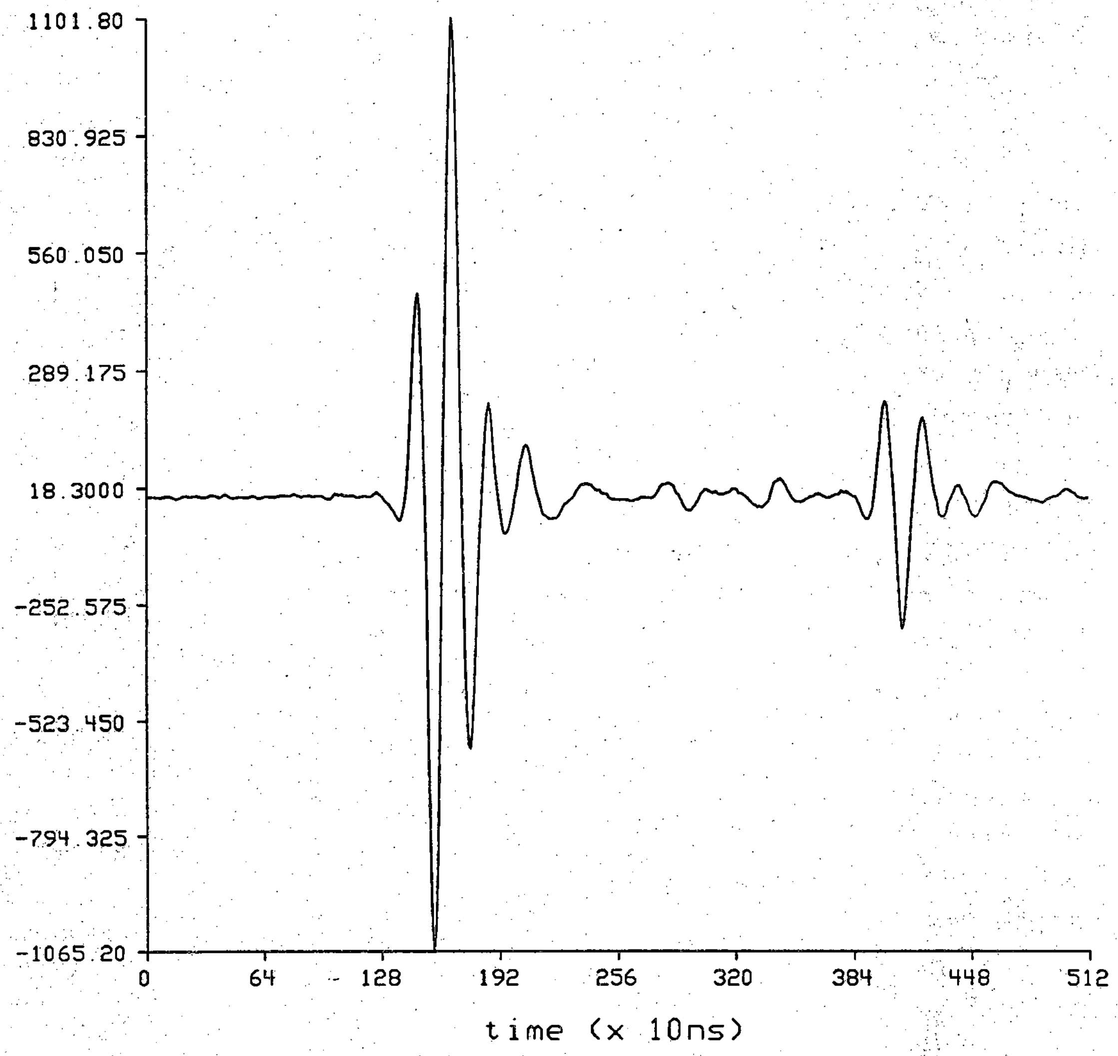

Figure (36) The echo from a small plexiglas rod of 0.125 inch diameter.

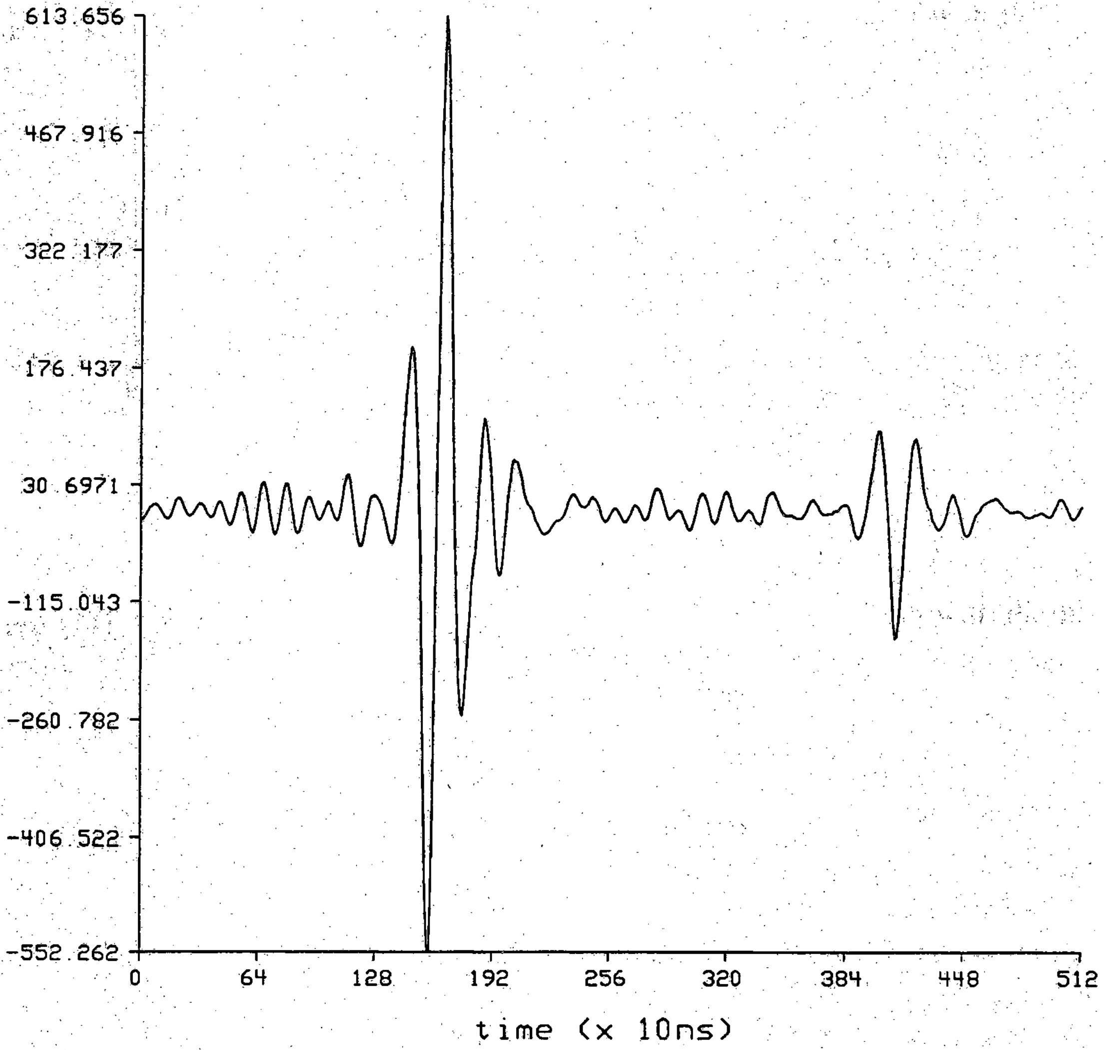

Figure (37) The echo from a small plexiglas rod after deconvolution with the line response.

the magnitude of the result and multiply it by two. The envelope of the rod echo is plotted in figure (38). As shown the 2 peaks in the envelope aren't nearly impulse functions.

As a more serious example the experimentally measured backscatter from a thin slice of a natural sponge is plotted in figure (39). The deconvolved and envelope detected sponge echo are presented in figures (40) and (41) respectively.

To use filtered backscatter to reconstruct the object, a sequence of tasks must be executed:

- ☐ zero pad and Fourier transform
- ☐ apply spectral extrapolation in the frequency space
- ☐ multiply the result by the function $\frac{2\omega}{jc}e^{j\omega l_0/c}$
- ☐ place the 1-D sequence on the appropriate line in the object's 2-D Fourier space.
- ☐ fill the 2-D Fourier space with backscatter measurements from around the object and then 2-D inverse Fourier transform.

Due to a lack of a suitable, weakly scattering object and a lack of time, the spectral extrapolation and frequency space filling can't be carried out by the time of printing.

3.5 Summary

The algorithm that has been presented makes use of a very simple scanning geometry that results in simple and efficient data collection. The output of the transducer is essentially a simple A-mode signal that requires little processing to provide spatial frequency samples of the object. Unfortunately, the algorithm alone suffers from a lack of low frequency information that can only be obtained with the use of spectral extrapolation or with the use of forward scattered field measurements. Another limitation to the type of objects that can be imaged is the physical size of the plane wave transducer. The transducer must provide a ripple free plane wave to the slice of the object being imaged and it must be physically long enough so that all of the backscattered field will impinge upon the surface of the transducer. Otherwise erroneous measurements of $\tilde{U}_{S,\hat{s}_0}(\cdot)$ will be obtained.

As briefly mentioned above, the combination of broadband backscattered and forward scattered fields could be used to obtain a nearly complete filling of the object's frequency domain.

The main assumptions used in developing the algorithm are 1) that only non-frequency dependent backscattering is observed and 2) that only weakly scattering objects can be imaged because of the Born approximation.

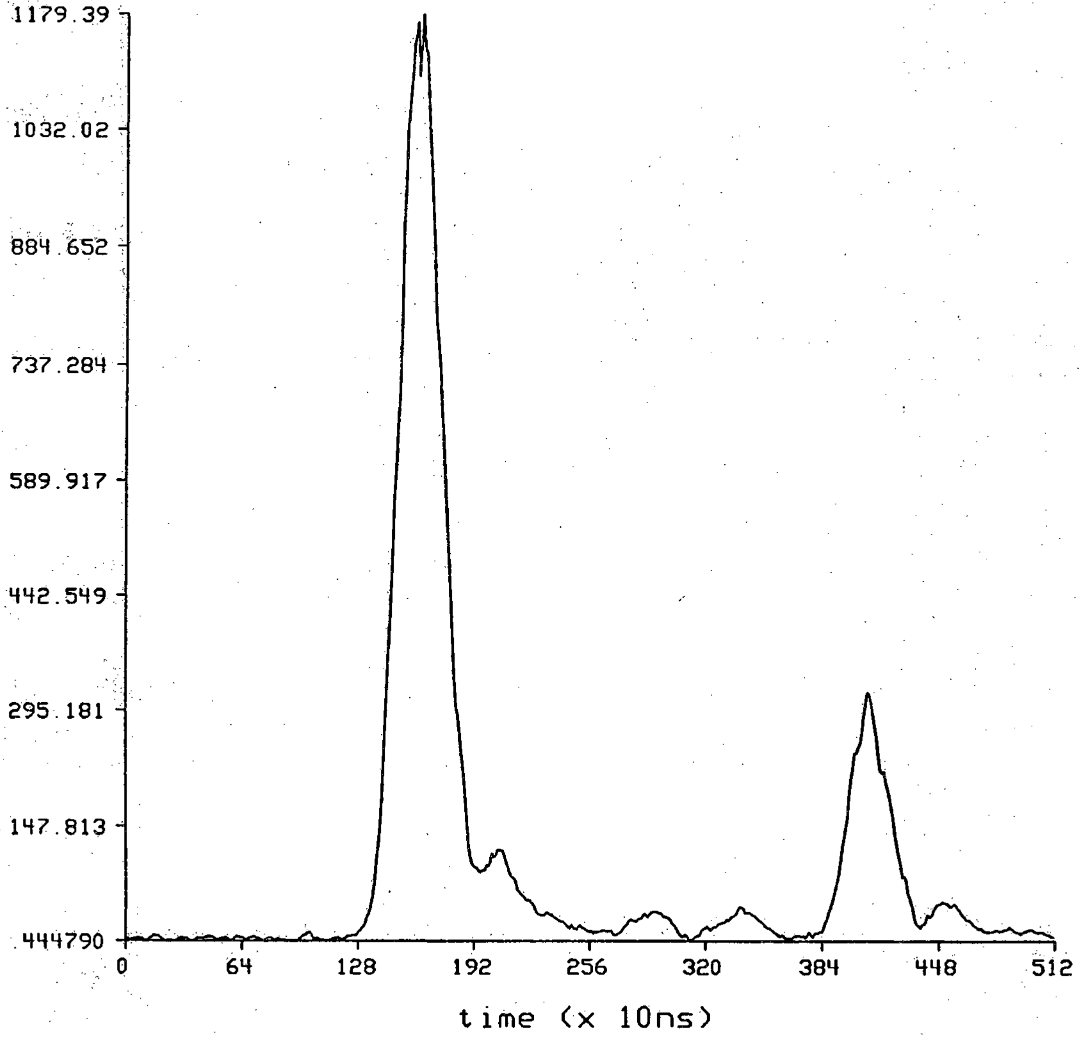

Figure (38) The envelope detected echo from a small plexiglas rod.

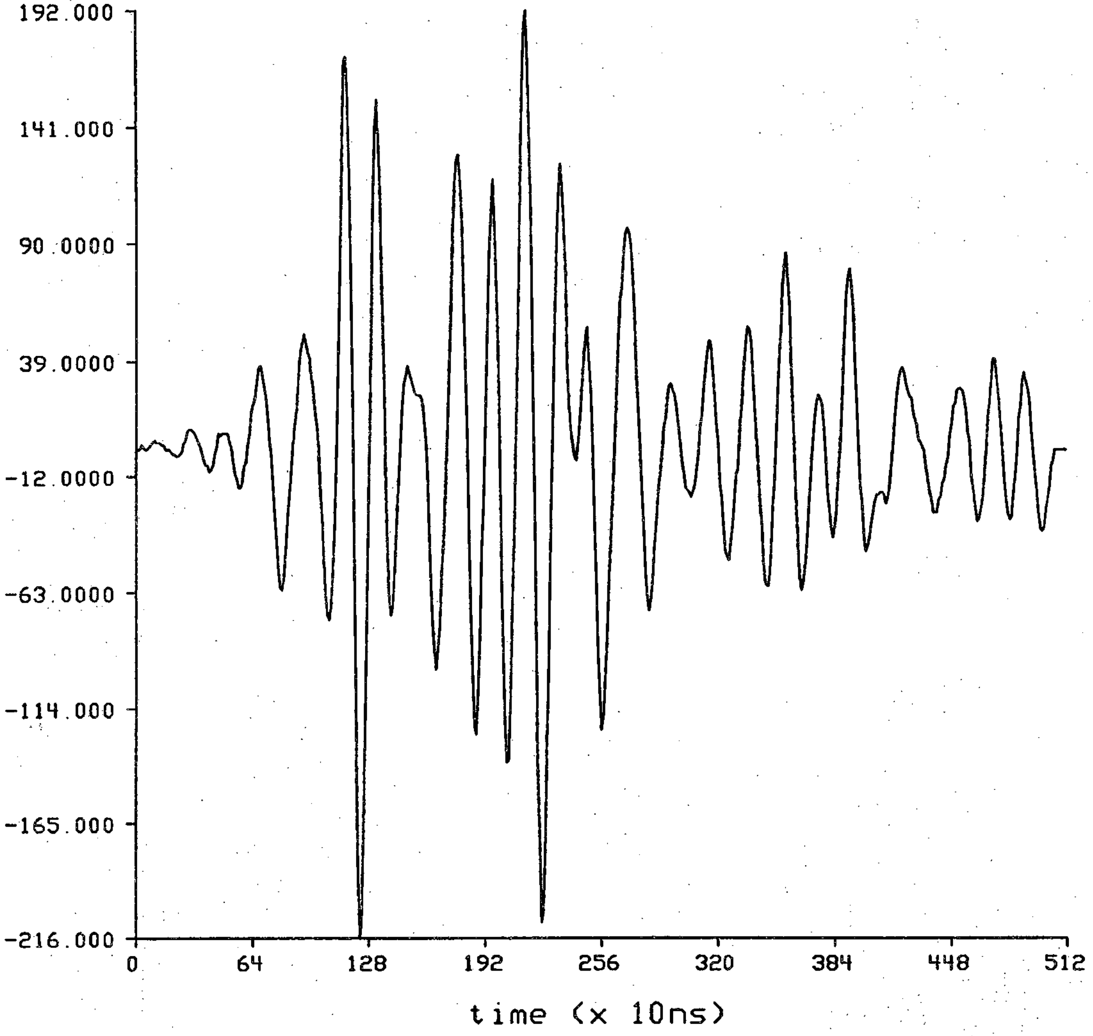

Figure (39) The echo from a thin slice of a natural sponge.

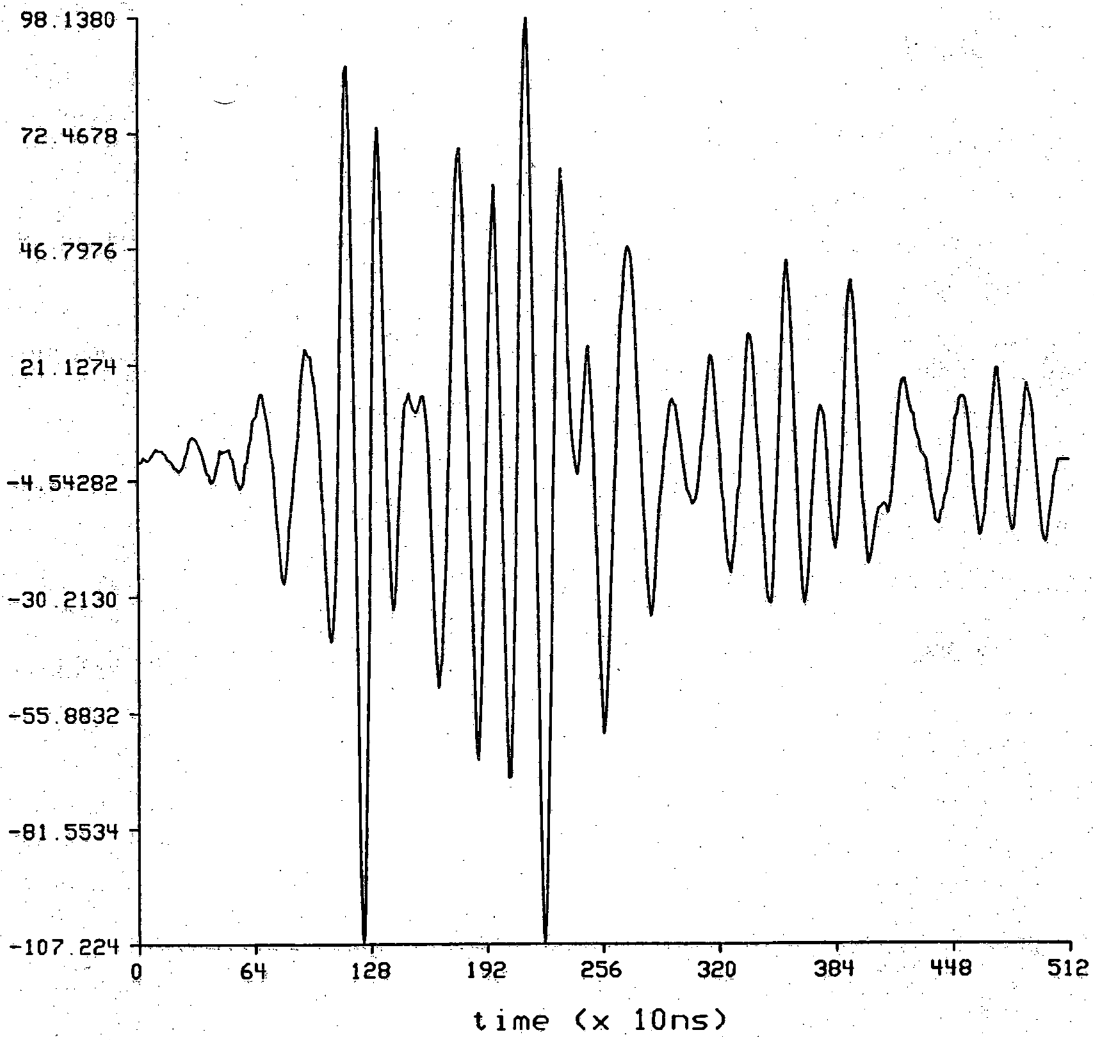

Figure (40) The sponge echo after deconvolution with the line response.

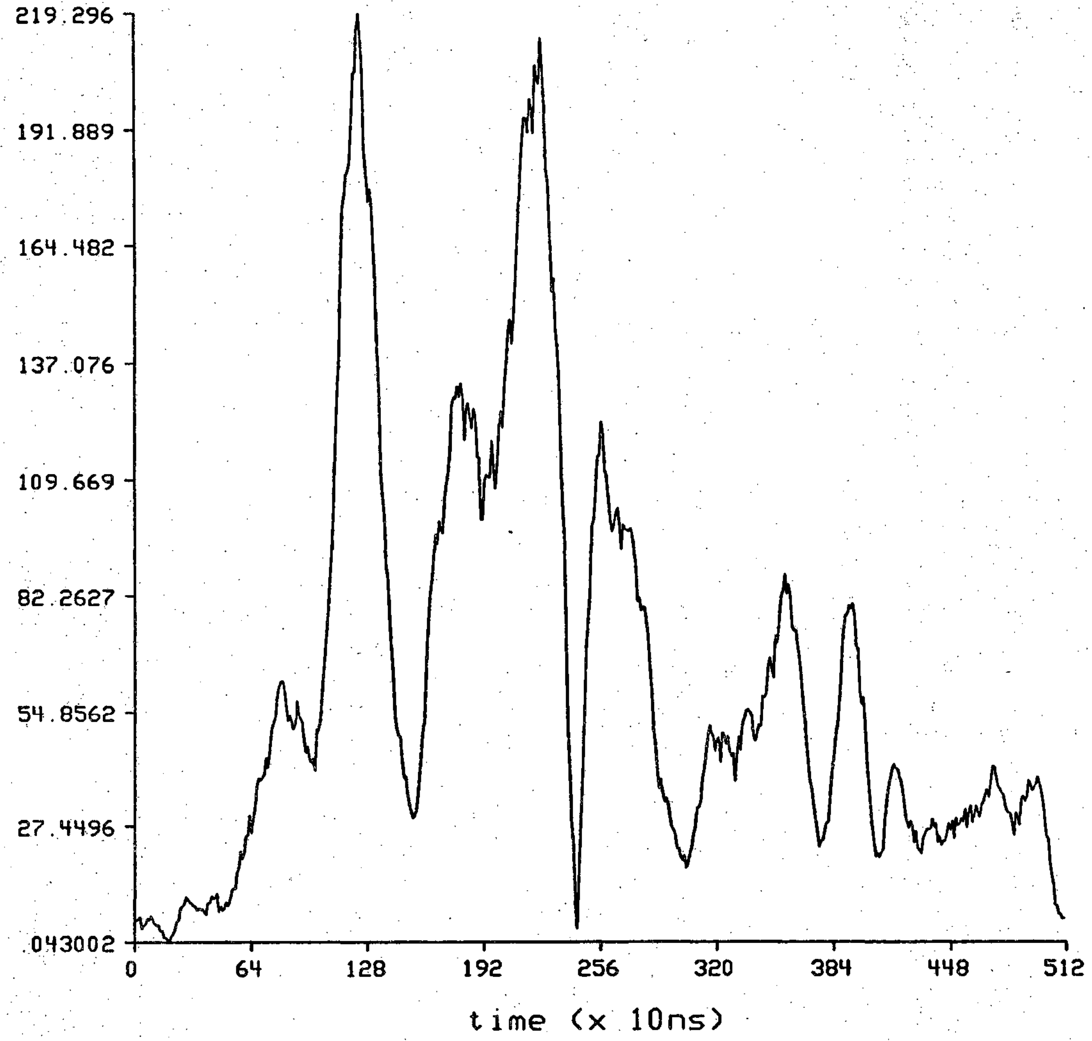

Figure (41) The envelope of the sponge echo.

CHAPTER 4

SPECTRAL EXTRAPOLATION

In this chapter various versions of the Gerchberg-Papoulis (GP) algorithm for spectral extrapolation will be presented and used to extrapolate simulated data. Within sections 4.1, 4.2 and 4.4 the results of applying the respective versions of GP will be presented.

4.1 The Gerchberg-Papoulis Technique of Spectral Extrapolation

In this section the spectral extrapolation approach that is used to gain an estimate to the missing low spatial frequency information, will be described. Other basic techniques to spectral extrapolation have been investigated but not presented in this document. The reader is referred to [Robr85].

The spectral extrapolation technique used within this presentation is the Gerchberg-Papoulis, GP, algorithm which has been discussed by many authors [Pap75,Trus84,Gerch74]. The paper by Sato et al. [Sato81] provides computer simulations of the GP algorithm extended to two dimensions.

The choice of the GP algorithm for use in extrapolating our simulated frequency domain data is based on its simplicity and power. An approach such as the maximum entropy (ME) technique is not suited to the needs of our problem; the ME technique is applicable only to non-negative functions and unfortunately the Fourier domain data we need to extrapolate fails this condition. The ME technique is well suited to the extrapolation of power spectra and digitized images consisting of positive gray levels.

In this presentation, spectral extrapolation will be carried out in only one dimension although our problem is inherently two dimensional. Limitation to one dimension is possible because of the symmetry of the object that is used in the computer simulations of the algorithm. In addition the A-mode signal obtained from the broad-band plane wave transducer provides information about a single slice of the

Fourier space of the object being insonified. Hence it makes sense to extrapolate each 1-D signal as it is obtained from the inverse filter as illustrated in figure (35).

The basic concept that enables the GP technique of spectral extrapolation to function, is the analytic property of the spectrum being extrapolated. In reference [Churc76], the following theorems are stated and proven:

1.) A function that is analytic in a domain D is uniquely determined over D by its values over a domain, or along an arc, interior to D.
2.) If two analytic functions, f_1 and f_2, with the domains D_1 and D_2, have a region of intersection, $D_1 \cap D_2$, f_1 must equal f_2 in the region of intersection.

It follows from the first theorem that the two functions are identical over both D_1 and D_2.

The GP algorithm will combine the analytic nature of the spectrum, the *a priori* spatial information, and a known range of the spectrum obtained from scattered wave measurements, to iteratively obtain the full spectrum. In our application, the known region of the Fourier domain, H(u,v), obtained from the backscattered waves, is a bandpass function which sets our application apart from the typical problem considered in the literature in which a low-pass frequency range is known. The knowledge of H(u,v) and the finite region of support of the object, is all that is necessary to begin extrapolating. The first estimate of f(x,y) is generated by the inverse transformation of H(u,v) which yields $h_0(x,y)$. The steps involved in the iterative extrapolation are outlined below:

i.) The initial step of the iteration consists of multiplying $h_{n-1}(x,y)$ by the region of support function, P(x,y)

$$P(x,y) = \begin{cases} 1 \text{ if } (x,y) \in R \\ 0 \text{ if otherwise} \end{cases}$$

to yield the function $f_n(x,y)$.

ii.) Secondly, $f_n(x,y)$ is transformed resulting in $F_n(u,v)$.

iii.) Thirdly, the region in which F(u,v) is known is restored to its original value, H(u,v), without disturbing the remainder of the frequency domain. The result of this step we shall call $H_n(u,v)$.

iv.) Finally, $H_n(u,v)$ is inverse transformed to obtain $h_n(x,y)$ and we return to step (i) to generate the (n+1)th estimate.

To aid in the description, a block diagram of the algorithm is provided in figure (42). Also for the sake of clarity, the relationships in the above steps are outlined below.

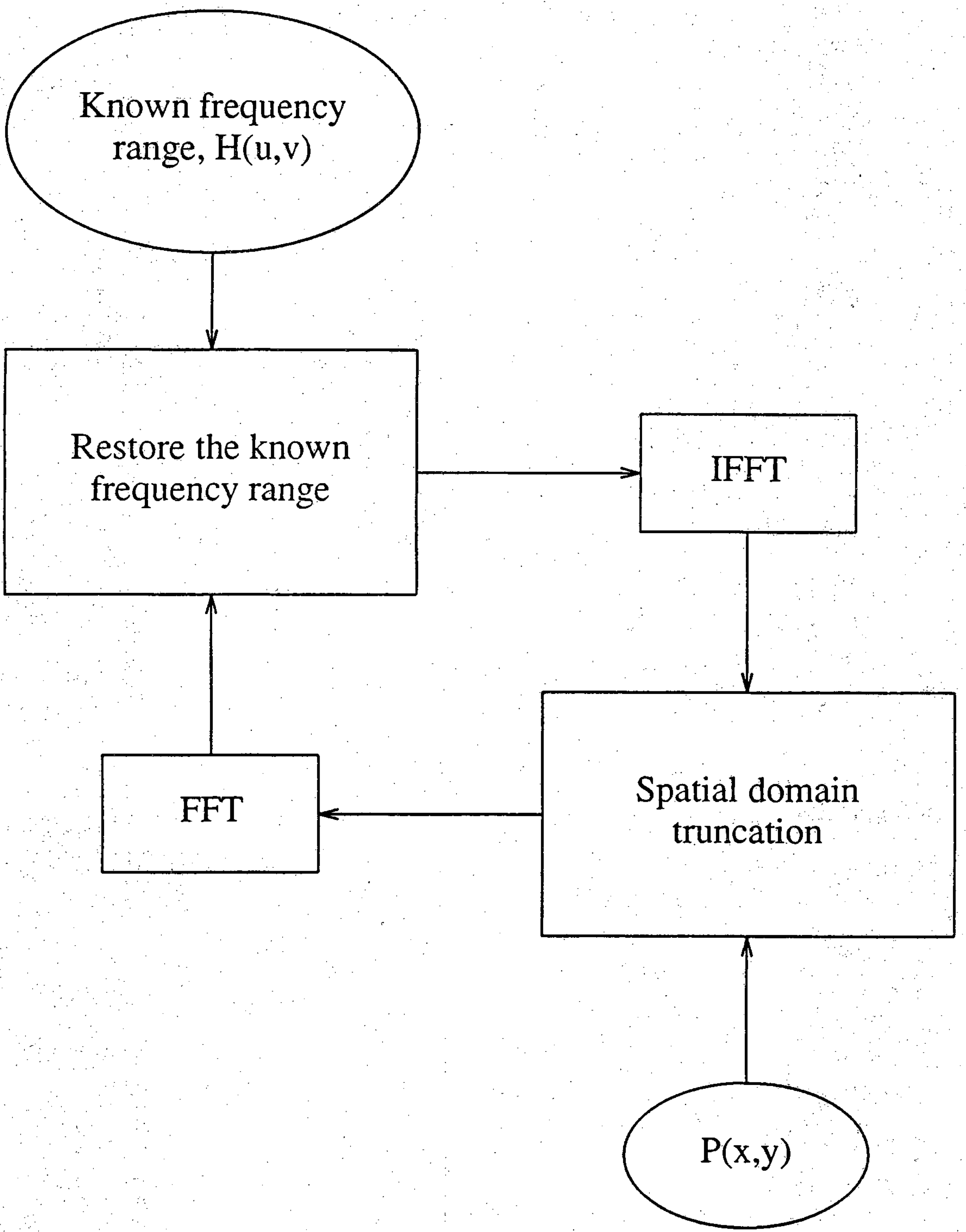

Figure (42) A block diagram of the steps taken in the Gerchberg-Papoulis algorithm of spectral extrapolation.

$$H_n(u,v) = \begin{cases} H(u,v) & ,(u,v) \in L \\ F_n(u,v) & ,\text{otherwise} \end{cases}$$

$$F_n(u,v) = \int\!\!\int_{-\infty}^{\infty} f_n(x,y)\, e^{-j(ux+vy)}\, dx\, dy$$

$$= \iint_R h_{n-1}(x,y)\, e^{-j(ux+vy)}\, dx\, dy \;.$$

In the above, L is the region in which H(u,v) is nonzero and R is the spatial domain region of support of the object.

Following the presentation in [Pap75], the mean square error of the estimate f_n, within one iteration, is twice reduced. With the aid of Parseval's equation, the following relationships hold:

$$\int\!\!\int_{-\infty}^{\infty} \left| f(x,y)-h_{n-1}(x,y) \right|^2 dx\, dy > \int\!\!\int_{-\infty}^{\infty} \left| f(x,y)-f_n(x,y) \right|^2 dx\, dy =$$

$$= \int\!\!\int_{-\infty}^{\infty} \left| F(u,v)-F_n(u,v) \right|^2 du\, dv > \int\!\!\int_{-\infty}^{\infty} \left| F(u,v)-H_n(u,v) \right|^2 du\, dv \;.$$

The inequalities are, of course, due to the relationships $\left| f(x,y)-h_{n-1}(x,y) \right| > \left| f(x,y)-f_n(x,y) \right|$ and $\left| F(u,v)-F_n(u,v) \right| > \left| F(u,v)-H_n(u,v) \right|$ that result from spatial limiting and frequency range restoration, respectively.

One possible iteration stopping criteria for the algorithm is

$$E_n = \int\!\!\int_{-\infty}^{\infty} \left| f_n(x,y)-f_{n-1}(x,y) \right|^2 du\, dv < \delta \;, \tag{63}$$

where δ is an acceptably small mean square error between iterations.

As shown in [Gerch74], the spectrum extrapolated by the GP algorithm has a resolution that is severely limited by the accuracy with which the known frequency range is known but doesn't seem to be very sensitive to noise.

In what follows, the GP algorithm will be used to extrapolate the simulated scattered wave data generated by the scanning apparatus described in chapter three section three.

In the actual digital implementation of extrapolation the use of the FFT does present the difficulty of having to deal with a simultaneously spatially-limited and band-limited function. Of course, the idea of having a spatially-limited object implies that the spectrum must be infinite in extent. By limiting the function's spectrum, the analytic nature of the spectrum is lost, but with the assumption that the function's spectrum is negligible outside the band-limited region, the analyticity of the spectrum is retained.

The one dimensional slices of the object's two dimensional Fourier transform obtained from the transducer's broad band measurements, have been processed by the GP technique with surprising results. Note that the simulated cylinder has a 2λ radius and that the region of support function, P(x), that is used has the value 1 for $|x| \leq 2\lambda$ and 0 elsewhere. Figures (43) and (44) present the extrapolated slices of the real part of the frequency domain obtained for both of the cylinders that were reconstructed previously. Figure (43a) is the slice of the cylinder of 1.01 refractive index after 150 iterations and (43b) is the result after 250 iterations of the GP algorithm. Likewise, figure (44) presents slices of the cylinder having a 1.1 refractive index. It is interesting to note how well the previously unknown frequency range, $-2k_{o_L} < v < 2k_{o_L}$ has been estimated.

The number of iterations of GP that are required is quite high but remember that very little information within the object's region of support was provided by the initial frequency domain coverage. As a result, more iterations were required.

In figure (15), it is obvious that the simulated slice deviates from the exact slice and yet extrapolation still provides an improved approximation to the exact slice which is plotted in figure (44). It is disturbing to see that the additional 100 iterations used to obtain (44b) did not improve the data noticeably. In subsequent sections new and improved extrapolations will be provided for both the 1.01 and the 1.1 refractive index cylinders.

At first glance the use of the GP technique seems impressive *but beware that the technique will not help at all if it is initially provided with inaccurate data.* This would imply that the fundamental limiting factor to the accuracy of the reconstructions obtained with the approach to diffraction tomography described in this chapter, is the Born approximation. If the Born approximation does not hold, the inaccurately known frequency range will be extrapolated by the GP technique into something that remains inaccurate.

The newly extrapolated slices in figures (43) and (44), when used to fill up the two dimensional frequency domain, yield the reconstructions whose real parts are presented in figures (45) and (46). The center slices of each reconstruction appear as solid lines and the true center slices appear as dashed lines in part (b) of each figure. The center slice plots aid in providing a feel for the accuracy of the amplitudes of the reconstructions. Note that these reconstructions are improved in magnitude and in shape over the reconstructions obtained without the use of extrapolation. This is of course due to the more accurate estimation of the low spatial frequencies. The reader familiar with this research might note that the extrapolated reconstructions are inferior

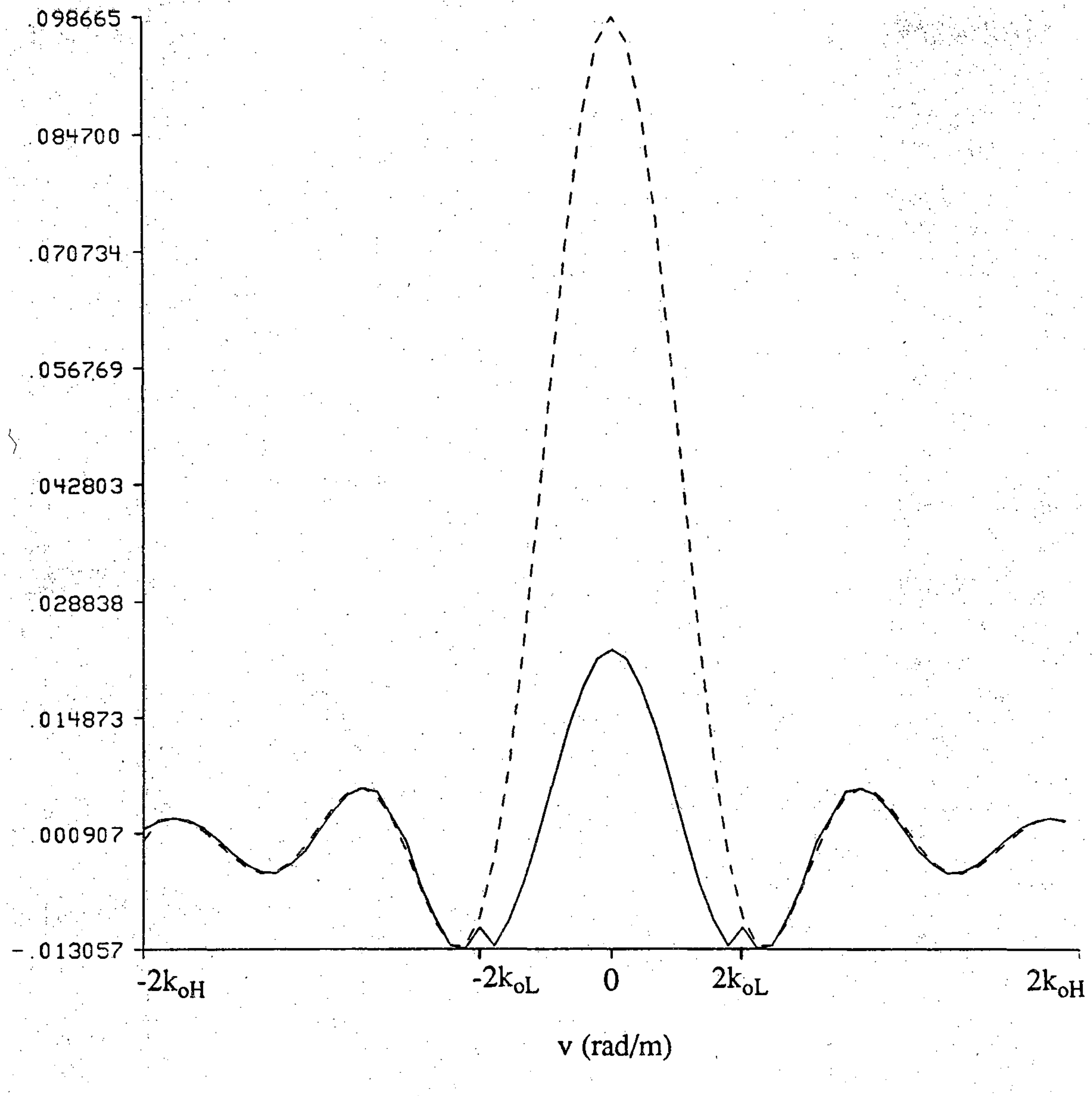

(a)

Figure (43) The result of the GP algorithm applied to the frequency domain slices in figure (14): (a) 150 iterations of the GP algorithm; (b) 250 iterations of the GP algorithm.

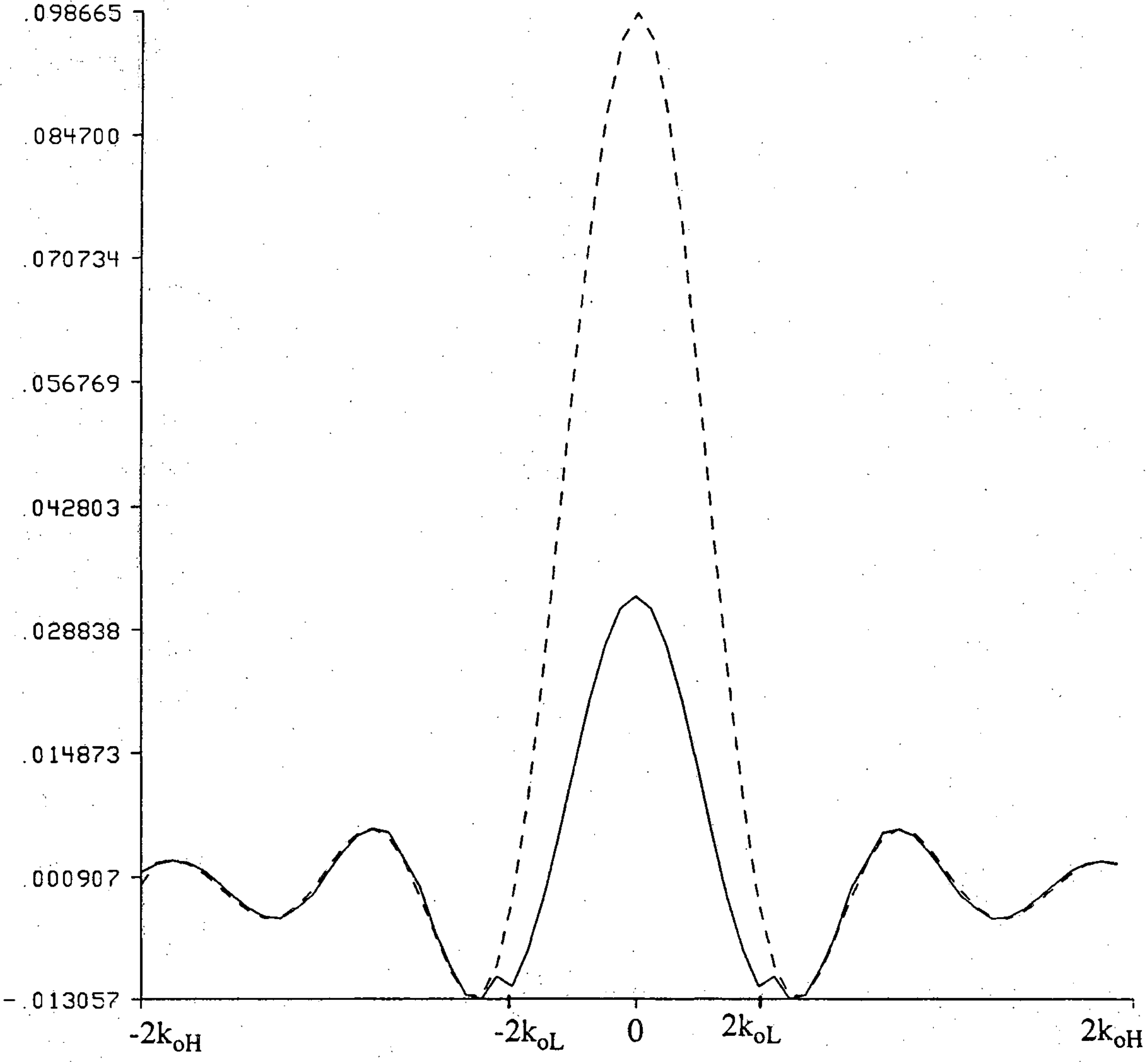

(b)

Figure (43), continued.

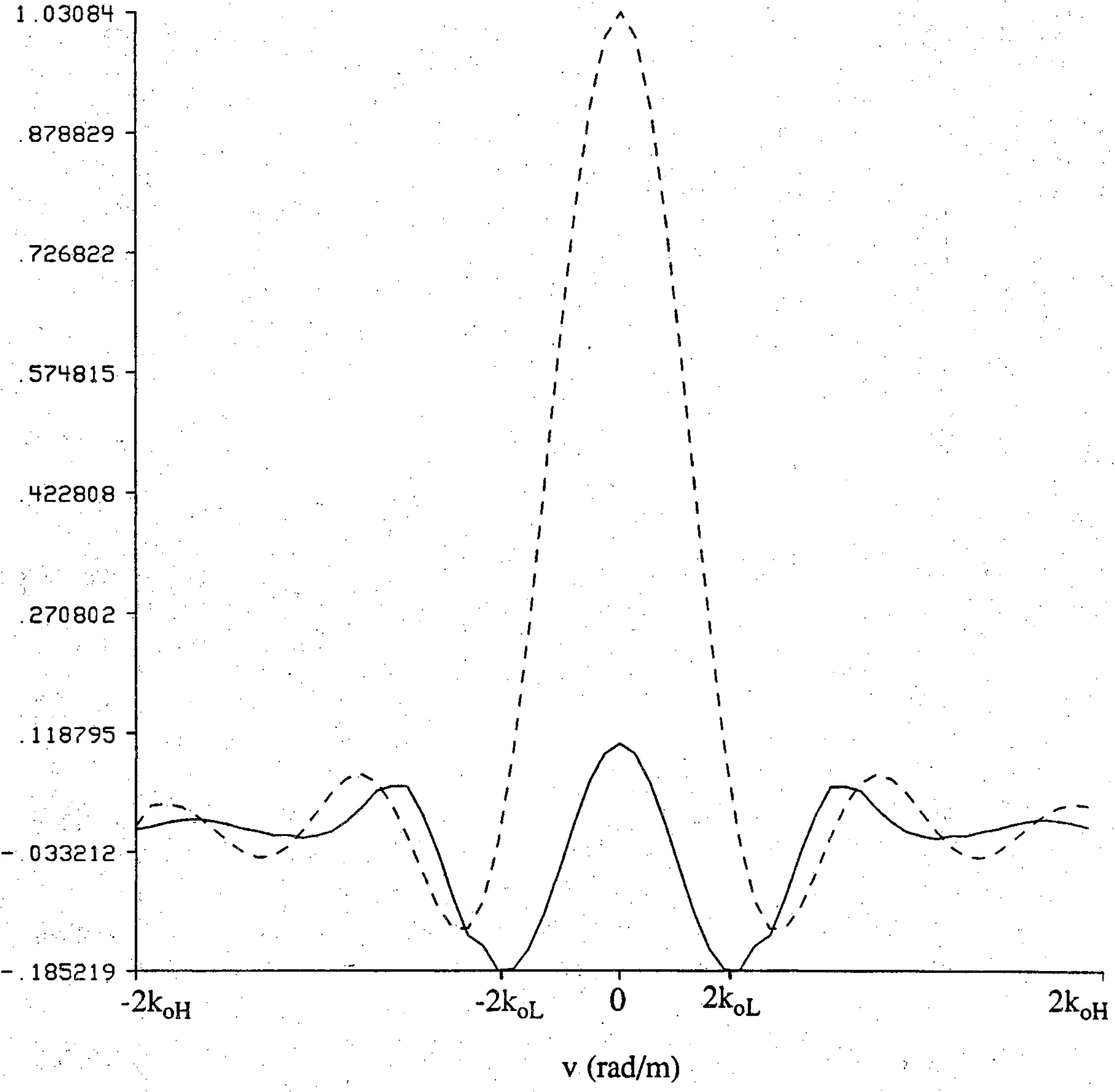

(a)

Figure (44) The result of the GP algorithm applied to the frequency domain slices in figure (15): (a) 150 iterations of the GP algorithm; (b) 250 iterations of the GP algorithm.

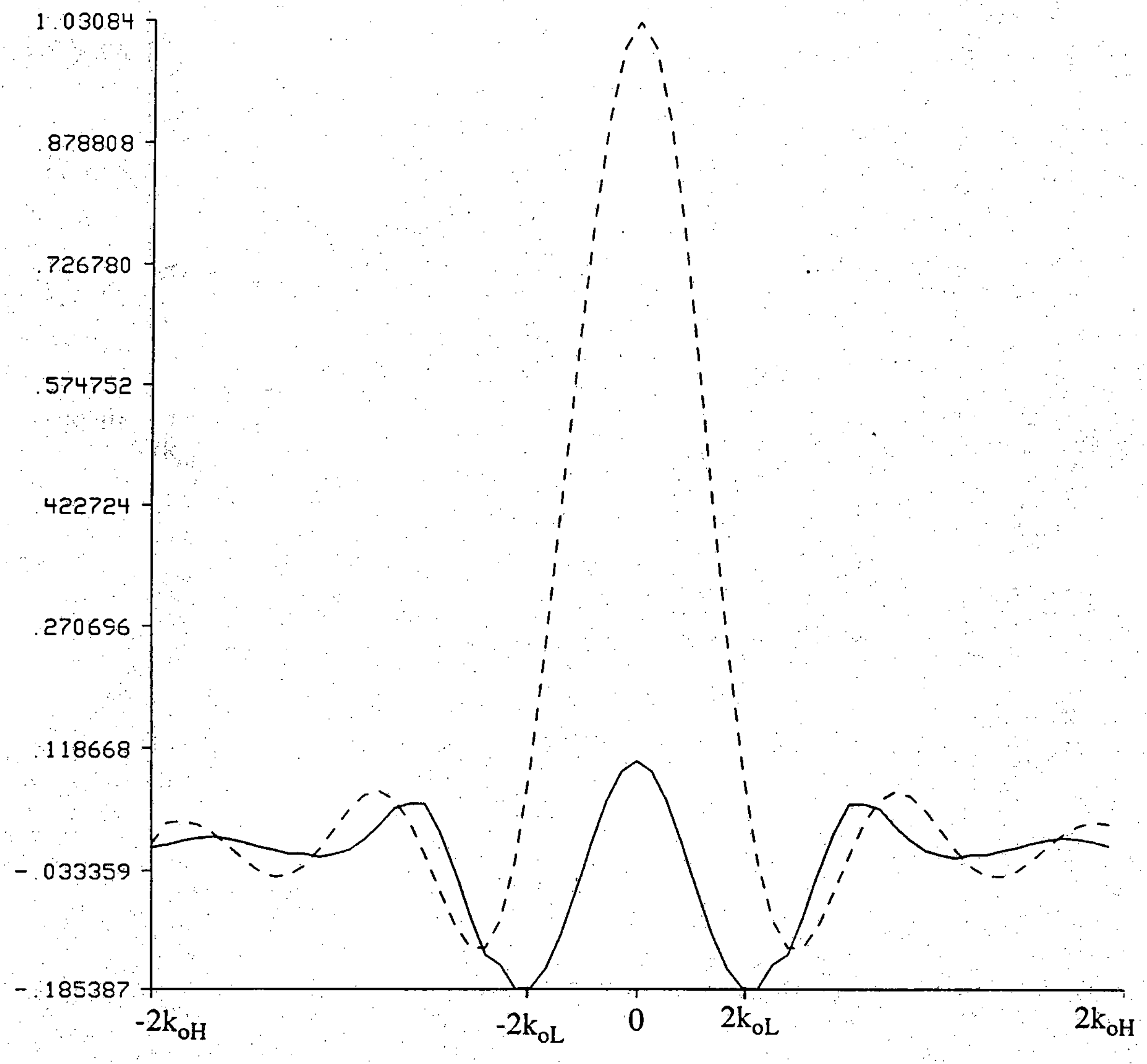

(b)

Figure (44), continued.

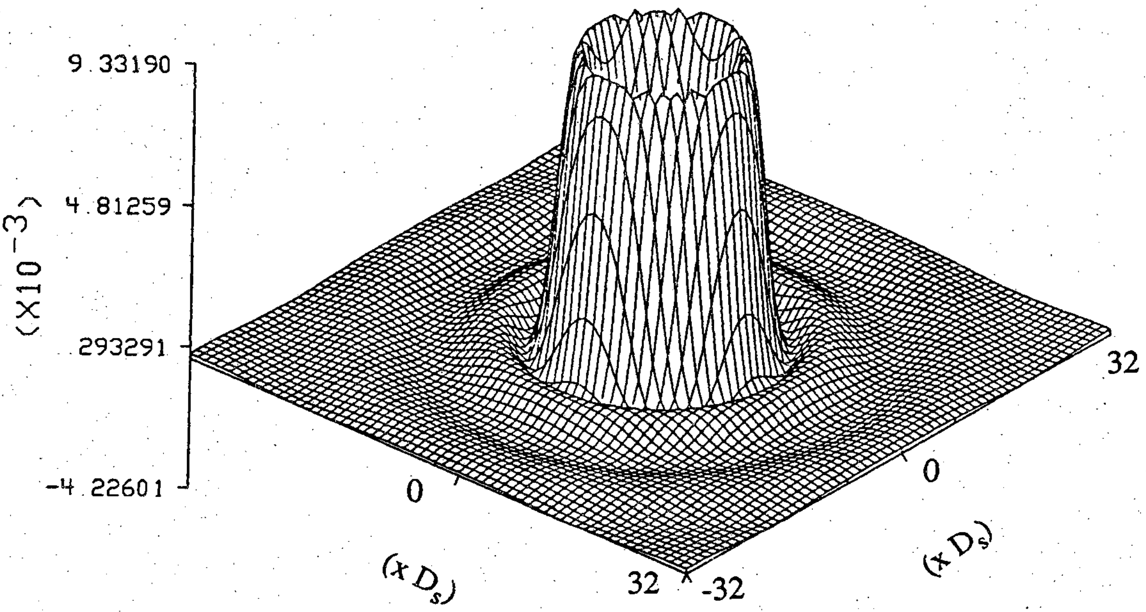

(a)

Figure (45) The real part of the cross section obtained with the use of GP enhanced frequency slice in figure (43) is plotted in (a). The solid line in (b) is the center slice of the reconstruction plotted along with the dashed line which is the true center slice.

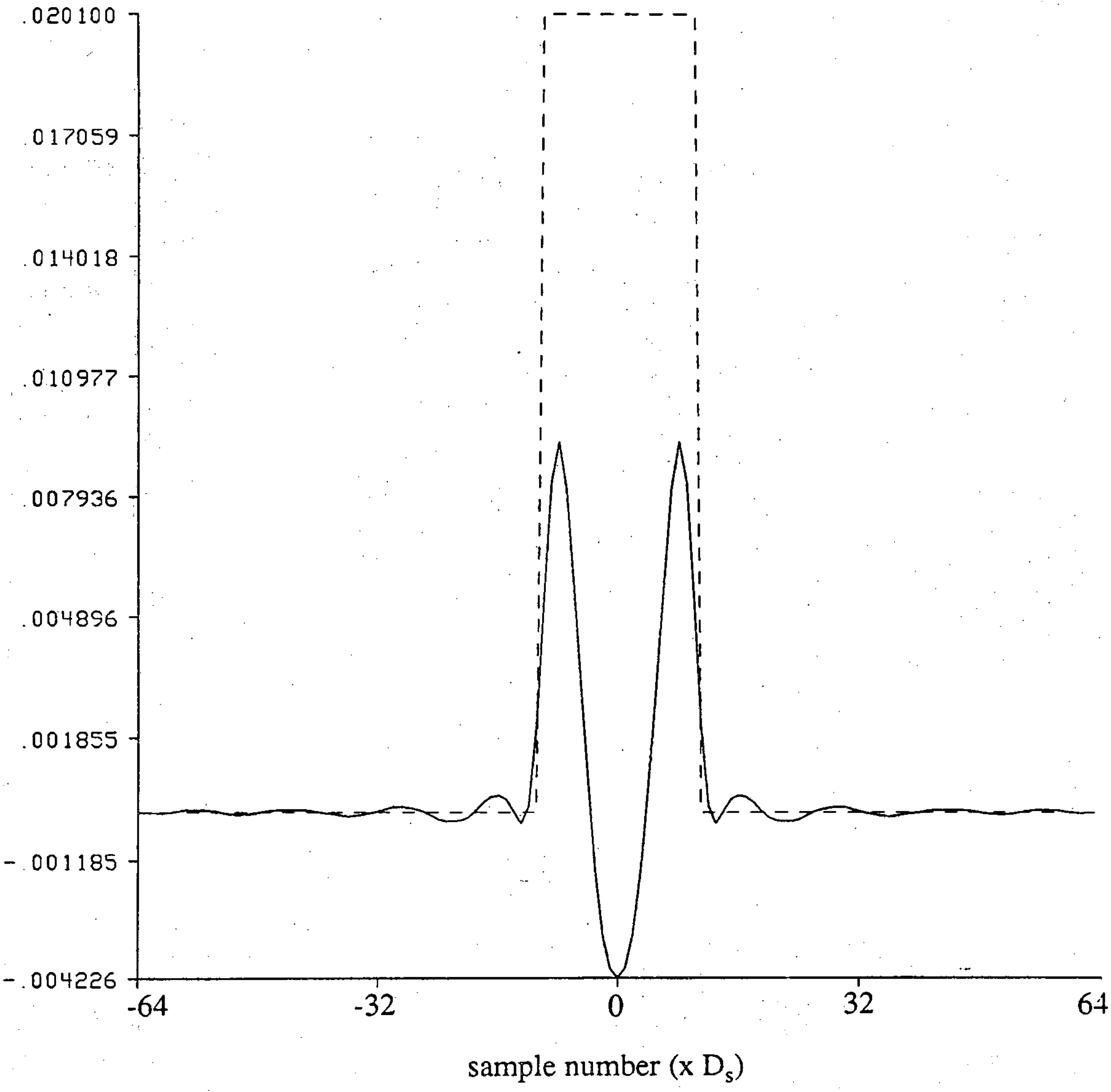

(b)

Figure (45), continued.

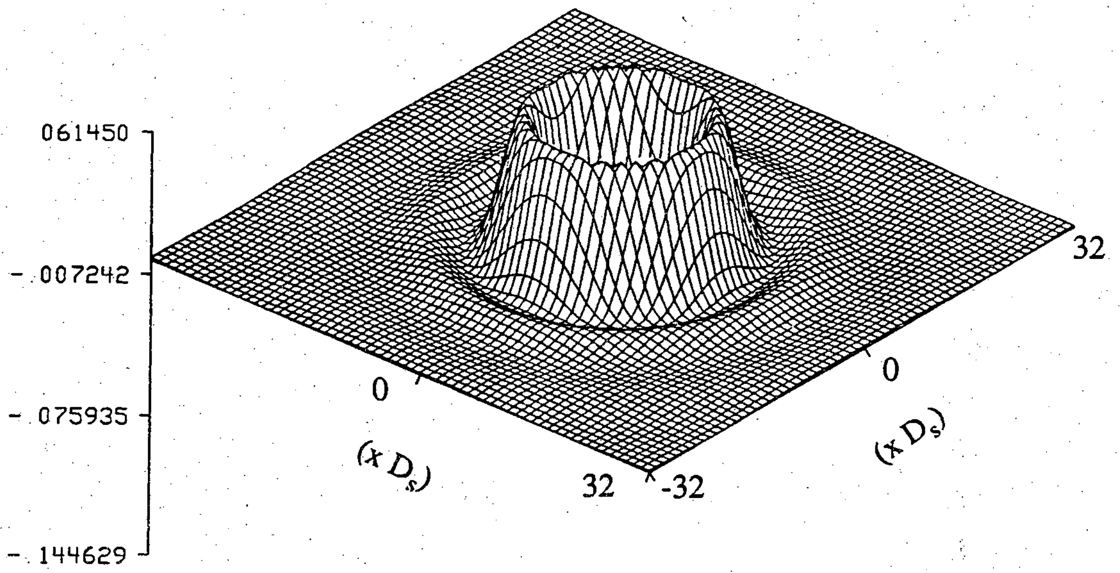

(a)

Figure (46) The real part of the reconstruction obtained with the use of GP enhanced frequency slice in figure (44) is plotted in (a). The solid line in (b) is the center slice of the reconstruction plotted along with the dashed line which is the true center slice.

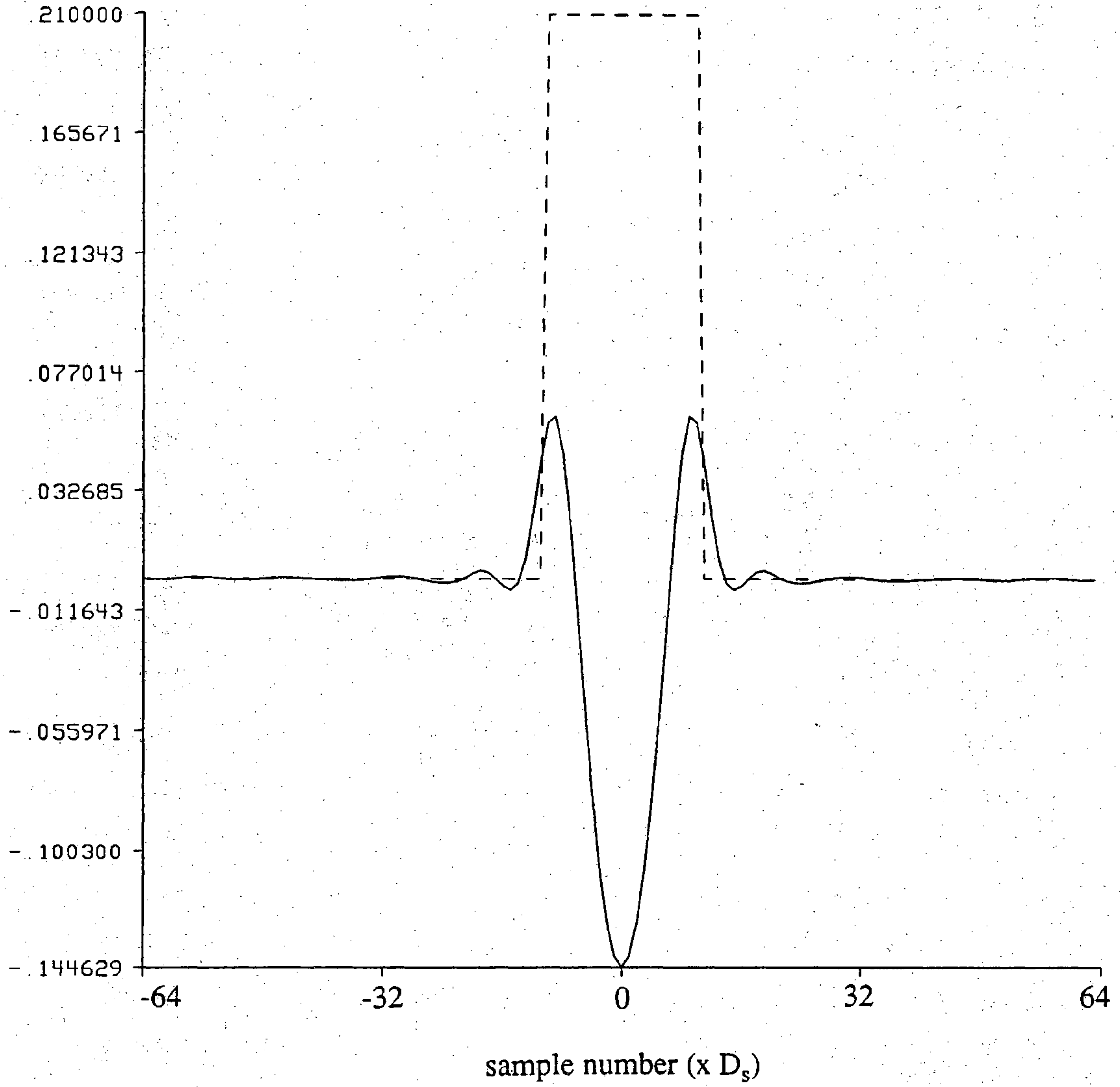

(b)

Figure (46), continued.

to the reconstructions of a cylinder of smaller radius which were presented in the preliminary document.

For the purpose of comparison, an array of reconstructions generated by each of the methods of extrapolation that are presented in this chapter is included at the end of the chapter.

4.2 A Noniterative Extrapolation Algorithm

In this section we will discuss a *noniterative* formulation of spectral extrapolation. Many authors have contemplated combining all of the projection operators, P_i, into one composite operator $T = P_1 P_2 P_3 \cdots P_n$ [Youla82]. Unfortunately the composite operator is of no benefit unless the projection operators are linear such that T will have the same effect as each of the operators applied individually.

The simple discrete Fourier transform operations that we are concerned with are

$$x(k) = \frac{1}{N} \sum_{n=0}^{N-1} X(n)\, W_N^{-nk}$$

$$X(n) = \sum_{k=0}^{N-1} x(k)\, W_N^{nk} \tag{64}$$

$$W = e^{-j\frac{2\pi}{N}}$$

which can be formulated conveniently as matrix-vector multiplications, [Ersoy]

$$\vec{X} = [F]\,\vec{x} \quad \vec{x} = [R]\,\vec{X}\ .$$

Fortunately within the GP algorithm, every term within the matrices [F] and [R] need not be calculated. This is pointed out with the aid of figures (14) and (47). In figure (14) the solid line is the plot of a slice of the known spatial frequency range and the dashed line is the true spectrum. Most importantly one should notice the portion of the solid line that has a solid zero value. That portion is the unknown low frequency range and it is only this range of the vector $\vec{X}$ that needs to be calculated during the iterative spectral extrapolation. Hence

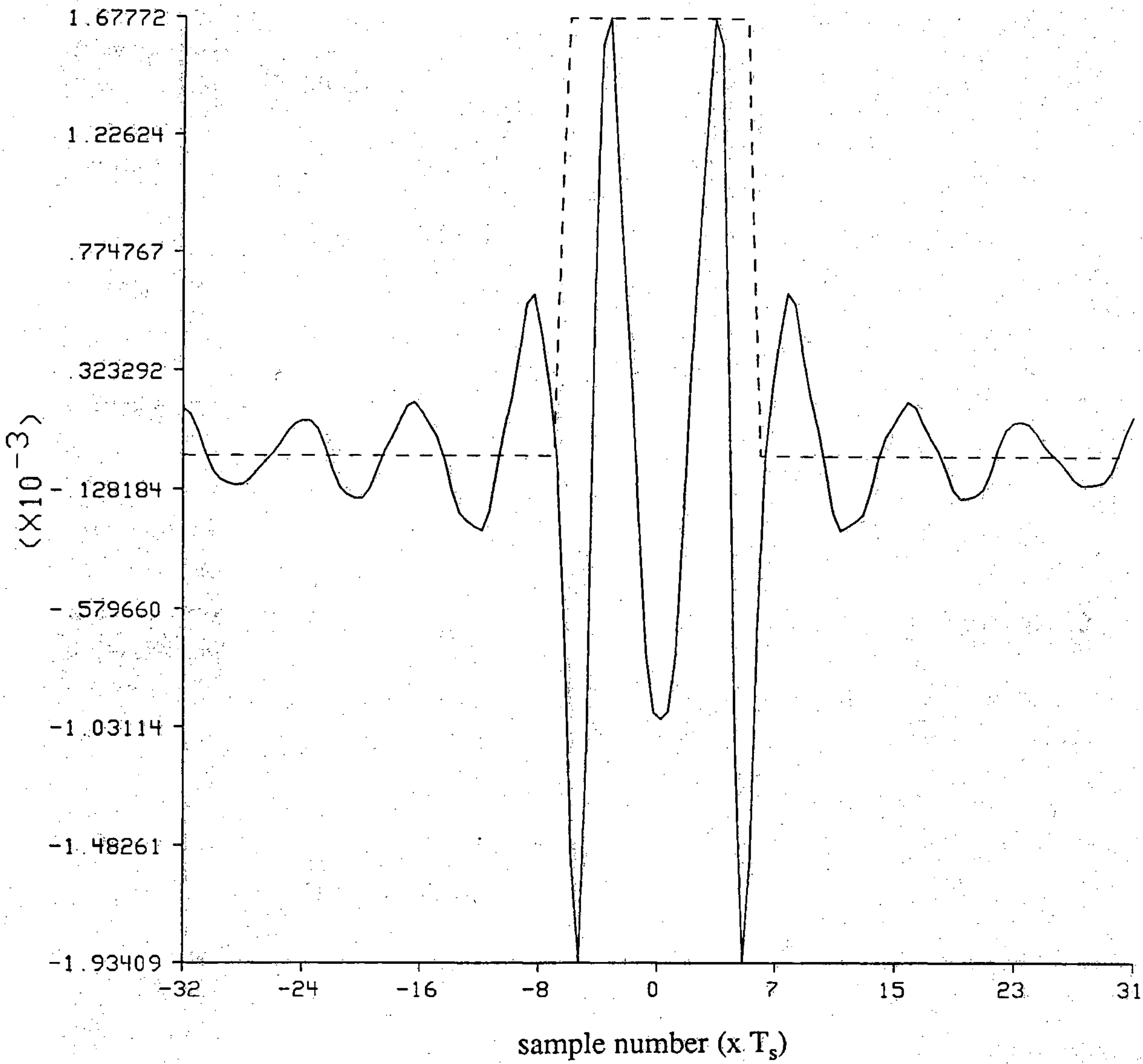

Figure (47) The inverse transform of the Fourier domain slice in figure (14) (the solid line) along with the region of support for the object (the dashed line).

$$[F_1] = \begin{bmatrix} 1 & \cdots\ \cdots & 1 & \cdots\ \cdots & 1 \\ \vdots & \cdots\ \cdots & \vdots & \cdots\ \cdots & \vdots \\ 1 & \cdots\ \cdots & W^{pk} & \cdots\ \cdots & W^{p(N-1)} \\ 0 & \cdots\ \cdots & 0 & \cdots\ \cdots & 0 \\ \vdots & \cdots\ \cdots & \vdots & \cdots\ \cdots & \vdots \\ 0 & \cdots\ \cdots & 0 & \cdots\ \cdots & 0 \\ 1 & \cdots\ \cdots & W^{(N-p)k} & \cdots\ \cdots & W^{(N-p)(N-1)} \\ \vdots & \cdots\ \cdots & \vdots & \cdots\ \cdots & \vdots \\ 1 & \cdots\ \cdots & W^{(N-1)k} & \cdots\ \cdots & W^{(N-1)(N-1)} \end{bmatrix} \tag{65}$$

The value of the index p, is determined by the bandwidth of the transducer used to obtain the frequency domain slices. Hence p can be exactly obtained for each type of transducer that would be used in the scanning apparatus.

In a similar manner we only need to use a sparse amount of the matrix [R] because in the spatial domain the region of support truncation will set to zero all values of x(k) outside of the range $g < k < N-g$. The dashed line in figure (47) is the region of support and the solid line is the inverse transform of the frequency domain slice in figure (14). Hence

$$[R_1] = \frac{1}{N} \begin{bmatrix} 1 & \cdots\ \cdots & 1 & \cdots\ \cdots & 1 \\ \vdots & \cdots\ \cdots & \vdots & \cdots\ \cdots & \vdots \\ 1 & \cdots\ \cdots & W^{-gk} & \cdots\ \cdots & W^{-g(N-1)} \\ 0 & \cdots\ \cdots & 0 & \cdots\ \cdots & 0 \\ \vdots & \cdots\ \cdots & \vdots & \cdots\ \cdots & \vdots \\ 0 & \cdots\ \cdots & 0 & \cdots\ \cdots & 0 \\ 1 & \cdots\ \cdots & W^{-(N-g)k} & \cdots\ \cdots & W^{-(N-g)(N-1)} \\ \vdots & \cdots\ \cdots & \vdots & \cdots\ \cdots & \vdots \\ 1 & \cdots\ \cdots & W^{-(N-1)k} & \cdots\ \cdots & W^{-(N-1)(N-1)} \end{bmatrix} \tag{66}$$

The maximum value of g is determined by the size of the largest object that will be imaged. Of course the size of the plane wave transducer as well as the limitations of the Born approximation, determine the largest object that can be imaged. Therefore to be conservative, the maximum value of g can be calculated and used to determine the $[R_1]$ matrix.

In the GP algorithm the first step is to inverse transform $\vec{X}$ and carry out the region of support truncation which can now be described as follows

$$\vec{x}_1 = [R_1]\,\vec{X}\ .$$

Step two is the transformation of $\vec{x}_1$ back into the frequency space and the restoration of the known frequency range. This is all accomplished by the following

$$\vec{X}_1 = [F_1]\,\vec{x}_1 + \vec{X} = [F_1]\,[R_1]\,\vec{X} + \vec{X}\ .$$

The vector $\vec{X}_1$ is the result of the first iteration of the algorithm. The result of the second iteration is described by

$$\vec{X}_2 = [P]\,\vec{X}_1 + \vec{X} = [P]^2\,\vec{X} + [P]\,\vec{X} + \vec{X}$$

where [P] is the matrix product $[F_1]\,[R_1]$.

The notable result of this formulation of the problem is the fact that n iterations of GP can be carried out by a single matrix-vector multiplication.

$$\vec{X}_n = [G]\,\vec{X} \qquad [G] = \sum_{k=0}^{n} [P]^k \tag{67}$$

The only difficulty encountered involves the calculation of the matrix [G]. This calculation could be quite time consuming although the matrix need only be calculated once for each combination of transducer and object size that is encountered in the lab.

The technique described above for turning GP spectral extrapolation into a noniterative algorithm, is not unique to this text. In fact Sabri and Steenaart [Sabri78] and Schafer et. al. [Schaf81] discuss the combination of general linear operators in a similar manner. In addition Cadzow [Cadzo79] has described a single step extrapolation procedure that involves solving a Fredholm integral equation of the first kind.

In [Sabri78] the geometric series in (67) is replaced with the equivalent expression

$$[G] = \left([I] - [P]^{n+1} \right) \left([I] - [P] \right)^{-1} \tag{68}$$

where [I] is the identity matrix. Calculating [G] in (68) would not be advantageous in our case. The additional matrix multiplication and subsequent matrix inversion necessary to calculate [G], would be more expensive than the approach that we have taken to calculate [G] by the method in (67). In our computer implementation, the following algorithm has been implemented on an FPS120 array processor

```
float G[m][n], T[m][n], F[m][n],   /* matrices */
      I[m][n];          /* the complex identity matrix */
int N;       /* number of iterations */

G = P;
T = P;
for(i=0;i< N-1 ;i++){
     F = G * T;
     G = F + T;
}
G = G + I;
```

A plot of the matrix [G] corresponding to 200 iterations of GP is provided in figure

(48). The matrix was constructed for a region of support having a radius of slightly greater than 2λ, and a transducer of center frequency 5 MHz and bandwidth 6 MHz just as in the preceding chapter. The diagonal ridge in the matrix is the result of the final addition of the identity matrix. The dashed lines in figure (49a) and (49b) are the true Fourier space slices obtained from backscattered wave measurements from the 1.01 and 1.1 refractive index cylinders respectively. The solid lines are the extrapolated versions of the dashed lines. These noniterative extrapolated slices are greatly improved over the iterative extrapolations in figures (43) and (44).

It is very interesting to examine the limit of [G] as the number of iterations, n, goes to infinity. This limit of (68) can be expressed in closed form if the norm of the matrix [P] is less than one,

$$[G] = \lim_{n\to\infty} \left([I]-[P]^{n+1}\right)\left([I]-[P]\right)^{-1} = \left([I]-[P]\right)^{-1} .$$

The norm of a matrix is defined to be the square root of the largest eigenvalue of $([P]^T[P])$. The norm measures the largest amount by which any vector is amplified by matrix multiplication [Stran80]. Essentially the magnitude of the largest eigenvalue of [P] must be less than one. The sufficiency of this condition is easily proven by examining the diagonalized version of [P]

$$[P] = [S]^{-1}[\lambda][S]$$

where [S] is a matrix whose columns are linearly independent eigenvectors and $[\lambda]$ is a diagonal matrix whose elements are eigenvalues. If indeed the eigenvalues of [P] all have a magnitude less than one, then

$$[G]^{\infty} = \lim_{n\to\infty} \sum_{k=0}^{n} [P]^k = \lim_{n\to\infty} \sum_{k=0}^{n} [S]^{-1}[\lambda]^k[S] = 0$$

Using the same simulated conditions as used for figure (48), figure (50) is a plot of the matrix $([I]-[P])^{-1}$. The matrix [P] is plotted in figure (51). The extrapolated slices obtained with the use of $[G]^{\infty}$ are the solid lines in figure (52). In (a) the slices pertain to the 1.01 refractive index cylinder and in (b) they pertain to the 1.1 refractive index cylinder. It is unsettling to observe that the dashed lines in figure (52), which are the true Fourier space slices, are much smaller than the extrapolated slices although the extrapolated slices are much smoother than that obtained with the matrix in figure (48).

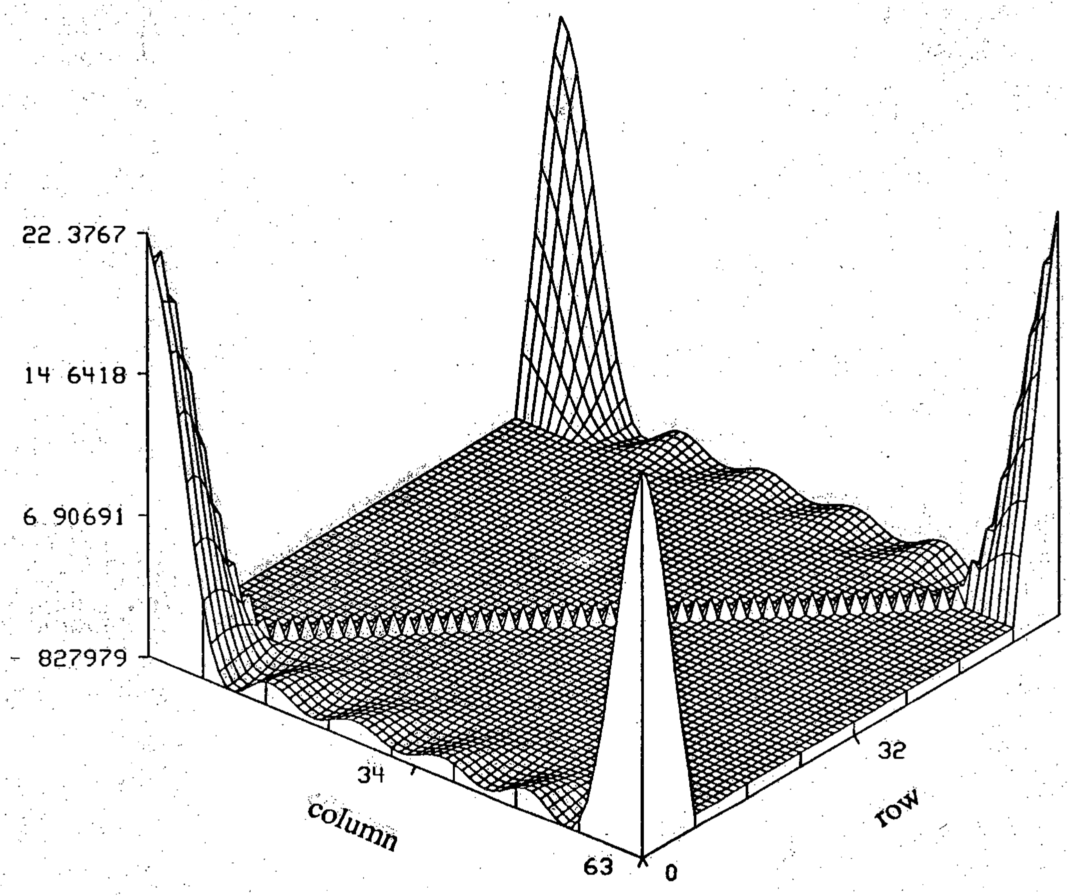

Figure (48) A plot of the GP extrapolation matrix corresponding to 200 iterations for an object of radius ≤ 2λ and with a transducer having the same bandwidth as the rest of the simulations.

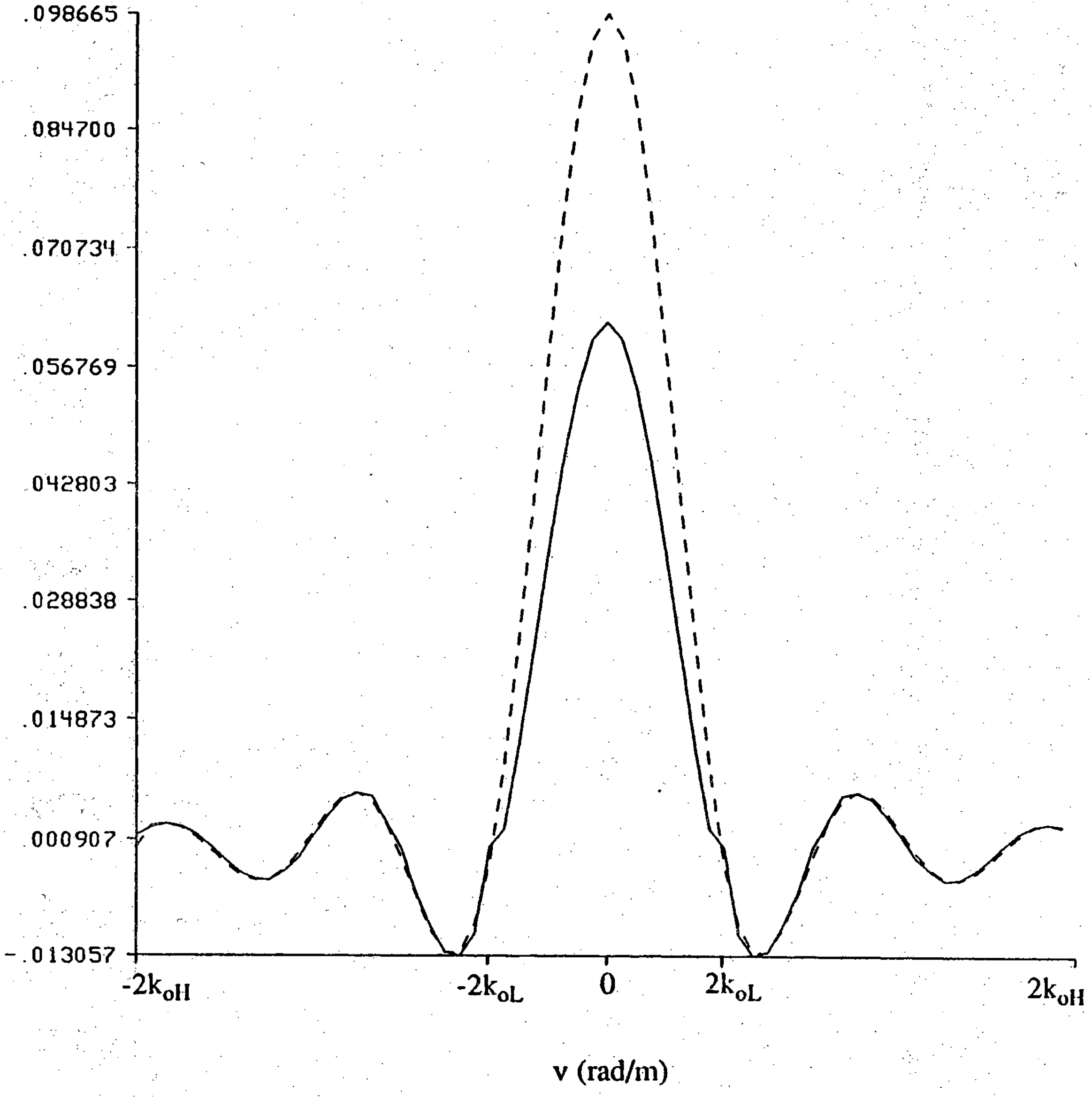

(a)

Figure (49) The extrapolated version of the Fourier space data plotted in figure (14) which corresponds to a 1.01 refractive index cylinder having a radius of 2λ is plotted in (a). The extrapolation is carried out by multiplying the data vector by the extrapolation matrix in figure (48). In (b) the extrapolated version of the Fourier space data plotted in figure (15) which corresponds to a 1.1 refractive index cylinder having a radius of 2λ, is plotted.

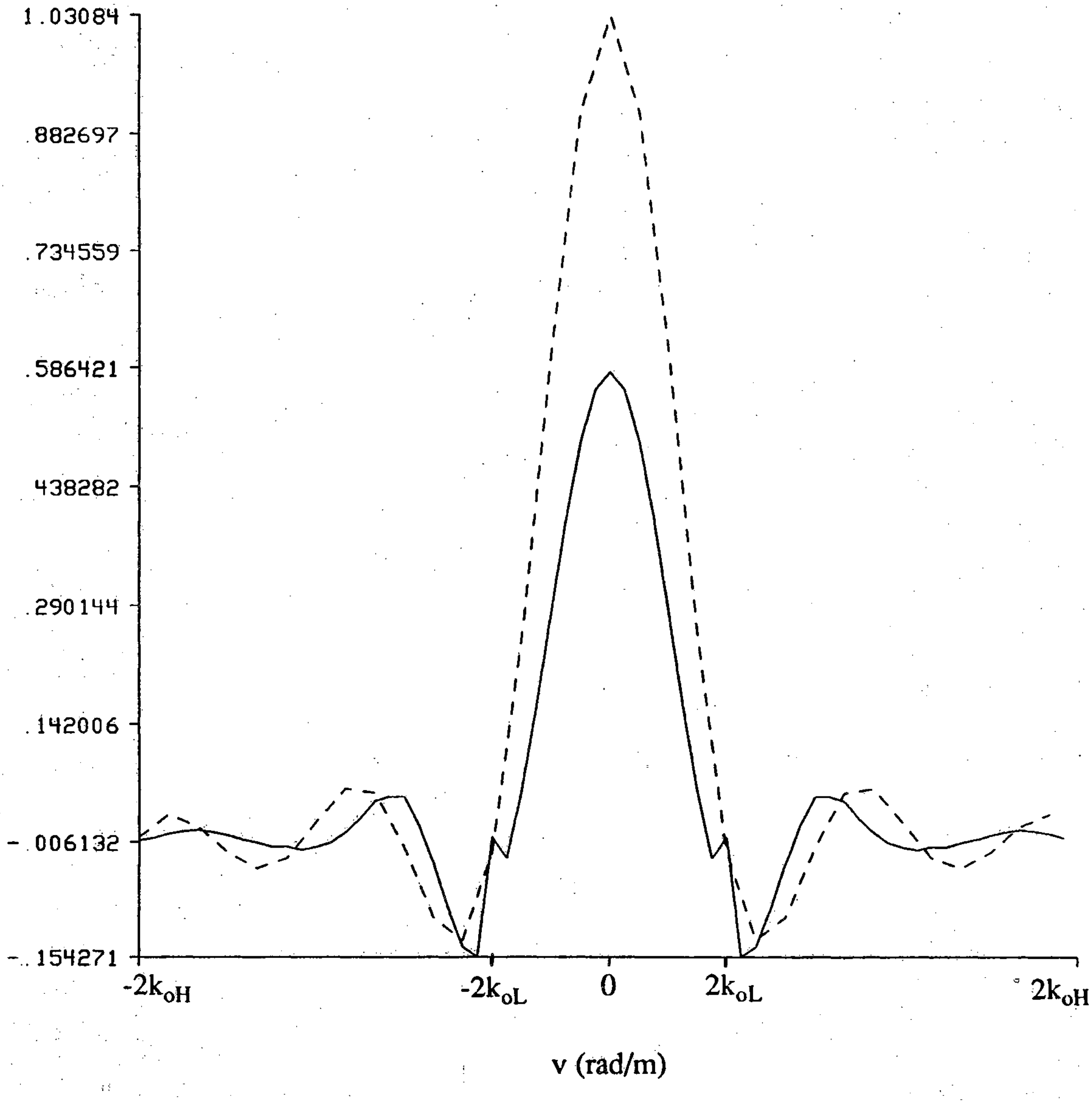

(b)

Figure (49), continued.

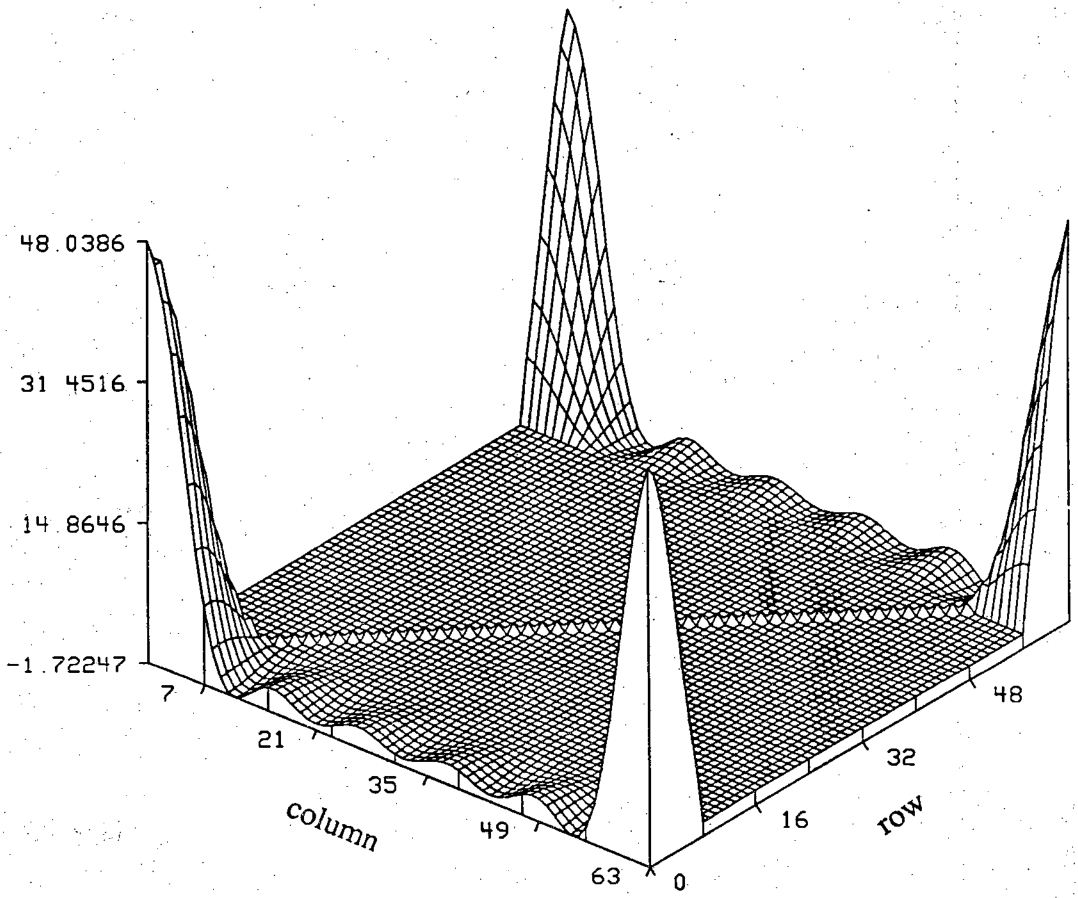

Figure (50) The extrapolation matrix $([I]-[P])^{-1}$ which corresponds to an infinite number of GP iterations.

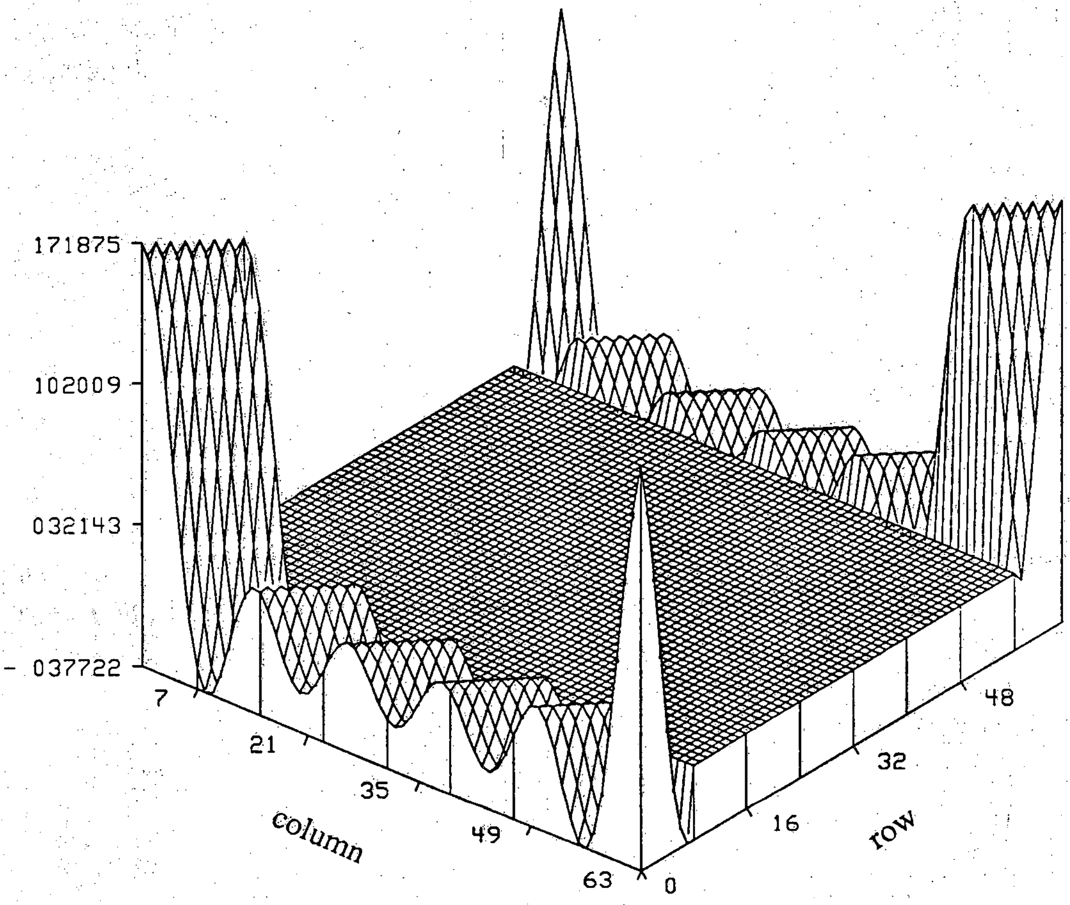

Figure (51) The matrix [P] which is the product of $[R_1]$ and $[F_1]$ for the simulated transducer and an object radius $\leq 2\lambda$.

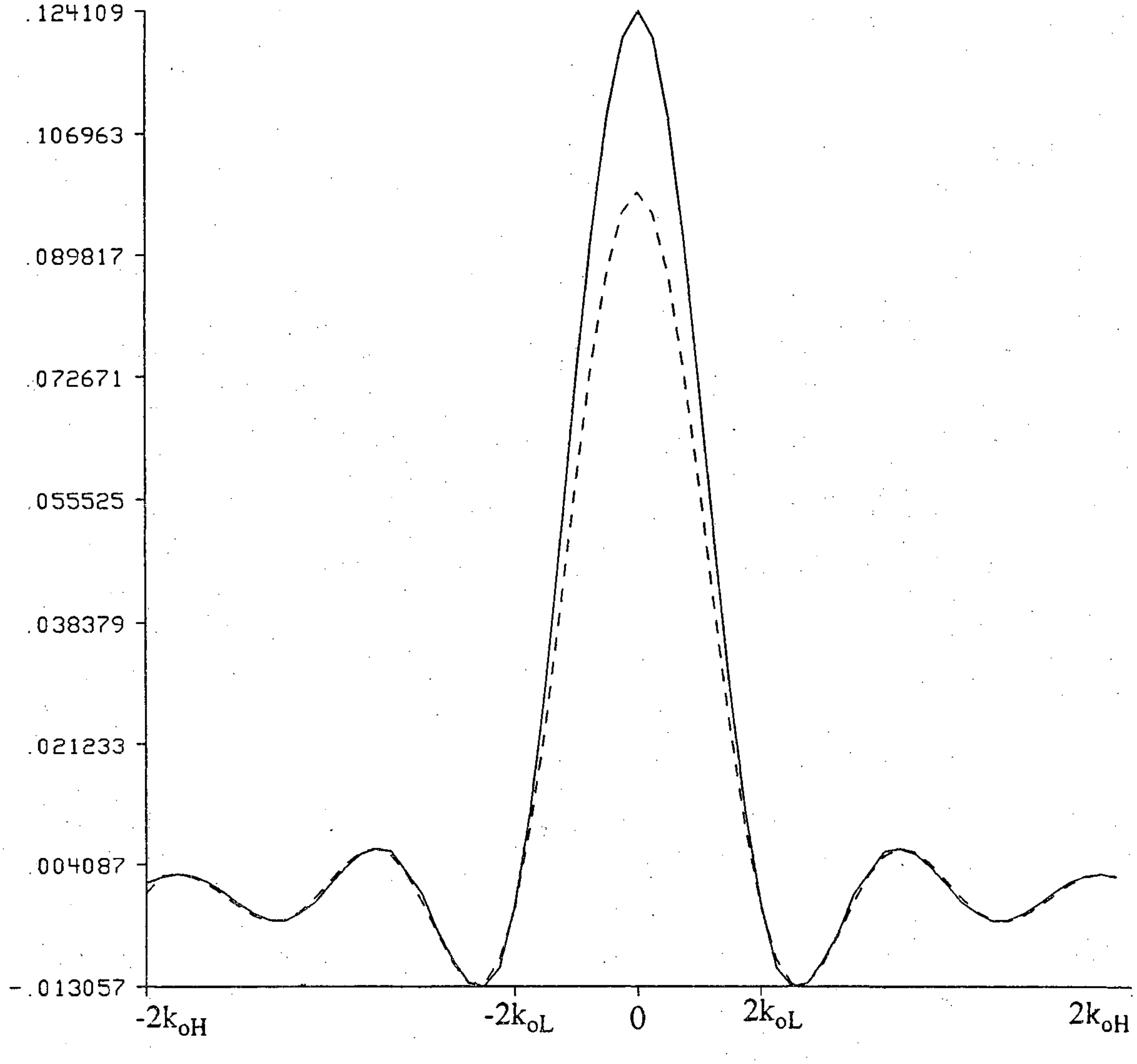

(a)

Figure (52) The extrapolated versions of the Fourier space data obtained with the matrix $([I]-[P])^{-1}$ corresponding to: (a) the data in figure (14); (b) the data in figure (15).

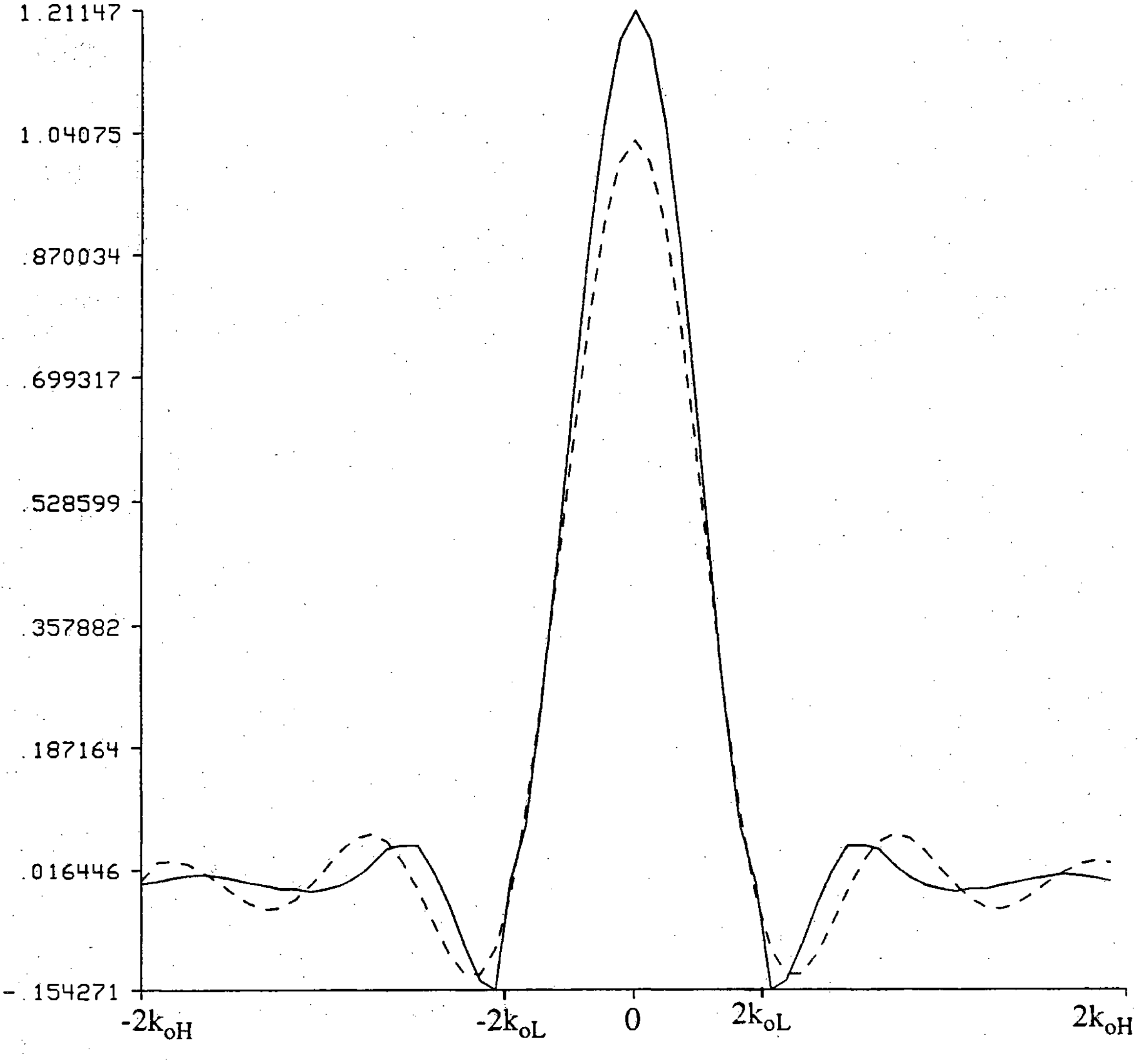

(b)

Figure (52), continued.

4.3 The Noniterative Extrapolation Algorithm Extended to 2-D

The same matrix formulation of GP can be applied to two dimensional functions that have limited frequency domain information and a finite region of support in the spatial domain. To begin the section the 2-D problem will be examined within a two dimensional framework and secondly the problem will be reduced into a 1-D problem.

4.3.1 Two Dimensional Formulation

The 2-D discrete Fourier transform relationships are

$$x(m,n) = \frac{1}{MN} \sum_{u=0}^{M-1} \sum_{v=0}^{N-1} X(u,v)\, W_M^{-um}\, W_N^{-vn}$$

$$X(u,v) = \sum_{m=0}^{M-1} \left[\sum_{n=0}^{N-1} x(m,n)\, W_M^{um} \right] W_N^{vn} \tag{69}$$

The previous equation illustrates the separability of the Fourier transform. The term in the brackets is the DFT of the n'th row of [x]. In matrix form the DFT relationships are written as [Rosen82]

$$x(m,n) = \sum_{u=0}^{M-1} \sum_{v=0}^{N-1} \left[e^{j2\pi nv/N} \right] \frac{1}{N}\, X(u,v) \left[e^{j2\pi mu/M} \right] \frac{1}{M} \tag{70}$$

$$[x] = [R][X][T] \qquad [X] = [Q][x][S]$$

where [Q] is an NxN matrix whose (n,v)'th element is $e^{-j2\pi nv/N}$ and $[R] = \frac{1}{N}[Q]^*$. Likewise [S] is an MxM matrix whose (u,m)'th element is $e^{-j2\pi mu/M}$ and $[T] = \frac{1}{M}[S]^*$. If the image is square, matrix [T] will equal [R] and [Q] will equal [S].

The region of support for the image is illustrated by the shaded region in figure (53). Given this region it becomes evident that not all of the of elements within the matrices [R] and [T], must be known. Considering that only the rows of [x] falling into the ranges of 0 to α and N$-\alpha$ to N$-$1 need to be calculated, only the rows of [R] within the same ranges are needed. Likewise, only the columns of [T] within the range of 0 to β and N$-\beta$ to N$-$1 are needed since only the elements of [x] within this range of columns must be calculated. These new matrices, identified as $[R_1]$ and $[T_1]$, allow the inverse transform of [X] and the region of support truncation to be expressed as

$$[x_1] = [R_1][X][T_1] \quad .$$

When transforming the matrix $[x_1]$ it is only necessary to calculate the zero valued elements of [X] and subsequently add to that result the matrix [X]. Two types

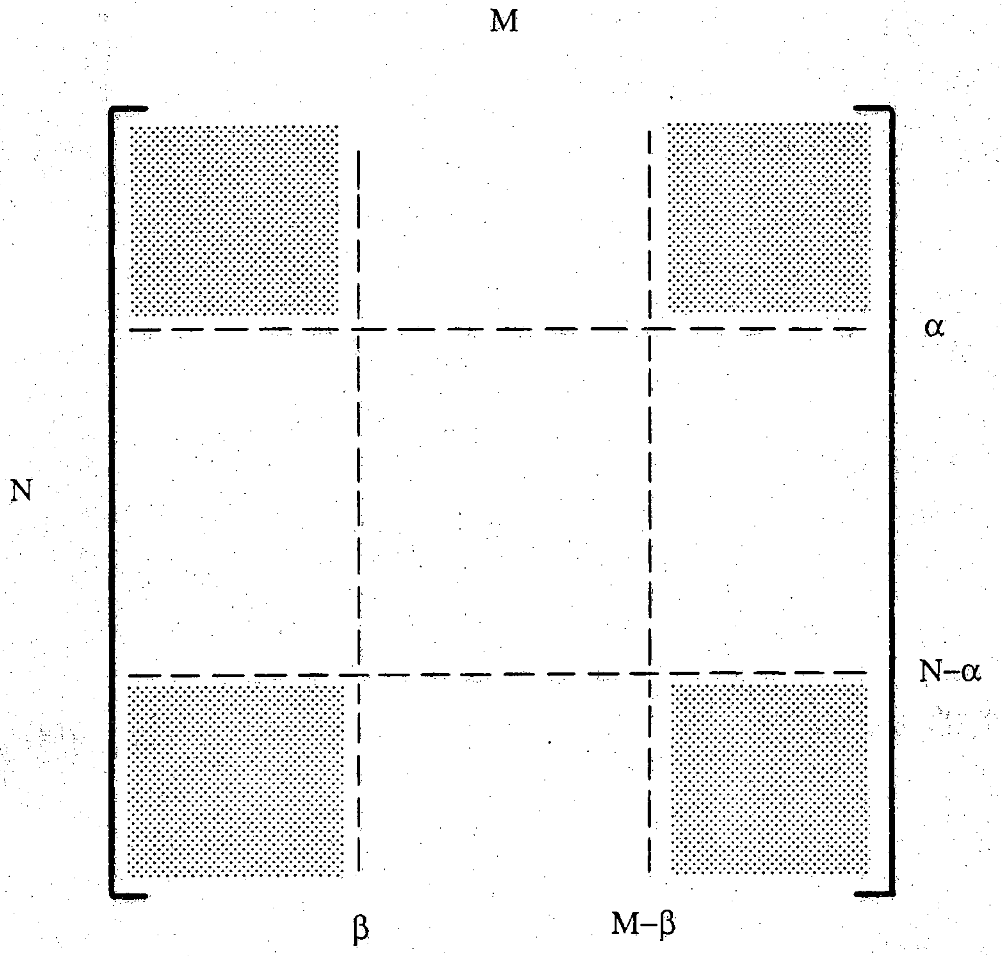

Figure (53) The region of support for the 2-D image is illustrated by the shaded region.

of Fourier domain coverage are of interest and will be discussed here. The first type is a lowpass coverage in which low frequency information is known in advance although high frequency information is missing. In figure (54) the shaded area is the unknown frequency region. Given this unknown frequency region, the operation of transforming the image $[x_1]$ is reduced to

$$[X_1] = [Q_1][x_1][S_1] + [X] \ .$$

The zero portions of the matrices $[Q_1]$,$[S_1]$,$[R_1]$ and $[T_1]$ are indicated in figure (55).

The matrix $[X_1]$ is just the first iteration of the algorithm. In a manner similar to that described in the last subsection, higher order iterations can be obtained by a summation of matrix multiplications,

$$[X_n] = [P_b]^n[X][P_a]^n + [P_b]^{n-1}[X][P_a]^{n-1} + \cdots + [X]$$

$$[P_a] = [T_1][S_1] \qquad [P_b] = [Q_1][R_1] \ .$$

The second type of Fourier domain coverage is a bandpass coverage that is obtainable from backscattered ultrasound measurements made at regular intervals around the object of interest. The resulting unknown frequency region, indicated by the shaded region in figure (56), is unique because the boundaries of the region lie neither along a row nor a column of the matrix.

It is unreasonable to assume that nonshaded regions in figures (54) and (53) will be fully known. In other words, it is unlikely that the region of support and the known frequency range will have a rectangular shape. For example it is more likely that a circular region of the frequency domain, noted with the dashed lines in figure (54), will be known with confidence. The gap outside of the dashed arcs but still within the nonshaded region, presents a problem to this 2-D formulation of GP. To attempt a solution to this problem one could first decrease the values of γ and δ until the gap disappears. Secondly a new operator would have to be introduced that would truncate the part of $[X_1]$ outside of the potentially circular region in which the frequency domain data are known.

$$[x'_1] = O\left\{ [R_1][X][T_1] \right\} + [X] \ .$$

The operator O would simply "and" the matrix product with a mask indicating the elements of the matrix product that should have a nonzero value. Unfortunately this operation will make unfeasible the possibility of precalculating the extrapolation matrix as was done when dealing with 1-D signals.

In summarizing this subsection I believe that it is safe to assume that the matrix formulation does very little to speed up the extrapolation algorithm. In fact for small n it is quite possible that using the FFT algorithm to actually iterate between the Fourier

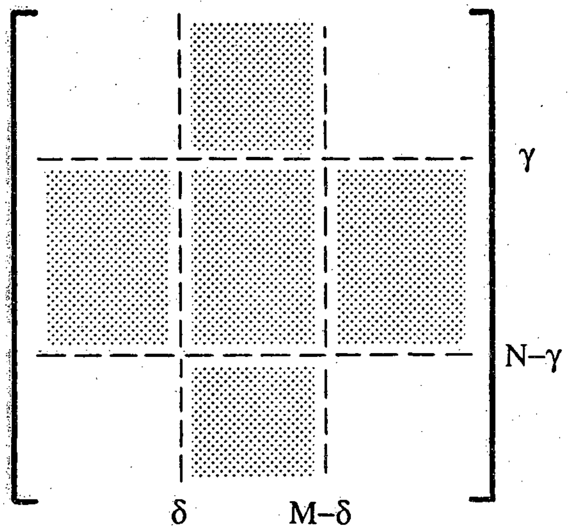

Figure (54) The shaded area is the unknown frequency region.

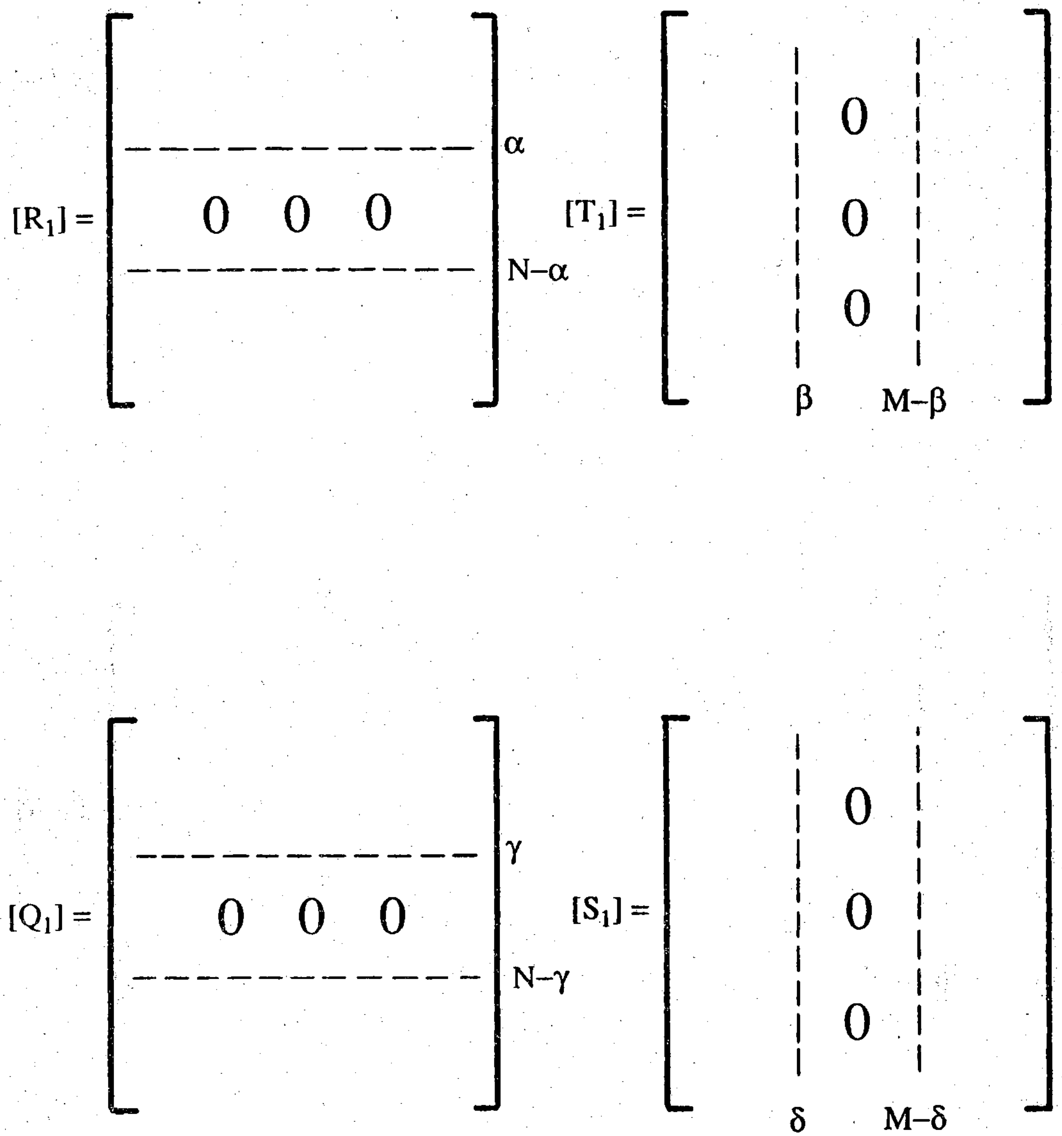

Figure (55) The zero portions of the matrices $[Q_1]$,$[S_1]$,$[R_1]$ and $[T_1]$ are indicated here.

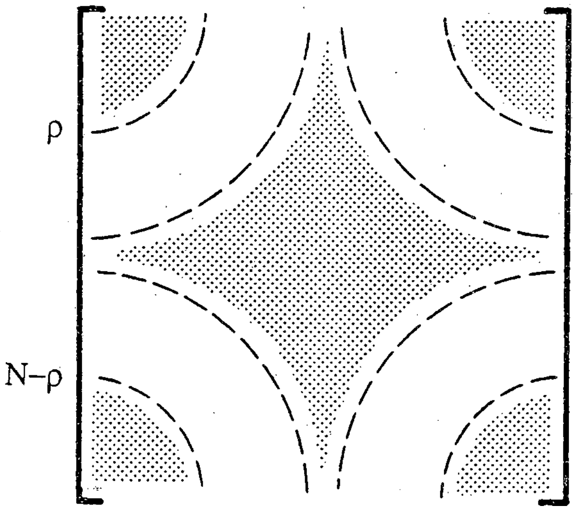

Figure (56) The unknown frequency region that results when an image is known only within a frequency bandpass, is indicated by the shaded region. The boundaries of the region lie neither along a row nor a column of the matrix therefore making noniterative 2-D GP impossible.

and spatial domains, would be quicker that carrying out the matrix multiplications even if the matrices are precalculated.

4.3.2 One Dimensional Formulation

In this subsection it will be shown that the 2-D image extrapolation problem discussed in subsection 4.3.1 can be posed as a 1-D problem. To achieve a 1-D formulation, the discretized 2-D image x(m,n) of dimension (N×M), is expressed as the vector $x'(k)$ of length NM in which the (M+1)'th element is x(0,1).

$$\vec{x}' = [x(0,0), \cdots, x(M-1,0), x(0,1), \cdots, x(M-1,N-2), x(0,N-1), \cdots, x(M-1,N-1)]^T$$

To compute element (u,v) of the Fourier transform of the image, one need only compute the dot product of the vectors $\vec{A}_{u,v}$ and $\vec{x}'$ where

$$A_{u,v}(k) = \exp\left[-j2\pi \left[\frac{u\,(k \bmod M)}{M} + \frac{v\,\lfloor k/M \rfloor}{N} \right] \right]$$

$$X(u,v) = \sum_{m=0}^{M-1} \sum_{n=0}^{N-1} x(m,n)\, e^{-j2\pi\left[um/M + vn/N \right]}$$

The index k used in the last equation is equal to (nM + m).

To construct a transformation matrix one has only to construct a matrix [A] of dimension NM × NM whose rows are the vectors $\vec{A}_{u,v}$. The result of the matrix-vector product, $[A]\,\vec{x}'$, will be the vector $\vec{X}'$ which is the Fourier transform of the image expressed as a vector.

$$\vec{X}' = [X(0,0), \cdots, X(M-1,0), X(0,1), \cdots, X(M-1,N-2), X(0,N-1), \cdots, X(M-1,N-1)]^T$$

$$[A] = \begin{bmatrix} \vec{A}_{0,0} \\ \vdots \\ \vec{A}_{M-1,0} \\ \vec{A}_{0,1} \\ \vdots \\ \vec{A}_{M-1,N-1} \end{bmatrix}$$

Likewise the inverse transform takes the form

$$\vec{x}' = [B]\,\vec{X}', \quad [B] = \frac{1}{MN}\,[A]^* \,.$$

Carrying out the GP iteration becomes quite simple given the above relationships. The starting point, the Fourier domain of the image $\vec{X}'$, must be inverse transformed and the result must be truncated by the region of support. This can all be accomplished in one step with the aid of the diagonal matrix [L].

$$\vec{x}'_1 = [L]\,[B]\,\vec{X}'$$

The [L] matrix has a one on the diagonal to correspond to every pixel of $\vec{x}'$ within the region of support. To complete the first iteration of the algorithm one must transform $\vec{x}'_1$ and retain only the elements of the Fourier domain previously unknown and add to that result the original known frequency data, $\vec{X}'$.

$$\vec{X}'_1 = [K]\,[A]\,\vec{x}'_1 + \vec{X}'$$

The matrix [K] is the unknown frequency range mask just as the matrix [L] is the region of support mask.

The result of n iterations of this algorithm is

$$\vec{X}'_n = \left[[P]^n + [P]^{n-1} + \cdots + [P] + [I] \right] \vec{X}'$$

in which [P] = [K] [A] [L] [B].

Since it is the frequency space data that we wish to extrapolate, it is beneficial to limit the discussion to manipulations on the Fourier space of the image, $\vec{X}'$. It is interesting to note that the product [A][L][B] constitutes a Fourier space convolution with a ''region of support'' filter.

4.4 Overrelaxed Extrapolation

In the paper by Youla and Webb [Youla82], the GP algorithm is reformulated such that extrapolation is accomplished by iteratively projecting onto convex sets. This reformulation enables the enforcement of each constraint involved in the algorithm to be described as a projection of a data vector onto a set of functions satisfying that particular constraint. This formalism makes it intuitively easy to include many constraints on the extrapolation. It is also convenient to use this formalism when discussing overrelaxation. Additional information on the method of projection onto convex sets is provided in [Sezan82,Schaf81].

In the first subsection more information about projecting onto convex sets is provided and in the second subsection overrelaxation is described and simulation results are presented.

4.4.1 Projection onto Convex Sets

The paper by Youla and Webb [Youla82] formulates the iterative reconstruction algorithms, such as GP, in terms of a sequence of projections of the data vector onto a collection of convex sets in Hilbert space. Each convex set is a constraint upon, or a desired property of the reconstructed data. Of course the intersections of all such convex sets is the space in which the reconstructed data vector will lie. With GP, convex sets are constructed from each constraint used in the iterative extrapolation. Examples of convex sets obtained from basic GP are

$$P_1 d \leftrightarrow w(f)D(f) \ , \quad w(f) = \begin{cases} 1, & a \le |f| < b \\ 0, & \text{elsewhere} \end{cases}$$

which indicates that the frequency space of the data, D(f), is bandlimited to the frequency range [a,b] and

$$P_2 d = r(x)d(x) \ , \quad r(x) = \begin{cases} 1, & c > |x| \\ 0, & \text{elsewhere} \end{cases}$$

which reflects the region of support truncation. To ensure convergence of the iterative application of the projections, each projection must be nonexpansive. For a projection to be labelled nonexpansive the distance between two vectors to which the projection has been applied, must be less than the distance between the original data vectors.

$$\|P_a x - P_a y\| \le \|x - y\|$$

where

$$\|x\| = \left[\sum_{n=-\infty}^{\infty} |x(n)|^2 \right]^{\frac{1}{2}}$$

To finish this subsection the following are a few intuitive comments about extrapolation under this new formalism. The uniqueness of the solution obtained is dependent upon the "size" of the intersection of the convex sets used. It is important to note that vectors that already lie within set i are unmodified by projection i, P_i. The effect of making an accurate first guess decreases the likelihood that the iteration will diverge.

4.4.2 Noniterative Overrelaxed Extrapolation

Overrelaxation is used to speed the extrapolation process of iteratively applying projection operators. The basic change made by overrelaxation concerns the form of the projections that are used. When using overrelaxation a projection no longer projects onto the border of its convex set, rather the projection takes the data past the boundary and into the set itself. The new projection operator becomes

$$P_{or_i} = (1-\lambda_i)I + \lambda_i P_i = \kappa_i I + \lambda_i P_i$$

The operator P_{or_i} is clearly nonexpansive if P_i is nonexpansive when $0 \le \lambda_i \le 1$ although when $1 < \lambda_i$ it must be shown that P_{or_i} is still nonexpansive. This is proven in the appendix of [Youla82] and will not be repeated here. Therefore the range of overrelaxation constant, λ_i, is $0 \le \lambda_i \le 2$.

The two projection operators that were discussed and implemented throughout the beginning of this chapter, are the "spatial truncation" and the "frequency restoration" operators. The overrelaxed version of the spatial truncation operator can be expressed as

$$\vec{x}_{k-1} = \left[\lambda_T[R_1] + \kappa_T[R]\right] \vec{X}_{k-1} = [T_T]\, \vec{X}_{k-1}$$

in which $[R_1]$ is as defined in (66). In a similar fashion the overrelaxed frequency restoration operator is

$$\vec{X}_k = \left[\lambda_R[F_1] + \kappa_R[F]\right] \vec{x}_{k-1} + \lambda_R \vec{X} = [T_R]\, \vec{x}_{k-1} + \lambda_R \vec{X}$$

Combining the operators results in

$$\begin{aligned} \vec{X}_k &= [T_R][T_T]\, \vec{X}_{k-1} + \lambda_R \vec{X} \\ &= \left[[T_R][T_T]\right]^2 \vec{X}_{k-2} + \lambda_R [T_R][T_T]\, \vec{X} + \lambda_R \vec{X} \\ &= \left[[T]^n + \lambda_R [T]^{n-1} + \cdots + \lambda_R [T] + \lambda_R [I]\right] \vec{X} \end{aligned}$$

in which $[T] = [T_R][T_T]$. The hope is that relaxation will result in fewer iterations to obtain a desired mean squared error between the extrapolated and true Fourier space data.

In figure (57) sixteen reconstructions obtained with sixteen different combinations of the relaxation constants, λ_T and λ_R, are plotted. There doesn't seem to a clearly superior reconstruction within the array of reconstructions. Therefore we draw the conclusion that overrelaxation is of very limited benefit to STRMDT.

4.5 Summary

In this chapter investigation into the different forms of the GP method of spectral extrapolation is carried out. To aid in comparing the different formulations of extrapolation, figures (58), (59), (60) and (61) illustrate cylinder reconstructions over a

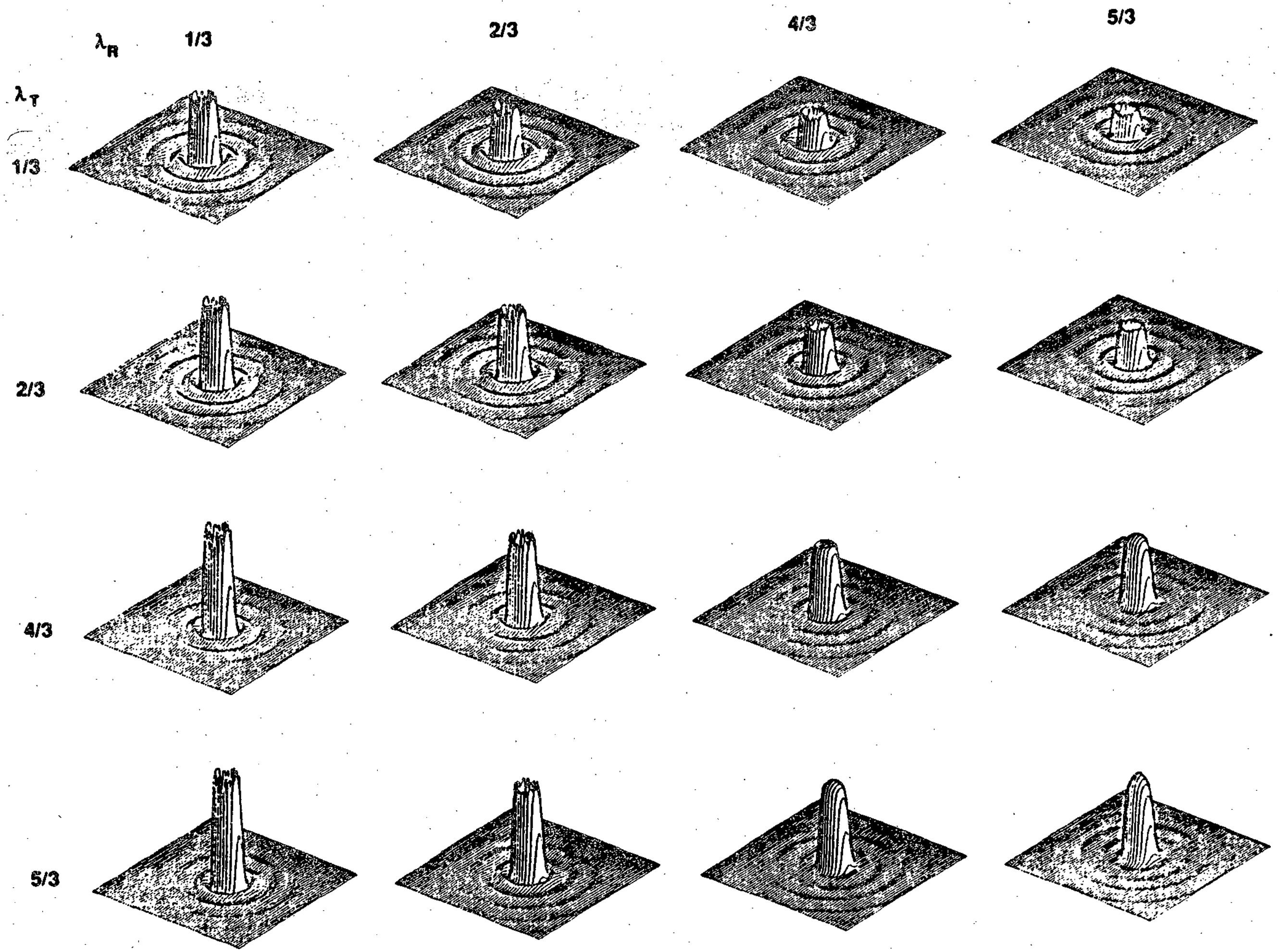

Figure (57) The real part of a cylinder reconstructions in which the cylinder radius is 2λ and the refractive index is 1.01. These reconstructions are generated with the use of overrelaxed GP over a range of relaxation constant combinations.

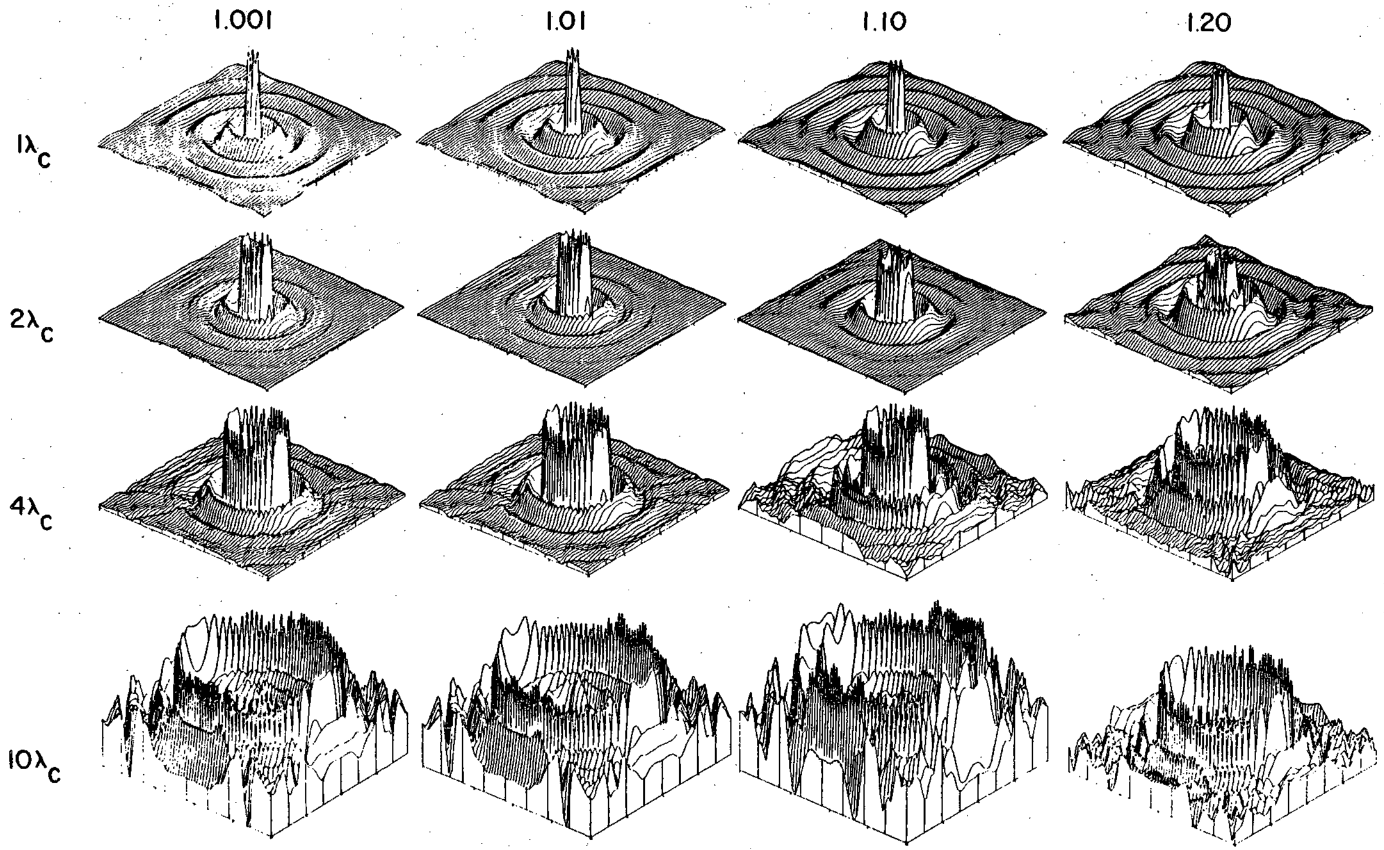

Figure (58) The real part of cylinder reconstructions over a range of one to ten λ in radius and 1.001 to 1.20 in refractive index. These reconstructions are obtained without the aid of spectral extrapolation. They illustrate the quality of reconstructions without low frequency information.

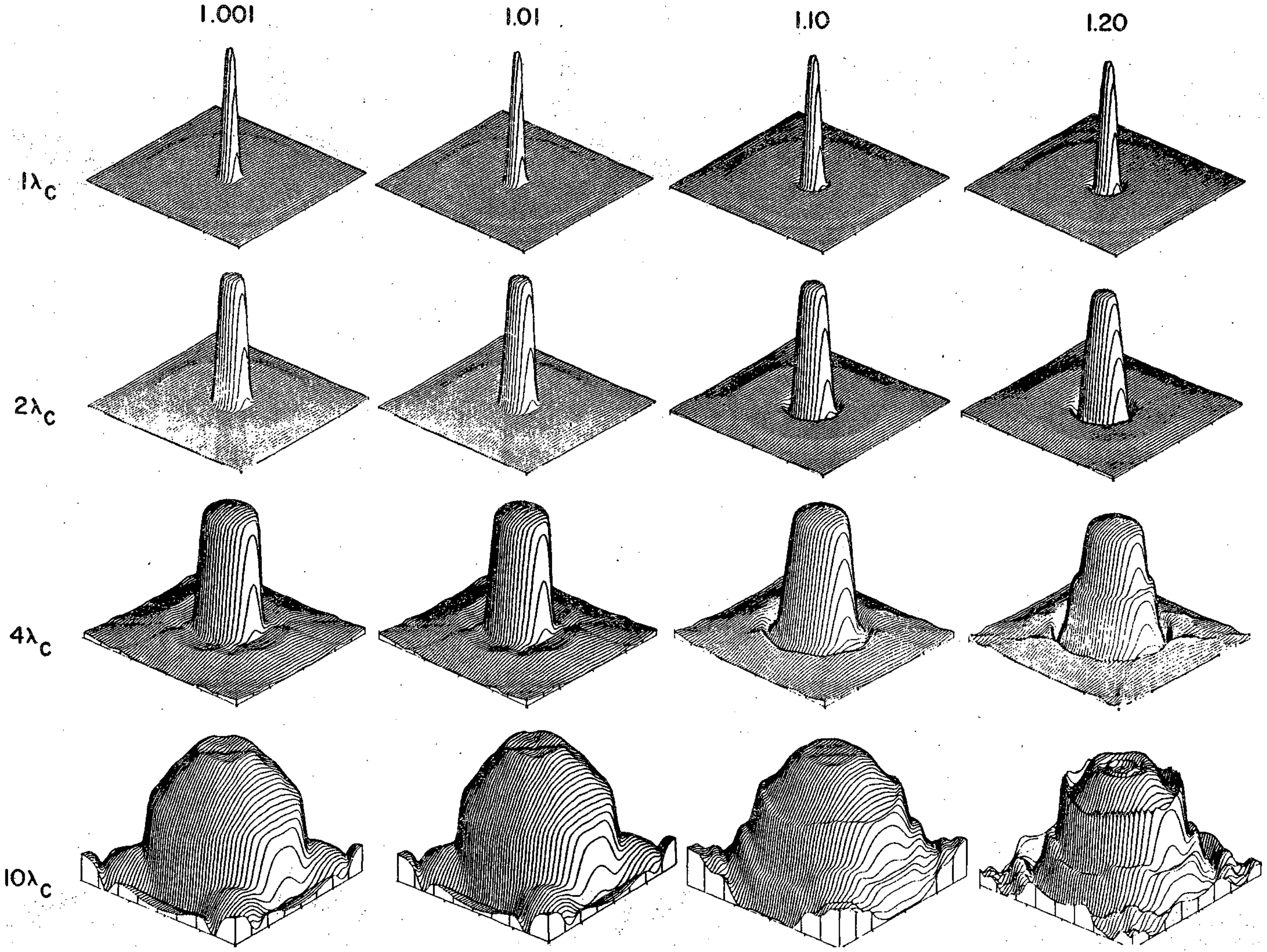

Figure (59) The real part of cylinder reconstructions over a range of one to ten λ in radius and 1.001 to 1.20 in refractive index. These reconstructions are obtained with the use of an "infinite" bandwidth transducer.

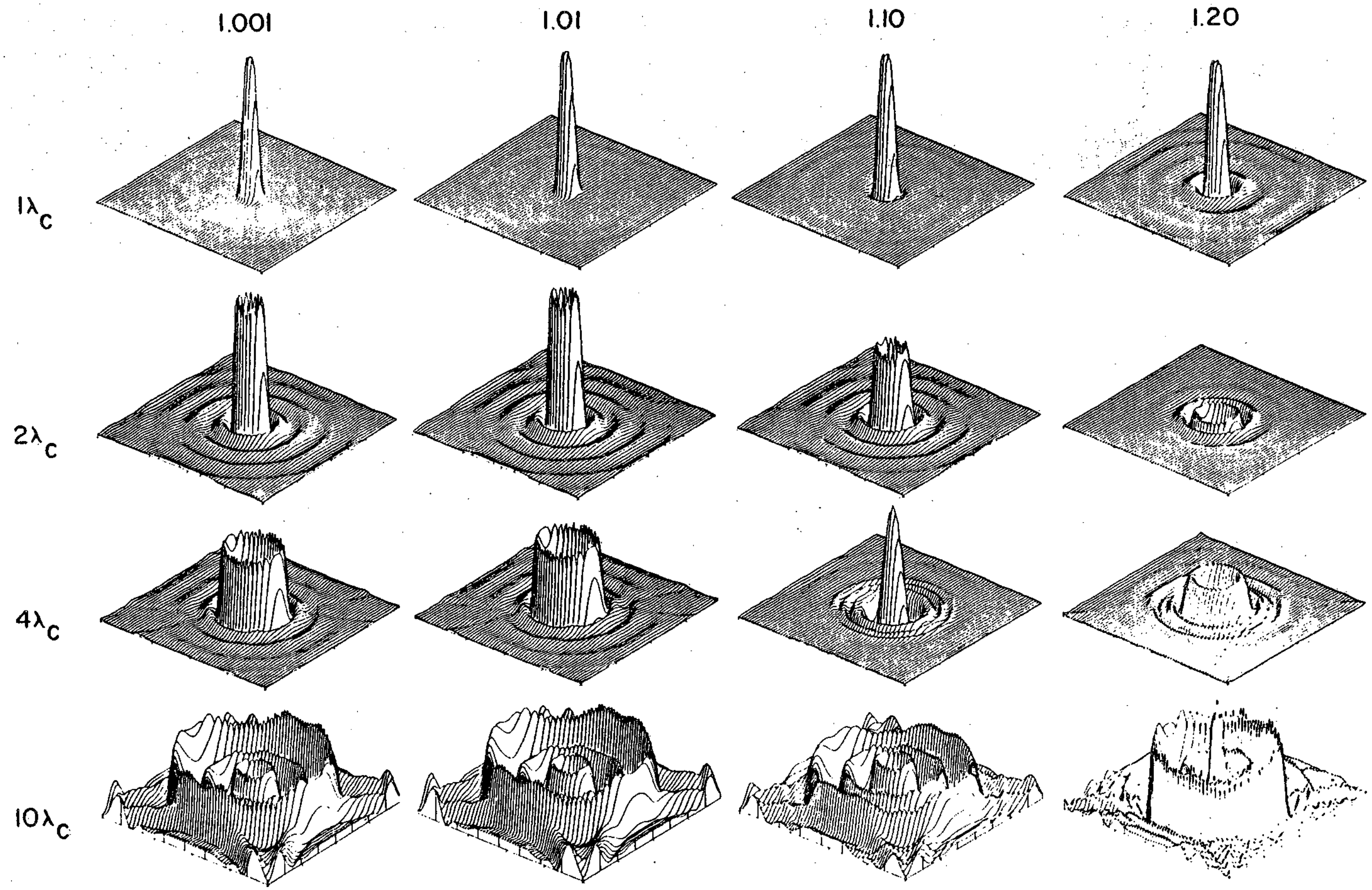

Figure (60) The real part of cylinder reconstructions over a range of one to ten λ in radius and 1.001 to 1.20 in refractive index. These reconstructions are obtained with the aid of iterative spectral extrapolation.

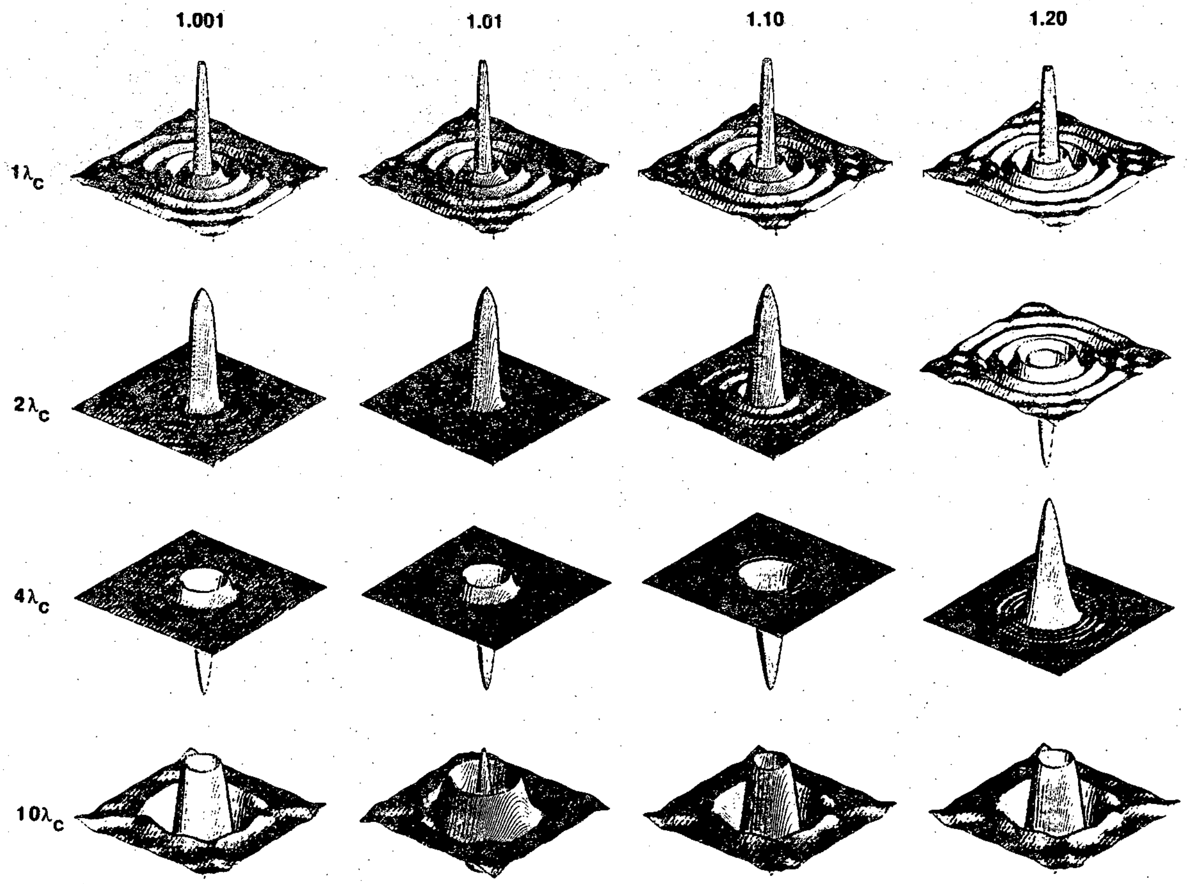

Figure (61) The real part of cylinder reconstructions over a range of one to ten λ in radius and 1.001 to 1.20 in refractive index. These reconstructions are obtained with the aid of noniterative spectral extrapolation of infinite "iteration."

range of one to ten λ in radius and 1.001 to 1.2 in refractive index. In all 4 figures the plots are of the object function $O(\mathbf{r}) = \left[n^2(\mathbf{r})-1\right]$. The reconstructions in figure (58) are obtained without spectral extrapolation. The reconstructions in figure (59) are obtained with the assumption that a transducer with infinite bandwidth was used to obtain the backscattered wave measurements. In figures (60) and (61) conventional iterative extrapolation and infinite noniterative extrapolation respectively, is used.

The reconstructions in figure (61) appear to be quite smooth although quite poor for the objects of larger radius. This is due to the horrible shape of the infinite extrapolation matrix for the particular object radii. This is not due to an excessive filling of the matrix $[R_1]$ which would only result in the matrix [P] approaching the identity matrix in form. As of the date of printing, we have no valid explanation for the degraded extrapolation matrices.

It is interesting to note that there is a curve that can be drawn through each figure to point out where reconstruction quality degrades rapidly. This curve serves to indicate the range of objects for which the Born approximation holds. The fact that the curve is the same in all 3 figures, emphasizes that it is the Born approximation that limits reconstruction quality.

For the interested reader the complexities of conventional and noniterative GP can be compared by comparing the number of operations necessary to carry out extrapolation. The number of calculations necessary to extrapolate an N sample data vector with the conventional approach is approximately $n(2N\log_2 N)$ complex multiplications and additions where n is the number of iterations. For noniterative extrapolation only N^2 multiplications and $N(N-1)$ additions are necessary. Although there is an additional one time cost of nN^3 multiplications and $n(N^2+N-1)+N$ additions just to calculate the extrapolation matrix. Hence for a 100 iterations of a 128 sample data vector, the noniterative approach is a factor of 10 "cheaper" in complex multiplies than its conventional counterpart.

The results of the application of GP extrapolation are quite good but the algorithm can successfully be applied only to the Fourier space data of objects for which the Born approximation holds. Essentially only good data can be extrapolated.

CHAPTER 5

SYNTHETIC APERTURE TOMOGRAPHY

In synthetic aperture diffraction tomography (SADT), for each position of the receiving plane/line, the object is insonified from a number of different directions and a scattered field measurement is made per each incident wave. As will be shown, the frequency domain coverage obtained in this manner by a single position of the receiving line, is far more dense than that obtained by a single incident wave as described in previous chapters. Hence fewer positions of the receiving array about the object are required. The cost of this benefit is the increased complexity of generating the incident waves.

5.1 Basic Theory and Limitations

Before starting the discussion lets consider an incident plane wave with propagation vector $\hat{s}_o$ and a receiving plane that is normal to the vector $\hat{s}_p$ such that $\hat{s}_o \cdot \hat{s}_p = \cos\phi$. To derive the effects of this new form of insonification we simply insert the new expression for the incident wave, $U_i(\mathbf{r}) = e^{jk_o \hat{s}_o \cdot \mathbf{r}}$, into Eq. (14) and follow steps similar to those used to derive Eq. (16). This yields the relationship

$$\tilde{U}_S(\alpha, y=l_0) = \frac{j}{2} \frac{e^{-j\sqrt{k_o^2-\alpha^2}\, l_0}}{\sqrt{k_o^2-\alpha^2}} \tilde{F}(\Lambda - k_o\hat{s}_o)$$

where $\Lambda = \left[\alpha, \sqrt{k_o^2-\alpha^2}\right]$. Figure (62) illustrates the geometry of the experiment and the resulting frequency domain coverage.

To keep the experiment truly reflection mode, in this presentation the angle ϕ will be limited to the range $[0, -\pi]$. When two such synthetic aperture measurements are made on opposite sides of the object, the resulting coverage of the object's spatial frequency domain, is illustrated by the shaded region in figure (63). This coverage looks promising because some low frequency information is obtained which would

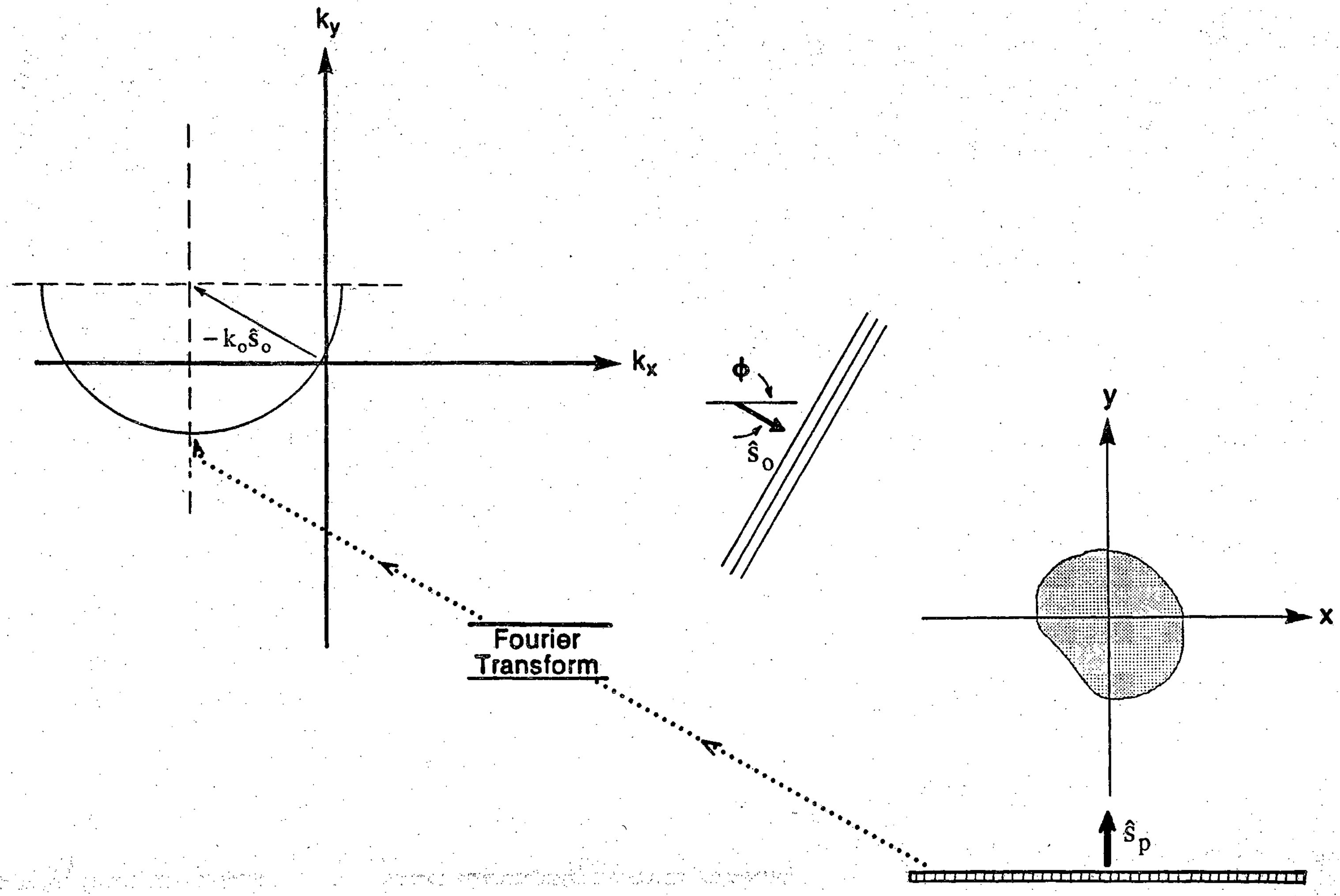

Figure (62) A illustration of the relationship between the object's spatial frequency domain and the scattered field resulting from an incident plane wave propagating in the direction $\hat{s}_o$.

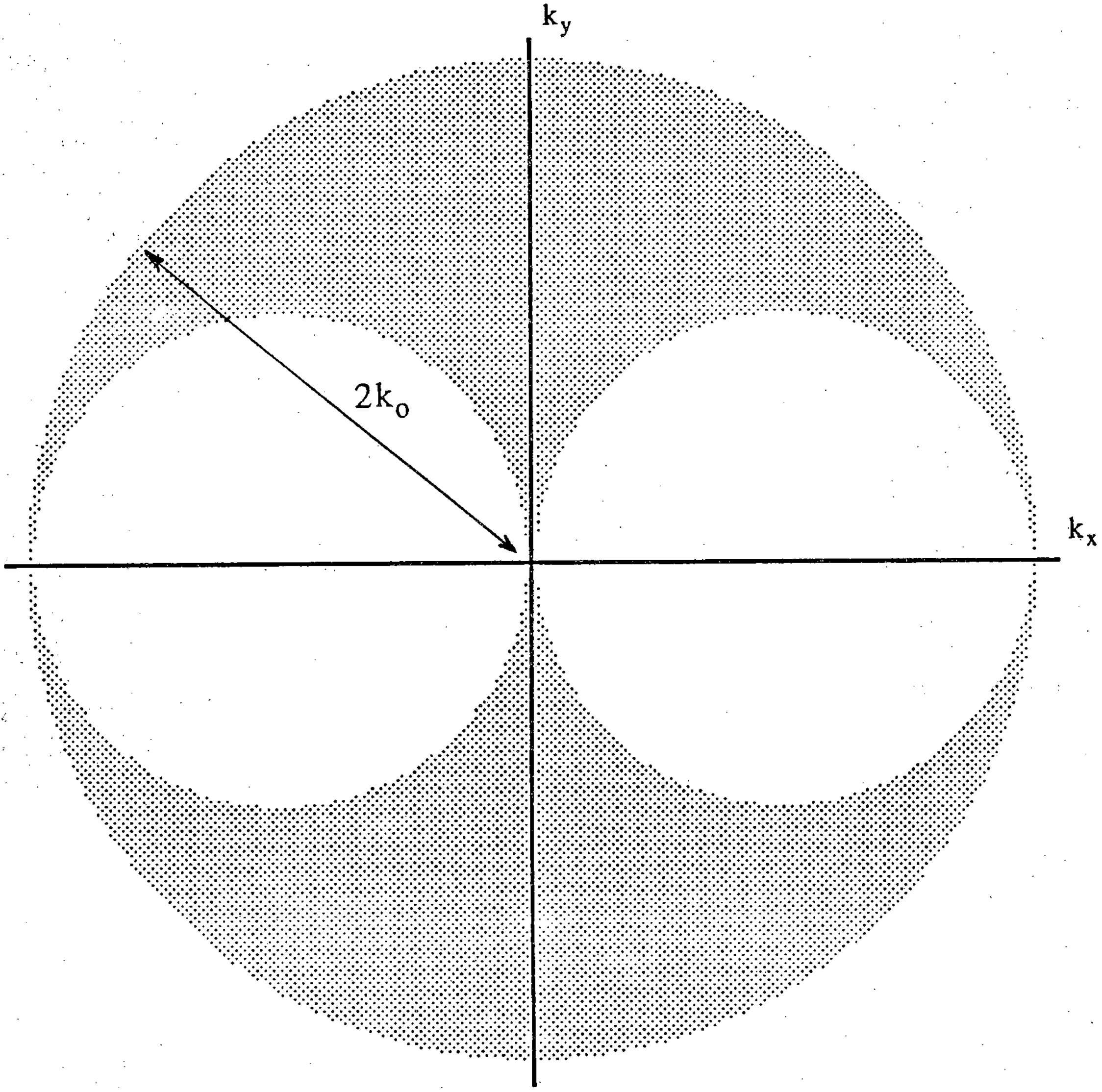

Figure (63) The object's frequency domain coverage obtained with synthetic aperture scattered field measurements from 2 positions of the transducer array.

enable the GP extrapolation algorithm to converge much more rapidly. Theoretically an estimate of the zero frequency sample is obtained. This fact will especially lower the number of iterations required for GP to extrapolate the unknown frequency range.

In reflection mode implementation, the scanning geometry could be quite hard to realize. A possible solution is to use an array of transducers lying on the receiver line [Nah84]. By pulsing each transducer individually and measuring the resulting scattered field with all transducers, the experiment could be implemented. Unfortunately, this requires that the transducer generated wave has a known plane wave expansion and assumes that the receiver line is infinitely long. Hence in implementation the obtainable range of ϕ is $[\psi,\pi-\psi]$ where ψ would be determined from the beamwidth of the transducer. This is only the author's opinion and has not been experimentally verified.

5.2 Synthetic Aperture with an Array of Point Sources

In this section a specific synthetic aperture reconstruction algorithm will be derived that utilizes an array of point sources lying on a infinite line. With this particular transducer array, each transducer in turn will serve as the insonifying source of energy while all of the transducers serve to receive the scattered sound waves. We will see that an interesting frequency domain coverage will result.

The type of incident wave desired is a monochromatic spherically diverging wave produced by a point transducer. This implies that the incident field, $u_i(\mathbf{r},t)$, satisfies a wave equation of the form,

$$\nabla^2 u_i(\mathbf{r},t) - \frac{1}{c^2}\frac{\partial^2 u_i(\mathbf{r},t)}{\partial t^2} = -e^{-j\omega t}\,\delta(\mathbf{r}-\mathbf{r}_o) \tag{71}$$

in which 'c' is the velocity of the generated wave in the medium. In the temporal frequency domain (71) takes the form

$$\nabla^2 U_i(\mathbf{r},\omega) + k_o^2 U_i(\mathbf{r},\omega) = \delta(\mathbf{r}-\mathbf{r}_o) \ . \tag{72}$$

in which $k_o = \omega/c$. Hence the field generated by the transducer which is positioned at $\mathbf{r}_o$, is described by

$$U_i(\mathbf{r},\omega;\mathbf{r}_o) = G_\omega(\mathbf{r}|\mathbf{r}_o)$$

as follows from the application of Eq. (8) to Eq. (72).

If the expression for U_i is inserted into Eq. (13) and then the Green's functions are replaced by their plane wave expansions as presented in Eq. (A6), we have

$$
\begin{aligned}
U_S(\mathbf{r},\omega;\mathbf{r}_o) &= \iiint_V F(\mathbf{r}')\, G_\omega(\mathbf{r}'|\mathbf{r}_o)\, G_\omega(\mathbf{r}|\mathbf{r}')\, dv_{\mathbf{r}'} \\
&= \frac{-1}{16\pi^2} \iiint_V F(\mathbf{r}') \int_{-\infty}^{\infty} dk_x\, e^{jk_x(x'-x_o)}\, \frac{e^{j\sqrt{k_o^2-k_x^2}\,|y'-y_o|}}{\sqrt{k_o^2-k_x^2}} \\
&\qquad \cdot \int_{-\infty}^{\infty} d\alpha\, e^{j\alpha(x-x')}\, \frac{e^{j\sqrt{k_o^2-\alpha^2}\,|y-y'|}}{\sqrt{k_o^2-\alpha^2}}\, dv_{\mathbf{r}'}
\end{aligned}
\tag{73}
$$

The above equation can be simplified by recognizing that $y'>y_o$ and $y_o=y$.

The first step in deriving the desired Fourier domain relationship is to interchange the order of integration in Eq. (73) and carry out the integration with respect to x' and y'. If one considers only those values of k_x and α that are of magnitude less than k_o, restricting our consideration to non-evanescent waves, the integration will Fourier transform the object function. Therefore,

$$
\begin{aligned}
U_S(x,l_0,\omega;x_o,l_0) &= \frac{-1}{16\pi^2} \int_{-\infty}^{\infty} d\alpha \int_{-\infty}^{\infty} dk_x\, \tilde{F}\left[\left(\alpha, -\sqrt{k_o^2-\alpha^2} \right) - \mathbf{K} \right] \\
&\quad \cdot e^{j\alpha x}\, e^{-jk_x x_o}\, \frac{e^{-j\sqrt{k_o^2-\alpha^2}\, l_0}}{\sqrt{k_o^2-\alpha^2}}\, \frac{e^{-j\sqrt{k_o^2-k_x^2}\, l_0}}{\sqrt{k_o^2-k_x^2}} \quad , \mathbf{K} = \left(k_x, \sqrt{k_o^2-k_x^2} \right) .
\end{aligned}
$$

The next step is to take the Fourier transform of U_S, resulting from a pulse transmitted from the transducer at location (x_o,l_0), as measured on the transducer line. Note that the consideration of the location of the transmitting transducer is crucial to the algorithm. The function $\tilde{U}_S(\cdot)$ will generically denote the Fourier transform of $U_S(\cdot)$ although one must pay attention to the arguments of the function to determine what the function truly represents. The reader will see what is meant in a moment. After taking the above mentioned transform we have

$$
\tilde{U}_S(u,l_0,\omega;\mathbf{r}_o) = \int_{-\infty}^{\infty} U_S(x,l_0,\omega;x_o,l_0)\, e^{-jux}\, dx \ .
$$

One further transformation with respect to the position of the transmitting transducer, x_o, results in the function

$$
\begin{aligned}
\tilde{U}_S(u,l_0,\omega;v,l_0) &= \int_{-\infty}^{\infty} \tilde{U}_S(u,l_0,\omega;x_o,l_0)\, e^{-jvx_o}\, dx_o \\
&= \frac{-1}{4}\, \tilde{F}\left[\left(u, -\sqrt{k_o^2-u^2} \right) - \mathbf{K} \right] \frac{e^{-j\sqrt{k_o^2-u^2}\, l_0}}{\sqrt{k_o^2-u^2}}\, \frac{e^{-j\sqrt{k_o^2-v^2}\, l_0}}{\sqrt{k_o^2-v^2}} \quad ,
\end{aligned}
$$

where $\mathbf{K} = \left(v, \sqrt{k_o^2-v^2} \right)$. It is the above equation, or other equations similar to it, that form the basis of the synthetic aperture imaging algorithm. The relationship described is the same type as that pointed out by the FDT. It leads to reconstruction through spatial frequency domain filling with the use of intricate measurements of backscattered energy.

Given the function $\tilde{U}_S(u,l_0,\omega;v,l_0)$ obtained from the scattered field measurements made from one position of the receiving transducer array, the coverage of $\tilde{F}(\cdot)$ illustrated by the shaded region in figure (64), can be achieved. The shaded region is constructed by a multitude of "Ewald" semi-circles whose centers are located by the vector **K**. If the receiving array is rotated by 180° about the object, and the frequency domain coverage obtained at that position is combined with the coverage from the first position, the result is the coverage illustrated in figure (63)

In actual implementation there might be N small piston type transducers along the receive line which would result in N measurements being taken from the transducers at each angular position of the line. This comes about due to the fact that each of the N transducers must in turn be used to insonify the object. After Fourier transforming each field measurement, such that the function $\tilde{U}_S(u,l_0,\omega;x_o,l_0)$ is obtained, the Fourier transform with respect to x_o must be taken. Effectively, we have carried out a 2D FT in which x and x_o form a 2D space. After the function $\tilde{U}_S(u,l_0,\omega;v,l_0)$ is obtained, it is a simple matter to use it to obtain values of $\tilde{F}(\cdot)$.

5.3 Summary

This chapter has explored the basics of synthetic aperture tomography and described a particular scanning geometry. This approach to tomography is characterized by a long data collection time per array position but fewer positions of the receiving transducer array are required. If one were working with forward scattered fields, the physical problem of how to insonify the object from different directions and obtain scattered field measurements would be trivial. For the reflection mode case, insonifying and receiving on the same side of the object is quite a complex job. An approximate theoretical solution to the problem has been discussed herein.

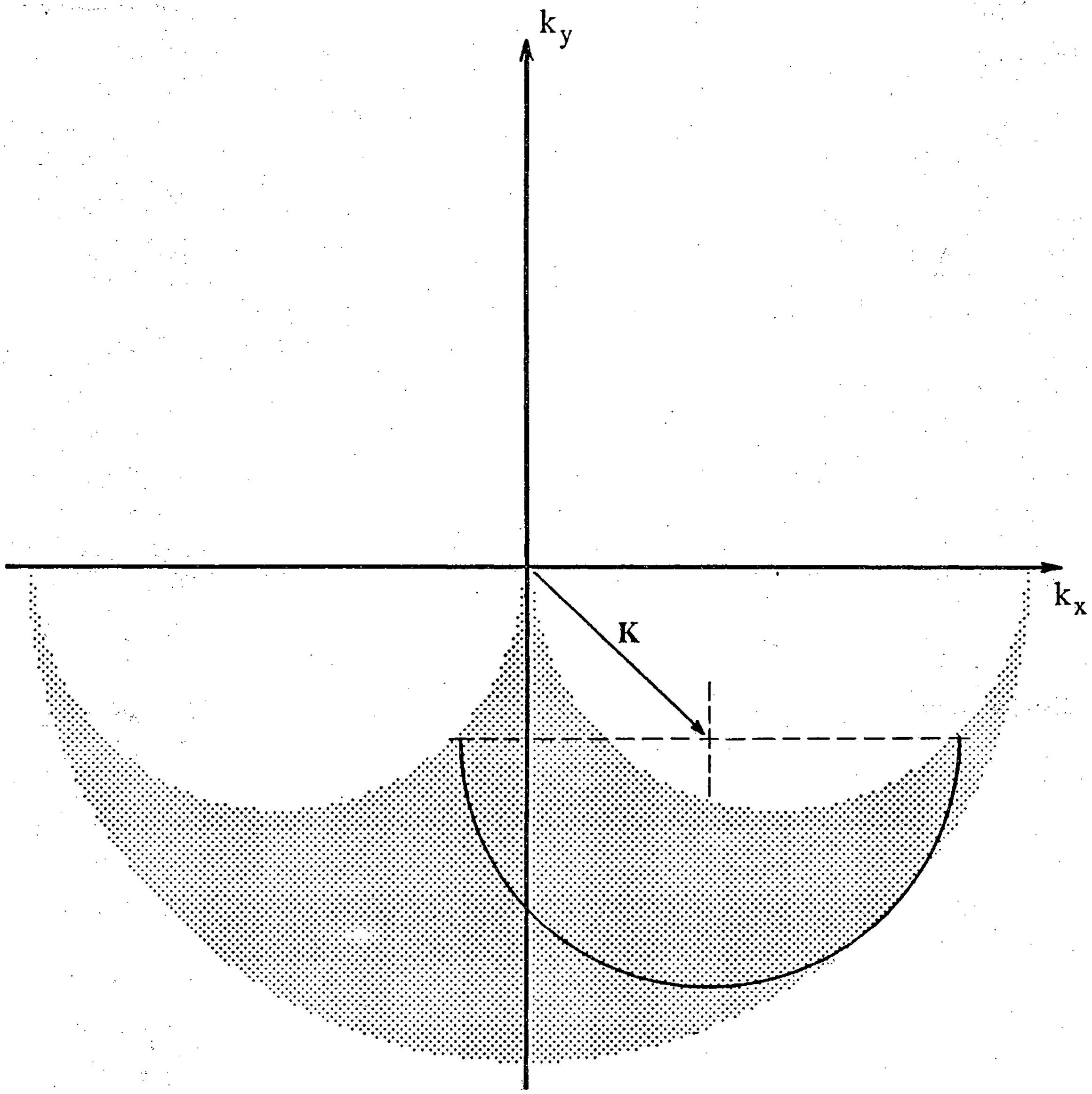

Figure (64) The object's frequency domain coverage obtained with synthetic aperture scattered field measurements from a single position of the transducer array.

LIST OF REFERENCES

LIST OF REFERENCES

[Andrws] L.C. Andrews, *Special Functions for Engineers and Applied Mathematicians*, Macmillan, 1985.

[Ardou85] J.P. Ardouin, and A.N. Venetsanopoulos, ''Modelling and restoration of ultrasonic phased-array B-scan images,'' *Ultrasonic Imaging*, Vol. 7, No. 4, pp. 321-344, Oct. 1985.

[Born] M. Born, and E. Wolf, *Principles of Optics* Pergamon Press, 1965.

[Cadzo79] J.A. Cadzow, ''An extrapolation procedure for band-limited signals,'' *IEEE Trans. ASSP*, vol. ASSP-27, no. 1, pp. 4-12, February 1979.

[Churc76] R.V. Churchill, J.W. Brown, and R.F. Verhey, *Complex Variables and Applications*, pp. 286-289, McGraw Hill, 1976.

[Dean] S.R. Dean, *The Radon Transform and Some of Its Applications*, Wiley, New York, 1983.

[Dev82] A.J. Devaney, ''A filtered backpropagation algorithm for diffraction tomography,'' *Ultrasonic Imaging*, Vol. 4, pp. 336-350, 1982.

[Dines87] K. Dines, ''Computed ultrasonic reflection tomography,'' *IEEE Trans. Ultrasonics, Ferroelectrics, and Frequency Control*, Vol. UFFC-34, No. 3, pp. 309-318, May 1987.

[Dunn62] F. Dunn, ''Temperature and amplitude dependence of aucoustic absorption in tissue,'' *J. Acoust. Soc. Am.*, Vol. 34, pp. 1545-1547, 1962.

[Ersoy] Okan Ersoy, *personal communication*, August 1986.

[Fate80] M. Fatemi, and A.C. Kak, ''Ultrasonic B-Scan Imaging: theory of image formation and a technique for restoration,'' *Ultrasonic Imaging*, Vol. 2, No. 1, pp. 1-47, 1980.

[Gerch74] G. Gerchberg, "Super-resolution through error energy reduction," *Optica Acta*, 21, pp. 709-720, 1974.

[Good68] J.W. Goodman, *Introduction to Fourier Optics*, McGraw Hill, 1968.

[Hunt72] B.R. Hunt, "Deconvolution of linear systems by constrained regression and its relationship to the wiener theory," *IEEE Trans. Automatic Control*, pp. 703-705, Oct. 1972.

[John77] S. Johnson, J. Greenleaf, M. Tanaka, B. Rajogopalan, and R. Bahn, "Quantitative synthetic aperture reflection imaging with correction for refraction and attenuation: application of seismic techniques in medicine," *IEEE Biomedical Symposium Proceedings*, 1978.

[Kak78] A.C. Kak, and K.A. Dines, "Signal processing of broadband pulsed ultrasound: measurement of attenuation of soft biological tissues," *IEEE Trans. Biomedical Engr.*, Vol. BME-25, No. 4, pp. 321-344, July 1978.

[KakRob] A.C. Kak, and B.A. Roberts, "Reconstruction from projections: applications in computerized tomography," *Handbook of Pattern Recognition and Image Processing*, Eds. T.Y. Young, K.S. Fu, Chap. 27, Academic Press, 1986.

[Kim84] J.H. Kim, S.B. Park, and S.A. Johnson, "Tomographic imaging of ultrasonic reflectivity with correction for acoustic speed variations," *Ultrasonic Imaging*, Vol. 6, pp. 304-312, 1984.

[ManiTR] M. Azimi, and A.C. Kak, "Multiple scattering and attenuation phenomena in diffraction imaging," Purdue University, School of Electrical Engineering, Technical Report, TR-EE-85-4, 1985.

[MorFes] P.M. Morse, and H. Feshbach, *Methods of Theoretical Physics*, Mc-Graw Hill, 1953.

[Morse] P.M. Morse, and K.U. Ingard, *Theoretical Acoustics*, McGraw Hill, 1968.

[Moun72] R.A. Mountford and P.N.T. Wells, "Ultrasonic liver scanning: the A-scan inthe normal and cirrhosis," *Phys. Med. Biol.*, Vol. 17, pp. 261-269, 1972.

[Nah84] D. Nahamoo, S.X. Pan, and A.C. Kak, "Synthetic aperture diffraction tomography and its interpolation-free computer implementation," *IEEE Transactions on Sonics and Ultrasonics*, SU-31, pp. 218-229, 1984.

[Nor79a] S. Norton, and M. Linzer, ''Ultrasonic reflectivity tomography: reconstruction with circular transducer arrays,'' *Ultrasonic Imaging*, Vol. 1, No. 2, pp. 154-184, 1979.

[Nor79b] S.J. Norton, ''Reconstruction of a two-dimensional reflecting medium over a circular domain: exact solution,'' *J. Acoust. Soc. Amer.,* 67, pp. 1266-1273, 1979.

[Nor81] S. Norton, and M. Linzer, ''Ultrasonic reflectivity imaging in three dimensions: exact inverse scattering solutions for plane, cylindrical and spherical apertures,'' *IEEE Transactions on Biomedical Engineering*, BME-28, pp. 202-220, 1981.

[Nor83] S. Norton, ''Generation of separate density and compressibility images in tissue," *Ultrasonic Imaging*, Vol. 5, pp. 240-252, 1983.

[OppScf] A.V. Oppenheim and R.W. Schafer, *Digital Signal Processing*, Prentice Hall, 1975.

[Pan83] S.X. Pan and A.C. Kak, ''A computational study of reconstruction algorithms for diffraction tomography: interpolation versus filtered backpropagation," *IEEE Transactions on Acoustics, Speech, and Signal Processing*, Vol. ASSP-31, No. 5, pp. 1262-1275, October 1983.

[Pap75] A. Papoulis, ''A new algorithm in spectral analysis and band-limited extrapolation,'' *IEEE Transactions Circuits and Systems*, CAS-22, pp. 735-742, 1975.

[Roseau] M. Roseau, *Asymptotic Wave Theory*, North-Holland Publishing Co., 1976.

[Robi84] D.E. Robinson and M. Wing, ''Lateral deconvolution of ultrasonic beams,'' *Ultrasonic Imaging*, Vol. 6, pp. 1-12, 1984.

[Robr85] B.A. Roberts and A.C. Kak, ''Reflection mode diffraction tomography,'' *Ultrasonic Imaging*, Vol. 7, No. 4, pp. 300-320, 1985.

[Rosen82] A. Rosenfeld and A.C. Kak, *Digital picture processing*, Academic Press, New York/London, 1982.

[Sabri78] M.S. Sabri and W. Steenaart, ''An approach to band-limited signal extrapolation: the extrapolation matrix,'' *IEEE Trans. Circs. Sys.*, vol. CAS-25, no. 2, pp. 74-78, February 1978.

[Sato81] T. Sato, S. Norton, M. Linzer, O. Ikeda, and M. Hirama, ''Tomographic image reconstruction from limited projections using iterative revisions in image and transform spaces,'' *Applied Optics*, 20, pp. 395-399, 1981.

[Schaf81] R.W. Schafer, R.M. Mersereau, and M.A. Richards, ''Constrained iterative restoration algorithms,'' *Proc. IEEE*, vol. 69, no. 4, pp. 432-450, April 1981.

[Sezan82] M.I. Sezan, and H. Stark, ''Image restoration by the method of convex projections: part 2 - applications and numerical results,'' *IEEE Transactions on Medical Imaging*, MI-1, pp. 95-101, 1982.

[Shew68] J.R. Shewell, and E. Wolf, ''Inverse diffraction and a new reciprocity theorem," *Journal Optical Society America*, Vol. 58, No. 12, pp. 1596-1603, December 1968.

[Slane84] M.G. Slaney, A.C. Kak, and L.E. Larsen, ''Limitations of imaging with first-order diffraction tomography,'' *IEEE Transactions on Microwave Theory and Techniques*, MTT-32, pp. 1262-1275, 1984.

[Stran80] G. Strang, *Linear algebra and its applications*, Academic Press, New York/London, 1980.

[Trus84] H. Trussell, ''The feasible solution in signal restoration,'' *IEEE Transactions Acoustics Speech and Signal Proccessing*, ASSP-32, pp. 201-212, 1984.

[Wells75] P.N.T. Wells, ''Absorption and dispersion of ultrasound in biological tissue,'' *Ultrasound in Med. & Biol.*, Vol. 1, pp. 369-376, Pergamon Press, 1975.

[Youla82] D.C. Youla and H. Webb, ''Image restoration by the method of convex projections: part I - theory,'' *IEEE Trans. Med. Img.*, MI-1, pp. 81-94, 1982.

APPENDICES

Appendix A Green's Functions

In this appendix two different Green's functions will be described that satisfy two different wave equations. The discussion will entail 2 dimensional and 3 dimensional functions.

The solution to the following wave equation is called a Green's function.

$$\nabla^2 G_\omega(\mathbf{r}) + k_o^2 G_\omega(\mathbf{r}) = -\delta(\mathbf{r}-\mathbf{r}_o) \ . \tag{A1}$$

The form of the equation indicates that $G_\omega(\cdot)$ represents the spatial variation of the wave generated by a unit harmonic point source at $\mathbf{r}_o$. In free space the Green's function takes the form

$$G_\omega(\mathbf{r}\,|\,\mathbf{r}_o) = \frac{1}{4\pi\,|\mathbf{r}-\mathbf{r}_o|}\, e^{j\frac{\omega}{c}|\mathbf{r}-\mathbf{r}_o|} \ . \tag{A2}$$

The argument of $G_\omega(\mathbf{r}\,|\,\mathbf{r}_o)$ denotes the function's dependence upon $\mathbf{r}_o$. Next, let us look at the spatial Fourier transform of the three dimensional free space Green's function in Eq. (A2). If we look at the wave equation, Eq. (A1), satisfied by the Green's function, we can see that the following equation holds when we take the spatial Fourier transform of Eq. (A1).

$$(-K^2+k_o^2)\tilde{G}_\omega(\mathbf{K}\,|\,\mathbf{r}_o) = -e^{-j\mathbf{K}\cdot\mathbf{r}_o}$$

This implies that

$$\tilde{G}_\omega(\mathbf{K}\,|\,\mathbf{r}_o) = \frac{e^{-j\mathbf{K}\cdot\mathbf{r}_o}}{|\mathbf{K}|^2-k_o^2} \quad \text{and} \tag{A3}$$

$$G_\omega(\mathbf{r}\,|\,\mathbf{r}_o) = \frac{1}{(2\pi)^3}\iiint_{-\infty}^{\infty} \frac{e^{j\mathbf{K}\cdot(\mathbf{r}-\mathbf{r}_o)}}{|\mathbf{K}|^2-k_o^2}\, d^3\mathbf{K} \tag{A4}$$

where $\mathbf{K} = (K_x,K_y,K_z)$. The integration with respect to K_z is a contour integral of the form in Appendix B Eq. (B1) having poles located at $\pm\sqrt{k_o^2-K_x^2-K_y^2}$. The result of the integration takes the form of Eq. (B2) so that the point $\mathbf{r}_o$ will be a source of waves instead of a sink of wave energy. Using Eq. (B3), Eq. (A4) can be expressed as

$$G_\omega(\mathbf{r}\,|\,\mathbf{r}_o) = \frac{j\pi}{8\pi^3}\iint_{-\infty}^{\infty} e^{j\left[K_x(x-x_o)+K_y(y-y_o)\right]}\, \frac{e^{j\sqrt{k_o^2-K_x^2-K_y^2}\,|z-z_o|}}{\sqrt{k_o^2-K_x^2-K_y^2}}\, dK_x\, dK_y \tag{A5}$$

The above equation will be referred to in the text as the angular spectrum expansion of $G_\omega(\cdot)$.

In two dimensions the solution to Eq. (A1) is [Morse, pg. 364-366]

$$G_\omega(\mathbf{r}\,|\,\mathbf{r}_o) = \frac{j}{4} H_o(k\,|\mathbf{r}-\mathbf{r}_o|)$$

where $H_o(\cdot)$ is the Hankel function of zeroth order. The function $H_o(\cdot)$, which describes the wave backscattered from a unit harmonic line source has the angular spectrum expansion,

$$\frac{j}{4} H_o(k\,|\mathbf{r}-\mathbf{r}_o|) = \frac{j\pi}{4\pi^2} \int_{-\infty}^{\infty} e^{jK_x(x-x_o)} \frac{e^{j\sqrt{k_o^2-K_x^2}\,|y-y_o|}}{\sqrt{k_o^2-K_x^2}}\, dK_x \ . \tag{A6}$$

Now let us consider a different form of the wave equation in Eq. (A1),

$$\nabla^2 g(\mathbf{r},t) + k_o^2 g(\mathbf{r},t) = -\delta(\mathbf{r}-\mathbf{r}_o)\delta(t-t_o) \ , \tag{A7}$$

in which the forcing function contains an impulse at $t = t_o$. The function $g(\cdot)$ is the infinite bandwidth version of $G_\omega(\cdot)$ which holds only for the temporal frequency ω. The temporal impulse Green's function, $g(\mathbf{r},t)$, can be expressed as the inverse transform of the function $G_\omega(\cdot)$ [Morse, pg.321]

$$\begin{aligned} g(\mathbf{r},\tau) &= \frac{1}{2\pi} \int_{-\infty}^{\infty} \frac{1}{4\pi\,|\mathbf{r}-\mathbf{r}_o|}\, e^{j\frac{\omega}{c}|\mathbf{r}-\mathbf{r}_o|}\, e^{-j\omega\tau}\, d\omega \\ &= \frac{1}{4\pi\,|\mathbf{r}-\mathbf{r}_o|}\, \delta\left[\tau - \frac{|\mathbf{r}-\mathbf{r}_o|}{c}\right] \ . \end{aligned} \tag{A8}$$

where τ in the above equation is equal to $t-t_o$. Since $g(\cdot)$ depends explictly upon t_o and $\mathbf{r}_o$, all reference to this function will use the notation $g(\mathbf{r},t\,|\,\mathbf{r}_o,t_o)$.

Appendix B Common Contour Integrals

The contour integrals encountered within this paper are typically of the form

$$I = \int_{-\infty}^{\infty} \frac{e^{j\Lambda(z-z_o)}}{(\Lambda-\sqrt{k_o^2-p^2})(\Lambda+\sqrt{k_o^2-p^2})}\, d\Lambda \ . \tag{B1}$$

The problem with this integral is that the poles of the integrand lie on the real axis which implies a purely oscillatory, nonattenuating system which is not physically realizable. There is always a damping force acting upon the system which causes a wave to attenuate and eventually vanish [MorFes, pg.1334-1335]. In this case it is best to assume a complex wave number, $k_{c_o} = k_o + j\alpha$, in which α is responsible for the attenuation in the medium. The poles become

$$\Lambda_1 = \sqrt{k_o^2-\alpha^2-p^2+2jk_o\alpha} \qquad \Lambda_2 = -\Lambda_1 \ .$$

Since we will consider only nonevanescent waves, $|k_o|>p$, the pole Λ_1 lies above the real axis and Λ_2 lies below the real axis as in figure (B1). If $(z-z_o)>0$ then the contour must surround the upper half plane such that the integrand of the integral on the arc extending to infinity, will evaluate to zero, $\lim_{R\to j\infty} e^{jkR} = 0$. As a result, the contour contains Λ_1 and by Cauchy's integral equation,

$$I = 2\pi j \, \frac{e^{j\sqrt{k_{c_o}^2-p^2}\,(z-z_o)}}{2\sqrt{k_{c_o}^2-p^2}} \ , \quad (z-z_o)>0 \ .$$

If $(z-z_o)<0$ the contour must surround the bottom half plane thereby enclosing Λ_2 and yielding the result

$$I = -2\pi j \, \frac{e^{-j\sqrt{k_{c_o}^2-p^2}\,(z-z_o)}}{-2\sqrt{k_{c_o}^2-p^2}} \ , \quad (z-z_o)<0 \ ,$$

in which the $-2\pi j$ term is included due to the clockwise direction of the contour. The combination of the above two solutions is the following:

$$I = \pi j \, \frac{e^{j\sqrt{k_{c_o}^2-p^2}\,|z-z_o|}}{\sqrt{k_{c_o}^2-p^2}} \ . \tag{B2}$$

This solution of the integral leads to outgoing waves as if the point z_o were a source of wave energy.

If the complex wave number is negative, $k_{c_o} = -k_o - j\alpha$, and $|k_o|>p$, the Λ_2 pole lies above the real axis and Λ_1 lies below the real axis as in figure (B2). Repeating the

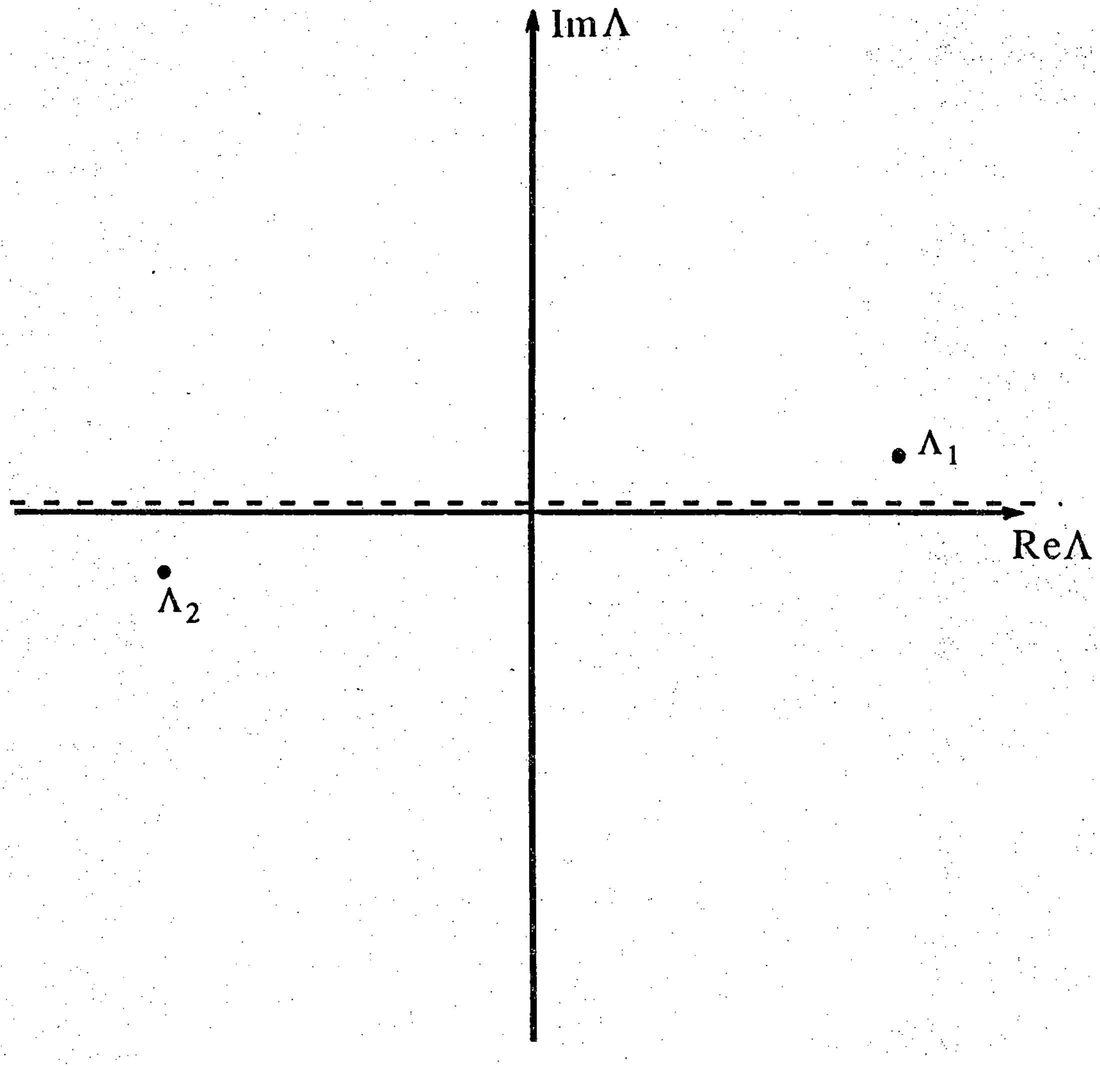

Figure (B1) Path of contour integration for the case of positive wavenumber.

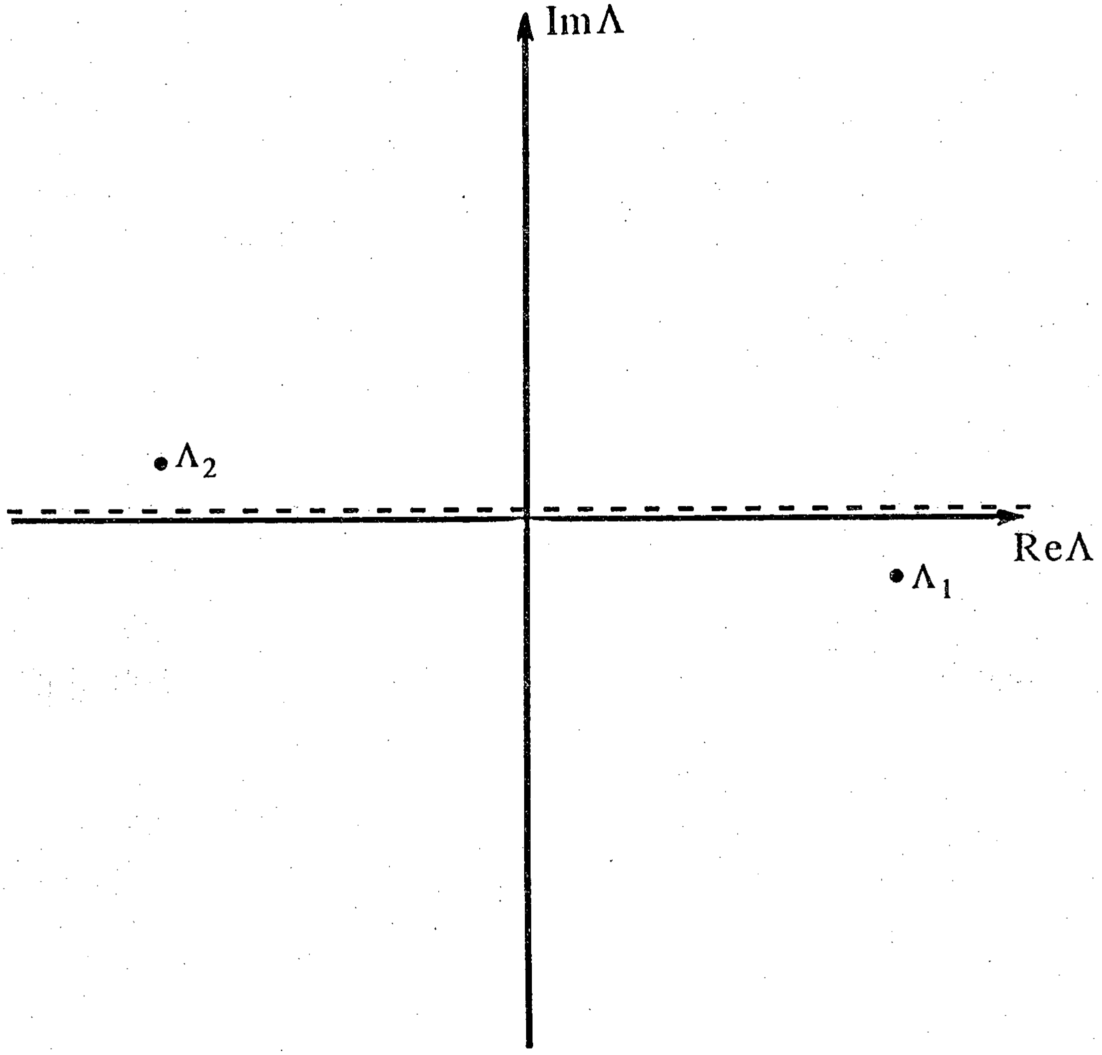

Figure (B2) Path of contour integration for the case of negative wavenumber.

above manipulations for this case leads us to the solution

$$I = -\pi j \, \frac{e^{-j\sqrt{k_{c_o}^2-p^2}\,|z-z_o|}}{\sqrt{k_{c_o}^2-p^2}} \; . \tag{B3}$$

which represents incoming waves as if the point z_o were a sink to wave energy.

All possible combinations of k_{c_o} and $(z-z_o)$ in the solution to I, are encompassed in equation

$$I = \int_{-\infty}^{\infty} \frac{e^{j\Lambda(z-z_o)}}{(\Lambda-\sqrt{k_o^2-p^2})(\Lambda+\sqrt{k_o^2-p^2})} \, d\Lambda =$$

$$= j\pi \, \mathrm{sgn}(k_{c_o}) \, \frac{\exp\left[j \, \mathrm{sgn}(k_{c_o}) \sqrt{k^{2_{c_o}}-p^2} \, |z-z_o| \right]}{\sqrt{k^{2_{c_o}}-p^2}} \tag{B4}$$

where $\mathrm{sgn}(k) = \begin{cases} -1, & k < 0 \\ 1, & k > 0 \end{cases}$.

Appendix C Evanescent Waves

The unimportance of evanescent waves is crucial to this thesis. Disregarding evanescent waves makes the Fourier diffraction theorem possible. Hence a few words explaining these waves are warranted.

Consider the time harmonic wave described by

$$W(u,v) = A(u,v)\, e^{j(ux+vy+\gamma z)}$$

where the vector **K** = (u,v,γ) indicates the direction of propagation and A(u,v) is the amplitude of the wave propagating in the direction (u,v). Since $\gamma = \sqrt{k_o^2 - u^2 - v^2}$, there are two possible classes of waves. The first class consists of evanescent waves [Shew68] for which $k_o^2 < u^2 + v^2$, resulting in

$$W(u,v) = A(u,v)\, e^{j(ux+vy)}\, e^{-\sqrt{u^2+v^2-k_o^2}\, z} \ .$$

These waves propagate in all possible directions perpendicular to the z axis and attenuate with distance along the z axis. The second class consists of waves for which $k_o^2 \geq u^2 + v^2$, resulting in waves propagating in all directions within 90 degrees of the z axis.

In all of the discussions within this thesis, only the second class of waves, non-evanescent waves, will be considered since evanescent waves attenuate rapidly and therefore can be ignored at a distance of a few wavelengths. As shown within the body of the proposal, ignoring evanescent waves makes the Fourier domain relationships possible.

Appendix D The Ultrasonic Imaging System (UIS)

This appendix will briefly describe the current configuration of the equipment in the laboratory that allows us to carry out tomography experiments. To start the appendix we will discuss the basic pieces of equipment and how they fit together. Throughout the discussion, the modifications that have been made to the system during the course of the research presented in this report, will be described.

As illustrated in figure (D1), the Panametrics pulser serves to drive all of the transducers in the lab, the output of which is digitized by a Biomation 8100 transient recorder. The recorder is controlled through the DMA parallel I/O board that is plugged into the motherboard of the lab's 68020 based computer that is named MALCOLM. The actual interface between the I/O board and the digitizer is provided by a board that was designed and built in the lab.

The motors that move the transducers are controlled by a 6800 μP which is itself controlled by one of MALCOLM's serial lines. These stepper motors can consistently be bumped in 1.8° increments which makes possible 5μm lateral movements in the transducers. Repeatibility of experiments is very good due to the accuracy of the motors and the accuracy with which the slides can find their home positions.

Just a short time ago, a 6809 micro was totally responsible for data collection. Once data had been stored in its small memory it would have to be uploaded to the now defunct ARPA machine. The rate of data transfer between the digitizer and computer memory, without considering upload time, has been more than double by the current system Today a C program compiled and executed on the MALCOLM machine can completely control the experiment, collect all the data and begin to use the data in a reconstruction algorithm in between data transfers. To accomplish this, a device driver had to be written so that the I/O board could be used. Along with the driver, a whole library of routines had to be written to implement full control of the Biomation and the 6800 motor controller. Effectively a UIS shell from which all computer controlled aspects of the system can be manipulated, had to be written.

The geometry of the reflection mode scanner is such that a single transducer can be moved in the X-Y plane under motor control. A third motor will have the object to be imaged mounted to its shaft and will provide rotation of the object.

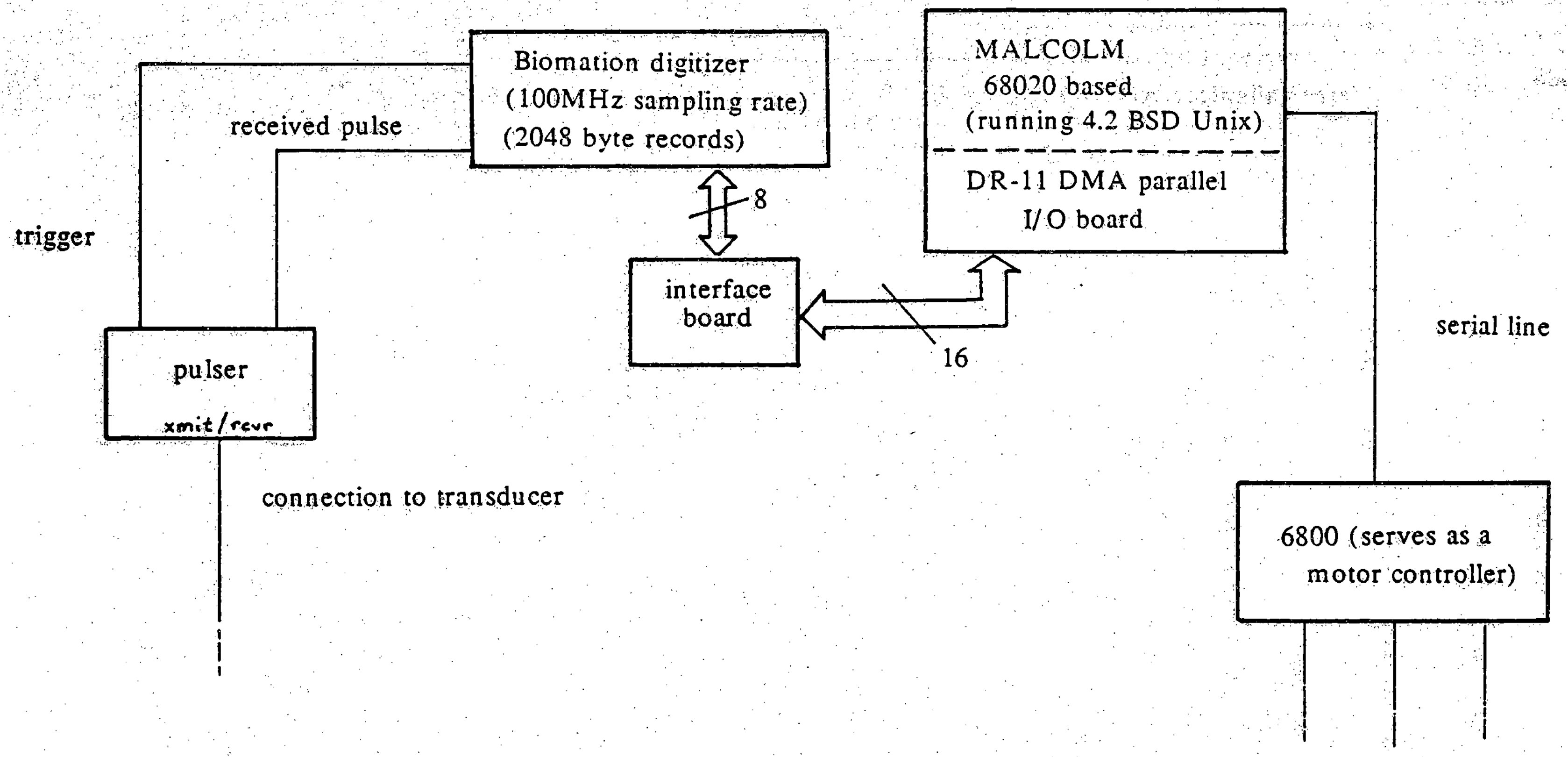

Figure (D1) A block diagram of the equipment in the lab that enables us to take experimental data for use in reconstruction algorithms.

Appendix E The Specifications of the Simulated and the Experimental Measurements

In what follows the experimental and the simulated backscatter measurement parameters will be presented. The conditions that were simulated, e.g. the transducer size, the object size and the distance between the transducer and object, will be presented in units of meters. In the reverse direction, the parameters of the plane wave transducer available for experimental measurements will be presented and coverted into units of wavelengths of the center frequency of the transducer.

Simulated

The simulated results that are presented in chapters 3 and 4 make use of a 5 MHz center frequency transducer with a bandwidth of 6 MHz. This implies the following values of wavelength and wave number given that the speed of sound in water at 25°C is $c_o = 1494.04$ meters/sec.

$$\frac{2\pi}{k_H} = \lambda_H = 186.76\ \mu\text{m} \qquad k_H = 33.6440\ \text{rads/mm} = \frac{2\pi f_H}{c_o}$$

$$\lambda_C = 298.81\ \mu\text{m} \qquad k_C = 21.02750\ \text{rads/mm}$$

$$\lambda_L = 747.020\ \mu\text{m} \qquad k_L = 8.411\ \text{rads/mm}$$

The transducer consists of 512 samples spaced $0.5\lambda_H$ apart which is equivalent to 4.78093cm (1.88226 inches) in length. The distance of the face of the transducer from the center of the object is $l_0 = 20\lambda_H = 0.37351$cm (0.147051 inches). Since the highest spatial frequency used in the reconstruction is $2k_H = \frac{2\cdot 2\pi}{\lambda_H}$, the spatial nyquist frequency is $k_S = 4k_H$ rads/m and the temporal nyquist frequency is $f_T = 4k_H c_o/2\pi$ which is equivalent to 32MHz. Therefore the temporal signal that is the output of the transducer is sampled every $T_T = 0.25\lambda_H/c_o = 31.25$ ns. It is the maximum spatial frequency that determines the temporal nyquist frequency and not simply the highest temporal frequency within the bandwidth of the transducer. Since a 64x64 reconstruction grid is used, the spatial sampling interval in the reconstruction grid is

$$\Omega_S = 2k_H \frac{2}{64} = 2.10275\ \text{rads/mm} \quad .$$

Given Ω_S it is known that the 8th $(= 2k_L/\Omega_S)$ through the 32nd sample of the horizontal slice through the zero frequency sample of the grid, will be filled.

Experimental

The experimental backscattered wave measurements were made with a plane wave transducer focussed in the plane of the object with a focal length of 10 cm. The physical size of the transducer is 3 inches by 0.5 inch, and it has a center frequency of 5 MHz with a bandwidth of 3.5 MHz. Assuming that the full bandwidth of the transducer can be utilized, the highest and the lowest temporal frequencies are 6.75 MHz and 3.25 MHz respectively. Therefore

$$\lambda_H = 221.339\ \mu m \qquad k_H = 28.387 \text{ rads/mm}$$

$$\lambda_C = 298.81\ \mu m \qquad k_C = 21.02750 \text{ rads/mm}$$

$$\lambda_L = 459.705\ \mu m \qquad k_L = 13.668 \text{ rads/mm}\ .$$

The length of the transducer will be equivalent to 688.5358 $\frac{\lambda_H}{2}$. Since the focal length of the transducer is 10 cm it is logical to set l_0 equal to 10 cm = 451.795 λ_H.

The maximum sampling frequency of the lab's digitizer is $f_T = 100\text{MHz}$. Using this frequency, it follows that the spatial sampling frequency is $k_S = 2\pi f_T/c_o = 420.550$ rads/mm and the highest spatial frequency in the reconstruction grid is $0.5\, k_S = 14.815\, k_H$. Working backwards, if the desired maximum spatial frequency is $2k_H$ then the temporal sampling frequency need only be $f_T = 27\text{MHz}$ ($k_S = 113.549$ rads/mm). If $f_T = 27\text{MHz}$ is used, the reconstruction grid sampling interval is

$$\Omega_S = 2k_H \frac{2}{64} = 1.77419 \text{ rads/mm}$$

for the case of a 64x64 grid. The resulting coverage of the horizontal slice of the reconstruction grid that passes through the zero frequency sample, extends from the 15th sample to the 32nd sample. Obviously this coverage lacks samples 0 through 14 and is greatly inferior to the coverage that is simulated.

Appendix F The Dirac Delta Function

This appendix will briefly derive the form of the delta function in polar coordinates. To start the discussion we express the delta function in terms of the Fourier transform relationship which defines it,

$$\delta(x,y) = \int_{-\infty}^{\infty}\!\!\int e^{j2\pi(ux+vy)}\,du\,dv \ .$$

Carrying out the substitutions

$$x = r\cos\theta\ , \quad y = r\sin\theta$$

$$u = \rho\cos\phi\ , \quad v = \rho\sin\phi\ ,$$

and making use of the identity [Andrws]

$$J_o(\rho) = \frac{1}{2\pi}\int_0^{2\pi} e^{j\rho\cos\phi}\,d\rho\ ,$$

will yield the expression

$$\delta(x,y) = \int_0^{2\pi}\!\!\int_0^{\infty} e^{j2\pi rR\cos(\phi-\theta)}\,R\,dR\,d\phi$$

$$= 2\pi\int_0^{\infty} R\,J_o(2\pi rR)\,dR\ .$$

Using another Bessel function identity,

$$\int_0^{\infty} J_o(r\rho)\,\rho\,d\rho = \frac{\delta(r)}{|r|}\ ,$$

and noting that $\delta(\alpha x) = \delta(x)/|\alpha|$ since

$$\int_{-\infty}^{\infty} f(x)\,\delta(\alpha x) = \int_{-\infty}^{\infty} f(y/\alpha)\,\delta(y)\,\frac{dy}{|\alpha|} = \frac{f(0)}{|\alpha|} = \int_{-\infty}^{\infty} f(x)\,\frac{\delta(x)}{|\alpha|}\,dx\ ,$$

we have the proof of the transformation

$$\delta(x,y) \Longleftrightarrow \frac{\delta(r)}{2\pi|r|}$$

that results when the coordinate system is changed to the polar coordinate system.